IMPROVED GUST REJECTION FOR A MICRO COAXIAL HELICOPTER IN URBAN ENVIRONMENTS

A Thesis
Presented to
The Academic Faculty

by

Samuel R. Zarovy

In Partial Fulfillment
of the Requirements for the Degree
DOCTOR OF PHILOSOPHY in the
School of AEROSPACE ENGINEERING

Georgia Institute of Technology
DECEMBER 2014

IMPROVED GUST REJECTION FOR A MICRO COAXIAL HELICOPTER IN URBAN ENVIRONMENTS

Approved by:

Dr. Mark Costello, Advisor
School of Aerospace Engineering
School of Mechanical Engineering
Georgia Institute of Technology

Dr. William Singhose
School of Mechanical Engineering
Georgia Institute of Technology

Dr. Karen Feigh
School of Aerospace Engineering
Georgia Institute of Technology

Dr. Massimo Ruzzene
School of Aerospace Engineering
Georgia Institute of Technology

Dr. Eric Johnson
School of Aerospace Engineering
Georgia Institute of Technology

Date Approved: July 28, 2014

To my family and my pack

ACKNOWLEDGEMENTS

It has been a long, long journey and without the support and help of so many people I wouldn’t have made it. I would like to thank my advisor, Dr. Mark Costello, whose guidance, insight, and patience were invaluable to me. I applied to Georgia Tech because of its reputation; I choose to go to Georgia Tech after meeting him. I can’t say thank you enough. I would also like to thank the members of my committee, Dr. Eric Johnson, Dr. Karen Feigh, Dr. Massimo Ruzzene, and Dr. William Singhose for their time and advice helping to make my research the best that it could be.

My fellow graduate students provided me so much help, whether it was answering a question, being a sounding board, teaching me something new, or just being a friend, they were always there from me. So a hearty thank you to Mike Abraham, Jonny Rogers, Ryan Letniak, Eric Beyer, Vasu Manivannan, Jenna Stahl, Mike Ward, Kyle French, Jim Wright, Luisa Fairfax, Jessica Newman, Carlos Montalvo, Jack Mooney, Ed Scheuermann, Matt Gross, Thomas Herrmann, Dooroo Kim, and Martin Cacan. A special thank you to Emily Leylek who was not only a labmate and friend, but also a great roommate. When I started here it was simply the Costello Research Group and I couldn’t have asked for a better group.

Finally, thank you to my family. The unconditional love and support I have received from my entire family has been truly humbling. Mom, Dad, Jack, Anna, and Jess, I love you all. To my future wife, Dr. Kristen Gardner, all I can say is I love you. Thank you for everything you have done to help me get through this, and I can’t wait to spend more time with my pack.

TABLE OF CONTENTS

CHAPTER

LIST OF TABLES

Page

LIST OF FIGURES

LIST OF ABBREVIATIONS

2D	two dimensional
4D	four dimensional
ADRC	active disturbance rejection control
ADS	aeronautical design standard
AERMS	attitude error root mean square
ATG	active turbulence grid
AVRMS	angular velocity root mean square
CG	center of gravity
CFD	computational fluid dynamics
EKF	extended Kalman filter
ESO	extended state observer
FEPS	flight envelope protection scheme
IFF	Indoor Flight Facility
GINA	guidance and inertial navigation assistant
GRC	gust rejection control
IMU	inertial measurement unit
MTE	mission task elements
MRAC	model reference adaptive control
PD	proportional -derivative
PID	proportional-integral-derivative
PPM	pulse-position modulation
PSD	power spectral density
PWM	pulse-width modulation
SAS	stability augmentation system
SEP	spherical error probable
SUN	satisfactory update number
USB	universal serial bus

LIST OF SYMBOLS

A	rotor disk area
A_n	amplitude of a summed cosine frequency for digital simulation of a random signal
a	lift coefficient for angle of attack
$\bar{a}^{des}$	desired linear acceleration vector
$\bar{\alpha}^{des}$	desired linear acceleration vector
α	angle of attack
α_A	airmass inclination angle
β	rotor blade flapping angle
β_0	rotor blade collective flapping angle
β_{1C}, β_{1S}	rotor blade cyclic longitudinal and lateral flap angles
χ, ξ	longitudinal and lateral wake skew angles
$\mathbb{C}_X(Y)$	vector component operator that outputs a column vector comprised of the components of the input vector *Y* expressed in the reference frame *X*
C_d, C_l	blade element coefficients of drag and lift
C_{LR}, C_{UR}	coefficients of motor thrust for the lower and upper rotors
C_{lon}, C_{lat}	coefficients of longitudinal and lateral swashplate angles
c	rotor blade chord
c_X	cosine of X
$\bar{\Delta}$	state uncertainty vector
$\bar{e}_a$	vector of errors between the vehicle attitude and the commanded attitude

ϵ	rotor blade hinge offset
e	nondimensional hinge offset
$\bar{e}_{meas}$	vector of errors between measured states and the estimated states of the ESO
$\bar{\eta}$	extended state observer error vector
η_1, η_2, η_3	extended state observer error terms
η_k	measurement noise
ϕ, θ, ψ	Euler rotation angles for roll, pitch, and yaw
Δ	model uncertainty
$\Delta \mathrm{D}, \Delta \mathrm{L}$	blade element lift and drag
Δr	blade element width
$\Delta \omega$	discrete frequency interval for digital simulation of a random signal
g	gravity constant (9.81 m/s^2)
γ	Lock number
$H_{Y/Z}^{X}$	Angular moment of reference frame *Y* with respect to reference frame *Z* about *X*
$\bar{I}_{XX}, \bar{J}_{XX}, \bar{K}_{XX}$	unit vectors in the specified XX reference frame
$I_{b_{AA}}$	moment of inertia of rotor blade in AA direction
$[I]$	moment of inertia matrix of the vehicle\
k_β	rotor blade spring constant
l^*	distance from the rotor hub to the center of gravity of a rotor blade
ℓ_1, ℓ_2, ℓ_3	extended state observer functions

L, M, N	components of the total external moment acting on the vehicle expressed in the body reference frame
λ_i	nondimesional induced rotor inflow
μ	nondimensional advance ratio
Ω	angular rate of rotor in the shaft frame
$\Omega_{xS}, \Omega_{yS}, \Omega_{zS}$	body angular rate components expressed in the shaft reference frame
m_b	mass of a rotor blade
m	mass of vehicle
n_m	number of measurements
p, q, r	Body reference frame components of angular rate for roll, pitch, and yaw
ϕ_n	random discrete frequency added for digital simulation of a random signal
ψ_A	airmass yaw reference angle
ψ_R	Rotor blade azimuth angle
r_x, r_y, r_z	position vector components from the rotor blade hinge offset point (F) to the blade element aerodynamic center
ρ	atmospheric density
R	rotor blade radius
R^2	coefficient of determination
$\bar{r}_{A\rightarrow B}$	position vector from point A to point B
σ	rotor blade solidity
σ_X	standard deviation of X
s_X	sine of X

S_{XY}	power spectral density of X and Y
$\mathbb{S}_X(Y)$	skew-symmetric matrix representation of the vector *Y* expressed in the reference frame *X*
S	reference area
S_F	fit error
St	Strouhal number
SS_R	regression sum of squares
SS_T	total sum of squares
t_X	tangent of X
t	current time
τ_M	motor time constant
τ_{SW}	swashplate time constant
$\theta(t)$	rotor blade pitch
θ_0	rotor blade collective pitch
θ_t	rotor blade twist pitch
θ_{1C}, θ_{1S}	rotor blade cyclic longitudinal and lateral pitch
$\bar{u}$	vector of vehicle control inputs, split into controller outer loop and inner loop by adding subscripts *O* and *I* respectively
u_R, u_T, u_P	aerodynamic velocity components at a rotor blade element aerodynamic center in the radial, tangential, and perpendicular directions
u, v, w	translational velocity components of the vehicle mass center expressed in the body reference frame

u_{CP}, v_{CP}, w_{CP}	translational velocity components at the center of pressure expressed in the body reference frame
u_w, v_w, w_w	wind velocity components expressed in the body reference frame
u_{LR}, u_{UR}	lower and upper motor throttle inputs
u_{ϕ}, u_{θ}	longitudinal and lateral cyclic swashplate inputs
V	body translational velocity magnitude
V_{atmA}	body translational velocity component A expressed in the hub frame
V_c	vertical climb velocity
V_{CP}	velocity magnitude at the center of pressure
V_T	velocity magnitude at the tail center of pressure
$\bar{V}_{B\backslash A}$	velocity vector of body with respect to the airmass
$\bar{V}_w$	wind velocity vector
$\tilde{V}_w$	ESO based estimate of the wind velocity vector
V_{0x}, V_{0y}, V_{0z}	body translational velocity components expressed in the hub frame
$\bar{v}_{CG}$	translational velocity vector of the vehicle's center of gravity
v_h	induced inflow velocity at hover
v_{ix}, v_{ix}, v_{ix}	induced inflow velocity components expressed in the hub frame
$\bar{\omega}_{X/Y}$	angular velocity vector of reference frame *X* with respect to reference frame *Y*
ω_n	Nth discrete frequency for digital simulation of a random signal
x, y, z	position vector components of vehicle expressed in the inertial reference frame

X, Y, Z	components of the total external force acting on the vehicle expressed in the body reference frame
$\bar{x}$	state vector, split into controller outer loop and inner loop by adding subscripts O and I respectively
$\bar{x}^C$	state command vector, a combination of the reference trajectory and flight envelope protection scheme modifications
$\bar{x}^T$	reference trajectory state vector
$\bar{y}$	vector of measured states

SUMMARY

Micro rotorcraft on the order of tens of grams have a vast variety of potential civilian and military applications. As a result of their ability to carry different payloads, operate in confined spaces, and high maneuverability, micro rotorcraft are ideally suited to missions in urban environments such as surveillance, reconnaissance, and exploration of damaged or collapsed buildings. However, wind fields near the ground among buildings and other obstacles as well as indoors are extremely complex. Flows vary significantly both spatially and temporally, and wind speeds commonly exceed the maximum flight speeds of these vehicles. The results are conditions which are dangerous to even the most basic micro rotorcraft operations. While urban winds propose a large roadblock to use of micro rotorcraft, very little research and analysis has been conducted to understand and improve vehicle performance in winds and gusts.

This dissertation starts to fill this void in the literature. Both experimental flight tests and modeling and simulation tools are developed and executed to analytically understand the challenges and potential solutions to enable rotorcraft to operate efficiently and robustly in urban environments. A set of performance metrics were developed to provide a framework to assess mission-level performance of micro rotorcraft in both flight experiments and simulation trade studies. Inspired by established handling qualities specifications for manned rotorcraft, the metrics give a common comparison for rotorcraft in different wind features, for changes to the control architecture, and for analyzing vehicle design changes. An experimental testing methodology was also developed to capture flight performance of micro rotorcraft under laboratory conditions. This included the construction of an active grid turbulence generator which was shown to be capable of creating realistic prototypical wind kernels micro rotorcraft will experience as well as the definition of testing produces to make flight tests repeatable. Flight experiments for a commercial coaxial helicopter were performed to capture baseline response of a micro rotorcraft platform to urban wind kernels. The results show how poorly current micro rotorcraft perform in urban winds as well as illustrate the usefulness of the performance metrics and the testing methodology.

A high fidelity dynamic model of a coaxial helicopter was developed to accurately simulate vehicle response to urban wind disturbances. The model was validated using flight experiments in a motion capture facility. Additionally, a dynamic inversion based Gust Rejection Control architecture was developed for the dynamic simulation which included a novel wind estimation algorithm that was utilized to improve controller performance and create a flight envelope protection scheme that ensures the platform remains stable even in high winds the exceed the maximum flight speed of the vehicle. The high fidelity dynamic model was employed to perform a variety of trade studies to: analyze vehicle response to prototypical urban wind kernels, understand the affect of wind estimation on the control architecture, assess the level of model fidelity required to adequately simulate vehicle response to urban winds, and identify key platform design parameter trends to improve wind disturbance capabilities. Overall the results show the challenges micro rotorcraft face in urban environments while highlighting some trends that can be helpful for future design and analysis efforts such as: the time required to tilt the thrust vector of an underacctuated system and the corresponding sensitivity to low frequency disturbances, the importance of wind estimation to controller performance, and conditions which higher fidelity models are required.

CHAPTER 1

INTRODUCTION

Due to their small size, relative covertness, and high maneuverability, micro rotorcraft are ideal for a plethora of civilian and military applications in urban environments including: surveillance, monitoring, mapping, exploration of hostile environments, and search and rescue in damaged or collapsed buildings [1-4]. It is envisioned that these vehicles will operate indoors in relatively small complex spaces and outside near the ground among buildings and other structures. The aerodynamic velocity fields around buildings and trees and even inside buildings are notoriously complex with the mean winds varying spatially and temporally. These flow fields consist of many features which create sharp changes in wind magnitude and direction over small distances. This results in significant air flows with velocity and spatial perturbations on the same order of magnitude as the maximum flight speeds of these vehicles leading to stall, large attitude perturbations, and loss of control [5]. Moreover, disturbances of this magnitude are expected in normal operation, thus preventing micro rotorcraft from carrying out even the most basic missions. While wind gusts and turbulence represent a large obstacle for micro rotorcraft, no practical vehicle design and control system solutions exist to enable these small aircraft to fly in urban environments. Furthermore, relatively little research has been conducted to quantify performance and analyze platform response to wind gusts.

This thesis is focused on filling this void on micro rotorcraft performance in gusty urban environments. In support of this objective, modeling and simulation tools are developed to analytically understand the key wind features that drive response in wind gusts/turbulence as well as indentify flight control architectures and physical design parameters that will enable reliable flight in these settings. Additionally, an experimental methodology is developed to quantify and capture performance of micro rotorcraft platforms in realistic gust disturbances under laboratory conditions.

1.1 Micro Rotorcraft Gust Environment

Investigating and predicting the effects of urban wind fields is an active area of research for many scientific communities including wind engineering, industrial aerodynamics, environmental engineering, and civil engineering. Aims of these research efforts cover a wide variety of topics such as local wind environments, structural response to wind loads, diffusion and dispersion of pollution, power generation, urban planning, pedestrian comfort, and building ventilation [6,7]. State of the art research in wind engineering is driven by the modeling and analysis of wind fields through: direct wind field measurements in areas of interest as evidence by the work of Lane, Barlow, and Wood [8] and Wan, Li, Nui, Zong, and Li [9], wind tunnel experiments such as the work of Kopps and Banks [10] and Au and To [11], and numerical methods such as computational fluid dynamics work performed by Uffinger, Ali, and Becker [12] and Brusiani, de Miranda, Patruno, Ubertini, and Vaona [13].

Flow fields around buildings in urban areas are highly dependent on local conditions. A variety of parameters including free stream wind conditions, building orientations, weather patterns, and relative building sizes interact to create flows that vary significantly both spatially and temporally [14]. Figure 1.1 illustrates common urban wind features based off the work of Frost and Shahabi [15] and Nagib and Corke [16]: shears, vortices, separated and reattached flow, recirculating eddies, regions of accelerated flow, and regions of dead air. Furthermore, the local wind speed can be quite high even relatively low to the ground. Figure 1.2 shows the time history of the wind speed on the edge of a 5 m story high rooftop (Fig. 1.3).

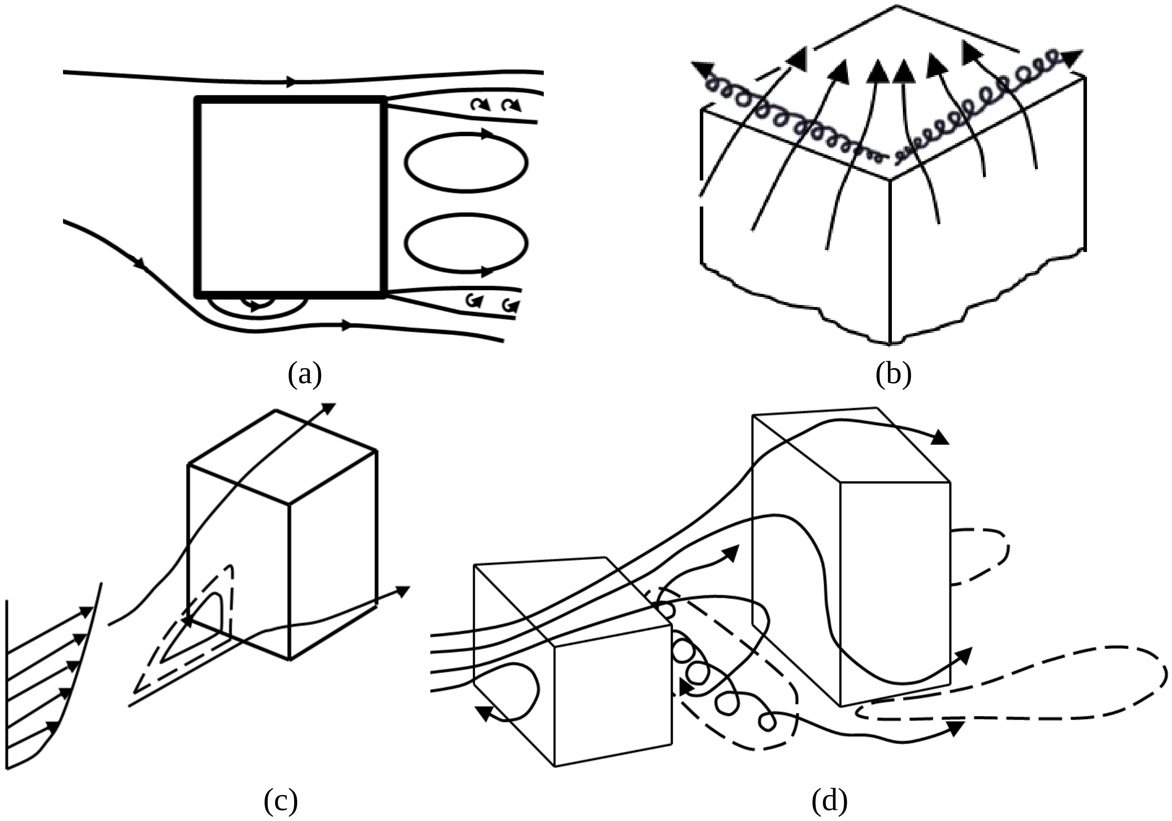
(a) (b)
(c) (d)

Figure 1.1. Illustrations of flow fields in urban areas. (a) Top view of a building (b) Roof top flow field (c) Boundary layer wind gradient acting on a building side (d) Interaction of two buildings.

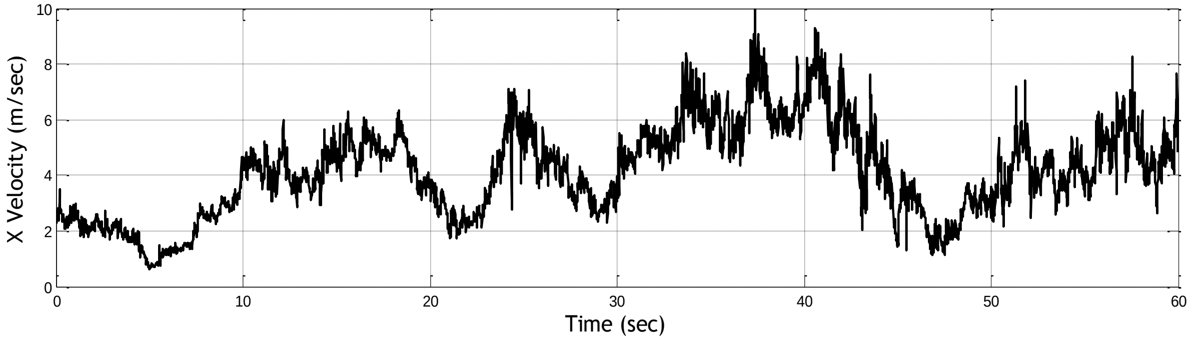

Figure 1.2. Horizontal wind speed measured on the edge of a one story rooftop.

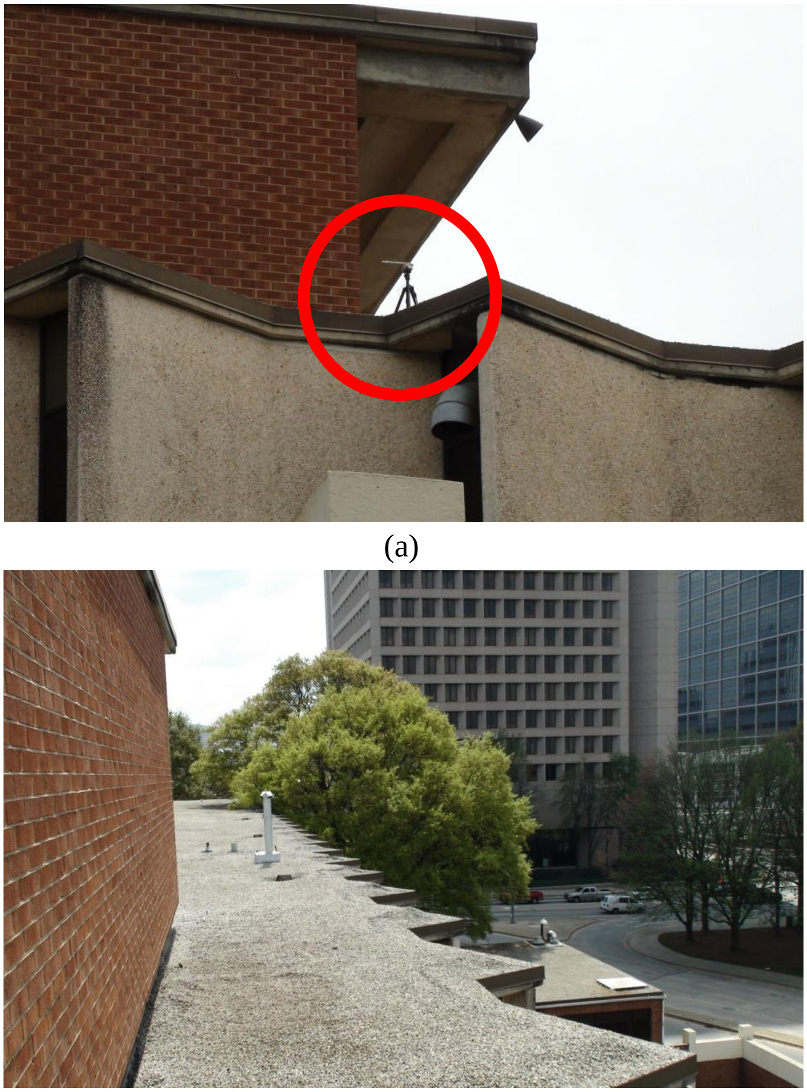

(a)

(b)

Figure 1.3. One story rooftop where wind speed was measured. (a) Hotwire on rooftop edge (b) View from rooftop of surrounding area.

The measurements were recorded using a hotwire anemometer on day where the average temperature was 82°F with a high of 95°F [17, 18]. The mean wind speeds reported at weather stations near the area were 3.2 m/s. In these average calm summer conditions, the wind speed on the rooftop varied from 1.0 m/s and 8.5 m/s in less than 40 seconds. It is clear micro rotorcraft must be able to operate in environments with complex flow structures where flight conditions can change rapidly to extreme levels—2 or more times greater than the maximum flight speed of micro rotorcraft.

Even in seemingly benign indoor environments the flow fields can have strong velocities and turbulent structures that make stable flight difficult. As described by Straube [19] , flow indoors comes from three main sources: pressure differences due to wind outside, temperature differences, and mechanical sources.

Wind acting on the outside front of a building creates pressure differences inside and on the rear side. Air flows are created by the pressure gradients through openings and leaks in the building (Fig. 1.4a). Johnson and Jacob found flow velocities at door openings as high as 5 m/s [20]. Building openings do not have to be perpendicular to the wind direction to cause air flows indoors. Computation fluid dynamics simulations performed by Hasma, Kato, and Ooka show that if there is an opening parallel to the flow a turbulent, circulating flow can be induced indoors, and depending on size of the opening and thickness of the wall different circulation patterns and vortex shedding frequencies are possible [21].

Temperature differences between the outdoor and indoor environments lead to air density differences which create air flows indoors (Fig. 1.4b). The “stack” effect is especially significant in regions where large temperature differences exist between the indoor and outdoor environments. When the outside temperature is much colder than the indoor temperature the density differences draw air in from the bottom of the building and push it out the top, while direction is reversed when the outside temperature is hotter than the indoor temperature [19].

Mechanical sources of indoor air flows include fans, air conditioning vents, grille intakes, diffusers, and all other HVAC equipment. As described by Conceição, Vicentea, and Lúciob, while general air quality and human comfort guidelines set by HVAC engineers require velocities to be relatively low in places occupied by people—less than 0.5 m/s in most cases—near mechanical sources the flow velocities can as high as 5 m/s [22].

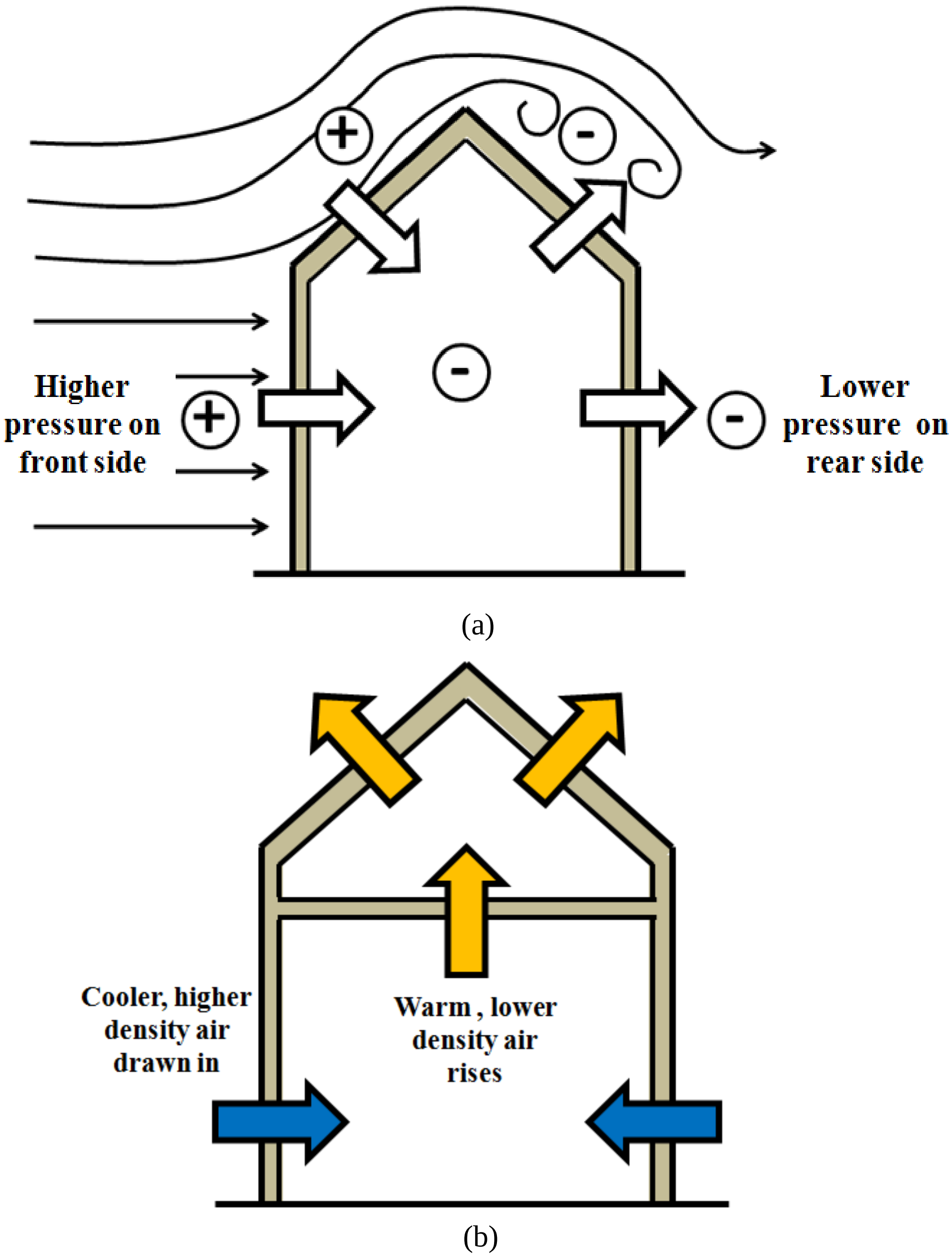

Figure 1.4. Illustrations of indoor gusts. (a) Pressure gradients (b) Stack effect.

While the maximum flight speeds of micro rotorcraft vary greatly for different platforms, published works show flight speeds to be as low as 2.0 m/s for coaxial rotor configurations reported by Pines and Bohorques [23] up to 10 m/s for a commercial single main rotor configuration by Proxdynamics [24]. It is expect that other configurations such as quadrotors would also fall around this range. Thus the wind gusts experienced during normal operation of micro rotorcraft are expected to be at least as large as maximum flight speeds of the vehicles. This issue is unique to micro rotorcraft as larger unmanned platforms and manned vehicles almost always have the control authority to dominate wind disturbances.

1.2 Unmanned Rotorcraft in Gusts

As mentioned earlier, the key aspects for operation in urban winds/gusts are modeling, control architecture, vehicle design, and response analysis. While there has been substantial research in these areas for unmanned rotorcraft overall, most of it has been performed for larger vehicles where the wind disturbances did not match or exceed the maximum flight speeds.

Dynamical modeling of unmanned rotorcraft (less than 100 kg) has been an active focus of research for more than two decades. Linear models with simplified rotor dynamics have been shown to adequately capture vehicle dynamics around hover, particularly for use in control law design. Mettler, Tischler, and Kanade developed a linearized model with first order rotor flapping dynamics and linear thrust coefficients to simulate the response of a 44 kg single main rotor helicopter [25]. They later extended this method to a nonlinear model of a single main rotor helicopter with simplified first order rotor dynamics [26]. Subsequent research has used first order rotor dynamics on small unmanned rotorcraft including single main rotor helicopters ranging from 9.4 kg to 300 g as well as coaxial helicopter platforms as small as 80 g [27-29]. However, simplified first order rotor dynamics and closed form thrust models do not account for wind gradients over the rotor disk which generate large aerodynamic moments on the helicopter. Additionally, research on full-size rotorcraft by Costello, Gaonkar, Prasad, and Schrage [30, 31] has demonstrated that to accurately capture the high frequency vehicle motion due to gusts and turbulence the local wind components on rotor blade elements must be taken into account. Simple, first order models do not appropriately capture the full affect of wind and gust disturbances on the rotor loads which limits their usefulness in simulating vehicle response in realistic wind environments.

Another active area of research is the design of gust rejection control algorithms for larger unmanned rotorcraft. This includes the work of Cherivon, Chriette, and Plestan who designed a robust control law through backstepping for a 7.3 kg helicopter with a maximum forward flight speed 30 m/s, and then used a high gain observer to estimate a spatial gust in simulation [32].The simulated lateral wind disturbance ramped from 0.0 m/s to 4.4 m/s and back in 4 seconds. A high gain observer was also used by Léonard, Martini, and Abba as part of the design of an adaptive feedback linearization controller. The controller was applied to a 625 g helicopter with a maximum forward flight speed of approximately 10 m/s [33, 34]. Test stand experiments and simulations, performed in constant wind gusts of 0.6 m/s, demonstrated improved gust rejection in the vertical and yaw channels.

Instead of estimating the wind, Bisgaard, la Cour-Harbo, and Danapalasingam presented a feedfoward control algorithm which used direct wind measurements to improve gust rejection of a 1 kg single main rotor helicopter [35]. For this work, the wind was measured using a ground station 3D ultrasonic anemometer which transmitted the information to an off board computer for control computation during flight in 8 m/s wind gusts. Yang, Pota, and Garratt proposed another approach, employing moving average filters on vertical velocity and acceleration measurements to estimate changes in main rotor thrust due to horizontal wind gusts [36]. Simulating an 8 kg helicopter in slowly varying turbulent winds with a maximum of 15 m/s, disturbance estimates were used to improve landing maneuvers. The simulated disturbances represented approximately 40-50% of the maximum flight speed. Alexis, Nikolakopoulos, and Tzes also developed controller for a 538 g quadrotor in higher gust levels [37]. An extended Kalman filter was used to estimate a disturbance vector, and gimbaled test stand experiments validated that a model predictive controller could reject a 5.5 m/s discretely changing gust. This disturbance magnitude represented 60% of the maximum flight speed. The work of Yang, Pota, and Garratt and Alexis, Nikolakopoulos, and Tzes are two of the very few examples of control law design for disturbances that represent 50% of the vehicle's maximum forward flight speed.

While there has been some development of control algorithms for gust rejection, very little research has been reported on analyzing performance in wind gusts and identifying design improvements to increase micro rotorcraft gust rejection. Two exceptions are the works of Hrishikeshavan and Chopra, and Rezgui, Lowenberg, and Bunniss. Hrishikeshavan and Chopra performed experimental tests of a 260 g shrouded rotor micro air vehicle in constant gusts to analyze attitude stability and gust rejection capabilities [38]. Bench-top experiments performed by placing the vehicle on a gimbaled stand at the exit nozzle of a wind tunnel measured the response of the rotorcraft to wind disturbances to determine the maximum gust magnitude and direction the platform could reject. It was found the shrouded rotor platform had the control authority to reject gusts up to 1.9 m/s. Rezgui, Lowenberg, and Bunniss considered useful design modifications of a 200 g coaxial helicopter to improve stability and controllability in wind gusts and turbulence [39]. Based on qualitative pilot feedback, changes including moving the center of gravity forward and increasing the size the of the vertical fin allowed the vehicle to be manually flown in slow ramping gusts up to 4 m/s in strength. In both the works of Hrishikeshavan and Chopra, and Rezgui, Lowenberg, and Bunniss, the rotorcraft were subjected to mostly smooth constant gust disturbances which, while helpful in developing baseline vehicle gust rejection, does not take into account the highly complex and varying gust and turbulence fields micro rotorcraft encounter.

1.3 Full-Scale Manned Aircraft in Wind Environments

Atmospheric disturbances have challenged aircraft designers since first flight, and there is an extensive background of literature on the subject. Thus, it is insightful to examine the aircraft specifications and handling qualities used to analyze vehicle response to wind and gust disturbances as well as relevant research on modeling and control algorithm design for operations in complex flow fields similar to the ones expected in urban environments.

Fixed wing aircraft flying qualities in atmospheric disturbances are generally assessed through simulations models where the turbulence model parameters are known or with flight tests where measurements are used to estimate turbulence intensity and length scale as described by Hoblit [40]. At high altitudes, continuous random turbulence models such as the von Karman and Dryden models are used to replicate disturbances [41]. For low altitudes, models of discrete gusts and wind shears are also employed. According to military specifications, fixed wing aircraft flying qualities are quantitatively and qualitatively assessed for various mission flight phases using the appropriate disturbance models for light (5 m/s), moderate (15 m/s), and serve (23 m/s) mean wind speeds [42].

Specifications for assessing the flying qualities of V/STOL aircraft are similar to fixed wing vehicles as vehicle performance is analyzed during various mission flight phases for select atmospheric disturbances [43]. The aeronautical design standard (ADS-33E-PRF) assesses performance of rotorcraft though the completion of Mission Task Elements (MTEs) such as hover, hover turns, pirouettes, and vertical maneuvering in moderate winds (steady wind components of 10 to 18 m/s). Satisfactory completion of the MTEs is achieved through a combination of position and attitude error limits, time to complete the task, and pilot handling quality ratings [44]. Additionally, response to gusts and turbulence is associated with pilot and flight control system bandwidth thresholds; cut off frequencies are established from frequency response analysis as reported by Labows [45].

As mentioned in the previous section, local wind components on rotor blade elements must be taken into account to accurately model aircraft response to spatially varying gusts and turbulence. The rotational motion of the blades through a spatially varying wind fields results in sustainably different atmospheric velocities at rotor blades than on non-rotating aircraft components inducing moments on the rotorcraft. The rotational effects decrease for increasing flight speed, thus it is important to account for them at low speed flights and near the ground where spatial variation of the wind field is most significant.

One such scenario is when rotorcraft operate in ship airwakes. The atmospheric wind conditions and sharp edges of a naval-ship super structure interact to create highly turbulent, spatially varying, recirculating flows; which is an analogous environment to what micro rotorcraft experience in urban environments. Hess employed simplified models to study piloted rotorcraft near ships and found that ship airwake conditions drastically increase pilot workload and risk when operating on and around ship [46]. Lusardi, Tischler, Blanken, and Labows experimentally re-created this operating scenario by measuring the response of a UH-60 Black Hawk to turbulent conditions while hovering behind a “cube-like” hangar on a windy day [47]. Lee and Horn simulated flight response data of a helicopter using CFD ship airwake models and a high fidelity helicopter model, GENHEL [48]. In both cases, turbulent gust models were developed by creating spectral filters which, when driven by white noise, replicate the power spectral density of the disturbances. It was found that spectral filter gust models accurately simulated helicopter response.

Solutions to improving rotorcraft performance in highly turbulent wind fields such as ship airwakes has been mainly focused on enhancements to the flight control system. Various control architectures including stability augmentation system (SAS), H_2, H_∞, and nonlinear model following were used to increase gust rejection of the UH-60 Black Hawk. The V-22 osprey has also shown sensitivity to ship airwake turbulence. In the spatially varying velocity flow field, asymmetric rotor impingement caused by lateral separation of the rotors dangerously reduces roll stability. High fidelity simulations and validation flight tests were used by Miller, Morse and Wood [49] and Miller, de Brun, Lu, and Hagar [50] to demonstrate that active digital flight control technologies and structured software design improved operational effectiveness and roll stability of the vehicle.

While gust rejection and operation in turbulent environments has been a challenging problem for manned rotorcraft, the gusts and mean wind magnitudes are still much smaller relative to the maximum vehicle flight speeds. The 15 m/s wind over deck scenario studied by Horn, Bridges, and Lee [51, 52] and the 8.6 m/s average wind gust measured by Lusardi, Tischler, Blanken, and Labows [47] respectively represent 19% and 11% of the 78 m/s maximum flight speed of a UH-60A Black Hawk [53]. Even taking into consideration the roll instability created by asymmetric rotor impingement of the V-22; these wind conditions still represent a small percentage of the vehicle’s 128 m/s maximum forward flight speed [54]. For micro rotorcraft, the expected wind fields represent much larger disturbances and need to be dealt with differently than for full sized manned vehicles or larger unmanned systems.

1.4 Thesis Description

This thesis starts to fill the void in research on micro rotorcraft operating in urban environments by studying means to improve the performance of a micro coaxial helicopter in realistic urban winds. Contributions of this thesis include:

1. Creation of general metrics relevant for quantifying and assessing micro rotorcraft performance in realistic gust disturbances
2. Understanding the role of spatial and temporal wind gust structure on the response of micro rotorcraft
3. Exploration of a specialized gust rejection control architecture for micro rotorcraft which estimates local wind conditions in realtime and specifically accounts for flight in wind velocities which exceed the maximum flight speed of the vehicle
4. Identification of key vehicle platform design parameters of a coaxial helicopter that are important for gust rejection.

This thesis is composed of seven chapters. Chapter 1 serves as the introduction including a description of the problem statement, the previous work on the topic, and the contributions of the present work. Chapter 2 details an experimental methodology for analyzing micro rotorcraft gust performance—novel performance metrics and an associated experimental setup for assessing the wind/gust rejection capabilities of micro rotorcraft. A baseline study of a micro coaxial helicopter is performed to demonstrate the methodology. Chapter 3 derives a nonlinear mathematical model for a micro coaxial helicopter used in simulation trade studies. The model parameters are identified for an experimental helicopter in Chapter 4. Model accuracy is also assessed. Chapter 5 develops the Gust Rejection Controller—a nonlinear control architecture which estimates and adapts to wind disturbances, as well as includes a protection scheme to ensure the vehicle does not go unstable when operating in wind velocities that exceed the maximum flight speed. Using the validated dynamic models and the Gust Rejection Controller, trade studies are performed and reported in Chapter 6. Trade studies include response to fundamental wind and gust field features, control architecture differences, model fidelity for simulation of wind gradients, and the effects of vehicle platform design parameters on gust rejection capabilities. Chapter 7 discusses additional applications of the wind estimation algorithm developed as part of the Gust Rejection Controller and shows initial results of a helicopter mass estimation trade study. Chapter 8 finishes the thesis with conclusions and future work.

CHAPTER 2

EXPERIMENTAL METHOD FOF ANALYIZING MICRO ROTORCRAFT GUST PERFORMANCE

As noted in the previous chapter, there is not much literature on the abilities of micro rotorcraft to operate in realistic wind fields. As a result, there is very little understanding of the flight control system and vehicle design guidelines that should be followed to ensure rotorcraft of this scale operate safely and reliably in urban wind fields. In response, a novel methodology was created to evaluate the capabilities of micro rotorcraft in realistic wind conditions. The concept is similar to rotorcraft design and handling qualities manuals such as ADS-33E where a set procedure is employed to analyze flight response of a rotorcraft platform in relevant wind environments. To achieve this, a micro rotorcraft platform is subjected to prototypical wind and gust fields while performing mission-based flight maneuvers. Afterward, the vehicle's ability to operate in the presence of the disturbance is assessed.

This methodology can be applied in both laboratory and simulated flight test experiments. In the laboratory, a synthetic wind generation system was constructed to create repeatable and controllable gust excitations; then a motion capture system was used for precise measurement of vehicle response. In simulation, wind and gust models were developed based on the experimental flow fields, and when combined with a high fidelity vehicle dynamic model, the same procedure can be applied. For both settings, performance metrics associated with the accuracy of command tracking, angular rate excursions, control input variation, and total energy consumed were created to quantify vehicle capabilities at different excitation levels. Metrics were meant to be platform and controller independent to allow evaluations of different vehicle configurations.

Overall, the experimental method is flexible, enabling any rotorcraft platform to be assessed in realistic expected wind fields for mission-relevant flight maneuvers. This chapter details the wind generation system and derived wind models, the motion capture system used in laboratory testing, and the performance metrics for assessment. Also reported are the results of a baseline study for a micro coaxial helicopter using the experimental method.

2.1 Synthetic Wind Generation System and Wind Modeling

In order to assess micro rotorcraft flight performance in urban winds, realistic wind fields are required to be generated in the laboratory and modeled for use in simulation. Since real world urban wind environments are incredibly complex, it was necessary to create several baseline wind gust kernels that simulated prototypical urban wind features. This section details the equipment built to generate the gust kernels reliably in laboratory conditions as well as the method used to develop simulation models from the experimental flow fields.

The synthetic wind generation system built for this work consists of an eight foot diameter fan, an active turbulence grid (ATG), and a hotwire anemometer. The fan pushes air through the ATG which injects energy at different frequencies into the flow to create realistic spatially and temporally varying gust flow fields. The ATG is comprised of a large square frame with rotating vanes that have diamond shaped plates mounted to the surface. These vanes come in two sets, eight that spin horizontally and eight that spin vertically. The vanes are then controlled by stepper motors to obtain precise rotation. The design is similar to that of Makita [55] and is modeled after smaller grid built by Sytmsa and Ukeiely [56]. Figure 2.1 shows the fan with the vanes closed (Fig. 2.1a), with the vanes open (Fig. 2.1b), and the hotwire anemometer used to measure generated flows.

By controlling the position and rotational speed of the motors, the ATG can generate wind fields with harmonic content as well as different realistic features. For example, by driving the vanes back and forth in a sinusoidal manner, a sinusoidal velocity profile is induced as seen in Fig. 2.2 where the main low frequency signal can be seen along with a high frequency noise component.

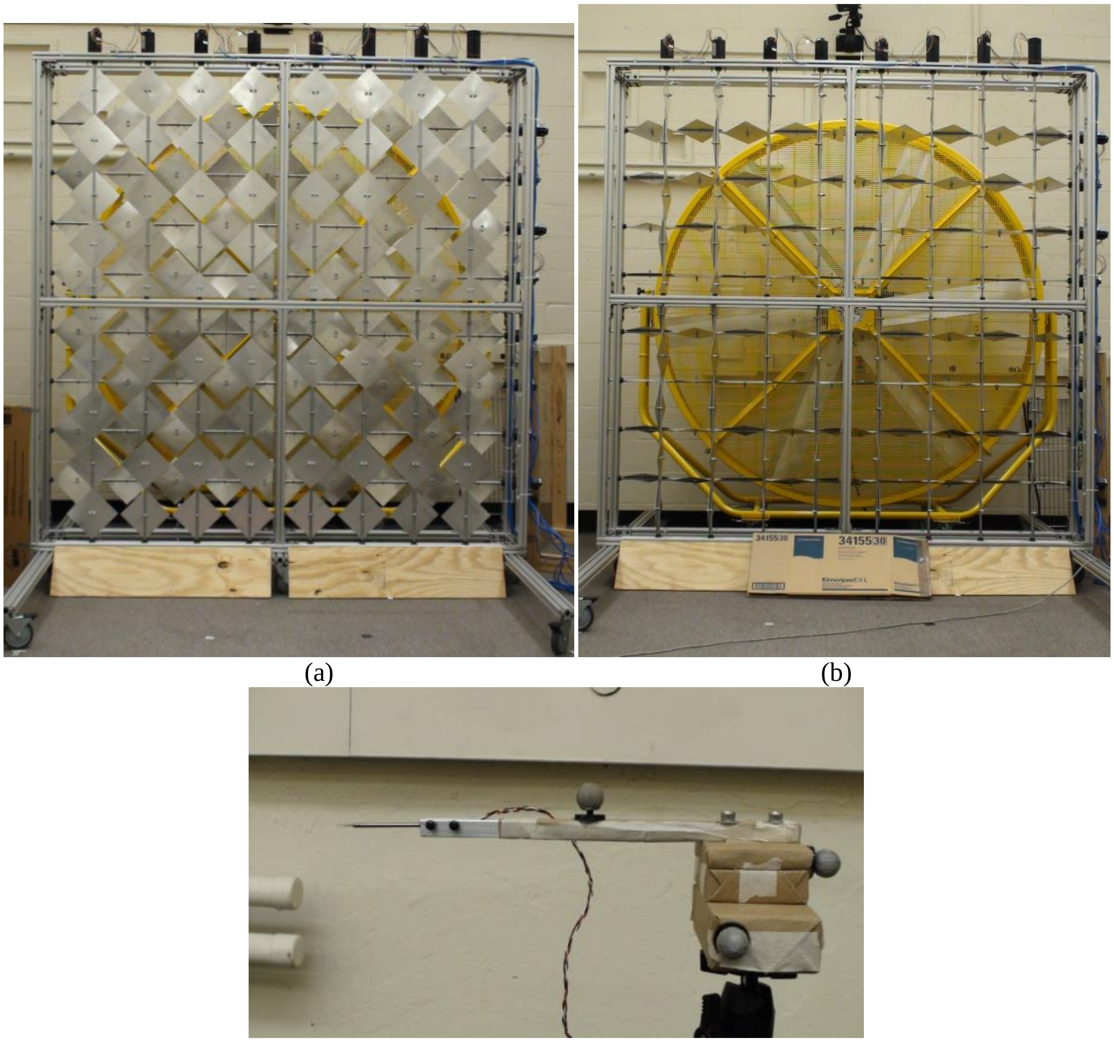

(a) (b)

(c)

Figure 2.1. Synthetic gust generation system. (a) Fan and active turbulence grid, grid closed (b) Fan and active turbulence grid, grid open (c) Hotwire anemometer.

Since the motor can be controlled to move in any manner desired, the ATG can produce a wide variety of wind gust kernel including:

- Engulfing, where the vanes are slowly opened to simulate a gust that gradually increases in velocity 'engulfing' the vehicle.
- Discrete shutter, which is created by a discrete opening of the wind vanes moving from fully closed to fully open as quickly as possible. This wind kernel represents a rapid change in local wind velocity such as when a vehicle flies by an open window or air conditioning vent.
- Continuous Shutter, a mixture of the discrete shutter and engulfing kernels results in a more gradual rise to a sharp peak.

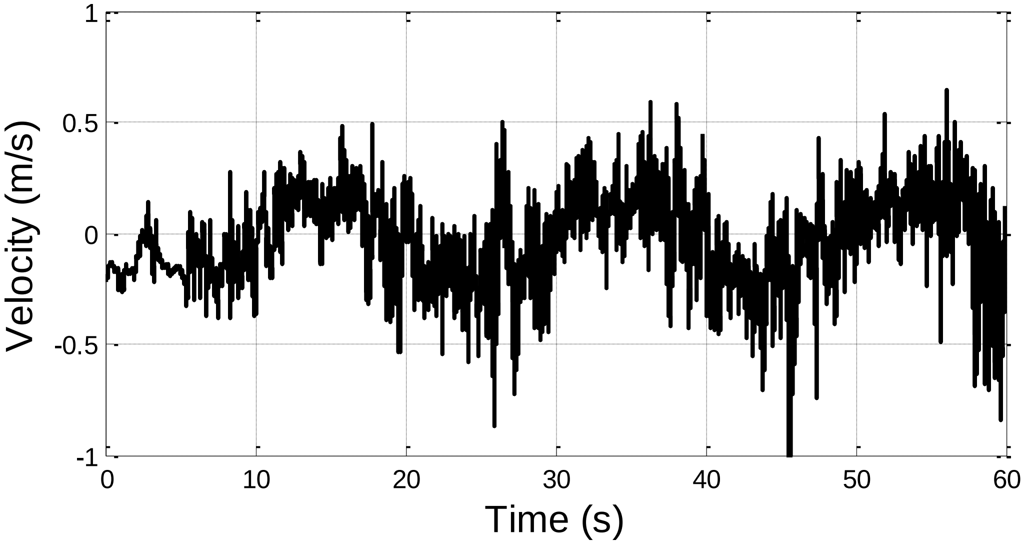

Figure 2.2. Experimental sinusoidal wind kernel.

The flow field is measured using a hotwire anemometer (Fig 2.1.c) to capture time histories of the velocity components at multiple locations in the flow. A single X-wire anemometer records the flow velocities created by the ATG at one location. After which the hotwire is moved, the vane motion of the ATG is rerun, and the process is repeated. The flow is assumed to be a frozen field where the flow convects over the sensor with a mean wind speed. Therefore discrete spatial measurements taken can be used to construct a three dimensional time history map of the flow velocities to document experimental fields as well as build simulation models of flow fields. A wind gust kernel model is then developed using a shaping filter driven by white noise with the same power spectral density (PSD) content as the measured field. This approach is based on the work of Shinozuka [57, 58], and is similar to turbulence models developed for full-scale helicopters operating in ship airwakes as described in Chapter 1 [46-48]. The PSD for a signal is created as

$$f(t) = \sqrt{2}\sum_{n=0}^{N-1} A_n \cos(\omega_n t + \Phi_n) \tag{2.1}$$

Given:

$$A_n = \left(2S_{f_of_o}(\omega_n) \bigtriangleup \omega\right)^{1/2} \tag{2.2}$$

$$\omega_n = N \bigtriangleup \omega \tag{2.3}$$

$$A_0 = 0 \text{ and } S_{f_of_o}(0) = 0 \tag{2.4}$$

where $S_{f_of_o}$ represents the PSD. After the PSD is obtained a series of cosine waves are summed together with their amplitudes and frequency calculated from the PSD each having a random period shift. This ensures that the simulated wave has approximately the same PSD as the sampled signal. The mean is then added back into the simulated signal. Figure 2.3 shows a comparison of the PSD of the experimentally measured sinusoidal wind kernel with the simulated data—where 1200 points are used to reconstruct the PSD so it contains the same total energy as the experimental wind. Figures 2.4 through 2.7 compare velocity wind histories for the experimental and simulated wind kernels: sinusoidal, engulfing, discrete shutter, and continuous shutter respectively. The figures show how accurately the modeling methodology can reproduce experimental results.

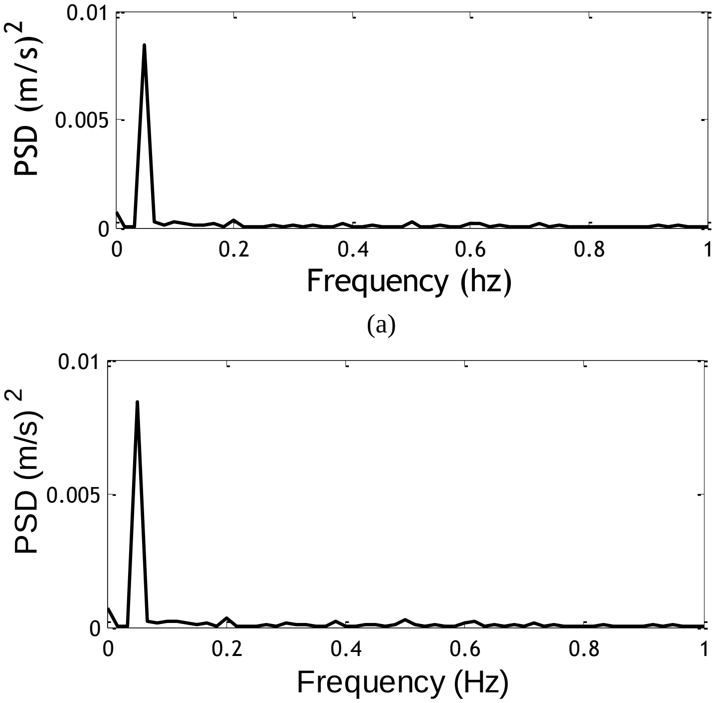

(a)

(b)

Figure 2.3. Power spectral density of sinusoidal wind kernel. (a) Experimental (b) Simulation.

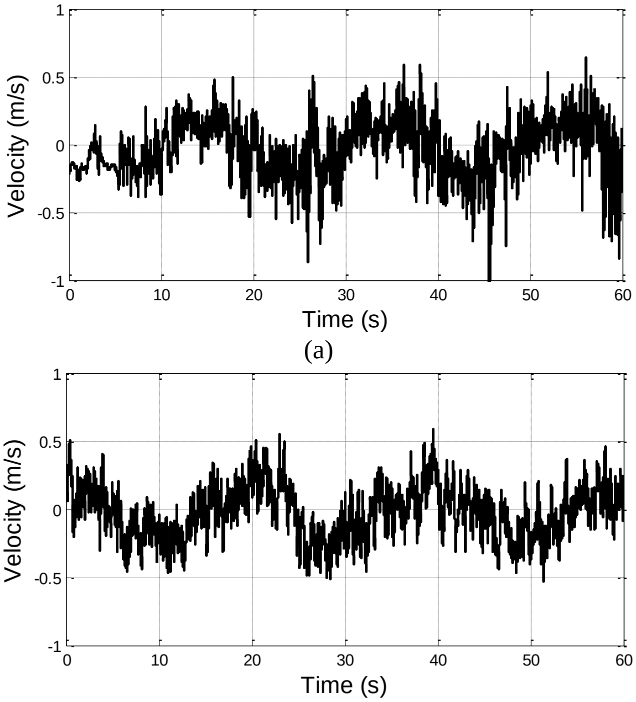

(a)

(b)

Figure 2.4. Velocity time history of sinusoidal wind kernel. (a) Experimental (b) Simulation.

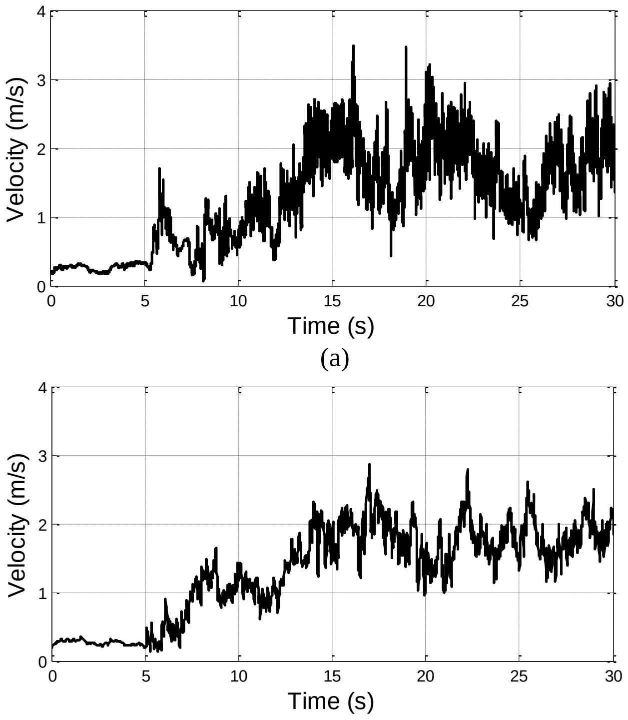

(a)

(b)

Figure 2.5. Velocity time history of engulfing wind kernel. (a) Experimental (b) Simulation.

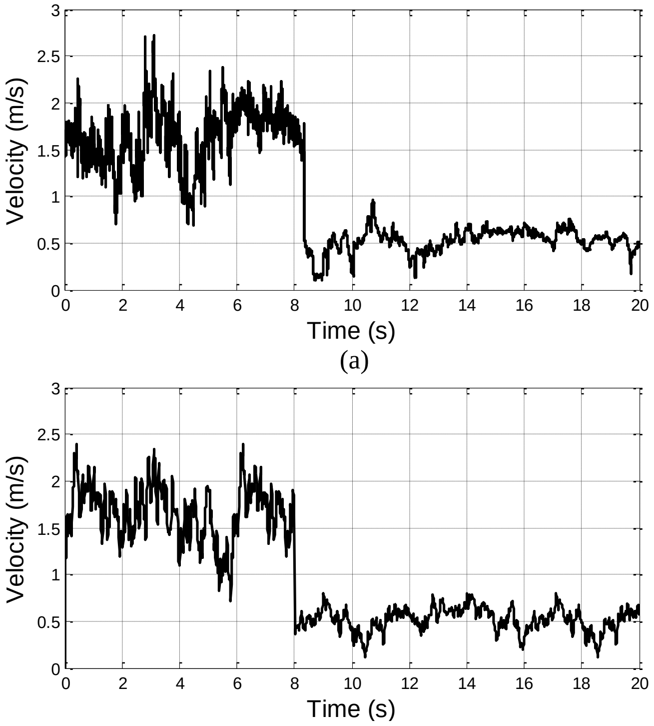

(a)

(b)

Figure 2.6. Velocity time history of discrete shutter wind kernel. (a) Experimental (b) Simulation.

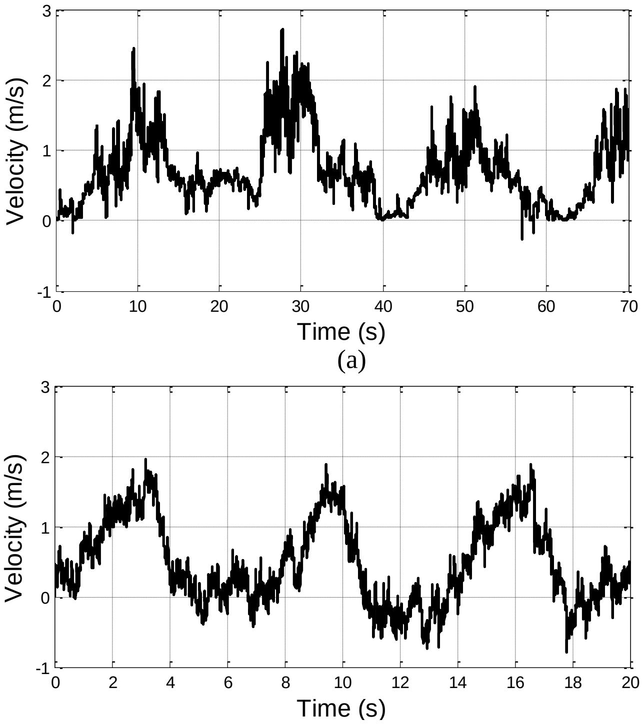

(a)

(b)

Figure 2.7. Velocity time history of continuous shutter wind kernel. (a) Experimental (b) Simulation.

For each kernel, the number of points for simulation is selected to match the total energy in the power spectral density. Once the wind kernel model has been derived, the model parameters such as mean wind magnitude, driving frequency, and turbulence scale factor can be adjusted to simulate a variety of cases to test micro rotorcraft. The ATG enables micro rotorcraft to be flight tested in realistic prototypical urban gust fields as well as provide an experimental basis to derive realistic models for use in simulation.

Overall the simulations capture the general motion and frequency content of the experimental winds, however there is some very high frequency content that is not matched exactly. This is due to the limited number of points used to reconstruct the PSD and while it does demonstrate that the model is an approximation of the real signal, the high frequency changes happen so quickly that the effect on micro rotorcraft flight dynamics is minimal.

The measurements of wind speeds and velocity profiles for the wind kernels described in this section represent a limited number of scenarios. As mentioned in Chapter 1, the existing data for urban wind environments is generally collected through field measurements such as the work of Rotach [59], wind tunnel experiments such as the work of Frank and Mauch [60] and Farrel and Iyengar [61], and computational fluid dynamics such as the work of Straw, Baker, and Robertson [62]. In general, most work focuses on capturing the complex flow fields in different urban settings. Some work such as Nagib and Corke [16] and Tamai, Okuda, and Katsura [63] have looked specific prototypical features which are similar to the approach taken here. The limitations of the ATG to replicate urban winds are mainly due to fan dynamics, vortex shedding from the grid, and air flow and room geometry. The 8 foot diameter fan adds a small rotational energy to the flow which is not corrected, however if this was a large issue a flow straightener could be added to the system between the fan and the active grid. When the vanes are held open to achieve a steady state flow, the rods of gird create shed vortices on the length scale of the grid spacing—0.25 m. This grid spacing was chosen on purpose to be on the order of the length of micro rotorcraft as to excite the vehicles at frequencies where they are sensitive. Additionally there are some long term fluctuations in the wind velocity which are caused by the dynamics of the flow in the laboratory. This is because the laboratory is a closed room with no air return. Fluctuations due to room geometry can be seen in the high wind phases of the experimental engulfing (Fig. 2.5a from 15 seconds to 30 seconds) and discrete shutter winds (Fig. 2.6a from 0 seconds to 8 seconds). While these issues limit the ability of the ATG to precisely control the laboratory wind fields, the flows generated still capture the overall effect of each wind kernel described.

2.2 Motion Capture System

A motion capture system is employed to measure rotorcraft response to gusts during experimental flight tests. Measurements are highly accurate and can be set to a sufficiently high sampling rate without the need to add sensors to the platform. The motion capture system in the Indoor Flight Facility (IFF) at Georgia Tech consists of a twelve camera VICON motion capture system as shown in Fig. 2.8. The infrared cameras use 3D optical position analysis to calculate the position of spherical retro-reflective markers to within 1 mm accuracy [64, 65]. In real time, the marker positions are used to calculate vehicle position and attitude. Through appropriate filtering, state derivatives are calculated allowing real-time full state feedback for the vehicle. This system allows the flexibility and space to construct realistic wind environments and study micro rotorcraft free flight response in such conditions.

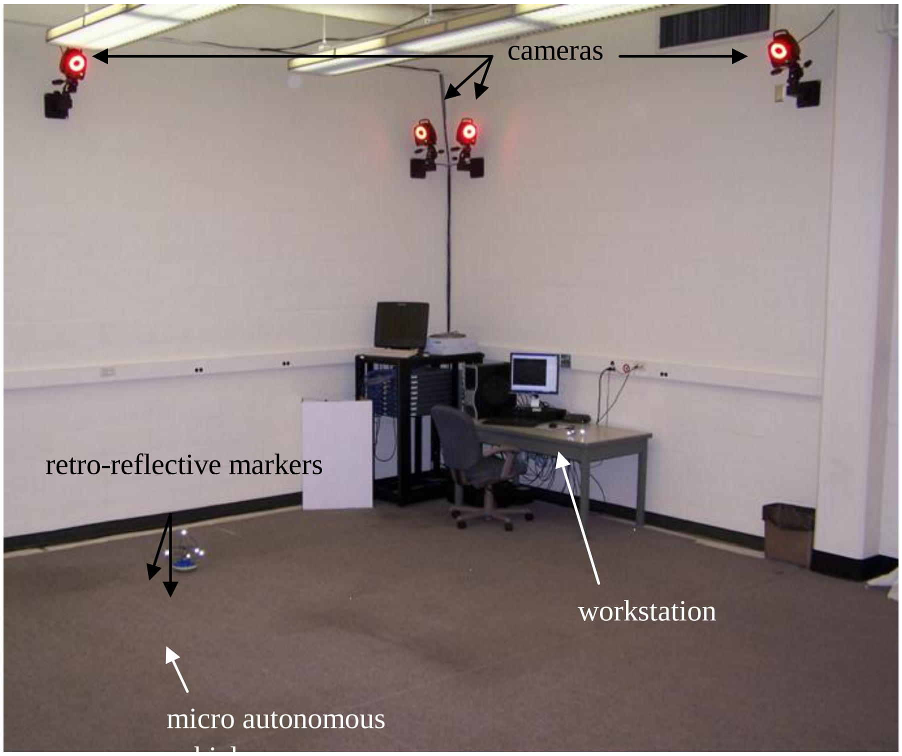

Figure 2.8. Georgia Tech Indoor Flight Facility with VICON motion capture system.

2.3 Performance Metrics

Performance metrics are defined to evaluate vehicle performance while operating in urban wind fields. Similar to ADS-33E-PRF, metrics for command tracking accuracy and workload during flight are measured during basic mission task elements expected of micro rotorcraft. These metrics are tailored specifically for autonomous micro rotorcraft and allow users to evaluate performance in different wind gust fields, assess vehicle design, and compare distinctly different types of platforms. Since micro rotorcraft most commonly operate near hover, the performance metrics are focused on mission task elements for the hover and near hover flight regimes, but can be easily extended to any flight maneuvers.

An important attribute of micro rotorcraft is the ability to precisely hover, which enables operation in tight complex urban environments. The spherical error probable (SEP) is defined as the radius of a sphere centered at a commanded hover position that encircles 50% of the trajectory during a gust event (Fig. 2.9). The SEP provides a simple metric to assess position hold capabilities of a rotorcraft platform when excited by disturbances. It can also be extended to a time varying tracking by moving the commanded point along the specified trajectory.

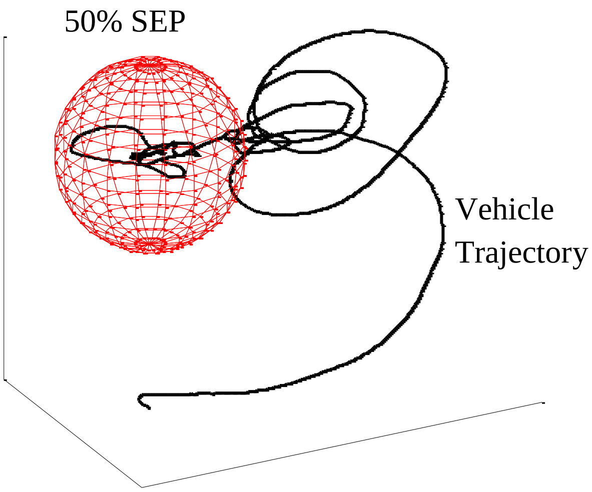

Figure 2.9. Illustration of SEP for a hover flight test.

Angular vibrations caused by wind disturbances affect attitude hold accuracy, as well as degrade data quality from onboard sensors. The angular velocity root mean square (AVRMS) is a simple measure of the variation of the magnitude of the angular velocity from the mean value during a flight event:

$$AVRMS = \sqrt{|\bar{\omega}|^2 + \sigma_{|\bar{\omega}|}^2} \tag{2.5}$$

where $|\bar{\omega}|$ is the mean angular velocity magnitude and $\sigma_{|\bar{\omega}|}$ is its standard deviation. Figure 2.10 shows experimental measurements of body angular velocity for 0 m/s and 2 m/s winds with the AVRMS overlaid. An example of vibrations affecting sensor data quality is pixel blur, which is a measure of the number of pixels a point travels during exposure. Figure 2.11 shows examples of pictures taken with pixel blur of 2 pixels and 40 pixels as examples of pixel blur can affect picture quality. The AVRMS metric captures attitude response during flight and is useful for understanding the limiting conditions for different sensor suites on a micro rotorcraft platform.

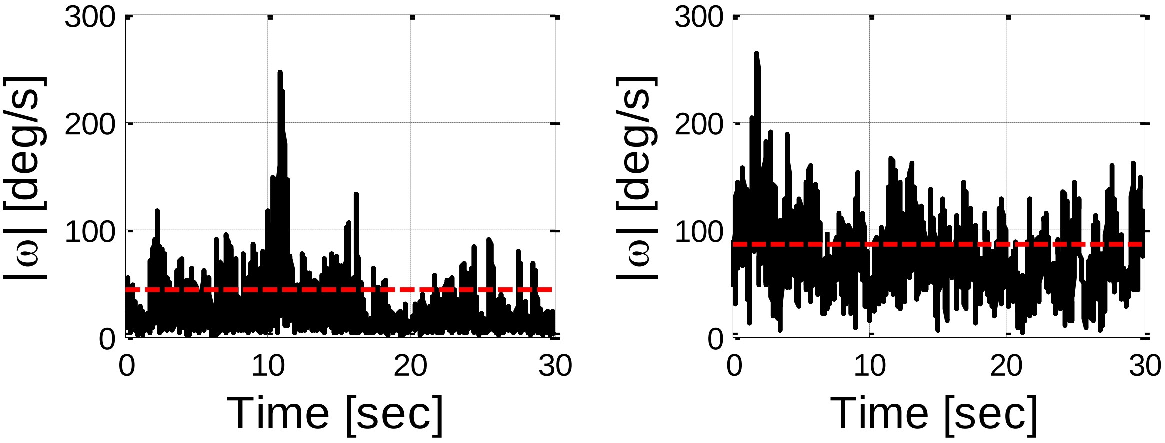

(a) (b)

Figure 2.10. Example time histories angular velocity magnitude with RMS value overlaid. (a) In no wind, 25.7 deg/s AVRMS (b) 2.0 m/s constant wind, 92.9 deg/s AVRMS.

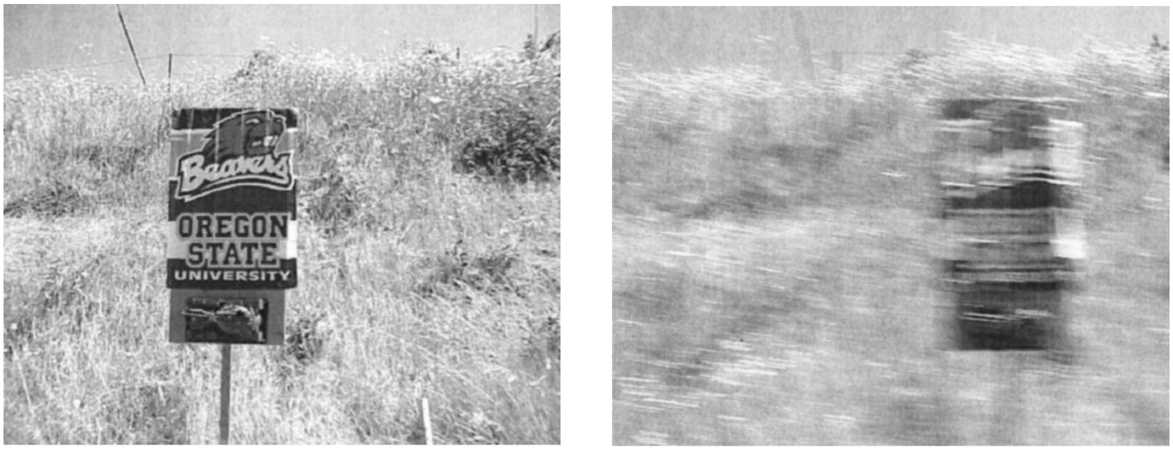

(a) (b)

Figure 2.11. Example of pixel blur from Frost and Costello [66]**.** (a) 2.0 ± 0.5 pixels (b) 40 ± 5.0 pixels.

A similar metric can be applied to the attitude tracking capabilities of the vehicle. The attitude error root mean square (AERMS) is defined as

$$AERMS = \sqrt{|\bar{e}_a|^2 + \sigma^2_{|\bar{e}_a|}} \tag{2.6}$$

where $\bar{e}_a$is the error between the vehicle attitude and the commanded values. Thus AERMS is a measure not only of attitude tracking accuracy but also of the variation of the vehicle attitude about the command value during flight.

While SEP, AVRMS, and AERMS all quantify position and attitude tracking performance, it is also insightful to capture control effort during flight. Since there is no pilot to provide feedback on rotorcraft handling qualities, numerical calculations are used. The standard deviation of control input response provides a convenient measure of the input variation about some mean. A large variation in control input implies the need for constant correction to fly the vehicle.

Therefore the standard deviation captures control workload. Even though the micro rotorcraft studied here are autonomous, making constant corrections achievable, control workload is an important assessment tool for ease of operation. Jenkins, Ifju, Abdulrahim, and Olipra propose that the micro air vehicles which are easiest to fly are the most successful in the real world [67]. It is expected that in gusty and turbulent wind fields the control standard deviation will increase for all platforms, however the relative control workload in windy environments is still insightful. Additional metrics that are used to understand control workload are average control margin during the mission task element and the percentage of flight time the control input is saturated. Control margin is defined as the percentage of control input between the current control state and the 100% maximum value. The average control margin is then calculated over the entire flight. The control metrics are calculated for each input channel during a flight event. Figure 2.12 shows how a steady wind effects control standard deviation for example time histories of throttle input in no wind and in 2.0 m/s wind. For no wind (Fig 2.12a), the throttle standard deviation is 0.15 PPM and the average control margin is 0.293 PPM over the entire flight which correspond to 15% and 29.3% of the total control margin respectively. Comparatively, in a 2.0 m/s wind the control standard deviation is 19.5%, the average control margin is 21.3%, and the throttle is saturated for 8.6% of the flight time. By capturing the control standard deviations, average control margin, and time saturated in multiple gust fields for a variety of micro rotorcraft platforms, a comparison of the control workload for each platform can be developed.

Endurance is another key characteristic of micro rotorcraft which limits the types of missions a vehicle can perform. Therefore understanding how urban wind fields affect the total energy consumed during flight is critical for the design and operation of micro rotorcraft. For experiments, there exist many “fuel gage” chips which measure energy used during flight [68]. If this is not practical, the total energy consumed during flight can be estimated through motor inputs. In micro rotorcraft the motors consume far more power than all other onboard electronics, thus a simple relation between power and throttle position can be derived from bench top tests.

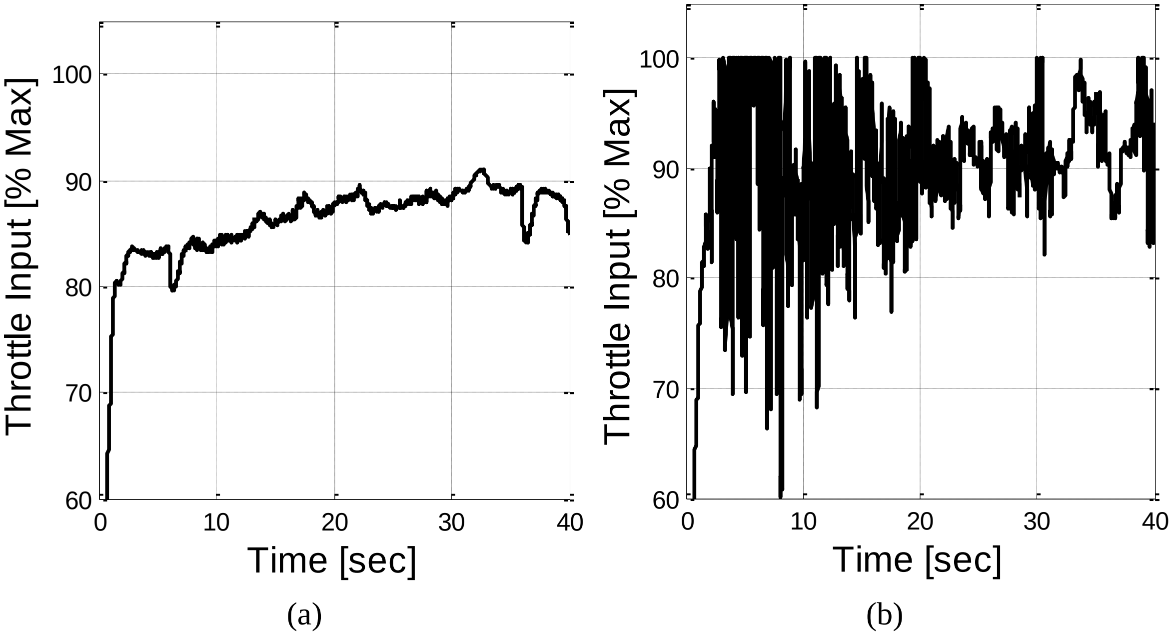

(a) (b)

Figure 2.12. Example time histories of throttle input (a) 0.0 m/s wind (b) 2.0 m/s.

Figure 2.13 shows example time histories of power—measured through a commercial fuel gage chip—and throttle input. The power measured from the fuel gage chip is noisy due to the PWM signals which drive the brushless motors, however it is clear that throttle position provides an accurate approximation of power consumed. The time history of the power consumed can be integrated to compute the total energy consumed during flight events. The power and total energy in turn capture the endurance of the platform while performing mission task elements in gust fields. Understanding how realistic wind disturbances impact endurance provides insight into mission feasibility and power systems design requirements for future micro rotorcraft.

The proposed metrics provide details on position and angular tracking, angular excitation, control workload, and energy consumed. Taken collectively the metrics quantify vehicle capabilities and characteristics during flight in gusty wind fields. The SEP, AERMS, and the controller workload metrics capture the guidance and control performance of a micro rotorcraft platform while AVRMS captures the angular excursions of a vehicle. Additionally power and total energy capture the endurance. The metrics are calculated for each flight event, and the results of multiple flight tests are used to calculate statistics for each metric.

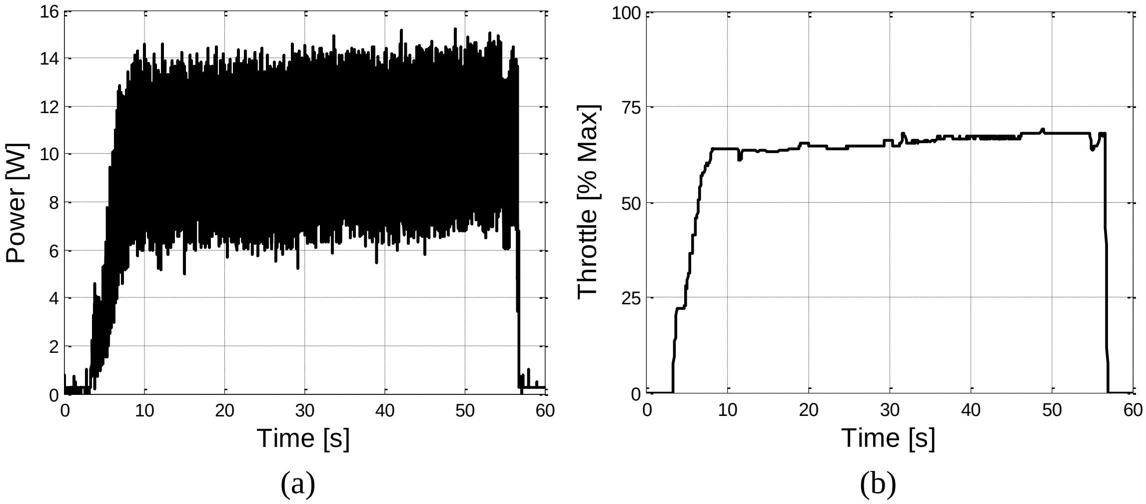

(a) (b)

Figure 2.13. Example time histories of measured power and throttle input (a) measured power consumed (b) throttle input to motor.

2.4 Coaxial Helicopter Experiments

To demonstrate the proposed experimental methodology, a set of experiments are carried out to capture the hover hold performance of a micro coaxial helicopter as gust level is increased. The nominal aircraft used for this experiment is a micro coaxial helicopter (Fig. 2.14). The vehicle weighs 60 g and has a main rotor diameter of 175 mm with two blades per rotor. The rotorcraft's two counter rotating rotors are driven by electric motors. Thrust is controlled by changing the speed of each rotor simultaneously while yaw control is achieved through changing the speed of each rotor differentially. A swash plate attached to the lower rotor is connected to two servo motors for cyclic pitch control, and the upper rotor is connected to a fly bar which improves lateral and longitudinal stability. The micro coaxial helicopter is powered by a LiPo battery and had an approximate maximum forward flight speed of 2.0 m/s. As seen in Fig. 2.14, the helicopter is outfitted with spherical retro-reflective markers for use in the motion capture system. The micro coaxial helicopter is also outfitted with a wireless IMU circuit board developed by the University of California, Berkeley (Fig. 2.15) [69]. The GINA mote provides wireless communication as well as control of servos and motors. Information was transmitted to and from the vehicle using a USB base station.

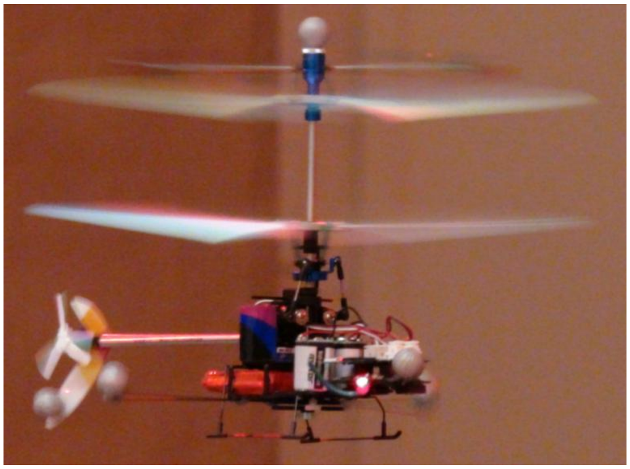

Figure 2.14 Micro coaxial helicopter hovering in the Indoor Flight Facility.

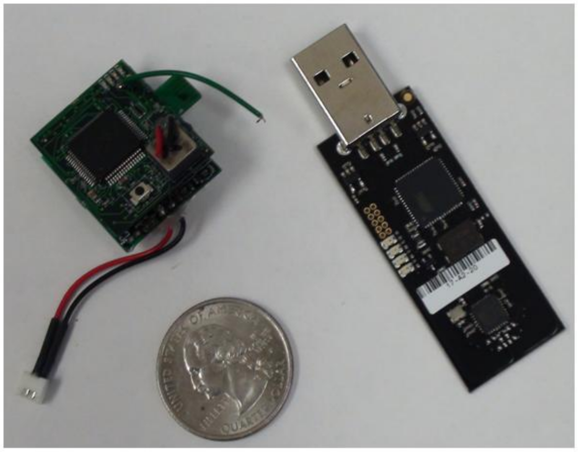

Figure 2.15 GINA 2.0 Mote (left) and base station (right).

A PID controller was chosen as a simple architecture to assess baseline performance. Figure 2.16 shows a block diagram of the control algorithm used for the autonomous flight experiments. Position and attitude measurements from the motion capture system are processed in real time. Control inputs are then calculated based on the measurements and state commands—position (*x*, *y*, *z*) and heading angle (ψ)—and discrete filters are used to calculate the derivative and integral feedback. In the proposed operational environment for micro rotorcraft—close around buildings and indoors—the wind field is expected to be highly variable both spatially and temporally. Thus, the flight regime of a vehicle has the potential to change rapidly and often. For these experiments it was assumed that the vehicle could not measure wind fields directly nor was given any information on the wind field a priori. With this in mind the controller gains are tuned for robust performance around hover and slow forward flight with no adjustment or gain scheduling made in flight.

For each flight test, the vehicle took off in little to no wind then rose into the full flow created by the synthetic gust generation system, where it was commanded to hover for 30.0 seconds before landing. The flow field was measured at 108 spatial points for 2 minutes each.. The wind magnitude is zero at the ground, increases with altitude, decreases downstream (x-direction), and was approximately 1.5 m wide (y-direction).

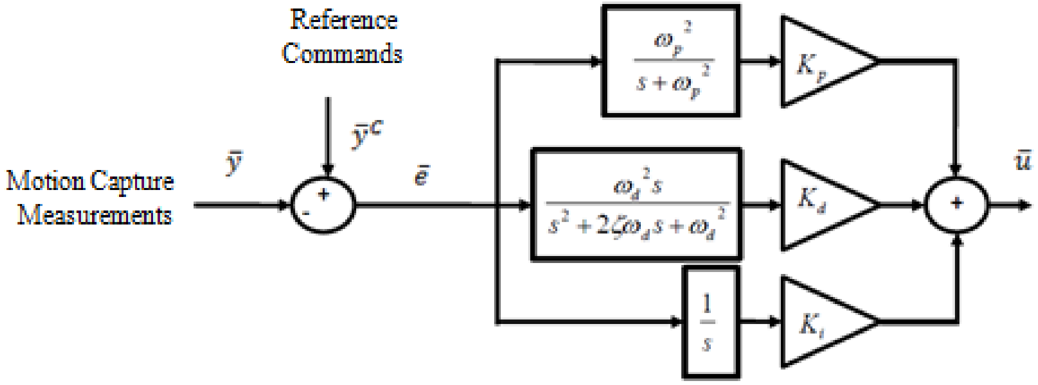

Figure 2.16 Autonomous control algorithm block diagram.

The wind vector at the vehicle center of gravity is estimated through 4-D interpolation, using the gust time history data from the spatial points and the measured vehicle position from flight test data as shown in Figure 2.17 where u_{wind}, v_{wind}, and w_{wind} are the body frame components of wind velocity. The wind magnitude is estimated to change from zero to 1.0 m/s in less than 5.0 seconds. The wind magnitude and direction were measured at the commanded hover position for all wind levels, and the mean and standard deviations are shown in Table 2.1. The standard deviations were found to be small compared to the mean values; therefore the wind gust field at a particular point in space is largely quasi-steady with small fluctuations in time. Strong spatial wind gradients persist at the edges of the gust generator so the helicopter experiences time dependent gusts caused by its ascension through the gust field. This velocity field simulates a simple version of expected real world conditions in and around buildings, such as flight around a corner of a building or across an open window or air vent.

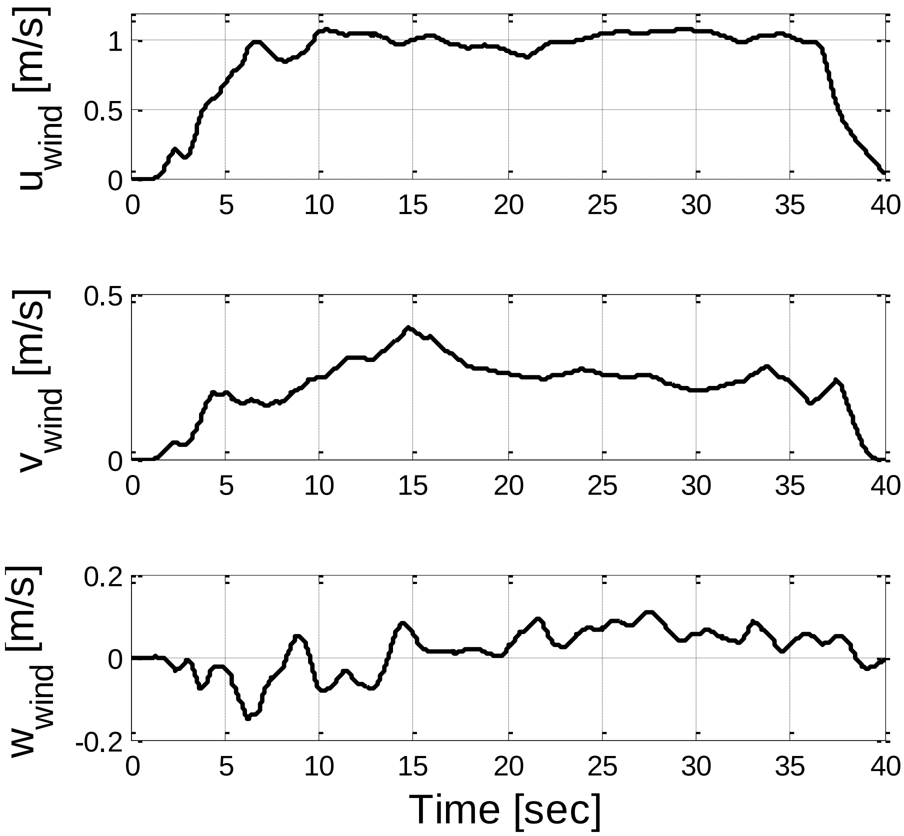

Figure 2.17 Estimated time histories for the inertial wind vector components at the vehicle based on experimental measurements. For a fan setting of 1.0 m/s.

Table 2.1. Experimental mean and standard deviation of wind magnitude and direction at the commanded hover position for each wind level.

	Magnitude [m/s]		Direction [deg]	
Wind Level	Mean	STD	Mean	STD
1	0.0	0.0	NA	NA
2	0.6895	0.0388	14.2895	0.8671
3	1.0684	0.0873	7.6053	1.9248
4	1.5500	0.0647	8.4474	5.2848
5	2.0216	0.0750	6.7210	3.2984

Figures 2.18 and 2.19 present time histories of vehicle position and attitude for flights in wind levels of 0.0 and 2.0 m/s. These figures illustrate the basic behavior of the vehicle when entering a wind gust field. At first, the helicopter is pushed downwind (positive x-direction) and to the right (negative y-direction) before the controller compensates for the disturbance and the vehicle returns closer to the commanded hover position. Significant orientation excursions are experienced in 2.0 m/s wind. As expected, vehicle performance seriously degrades in 2.0 m/s wind.

Figure 2.20 shows the average SEP values with 95% confidence intervals at each wind level tested includes, with the SEP at 2 m/s wind at least 3 times larger than the SEP with zero wind. Likewise, attitude tracking errors increase as wind level increases with the AERMS 7 times higher in 2 m/s wind (Fig. 2.21). The AVRMS is 3 times larger at 2.0 m/s wind than in no wind (Fig. 2.22). Significant increases controller work load are required at higher wind levels (Fig. 2.23), which can also be seen from the time history of the throttle input at different wind levels

(Fig. 2.24). For a horizontal wind, the total energy consumed decreases as wind speed increases which is expected from rotor theory (Fig. 2.25). However, the standard deviation of the 10 test flights performed at each wind speed lead to large confidence intervals on the data points. More runs are required to investigate power consumption.

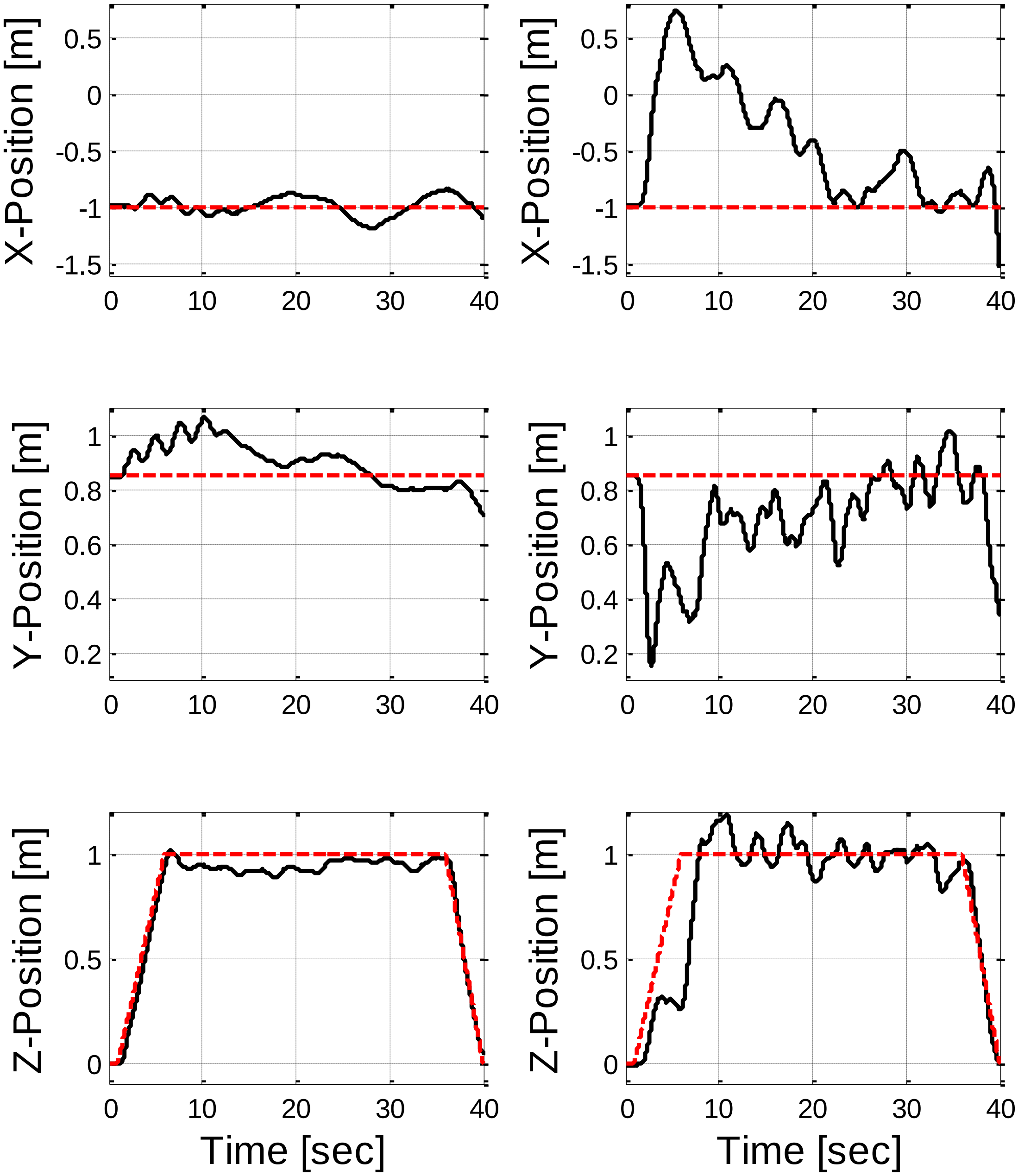

(a) (b)

Figure 2.18 Experimental example time histories of vehicle position in hover. The state measurements are shown as solid lines and the commanded positions are shown as dotted lines in **(**a) 0.0 m/s wind (SEP = 0.142 m) (b) 2.0 m/s wind (SEP = 0.507 m).

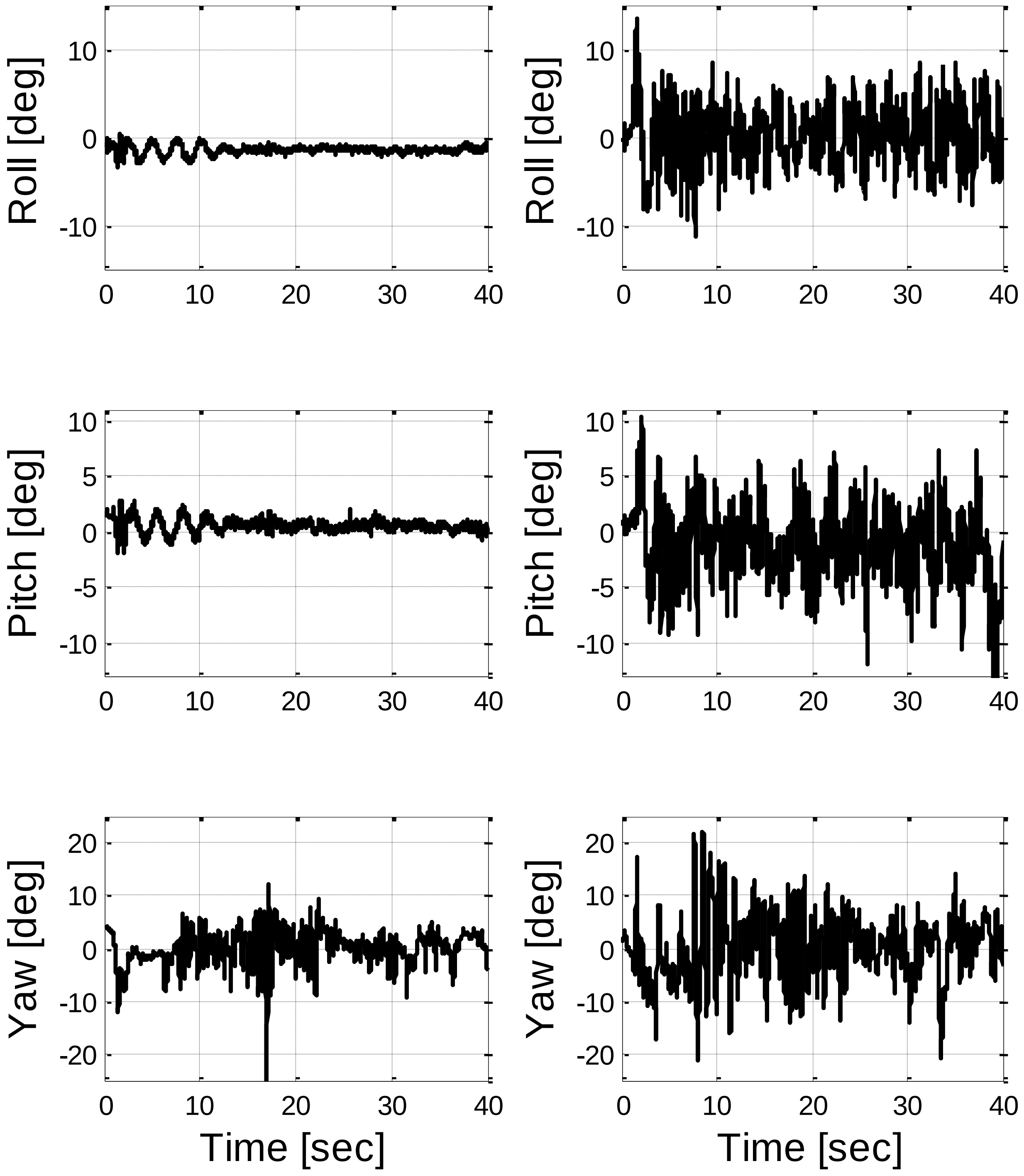

(a) (b)

Figure 2.19 Experimental example time histories of vehicle attitude in hover. (a) 0.0 m/s wind (AERMS = 5.2 deg, AVRMS = 42.7 deg/s) (b) 2.0 m/s wind (AERMS = 35.1 deg, AVRMS = 85.4 deg/s).

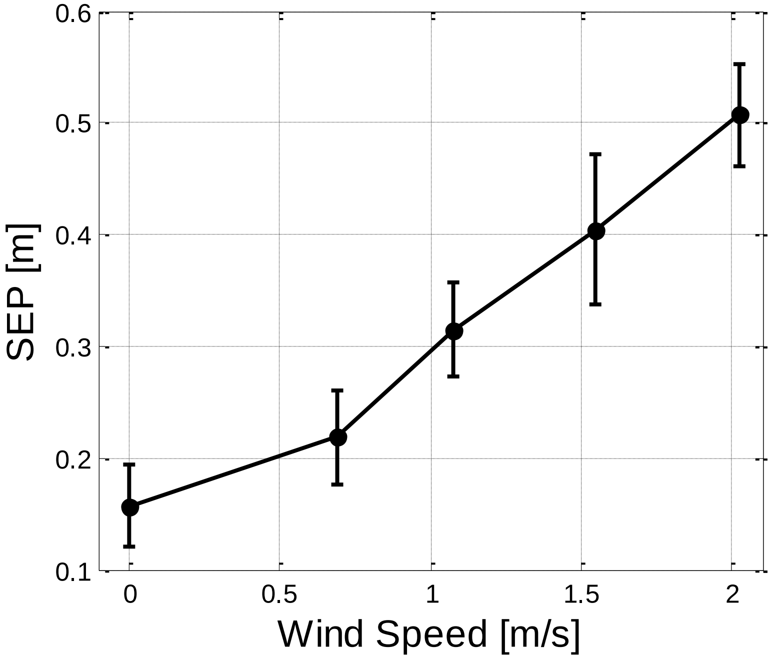

Figure 2.20 Experimental average SEP for increasing wind levels.

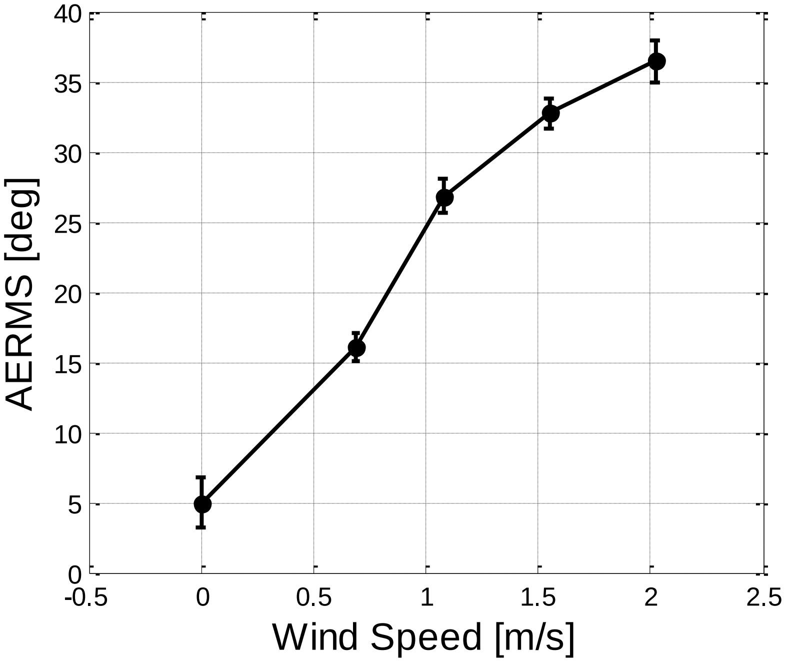

Figure 2.21 Experimental average AERMS for increasing wind levels.

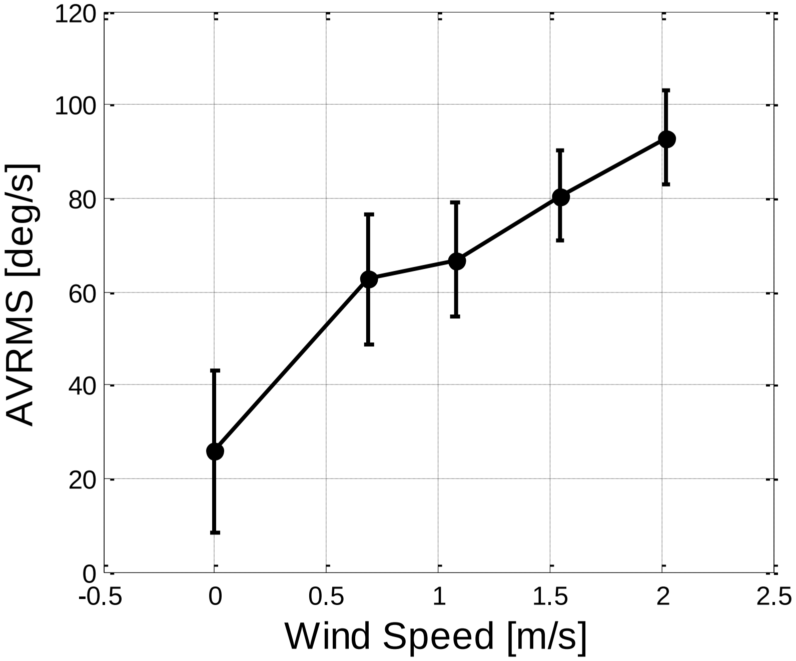

Figure 2.22 Experimental average AVRMS for increasing wind levels.

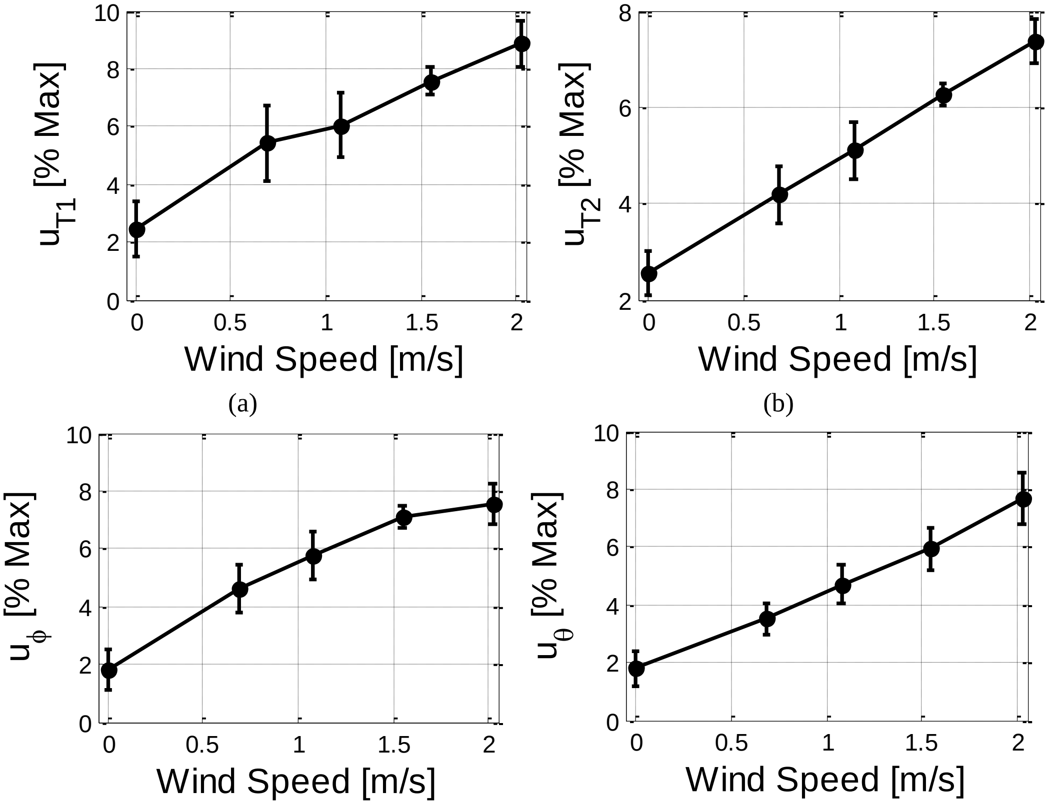

(a) (b)

(c) (d)

Figure 2.23 Experimental average control standard deviation for increasing wind levels (a) lower rotor throttle (b) upper rotor throttle (c) lateral cyclic (d) longitudinal cyclic.

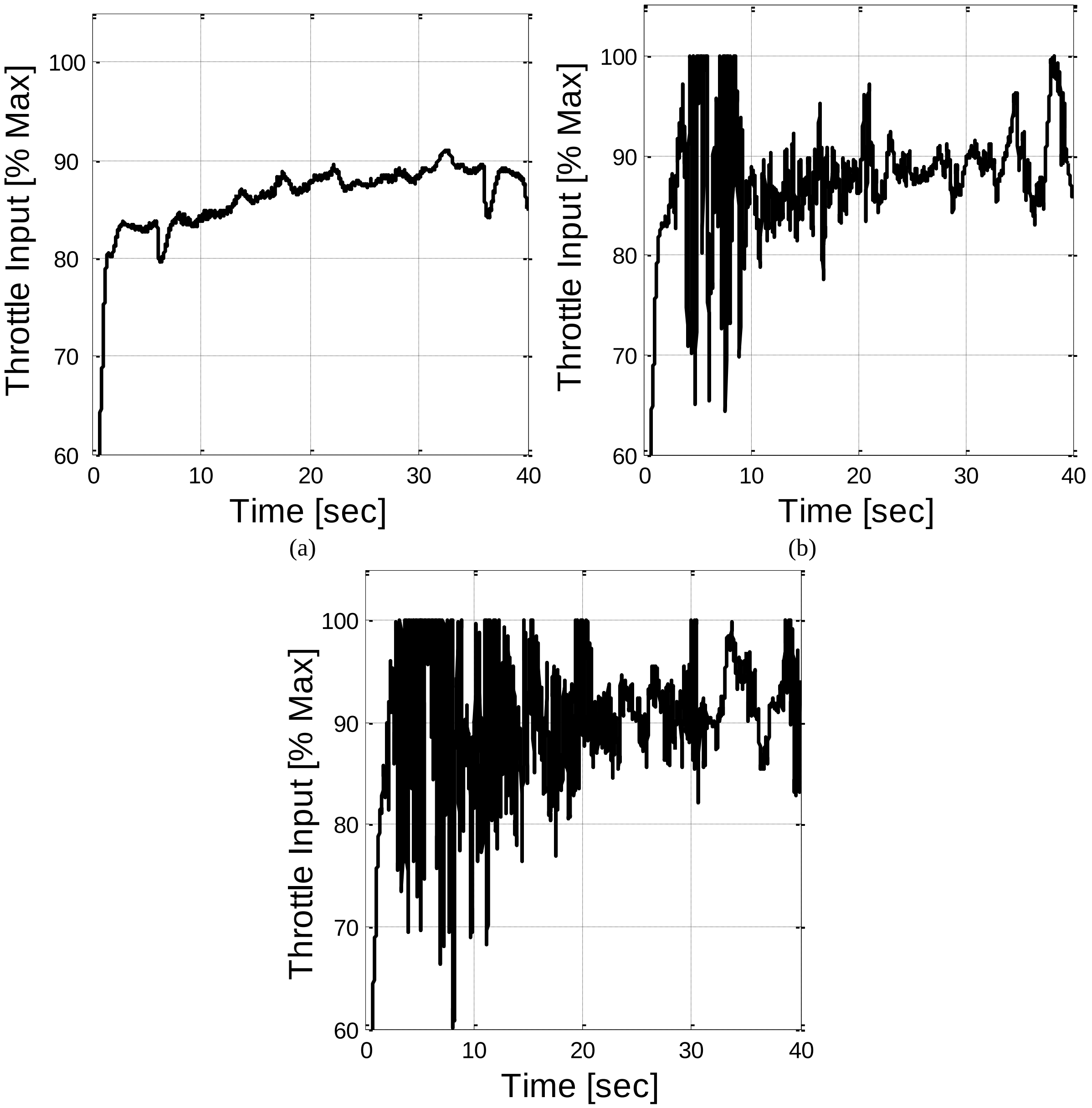

(a)

(b)

(c)

Figure 2.24 Experimental example time histories of throttle inputs for wind levels of (a) 0.0 m/s (STD = 4.45 % Max) (b) 1.0 m/s (STD = 8.29 % Max) (c) 2.0 m/s (STD = 11.75 % Max).

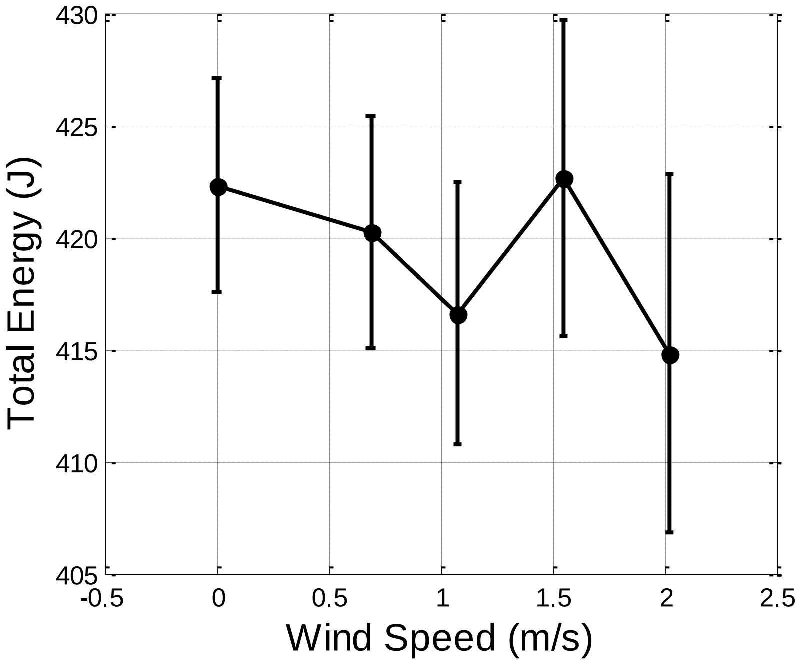

Figure 2.25 Experimental average total energy consumed for increasing wind levels.

2.5 Discussion of Experimental Results

Overall, the proposed metrics give a clear picture of how poorly micro rotorcraft perform in even light winds. The SEP, AERMS, and AVRMS provide quantitative measures of position and attitude response to wind disturbances while control standard deviation and mean control margin capture control workload. Though the 2.0 m/s wind level is very close to the maximum forward flight speed of the vehicle, the helicopter is able to reject the wind disturbance eventually. It should also be noted the metrics calculated for these results should be thought of as transient metrics, as they were calculated from the initial response to a disturbance. It may also be helpful to perform a longer test to capture the steady state metrics after the control system has had time to compensate for the initial disturbance.

CHAPTER 3

COAXIAL HELICOPTER DYNAMIC MODEL

In order to perform accurate trade studies on micro rotorcraft performance in complex wind fields, a dynamic model is developed for the coaxial helicopter detailed in Chapter 2—Fig. 2.14. It is expected that in complex environments flight conditions will change rapidly, therefore the nonlinear dynamic model is required to be valid over the entire flight envelope and simulate response to spatially and temporally varying wind disturbances. This chapter describes all major components of the nonlinear rotorcraft model including: airframe drag, rotor inflow and wake modeling, control motor and servo dynamics, and blade element models used to simulate rotor flapping dynamics and calculate rotor loads for the lower rotor, upper rotor, and fly bar.

The translational velocity of vehicle center of gravity can be expressed as

$$\bar{v}_{CG} = \dot{x}\bar{I}_I + \dot{y}\bar{J}_I + \dot{z}\bar{K}_I = u\bar{I}_B + v\bar{J}_B + w\bar{K}_B \tag{3.1}$$

where I and B represent the inertial and body reference frames, Fig. 3.1.

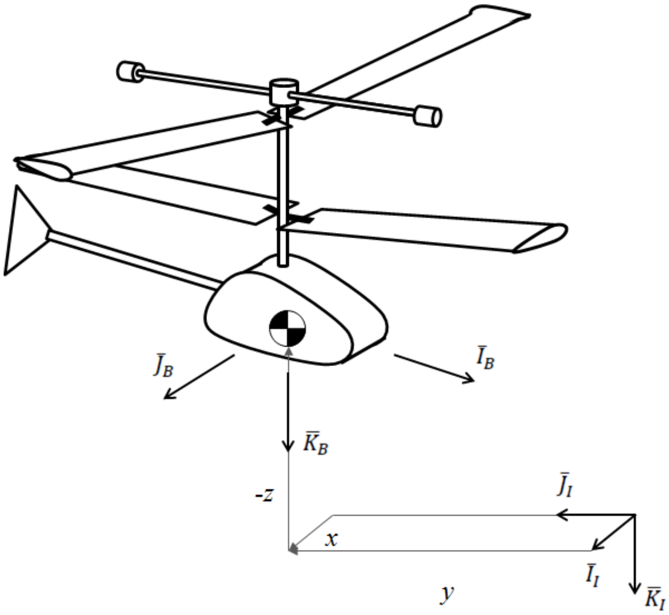

Figure 3.1. Illustration of Inertial (*I*) and Body (*B*) reference frames.

The inertial reference frame (*I)* is attached to the ground assuming a flat earth approximation and $\bar{K}_I$ down. The body reference frame (*B*) is fixed to the vehicle with its origin at the center of gravity. The $\bar{I}_B$ vector points out the vehicle nose, $\bar{J}_B$ out right side, and $\bar{K}_B$ down. The body-frame is related to the inertial frame through the conventional Euler angle transformation

$$\begin{Bmatrix} \bar{I}_B \\ \bar{J}_B \\ \bar{K}_B \end{Bmatrix} = \begin{bmatrix} c_\theta c_\psi & c_\theta s_\psi & -s_\theta \\ s_\phi s_\theta c_\psi - c_\phi s_\psi & s_\phi s_\theta s_\psi + c_\phi c_\psi & s_\phi c_\theta \\ c_\phi s_\theta c_\psi + s_\phi s_\psi & c_\phi s_\theta s_\psi - s_\phi c_\psi & c_\phi c_\theta \end{bmatrix} \begin{Bmatrix} \bar{I}_I \\ \bar{J}_I \\ \bar{K}_I \end{Bmatrix} = T_{IB} \begin{Bmatrix} \bar{I}_I \\ \bar{J}_I \\ \bar{K}_I \end{Bmatrix} \quad (3.2)$$

where $c_X = \cos(X)$ and $s_X = \sin(X)$. Thus the inertial and body frame velocity components are related through the translational kinematic differential equations.

$$\begin{Bmatrix} \dot{x} \\ \dot{y} \\ \dot{z} \end{Bmatrix} = T_{IB}^T \begin{Bmatrix} u \\ v \\ w \end{Bmatrix} \quad (3.3)$$

The angular velocity of the vehicle with respect to the inertial frame is written as

$$\bar{\omega}_{B/I} = \dot{\phi}\bar{I}_B + \dot{\theta}\bar{J}_N + \dot{\psi}\bar{K}_I = p\bar{I}_B + q\bar{J}_B + r\bar{K}_B \quad (3.4)$$

where *N* is an intermediate frame in the conventional Euler angle rotation. The rotational kinematic differential equations can be expressed as

$$\begin{Bmatrix} \dot{\phi} \\ \dot{\theta} \\ \dot{\psi} \end{Bmatrix} = \begin{bmatrix} 1 & s_\phi t_\theta & c_\phi t_\theta \\ 0 & c_\phi & -s_\phi \\ 0 & s_\phi / c_\theta & c_\phi / c_\theta \end{bmatrix} \begin{Bmatrix} p \\ q \\ r \end{Bmatrix} \quad (3.5)$$

The translational dynamic equations of the vehicle center of gravity are expressed in the body frame as

$$\begin{Bmatrix} \dot{u} \\ \dot{v} \\ \dot{w} \end{Bmatrix} = \begin{bmatrix} 0 & r & -q \\ -r & 0 & p \\ q & -p & 0 \end{bmatrix} \begin{Bmatrix} u \\ v \\ w \end{Bmatrix} + \begin{Bmatrix} X/m \\ Y/m \\ Z/m \end{Bmatrix} \quad (3.6)$$

where *m* is the vehicle mass and *X*, *Y*, and *Z* are the summed external forces acting on the vehicle frame. Likewise, the rotational dynamic equations can be written in the body frame as

$$\begin{Bmatrix} \dot{p} \\ \dot{q} \\ \dot{r} \end{Bmatrix} = [I]^{-1} \begin{bmatrix} 0 & r & -q \\ -r & 0 & p \\ q & -p & 0 \end{bmatrix} [I] \begin{Bmatrix} p \\ q \\ r \end{Bmatrix} + [I]^{-1} \begin{Bmatrix} L \\ M \\ N \end{Bmatrix} \tag{3.7}$$

where L, M, and N are the summed moments acting on the vehicle and $[I]$ is the mass moment of inertia matrix.

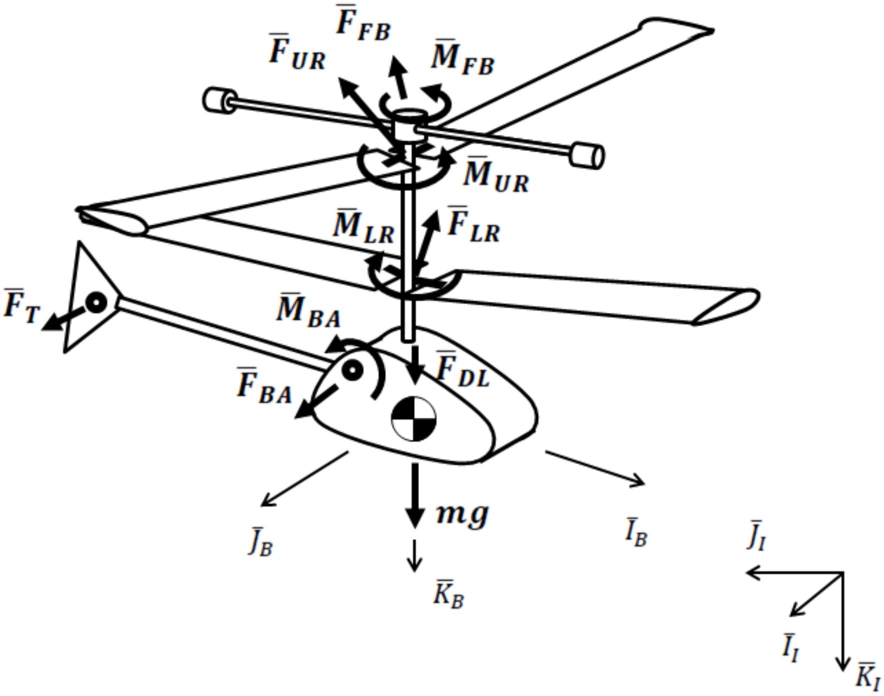

Figure 3.2. Illustration of all major forces and moments acting on a coaxial helicopter platform.

Figure 3.2 illustrates the major external forces and moments acting on the coaxial helicopter: gravity (*G*), aerodynamic drag (*BA*), the vertical tail (*T*), the rotors (*LR*, *UR*), the flybar (*FB*), and download due to the rotor wake (*DL*). Thus summed external forces and moments in Equations 3.6 and 3.7 are

$$\begin{Bmatrix} X \\ Y \\ Z \end{Bmatrix} = \begin{Bmatrix} X_G \\ Y_G \\ Z_G \end{Bmatrix} + \begin{Bmatrix} X_{BA} \\ Y_{BA} \\ Z_{BA} \end{Bmatrix} + \begin{Bmatrix} X_T \\ Y_T \\ Z_T \end{Bmatrix} + \begin{Bmatrix} X_{LR} \\ Y_{LR} \\ Z_{LR} \end{Bmatrix} + \begin{Bmatrix} X_{UR} \\ Y_{UR} \\ Z_{UR} \end{Bmatrix} + \begin{Bmatrix} X_{FB} \\ Y_{FB} \\ Z_{FB} \end{Bmatrix} + \begin{Bmatrix} X_{DL} \\ Y_{DL} \\ Z_{DL} \end{Bmatrix} \tag{3.8}$$

$$\begin{Bmatrix} L \\ M \\ N \end{Bmatrix} = \begin{Bmatrix} L_{BA} \\ M_{BA} \\ N_{BA} \end{Bmatrix} + \mathbb{S}_B(\bar{r}_{CG\to T}) \begin{Bmatrix} X_T \\ Y_T \\ Z_T \end{Bmatrix} + \begin{Bmatrix} L_{LR} \\ M_{LR} \\ N_{LR} \end{Bmatrix} + \mathbb{S}_B(\bar{r}_{CG\to LR}) \begin{Bmatrix} X_{LR} \\ Y_{LR} \\ Z_{LR} \end{Bmatrix} + \begin{Bmatrix} L_{UR} \\ M_{UR} \\ N_{UR} \end{Bmatrix} + \mathbb{S}_B(\bar{r}_{CG\to UR}) \begin{Bmatrix} X_{UR} \\ Y_{UR} \\ Z_{UR} \end{Bmatrix}$$

$$+ \begin{Bmatrix} L_{FB} \\ M_{FB} \\ N_{FB} \end{Bmatrix} + \mathbb{S}_B(\bar{r}_{CG\to FB}) \begin{Bmatrix} X_{FB} \\ Y_{FB} \\ Z_{FB} \end{Bmatrix} \tag{3.9}$$

Where $\bar{r}_{CG\to T}$, $\bar{r}_{CG\to LR}$, $\bar{r}_{CG\to UR}$, and $\bar{r}_{CG\to FB}$ are position vectors from the vehicle center of gravity to the tail aerodynamic center and the rotor hub centers respectively, and $\mathbb{S}_X(\bar{r})$ is the skew-symmetric matrix representation of a vector $\bar{r}$ in reference frame X.

3.1 Rotor System Model

In order to capture the effect of wind gusts and turbulence on flapping dynamics and rotor aerodynamics, a basic model of a generic rotor system is developed which specifically includes the effect of wind disturbances. The outputs of this system model are the rotor flapping response and rotor system constraint forces and moments.

The basis of the rotor system model lies in the flapping dynamics and constraint loads of a single rotor blade. Figure 3.3 illustrates the relevant reference frames needed for the rotor blade dynamics, these include the shaft, hub, and blade frames. The shaft frame (*S*) is fixed to the non-rotating shaft with its origin at the rotor hub, and is related to body frame by a 180 degree rotation about $\bar{J}_B$.

$$\begin{Bmatrix} \bar{I}_S \\ \bar{J}_S \\ \bar{K}_S \end{Bmatrix} = \begin{Bmatrix} -\bar{I}_B \\ \bar{J}_B \\ -\bar{K}_B \end{Bmatrix} \tag{3.10}$$

The hub frame (*H*) is fixed to rotating rotor hub with $\bar{I}_H$ pointing along the rotor blade and $\bar{K}_H$ pointing upwards along the rotor shaft, Fig. 3.3b. The hub frame is related to the shaft frame through the azimuth angle (ψ_R):

$$\begin{Bmatrix} \bar{I}_H \\ \bar{J}_H \\ \bar{K}_H \end{Bmatrix} = \begin{bmatrix} c_{\psi_R} & s_{\psi_R} & 0 \\ -s_{\psi_R} & c_{\psi_R} & 0 \\ 0 & 0 & 1 \end{bmatrix} \begin{Bmatrix} \bar{I}_S \\ \bar{J}_S \\ \bar{K}_S \end{Bmatrix} = T_{\psi_R} \begin{Bmatrix} \bar{I}_S \\ \bar{J}_S \\ \bar{K}_S \end{Bmatrix} \tag{3.11}$$

The blade reference frame (*BL*) is fixed to rotor blade with $\bar{I}_{BL}$along the blade, $\bar{J}_{BL}$pointing out the leading edge, and $\bar{K}_{BL}$ up. The blade frame is related to hub frame through blade flapping angle (β):

$$\begin{Bmatrix} \bar{I}_{BL} \\ \bar{J}_{BL} \\ \bar{K}_{BL} \end{Bmatrix} = \begin{bmatrix} c_{\beta} & 0 & s_{\beta} \\ 0 & 1 & 0 \\ -s_{\beta} & 0 & c_{\beta} \end{bmatrix} \begin{Bmatrix} \bar{I}_H \\ \bar{J}_H \\ \bar{K}_H \end{Bmatrix} = T_{\beta} \begin{Bmatrix} \bar{I}_H \\ \bar{J}_H \\ \bar{K}_H \end{Bmatrix} \tag{3.12}$$

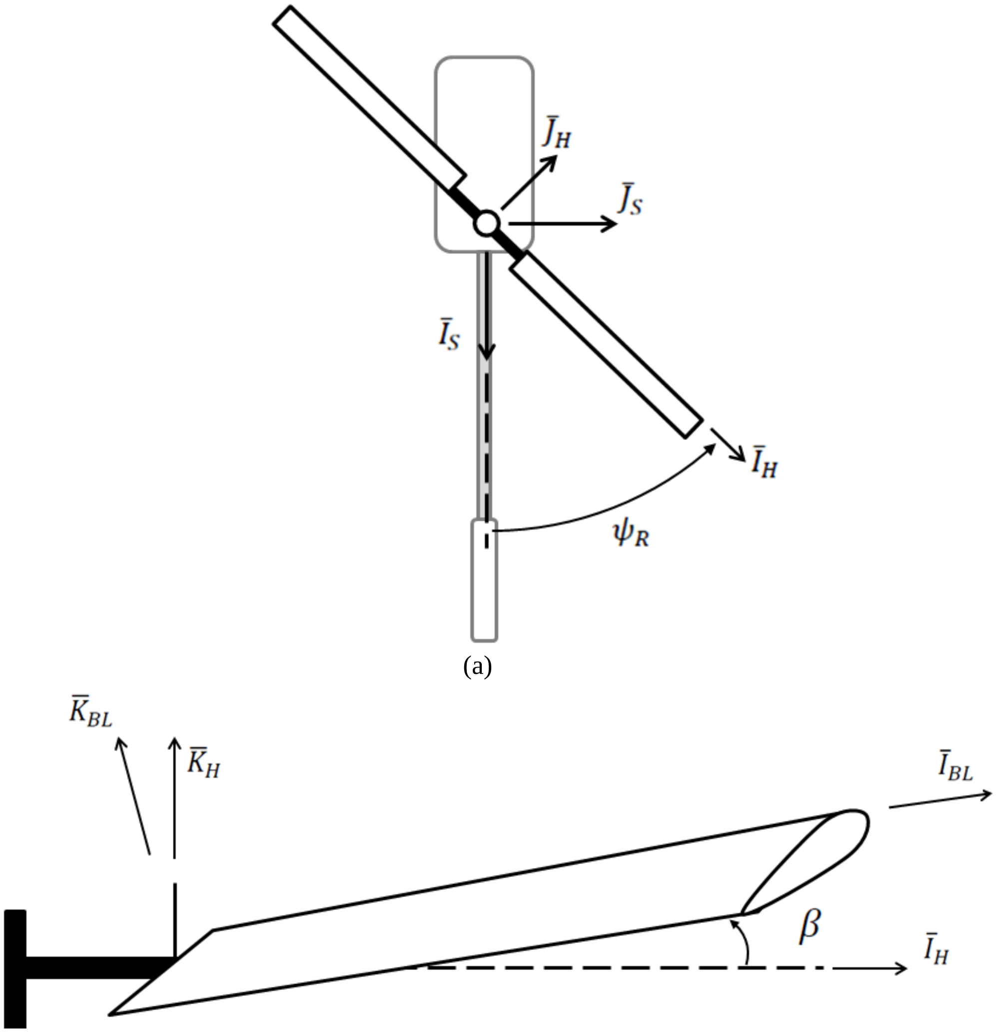

(a)

(b)

Figure 3.3. Illustrations of relevant reference frames for rotor blades. (a) Shaft (*S*) and Hub (*H*) (b) Hub and Blade (*BL*).

Figure 3.4 illustrates the basic parameters, states, forces, and moments associated with an individual rotor blade. The flexible rotor blade is approximated as rigid with an effective hinge offset and associated spring constant, and the blade's mass moment of inertia matrix is assumed to be diagonal.

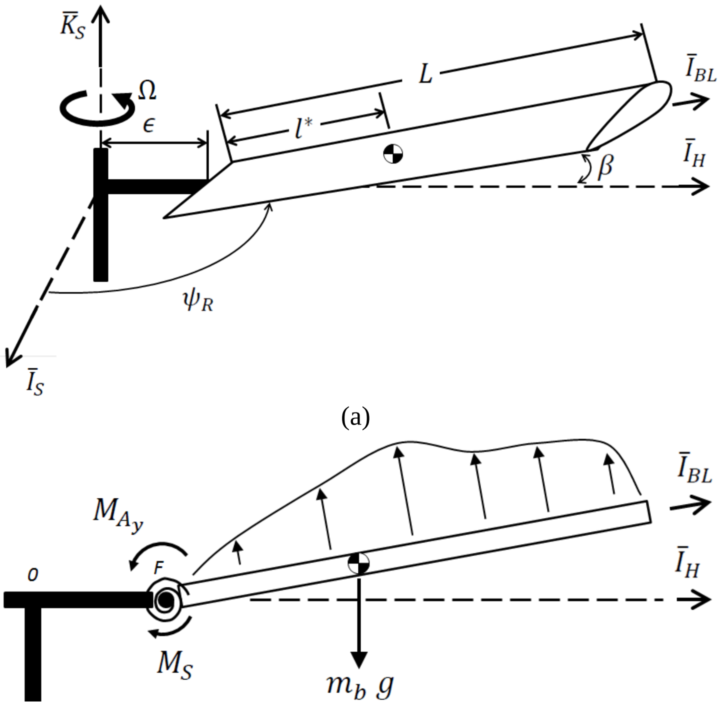

(a)

(b)

Figure 3.4. Illustrations of rotor blade flap. (a) Relevant parameters and states (b) Relevant free body diagram of blade.

Additionally, it is assumed that the rotor dynamics are sufficiently faster than vehicle body dynamics such that the body rates are constant; this includes body translation and angular velocities as well as rotor shaft angular velocity. The individual blade flapping dynamics are derived by taking the sum of moments about the blade hinge point (*F*), Fig. 3.4b,

$$\bar{M}_{RA} + \bar{M}_S + \bar{M}_G + \bar{M}_R = \frac{{}^{I}d\bar{H}^{CG}_{BL/I}}{dt} + \mathbb{S}_I(\bar{r}_{F\rightarrow cg})\mathbb{C}_I(\bar{a}_{cg}) \tag{3.13}$$

where $\overline{M}_{RA}$, $\overline{M}_S$, $\overline{M}_G$, and $\overline{M}_R$ are the moments generated by rotor aerodynamics, effective hinge spring, gravity, and hinge reactions respectively; $\overline{H}^{CG}_{BL/I}$is the blade angular momentum, $\bar{r}_{F\to cg}$ is the position vector from the hinge point to the blade center of gravity, $\bar{a}_{cg}$ is the acceleration of the blade center of gravity, and $\mathbb{C}_X(\bar{r})$ is the component operator for $\bar{r}$ expressed in the X frame. The single degree of freedom equation of motion for blade flapping is the $\bar{J}_{BL}$ component in equation 3.13, solving for the second derivative of the flap angle.

$$\ddot{\beta} = \frac{M_{RA_y}+k_\beta\,\beta+m_b g l^* c_\beta-H_0+m_b l^* A_0}{-I_{b_{yy}}-m_b {l^*}^2} \qquad (3.14)$$

Where $M_{RA_y}$is the aerodynamic moment generated by the rotor about the y-axis in the hub frame, k_β is the torsional spring constant, and the grouped terms H_0 and A_0 represent the parts of the right hand side of Eqn. 3.13 that do not include a second derivative of the flap angle. Full expansions of H_0 and A_0 are derived Appendix A.

The aerodynamic forces and moments generated by the rotor are calculated by splitting the rotor blade into a finite number of elements. Figure 3.5 shows an illustration of a two dimensional airfoil section at an arbitrary point *p* on the rotor blade.

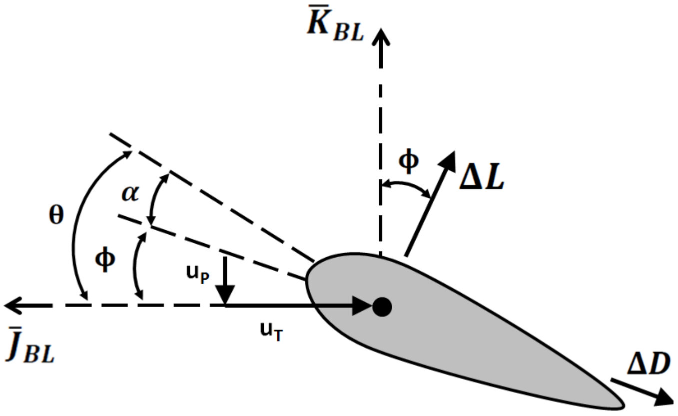

Figure 3.5. Illustrations of rotor blade airfoil section at arbitrary point p on the rotor.

The tangential and perpendicular aerodynamic velocity components of point p (u_T, u_P) are functions of the hub velocity, the body angular velocity, rotor angular velocity, induced rotor inflow, and wind disturbances at the blade section. Derivations of Equations 3.15 and 3.16 can be found in Appendix A.

$$\begin{aligned} u_T = {} & \epsilon\mathit{\Omega} + \epsilon\mathit{\Omega}_{zS} + \mathit{\Omega} r_x c_\beta + \mathit{\Omega}_{zS} r_x c_\beta - V_{atmy} c_\psi + V_{oy} c_\psi - \mathit{\Omega}_{xS} r_z c_\beta c_\psi - \mathit{\Omega} r_z s_\beta - \mathit{\Omega}_{zS} r_z s_\beta - \\ & \mathit{\Omega}_{xS} r_x c_\psi s_\beta + V_{atmx} s_\psi - V_{ox} s_\psi - \mathit{\Omega}_{yS} r_z c_\beta s_\psi - \mathit{\Omega}_{yS} r_x s_\beta s_\psi + c_\psi v_{iy} - s_\psi v_{ix} \end{aligned} \tag{3.15}$$

$$\begin{aligned} u_P = {} & \dot{\beta} r_x - V_{atmz} c_\beta + v_i c_\beta - c_\psi s_\beta v_{ix} - s_\beta s_\psi v_{iy} + V_{oz} c_\beta - \mathit{\Omega}_{yS} r_x c_\psi - \epsilon\mathit{\Omega}_{yS} c_\beta c_\psi + \\ & \mathit{\Omega}_{xS} r_y c_\beta c_\psi + \mathit{\Omega} r_y s_\beta + \mathit{\Omega}_{zS} r_y s_\beta + V_{Gx} c_\psi s_\beta - V_{ox} c_\psi s_\beta + \mathit{\Omega}_{xS} r_x s_\psi + \epsilon\mathit{\Omega}_{xS} c_\beta s_\psi + \\ & \mathit{\Omega}_{yS} r_y c_\beta s_\psi + V_{atmy} s_\beta s_\psi - V_{oy} s_\beta s_\psi \end{aligned} \tag{3.16}$$

Blade pitch is controlled through the swashplate as

$$\theta(t) = \theta_0 + \theta_{twist} \frac{\epsilon + r_x}{\epsilon + L} - \theta_{1C}(t)\cos(\psi_R) - \theta_{1S}(t)\sin(\psi_R) \tag{3.17}$$

where θ_0 is the collective pitch, θ_{twist} is the blade twist which is a function of the distance from the rotor hub, θ_{1C} is the longitudinal cyclic pitch and θ_{1S} is the lateral cyclic pitch. From Fig. 3.5, the angle of attack is

$$\alpha(t) = \theta(t) - \phi(t) = \theta(t) - \tan^{-1}\left(\frac{u_P}{u_T}\right) \tag{3.18}$$

Given the velocity components, blade pitch, and angle of attack, the section rotor aerodynamic loads can be calculated.

$$\begin{Bmatrix} \Delta \mathrm{F}_{\mathrm{RA_x}} \\ \Delta \mathrm{F}_{\mathrm{RA_y}} \\ \Delta \mathrm{F}_{\mathrm{RA_z}} \end{Bmatrix} = \begin{Bmatrix} 0 \\ -\mathrm{c}_\phi \mathit{\Delta D} - \mathrm{s}_\phi \mathit{\Delta L} \\ \mathrm{c}_\phi \mathit{\Delta L} - \mathrm{s}_\phi \mathit{\Delta D} \end{Bmatrix} = \frac{1}{2}\rho \mathrm{V}^2 \mathrm{c}\Delta \mathrm{r} \begin{Bmatrix} 0 \\ -\mathrm{c}_\phi \mathrm{C_d} - \mathrm{s}_\phi \mathrm{C_l} \\ \mathrm{c}_\phi \mathrm{C_l} - \mathrm{s}_\phi \mathrm{C_d} \end{Bmatrix} \tag{3.19}$$

$$\begin{Bmatrix} \Delta \mathrm{M}_{\mathrm{RA_x}} \\ \Delta \mathrm{M}_{\mathrm{RA_y}} \\ \Delta \mathrm{M}_{\mathrm{RA_z}} \end{Bmatrix} = \mathbb{S}_I(\bar{\mathrm{r}}_{\mathrm{F \to P}}) \begin{Bmatrix} \Delta \mathrm{F}_{\mathrm{RA_x}} \\ \Delta \mathrm{F}_{\mathrm{RA_y}} \\ \Delta \mathrm{F}_{\mathrm{RA_z}} \end{Bmatrix} \tag{3.20}$$

The aerodynamic forces and moments for each element section can then summed over the blade to obtain the total rotor blade aerodynamic load.

$$\begin{Bmatrix} \mathrm{F}_{\mathrm{RA}_\mathrm{x}} \\ \mathrm{F}_{\mathrm{RA}_\mathrm{y}} \\ \mathrm{F}_{\mathrm{RA}_\mathrm{z}} \end{Bmatrix} = \sum_{\mathrm{i}}^{\mathrm{NBE}} \begin{Bmatrix} \Delta\mathrm{F}_{\mathrm{RA}_\mathrm{x}} \\ \Delta\mathrm{F}_{\mathrm{RA}_\mathrm{y}} \\ \Delta\mathrm{F}_{\mathrm{RA}_\mathrm{z}} \end{Bmatrix}_{\mathrm{i}} \tag{3.21}$$

$$\begin{Bmatrix} \mathrm{M}_{\mathrm{RA}_\mathrm{x}} \\ \mathrm{M}_{\mathrm{RA}_\mathrm{y}} \\ \mathrm{M}_{\mathrm{RA}_\mathrm{z}} \end{Bmatrix} = \sum_{\mathrm{i}}^{\mathrm{NBE}} \begin{Bmatrix} \Delta\mathrm{M}_{\mathrm{RA}_\mathrm{x}} \\ \Delta\mathrm{M}_{\mathrm{RA}_\mathrm{y}} \\ \Delta\mathrm{M}_{\mathrm{RA}_\mathrm{z}} \end{Bmatrix}_{\mathrm{i}} \tag{3.22}$$

While the equations developed so far are for a single blade, a rotor system with N blades will have N degrees of freedom associated with the rigid rotor blade flapping. Rather than modeling each blade individually, the entire rotor system can be modeled as a whole. Since the blade pitch control inputs (Eqn. 3.17) excite the system in a first harmonic manner, it is reasonable to model the flapping response as first harmonic [70].

$$\beta(t) = \beta_0(t) + \beta_{1C}(t)\cos(\psi_R) + \beta_{1S}(t)\sin(\psi_R) \tag{3.23}$$

Where β_0 is the coning angle, β_{1C} is the longitudinal flap angle, and β_{1S} is the lateral flap angle. The three equations of motion for first harmonic flapping are found through harmonic balancing, where the first harmonic expansion is substituted into the flapping equations of motion and equating the constant, cosine, and sine harmonic components.

$$\ddot{\beta}_0 = \frac{1}{2\pi}\int_0^{2\pi} \ddot{\beta}\, d\psi_R \tag{3.24}$$

$$\ddot{\beta}_{1C} = \beta_{1C}\Omega^2 - 2\Omega\dot{\beta}_{1S} + \frac{1}{\pi}\int_0^{2\pi} \ddot{\beta}\cos(\psi_R)\, d\psi_R \tag{3.25}$$

$$\ddot{\beta}_{1S} = \beta_{1S}\Omega^2 + 2\Omega\dot{\beta}_{1C} + \frac{1}{\pi}\int_0^{2\pi} \ddot{\beta}\sin(\psi_R)\, d\psi_R \tag{3.26}$$

where Ω is the rotor angular velocity, $\Omega = \dot{\psi}_R$ and $\ddot{\beta}$ is calculated from Eqn. 3.14.

As mentioned previously, the purpose of the rotor model is to simulate rotor flapping response as well as calculate the rotor loads. The rotor forces and moments transferred to the vehicle frame are the reaction forces and moments at the rotor blade effective flap hinge joint. For flight dynamics analysis the constant rotor loads are the primary interest, and the total rotor forces and moments on the parent vehicle body are summed over the entire rotor disk as

$$\begin{Bmatrix} \mathrm{F}_{\mathrm{R}_\mathrm{x}} \\ \mathrm{F}_{\mathrm{R}_\mathrm{y}} \\ \mathrm{F}_{\mathrm{R}_\mathrm{z}} \end{Bmatrix} = \frac{\mathrm{N}_\mathrm{B}}{2\pi} \int_0^{2\pi} -\left[\mathrm{T}_{\psi_\mathrm{R}}\right]^T \left[T_\beta\right]^T \begin{Bmatrix} \mathrm{R}_\mathrm{x} \\ \mathrm{R}_\mathrm{y} \\ \mathrm{R}_\mathrm{z} \end{Bmatrix} \mathrm{d}\psi_\mathrm{R} \tag{3.27}$$

$$\begin{aligned} \begin{Bmatrix} \mathrm{M}_{\mathrm{R}_\mathrm{x}} \\ \mathrm{M}_{\mathrm{R}_\mathrm{y}} \\ \mathrm{M}_{\mathrm{R}_\mathrm{z}} \end{Bmatrix} = \frac{\mathrm{N}_\mathrm{B}}{2\pi} \int_0^{2\pi} -\left[\mathrm{T}_{\psi_\mathrm{R}}\right]^T \left[T_\beta\right]^T \begin{bmatrix} 1 & 0 \\ 0 & 0 \\ 0 & 1 \end{bmatrix} \begin{Bmatrix} \mathrm{m}_{\mathrm{R}_\mathrm{x}} \\ \mathrm{m}_{\mathrm{R}_\mathrm{z}} \end{Bmatrix} \mathrm{d}\psi_\mathrm{R} \\ + \frac{\mathrm{N}_\mathrm{B}}{2\pi} \int_0^{2\pi} -\left[\mathrm{T}_{\psi_\mathrm{R}}\right]^T \begin{bmatrix} 0 & 0 & 0 \\ 0 & 0 & -\epsilon \\ 0 & \epsilon & 0 \end{bmatrix} \left[T_\beta\right]^T \begin{Bmatrix} \mathrm{R}_\mathrm{x} \\ \mathrm{R}_\mathrm{y} \\ \mathrm{R}_\mathrm{z} \end{Bmatrix} \mathrm{d}\psi_\mathrm{R} \end{aligned} \tag{3.28}$$

where R_X and $\mathrm{m}_{\mathrm{R}_\mathrm{X}}$are the reaction forces and moments of a rotor blade. Expressions for the rotor blade reaction forces and moments are derived by taking linear acceleration of the blade and the sum of moments about the hinge point similar to Eqn. 3.13. The expressions will have inertia and aerodynamic terms; however it is assumed that the aerodynamic terms dominate the inertia terms. Therefore the reaction forces and moments are approximated as

$$\begin{Bmatrix} \mathrm{R}_\mathrm{x} \\ \mathrm{R}_\mathrm{y} \\ \mathrm{R}_\mathrm{z} \end{Bmatrix} \approx - \begin{Bmatrix} \mathrm{F}_{\mathrm{RA}_\mathrm{x}} \\ \mathrm{F}_{\mathrm{RA}_\mathrm{y}} \\ \mathrm{F}_{\mathrm{RA}_\mathrm{z}} \end{Bmatrix} \text{and} \begin{Bmatrix} \mathrm{m}_{\mathrm{R}_\mathrm{x}} \\ \mathrm{m}_{\mathrm{R}_\mathrm{z}} \end{Bmatrix} \approx - \begin{Bmatrix} \mathrm{M}_{\mathrm{RA}_\mathrm{x}} \\ \mathrm{M}_{\mathrm{RA}_\mathrm{z}} \end{Bmatrix} \tag{3.29}$$

The coaxial helicopter configuration includes the lower rotor, upper rotor, and flybar. The upper rotor revolves with positive angular velocity (in the shaft frame) and the rotor system model described above is used to simulate its response and rotor aerodynamics. The lower rotor rotates negatively in the shaft frame, changing the direction of the tangent velocities on the blade element in Fig. 3.5 which results in a sign change equation 3.19. The flybar model is a simplified version for the rotor blade system. The flybar is approximated as a teetering rigid rotor which only produces drag. Thus the flybar first harmonic flapping is

$$\beta(t) = \beta_{1C}(t)\cos(\psi_R) + \beta_{1S}(t)\sin(\psi_R) \tag{3.30}$$

and the segment aerodynamic forces are

$$\begin{Bmatrix} \Delta F_{RA_x} \\ \Delta F_{RA_y} \\ \Delta F_{RA_z} \end{Bmatrix} = \frac{1}{2}\rho V^2 c\Delta r \begin{Bmatrix} 0 \\ -c_\phi C_d \\ -s_\phi C_d \end{Bmatrix} \tag{3.31}$$

The upper rotor cyclic pitch inputs are controlled by the flybar through a pitch linkage (Fig. 3.6). It is assumed the flybar-upper rotor pitch linkages are rigid and do not affect the motion of the flybar. The relation between flybar flap angle and upper rotor pitch input is developed from linkage geometry as

$$\theta_{1cyc,UR}(\psi_{R,UR}) = \sin^{-1}\left[\frac{-\sin[\beta_{FB}(\psi_{R,UR}+\phi_{FB})]\ell_{FB}}{\ell_{UR}}\right] \tag{3.32}$$

where ϕ_{FB} is the phase angle between the flybar and upper rotor. Using Eqn 3.32, the upper rotor blade pitch can be written as

$$\theta_{UR}(\psi_{R,UR}, r_x) = \theta_{0UR} + \frac{(\epsilon+r_x)}{\epsilon+R}\theta_{tUR} - \sin^{-1}\left[\frac{-\sin[\beta_{FB}(\psi_{R,UR}+\phi_{FB})]\ell_{FB}}{\ell_{UR}}\right] \tag{3.33}$$

The rotors are driven by brushed DC motors which are modeled as first order systems

$$\begin{Bmatrix} \dot{\Omega}_{LR} \\ \dot{\Omega}_{UR} \end{Bmatrix} = \frac{1}{\tau_M}\begin{Bmatrix} C_{LR}u_{LR} - \Omega_{LR} \\ C_{UR}u_{UR} - \Omega_{UR} \end{Bmatrix} \tag{3.34}$$

where τ_M is the motor time constant, u_{LR} and $u_{UR}$are the motor throttle inputs, and C_{LR} and C_{UR} are the motor coefficients. The lower rotor is controlled by cyclic inputs of a swashplate which is driven by servo motors. The swashplate angles are also modeled as first order responses.

$$\begin{Bmatrix} \dot{\theta}_{1C} \\ \dot{\theta}_{1S} \end{Bmatrix} = \frac{1}{\tau_{SW}} \begin{Bmatrix} C_{lon}u_{lon} - \theta_{1C} \\ C_{lat}u_{lat} - \theta_{1C} \end{Bmatrix} \tag{3.35}$$

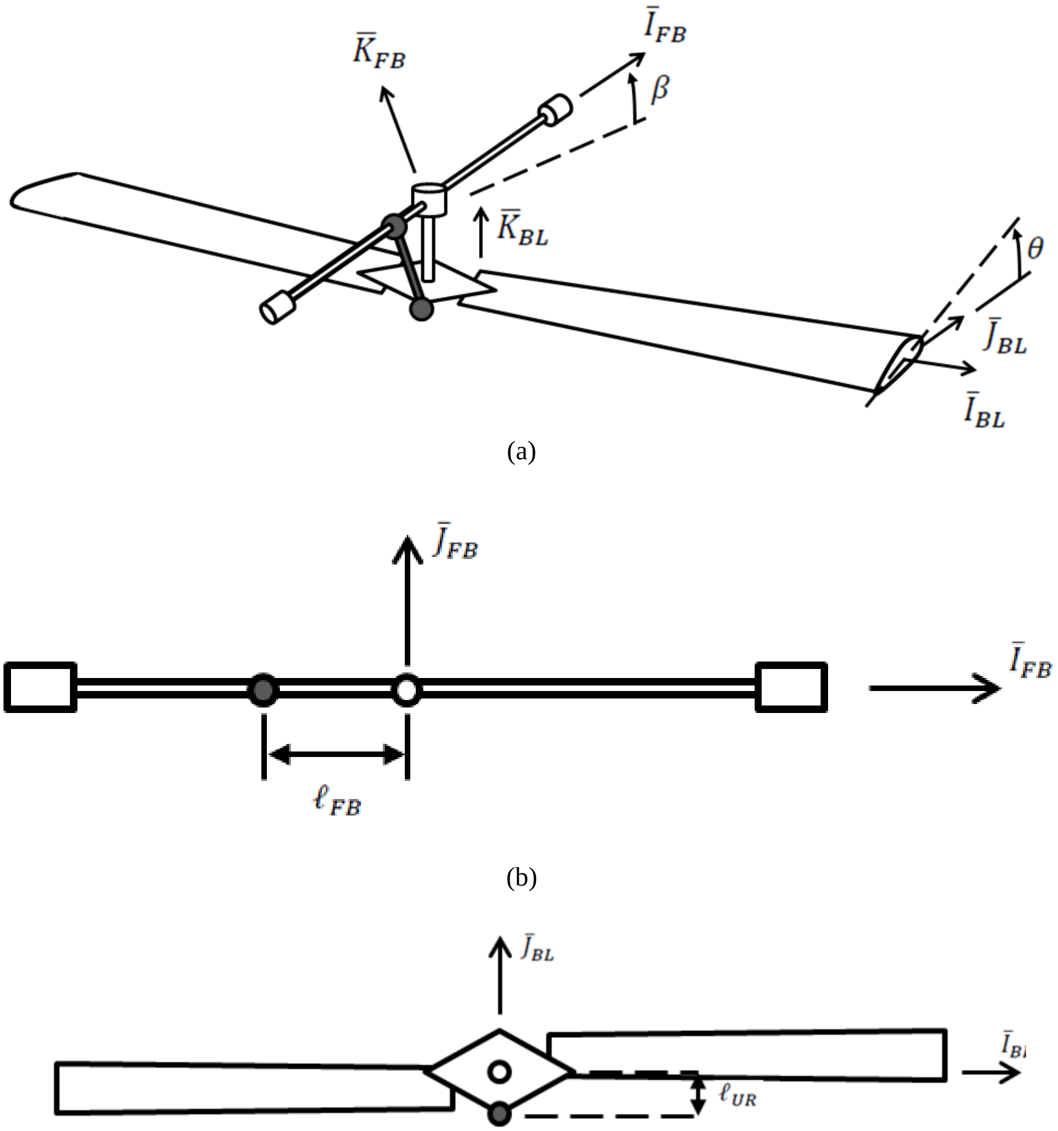

(a)

(b)

(c)

Figure 3.6. Illustration flybar-upper rotor linkage. (a) combined system (b) flybar (c) upper rotor.

3.2 Rotor Inflow and Wake

Rotor inflow is calculated using Glauret's flow model—Figure 3.7. It is assumed that the inflow is uniform across the rotor disk and is quasi-steady compared to all other vehicle dynamics.

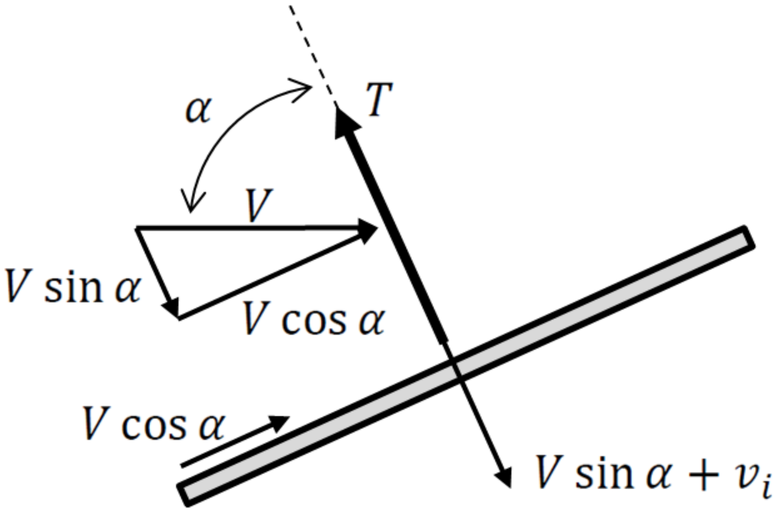

Figure 3.7. Illustration of momentum theory rotor disk inflow.

Through momentum theory of air moving through the rotor disk a transcendental equation is derived, and a Newton-Rhapson iteration is employed to solve for the inflow.

$$v_i^4 + 2V\sin(\alpha)\, v_i^3 + V^2 v_i^2 = \left(\frac{T}{2\rho A}\right)^2 \tag{3.36}$$

Momentum theory is not valid in axial descent when the rotor wake convects back up into the rotor. Leishman [70] proposed a continuous approximation for induced inflow given by

$$\frac{v_i}{v_h} = \kappa + k_1\left(\frac{V_c}{v_h}\right) + k_2\left(\frac{V_c}{v_h}\right)^2 + k_3\left(\frac{V_c}{v_h}\right)^3 + k^4\left(\frac{V_c}{v_h}\right)^4 \tag{3.37}$$

where V_c is the vertical climb velocity and v_h is the inflow velocity at hover. Equation 3.37 is valid for the range $-2 \le V_c/v_h \le 0$ when the vehicle is in vertical descent. It is assumed the rotor is in axial descent when the forward flight speed is less than 0.2 m/s; in all other operating states momentum theory is used. Figure 3.8 shows the inflow curve over a range of climb velocities.

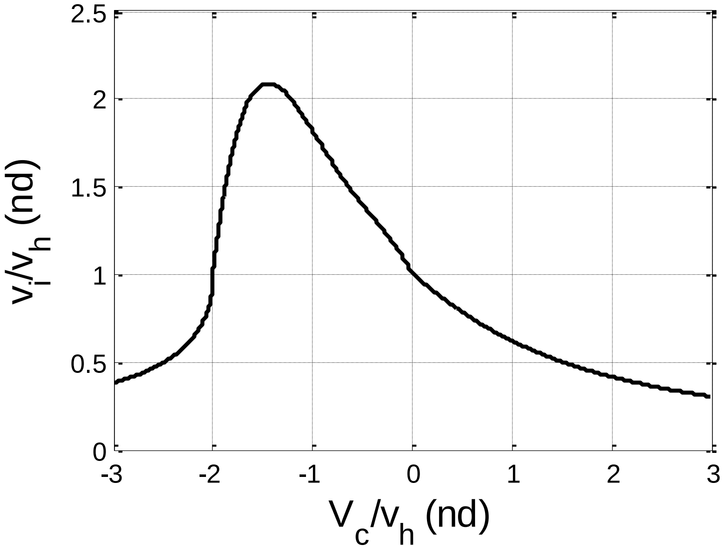

Figure 3.8. Induced inflow curve for axial climb and descent nondimensionalized by the hover inflow value.

The upper rotor wake affects the inflow of the lower rotor. For simplicity, it is assumed the wake is fully contracted. Using momentum theory it can be shown that a fully contracted rotor wake has a planar area of half the rotor disk area and the flow velocity is twice the inflow velocity at the rotor disk. To account for the convection of the wake in forward flight, longitudinal and lateral wake skew angles are used to determine the location of the wake relative to the lower rotor.

$$\chi = \tan^{-1}\left(\frac{v_{ox}-v_{atx}}{v_{oz}-v_{atz}+v_{i,u}}\right) \tag{3.38}$$

$$\xi = \tan^{-1}\left(\frac{v_{oy}-v_{aty}}{v_{oz}-v_{atz}+v_{i,u}}\right)$$

Figure 3.9 illustrates the wake affect of the upper rotor on the lower rotor including the longitudinal skew angle. It is assumed that the lower rotor has no effect on the upper rotor.

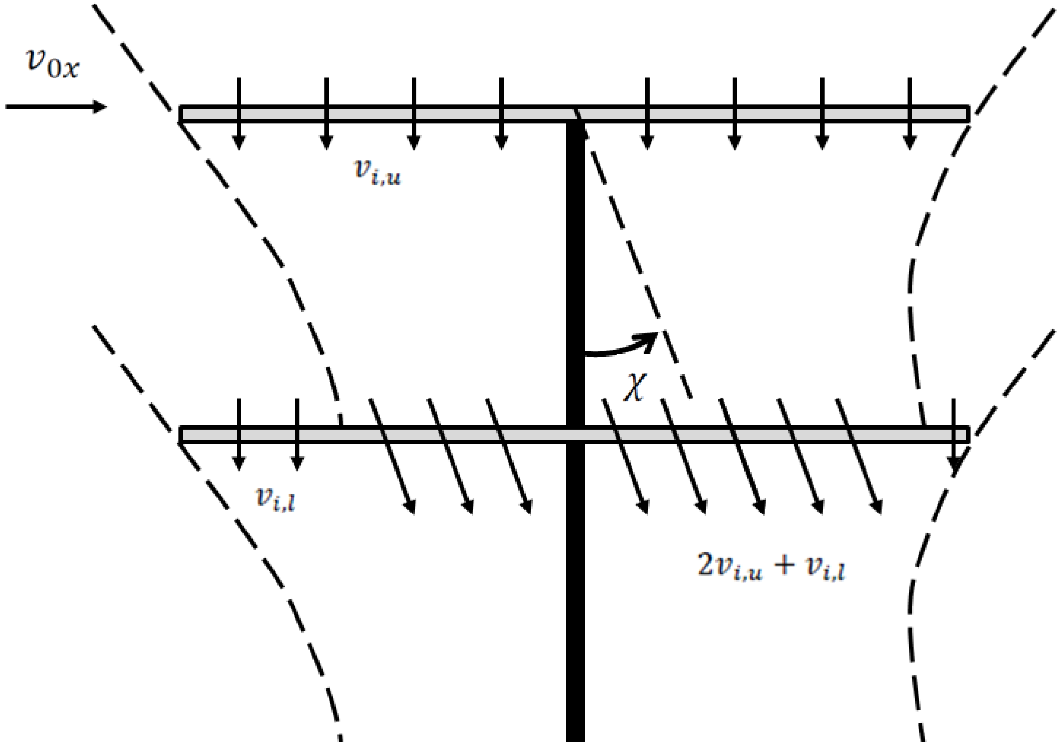

Figure 3.9. Illustration upper rotor-lower rotor wake interaction.

Vertical download force on the fuselage due to the wake was modeled according to Leishman [70] as

$$F_{DL} = \frac{1}{2}\rho\bar{v}^2 f_{DL} \tag{3.39}$$

where $f_{DL}$is the equivalent vertical flat plate drag area and $\bar{v}$ is the average velocity of the rotor wake.

3.3 Gravity, Aerodynamic Drag, and Actuator Dynamics

Besides rotor loads, the other external forces and moments acting on the helicopter airframe are gravity and aerodynamic drag on the fuselage and tail. The gravity forces in the body frame are:

$$\begin{Bmatrix} X_G \\ Y_G \\ Z_G \end{Bmatrix} = mg \begin{Bmatrix} s_\theta \\ -s_\phi c_\theta \\ -c_\phi c_\theta \end{Bmatrix} \tag{3.40}$$

The body aerodynamic forces are modeled acting on the vehicle center of pressure as:

$$\begin{Bmatrix} X_{BA} \\ Y_{BA} \\ Z_{BA} \end{Bmatrix} = -\tfrac{1}{2}\rho V_{CP} S \begin{Bmatrix} C_{D_x} u_{CP} \\ C_{D_y} v_{CP} \\ C_{D_z} w_{CP} \end{Bmatrix} \tag{3.41}$$

where

$$V_{CP} = \sqrt{u_{CP}^2 + v_{CP}^2 + w_{CP}^2} \tag{3.42}$$

The aerodynamic velocity components at the center of pressure can be expressed in the body frame as

$$\begin{Bmatrix} u_{CP} \\ v_{CP} \\ w_{CP} \end{Bmatrix} = \begin{Bmatrix} u \\ v \\ w \end{Bmatrix} + \mathbb{S}_B(\bar{\omega}_{B/I})\mathbb{C}_B(\bar{r}_{CG\to CP}) - \begin{Bmatrix} u_w(x,y,z,t) \\ v_w(x,y,z,t) \\ w_w(x,y,z,t) \end{Bmatrix} \tag{3.43}$$

where $\bar{r}_{CG\to CP}$ is a position vector from the center of mass to the center of pressure, and u_w, v_w, and $w_w$are the wind components at the vehicle center of gravity vary as functions of time and spatial location. The body aerodynamic moments about the center of mass are

$$\begin{Bmatrix} L_{BA} \\ M_{BA} \\ N_{BA} \end{Bmatrix} = \tfrac{1}{2}\rho V_{CP} S D^2 \begin{Bmatrix} C_{l_p} p \\ C_{m_q} q \\ C_{n_r} r \end{Bmatrix} + \mathbb{S}_B(\bar{r}_{CG\to CP}) \begin{Bmatrix} X_{BA} \\ Y_{BA} \\ Z_{BA} \end{Bmatrix} \tag{3.44}$$

The forces generated by the vertical tail are modeled similar to the body aerodynamic forces as:

$$\begin{Bmatrix} X_T \\ Y_T \\ Z_T \end{Bmatrix} = -\tfrac{1}{2}\rho V_T S_T \begin{Bmatrix} C_{DT_x} u_T \\ C_{DT_y} v_T \\ C_{DT_z} w_T \end{Bmatrix} \tag{3.45}$$

where the aerodynamic velocity components at the tail are expressed as

$$\begin{Bmatrix} u_T \\ v_T \\ w_T \end{Bmatrix} = \begin{Bmatrix} u - u_w \\ v - v_w \\ w - w_w \end{Bmatrix} + \mathbb{S}_B(\bar{\omega}_{B/I})\mathbb{C}_B(\bar{r}_{CG\to T}) \tag{3.46}$$

3.4 Closed Form Rotor System Validation Cases

In order to verify the rotor system model is correctly simulating rotor response, a series of simple steady state validation cases are performed for which the closed form solutions are known. To analytically solve for the steady state closed form solutions, several assumptions were made. For all cases:

(i) Small angle approximation is made for β and ϕ.

(ii) Body linear and angular rates are constant.

(iii) Rotor angular velocity is constant.

(iv) Induced inflow is constant and uniform across the rotor disk.

(v) Blade inertia terms have the following relations:

$$I_{b_{yy}} + \frac{m_b L^2}{4} = \bar{I}_b \tag{3.47}$$

$$-I_{b_{xx}} + I_{b_{zz}} \cong I_{b_{yy}} \tag{3.48}$$

(vi) Blade center of gravity is located at midpoint of blade, $l^* = \frac{L}{2}$.

(vii) The blade has constant chord, c, sectional lift coefficient, a, and sectional drag coefficient, C_d.

(viii) The blade section velocity components are related as $u_T \gg u_p$ thus $V^2 \approx u_T^2$ and $\approx \frac{u_P}{u_T}$.

(ix) The blade section parameters $C_d, \phi \ll 1$ thus $s_\phi C_d \approx 0$.

(x) The position vector from the blade hinge point to an arbitrary blade section is $\bar{r}_{F\rightarrow P} = r_x \hat{I}_{BL}$.

Additional assumptions made for individual cases are stated in the descriptions.

Case 1: Flapping Response to Control Inputs

For this case it is assumed the rotor blade has zero hinge offset, no hinge spring, and is in hover. With all these assumptions equation 3.7 simplifies to

$$\ddot{\beta} = \frac{-M_{RA_y}}{\bar{I}_b} - \frac{m_b g L}{2\bar{I}_b} - \Omega^2 \beta \tag{3.49}$$

From equation 3.14, the aerodynamic moment at the blade hinge point is

$$M_{RA_y} = \int_0^R -r_x \Delta F_{RA_z} \tag{3.50}$$

and the incremental z-direction aerodynamic force is given by equation 3.19

$$\Delta F_{RA_z} = \frac{1}{2}\rho c a \Omega^2 \left[{r_x}^2 \left(\theta_0 - \theta_{1C} c_{\psi_R} - \theta_{1S} s_{\psi_R} \right) + {r_x}^3 \theta_{twist} - {r_x}^2 \frac{\dot{\beta}}{\Omega} - r_x \frac{v_i}{\Omega} \right] dr \tag{3.51}$$

Thus the total aerodynamic moment about the blade hinge is

$$M_{RA_y} = -\rho c a \Omega^2 R^4 \left[\frac{1}{8} \left(\theta_0 - \theta_{1C} c_{\psi_R} - \theta_{1S} s_{\psi_R} \right) + \frac{1}{10} \theta_{twist} - \frac{1}{8} \frac{\dot{\beta}}{\Omega} - \frac{1}{6} \frac{v_i}{\Omega \mathrm{R}} \right] \tag{3.52}$$

Substituting this into equation 3.49, dividing both sides by a factor of Ω^2 and rearranging the terms as

$$\frac{\ddot{\beta}}{\Omega^2} + \frac{\gamma}{8} \frac{\dot{\beta}}{\Omega} + \beta = \frac{\gamma}{8} \left(\theta_0 - \theta_{1C} c_{\psi_R} - \theta_{1S} s_{\psi_R} \right) + \frac{\gamma}{10} \theta_{twist} - \frac{\gamma}{6} \lambda_i - \frac{m_b g L}{2\bar{I}_b \Omega^2} \tag{3.53}$$

where γ is the Lock number, $\gamma = \frac{\rho c a R^4}{\bar{I}_b}$, and λ_i is the nondimensional induced inflow. There are many methods for transforming the individual blade flapping described by equation 3.53 into the first harmonic rotor system states, a simple technique is to note the relation between azimuth angle and rotor angular rate, $\psi_R = \Omega \mathrm{t}$, and using the following transformations:

$$\dot{\beta} = \frac{\partial \beta}{\partial t} = \frac{\partial \psi_R}{\partial t} \frac{\partial \beta}{\partial \psi_R} = \Omega \beta^* \tag{3.54}$$

$$\ddot{\beta} = \Omega^2 \beta^{**} \tag{3.55}$$

From equation 3.23 expressions for $\beta^*$and β^{**} can be written:

$$\beta^* = -\beta_{1C} s_{\psi_R} + \beta_{1S} c_{\psi_R} \tag{3.56}$$

$$\beta^{**} = -\beta_{1C} c_{\psi_R} - \beta_{1S} s_{\psi_R} \tag{3.57}$$

Substituting these transformations into equation 3.53 and employing harmonic balancing, the constant, cosine, and sine terms provide the steady state rotor flap angles as a result of control inputs.

$$\beta_0 = \frac{\gamma}{8}\theta_0 + \frac{\gamma}{10}\theta_{twist} - \frac{\gamma}{6}\lambda_i - \frac{mgL}{2\bar{I}_b\Omega^2} \tag{3.58}$$

$$\beta_{1C} = \theta_{1S} \tag{3.59}$$

$$\beta_{1S} = -\theta_{1C} \tag{3.60}$$

Table 3.1. Rotor system model parameters for Case 1.

Parameter	Value	Units		Parameter	Value	Units
m_b	0.001	kg		c	0.0131	m
$I_{b_{xx}}$	1.40e-08	kg m^2		R	0.086	m
$I_{b_{yy}}$	6.33e-07	kg m^2		a	5.7	1/rad
$I_{b_{zz}}$	6.44e-07	kg m^2		Ω	550.0	rad/s
v_i	1.25	m/s		v_i	1.25	m/s
θ_{twist}	-14.9771	deg		θ_{1C}	1.5	deg
θ_0	21.4	deg		θ_{1S}	-2.1	deg

Table 3.1 shows the parameter values used for the Case 1 simulation and Figure 3.10 shows the resulting time histories for the rotor flap angles compared to the analytical steady state values where the numerical rotor system converges to the steady state values in less than 0.1 seconds.

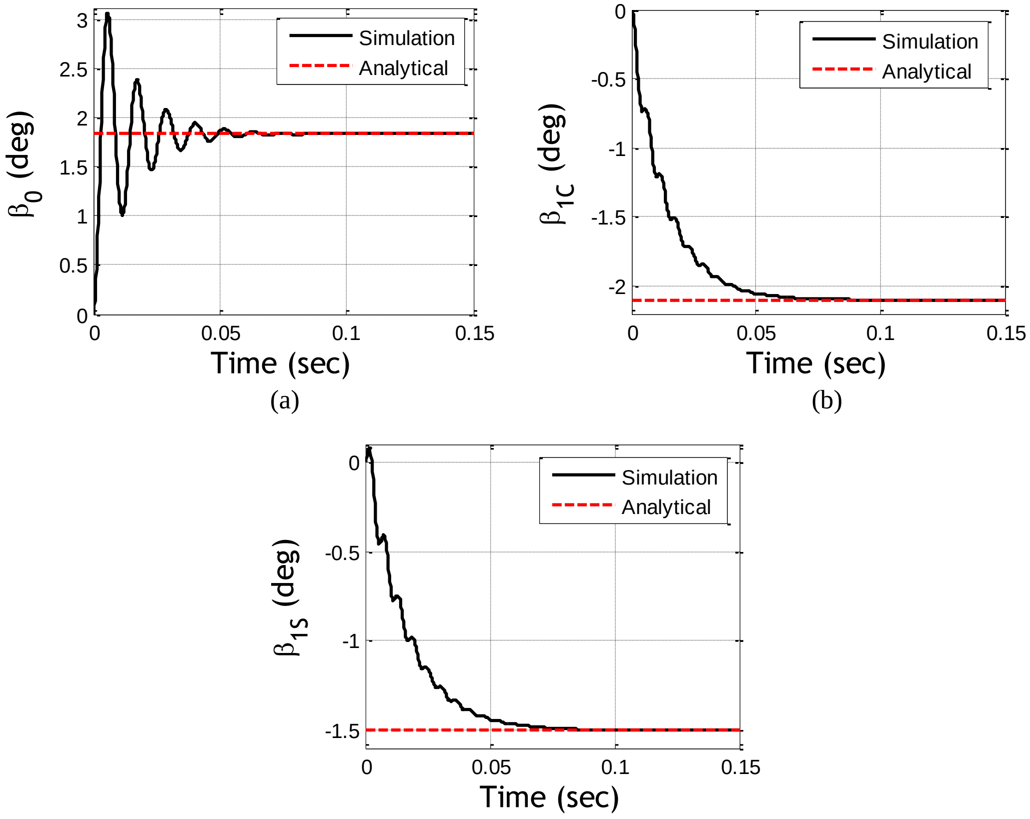

(a) (b) (c)

Figure 3.10. Comparison of rotor system model response to closed from solutions for Case 1, flapping response to control inputs. (a) coning angle (b) longitudinal flapping angle (c) lateral flapping angle.

Case 2: Constant Pitch Rate

For this case, the vehicle is pitching at a constant rate with no translational velocity while the rotor has no rotor inflow, blade pitch, or hinge offset. The body angular rate is written as

$$\bar{\omega}_{B/I} = q\bar{J}_B = q\bar{J}_S \tag{3.61}$$

It is assumed that the pitch rate is small thus $q^2 \approx 0$. Using the same process as in Case 1, the closed form solutions for the first harmonic blade flapping equations are:

$$\beta_0 = -\frac{m_b g L}{2\bar{I}_b \Omega^2} \tag{3.62}$$

$$\beta_{1C} = -\frac{16q}{\gamma\Omega} \tag{3.63}$$

$$\beta_{1S} = -\frac{q}{\Omega} \tag{3.64}$$

Using the same blade properties as in Case 1 (Table 3.1), Figure 3.11 shows the Case 2 rotor response time histories for a constant pitch rate of 10.23 degrees.

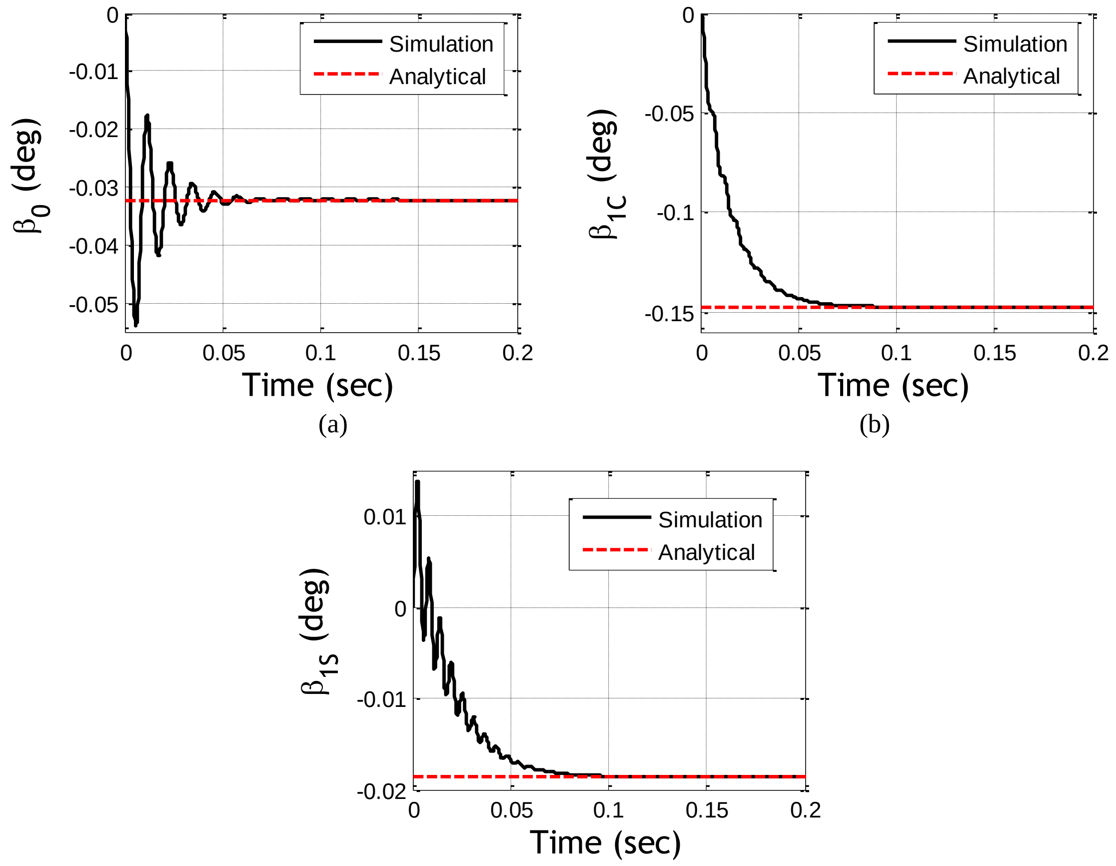

(a) (b)

(c)

Figure 3.11. Comparison of rotor system model response to closed from solutions for Case 2, constant pitch rate. (a) coning angle (b) longitudinal flapping angle (c) lateral flapping angle.

Case 3: Constant Roll Rate

Making the same assumptions as in case 2 for a constant body roll rate of

$$\bar{\omega}_{B/I} = p\bar{I}_B = -p\bar{I}_S \tag{3.65}$$

the closed form steady state solutions are:

$$\beta_{1C} = -\frac{p}{\Omega} \tag{3.66}$$

$$\beta_{1S} = \frac{16p}{\gamma\Omega} \tag{3.67}$$

Figure 3.12 shows the simulation response for a constant roll rate of -5.4 degrees per second.

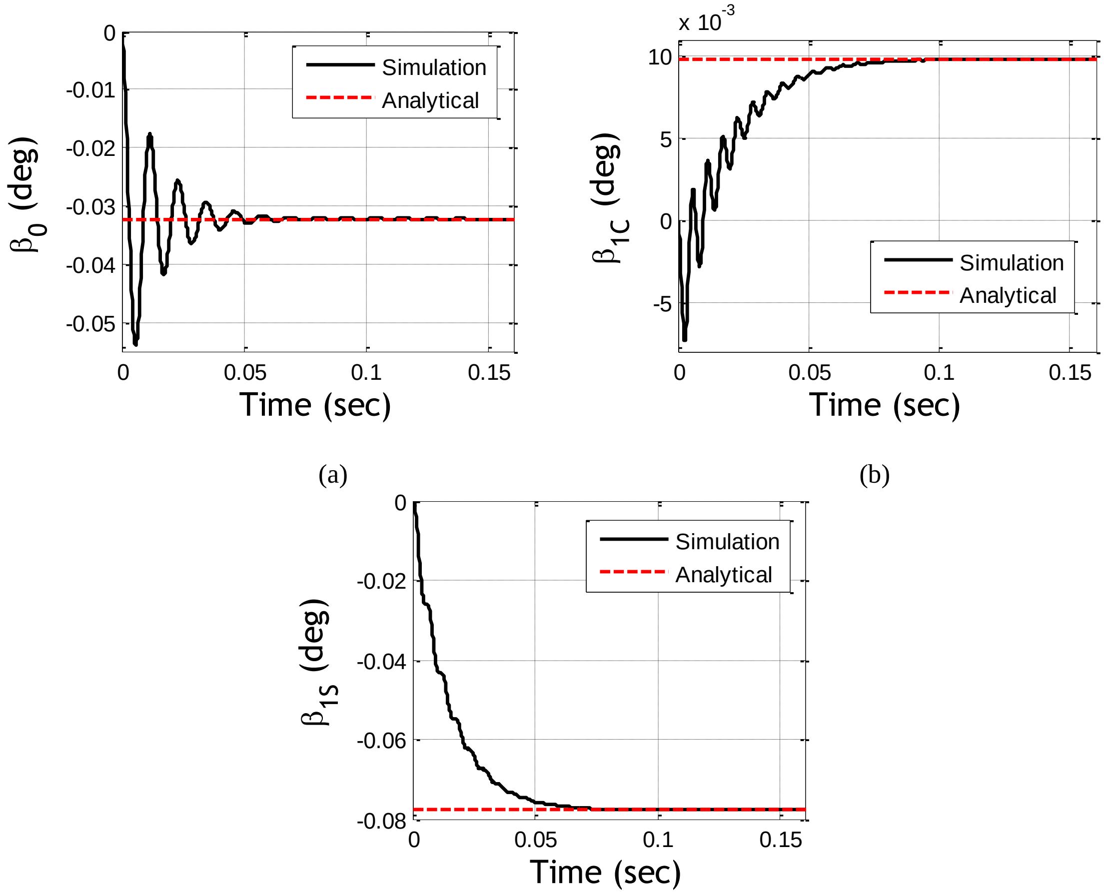

(a) (b)

(c)

Figure 3.12. Comparison of rotor system model response to closed from solutions for Case 3, constant roll rate. (a) coning angle (b) longitudinal flapping angle (c) lateral flapping angle.

Case 4: Constant translational rate, u

With a constant body translational rate

$$\bar{v}_{CG} = u\bar{I}_B = -u\bar{I}_S \tag{3.68}$$

and assuming no vehicle body angular rates, hinge offset, hinge spring, or cyclic pitch inputs the closed form solutions are:

$$\beta_0 = \frac{\gamma}{8}\theta_0(1+\mu^2) - \frac{\gamma}{6}\lambda_i - \frac{m_b g L}{2\bar{I}_b\Omega^2} \tag{3.69}$$

$$\beta_{1C} = \frac{2\mu\left(\lambda_i - \frac{4}{3}\theta_0\right)}{1-\frac{\mu^2}{2}} \tag{3.70}$$

$$\beta_{1S} = -\frac{4}{3}\frac{\mu\beta_0}{1+\frac{\mu^2}{2}} \tag{3.71}$$

where μ is the nondimensional advance ratio

$$\mu = \frac{u}{\Omega R} \tag{3.72}$$

Figure 3.13 shows the rotor response time histories for a forward flight speed of 2.0 m/s. It is interesting to see that the flapping response due to translational rates is much slower than the response due angular rates. This may be due the fact that angular rates directly affect the flapping equations of motion while linear velocities only cause changes to the blade aerodynamic lift and drag.

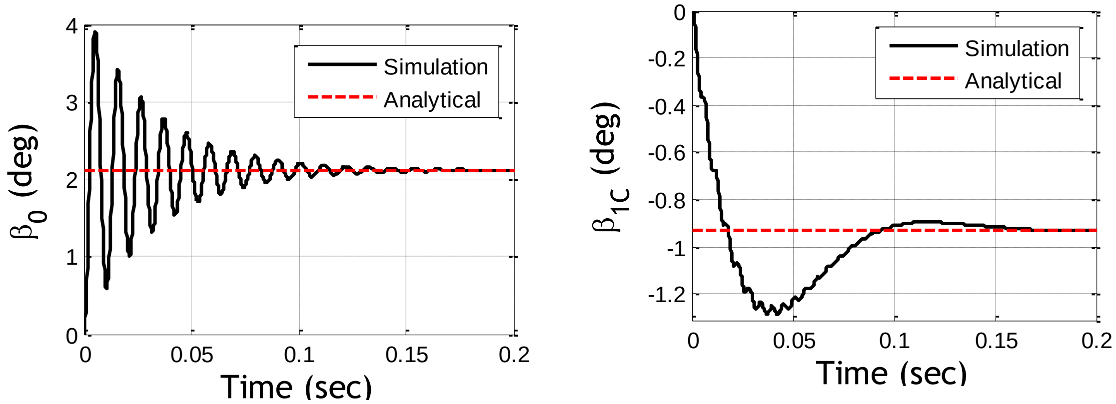

(a)

(b)

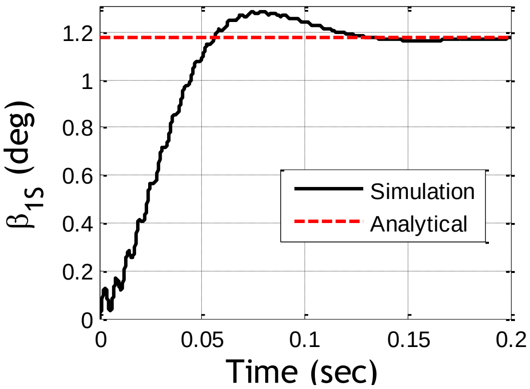

(c)

Figure 3.13. Comparison of rotor system model response to closed from solutions for Case 4, constant translational rate, u. (a) coning angle (b) longitudinal flapping angle (c) lateral flapping angle.

Case 5: Uniform wind disturbance V_{atm_y}

A uniform wind disturbance acts on the rotor system in much the same way as a constant body translational rate does. A constant wind disturbance in the y-axis of the body frame can be expressed as

$$\bar{V}_{atm} = V_{atm_y}\bar{J}_B \tag{3.73}$$

Assuming the vehicle has no hinge offset, hinge spring, or cyclic pitch inputs the closed form solutions are:

$$\beta_0 = \frac{\gamma}{8}\theta_0(1 + {\mu_{atm}}^2) - \frac{\gamma}{6}\lambda_i - \frac{m_b g L}{2\bar{I}_b\Omega^2} \tag{3.74}$$

$$\beta_{1C} = \left(\frac{4}{3}\right)\left(\frac{\mu_{atm}\beta_0}{1+\frac{\mu_{atm}^2}{2}}\right) \tag{3.75}$$

$$\beta_{1S} = \frac{2\mu_{atm}\left(\lambda_i - \frac{4}{3}\theta_0\right)}{1-\frac{\mu_{atm}^2}{2}} \tag{3.76}$$

where μ is the nondimensional advance ratio

$$\mu_{atm} = \frac{V_{atm_y}}{\Omega R} \tag{3.77}$$

Figure 3.14 shows the simulation responses for a wind disturbance of -2.34 m/s. Similar to translation rates, the flapping responses due to wind disturbances are slower than those for angular rates.

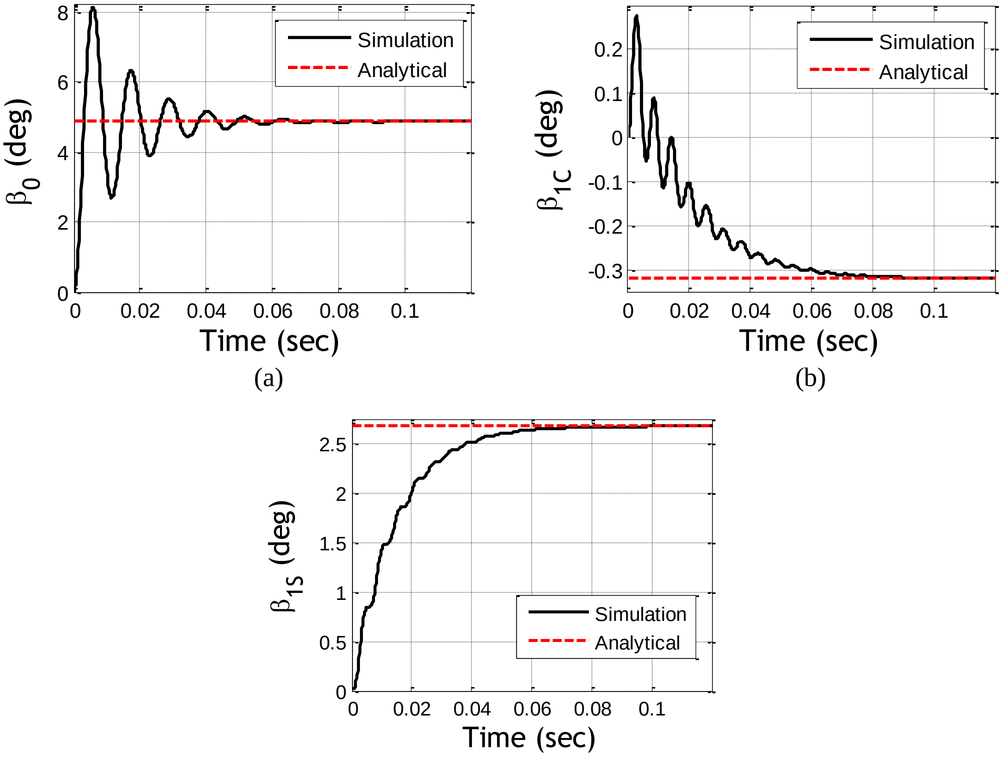

(a)

(b)

(c)

Figure 3.14. Comparison of rotor system model response to closed from solutions for Case 5, uniform wind disturbance. (a) coning angle (b) longitudinal flapping angle (c) lateral flapping angle.

Case 6: Control inputs with hinge offset and hinge spring

The hinge offset and blade length from hinge to tip can be expressed as

$$\epsilon = eR \quad \text{and} \quad L = R(1-e) \tag{3.78}$$

Assuming the vehicle is in hover, the steady state flap angles simplify to

$$\beta_0 = \frac{1}{\nu}\Big[\gamma\theta_0\left(\frac{1}{8} + \frac{e}{3(1-e)} + \frac{e^2}{4(1-e)^2}\right) + \gamma\theta_{twist}\left(\frac{1}{10} + \frac{11e}{40} + \frac{e^2}{2(1-e)} + \frac{e^3}{4(1-e)^2}\right)$$

$$-\gamma\lambda_i\left(\frac{1}{6}+\frac{e}{4(1-e)^2}\right)-\frac{mg\ell^*}{\bar{I}\Omega^2}\Bigg] \tag{3.79}$$

$$\beta_{1C}\left(\frac{1}{8}+\frac{e}{6(1-e)}\right)-\frac{\beta_{1S}}{\gamma}\left(\frac{mR^2e(1-e)}{2\bar{I}}+\frac{k_\beta}{\bar{I}\Omega^2}\right)=\theta_{1S}\left(\frac{1}{8}+\frac{e}{3(1-e)}+\frac{e^2}{4(1-e)^2}\right) \tag{3.80}$$

$$\frac{\beta_{1C}}{\gamma}\left(\frac{mR^2e(1-e)}{2\bar{I}}+\frac{k_\beta}{\bar{I}\Omega^2}\right)+\beta_{1S}\left(\frac{1}{8}+\frac{e}{6(1-e)}\right)=-\theta_{1C}\left(\frac{1}{8}+\frac{e}{3(1-e)}+\frac{e^2}{4(1-e)^2}\right) \tag{3.81}$$

where $\nu = 1+\frac{m_bR^2e(1-e)}{2\bar{I}}+\frac{k_\beta}{\bar{I}\Omega^2}$. Figure 3.15 shows the resulting time histories of the rotor flap angles for $k_\beta = 1.1\ Nm/rad$ and $e = 0.1$.

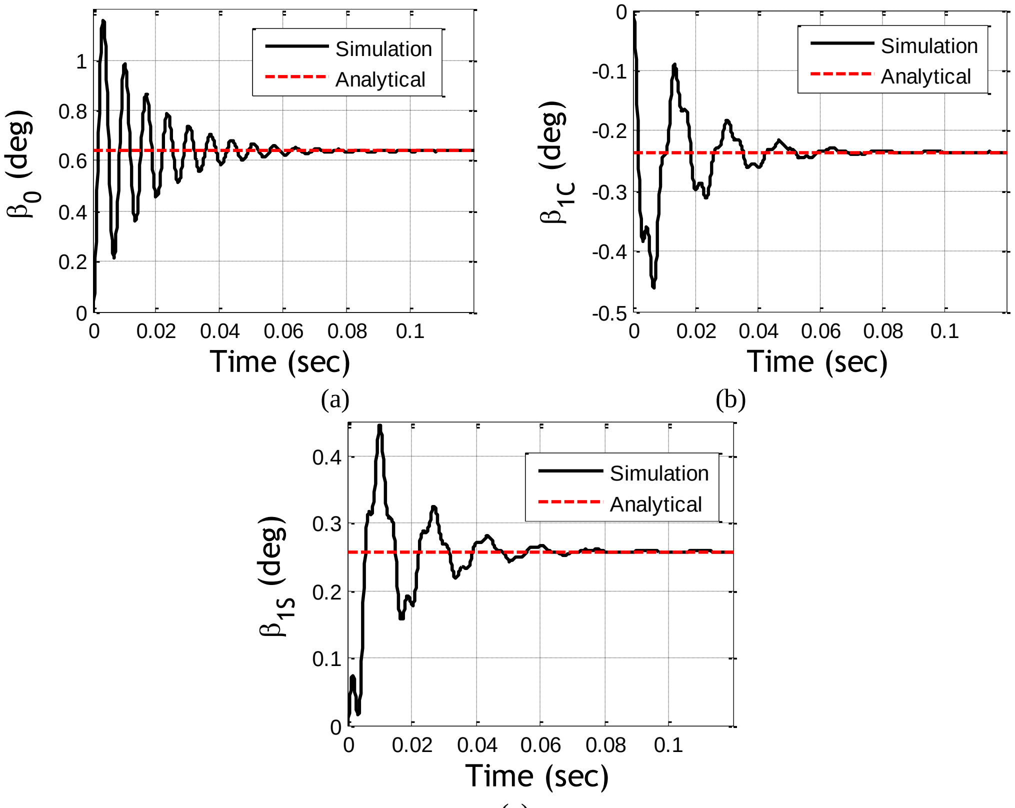

(a) (b)

(c)

Figure 3.15. Comparison of rotor system model response to closed form solutions for Case 6, control inputs with hinge offset and hinge spring. (a) coning angle (b) longitudinal flapping angle (c) lateral flapping angle.

Case 7: Rotor forces and moments

The same process used to develop closed form solutions for rotor flapping response can also be employed to solve for analytical expressions for the rotor system forces and moments. For a vehicle in hover with the standard assumptions:

$$\begin{aligned} F_{RX} = \rho\pi R^2\,(\Omega R)^2 \Big\{ -a\sigma(1-e)\Big[\big((e-3)\beta_{1C} + (1+e)\theta_{1S}\big)\frac{\lambda_i}{8} + (e^2+e+4)\frac{\beta_{1C}\theta_0}{24} \\ -(e^2+e+1)\frac{\beta_0\theta_{1C}}{12} + (e^3+e^2+e+3)\frac{\beta_{1C}\theta_{twist}}{24} + (e^2+e-2)\frac{\beta_0\beta_{1s}}{24}\Big]\Big\} \end{aligned} \quad (3.81)$$

$$\begin{aligned} F_{RY} = \rho\pi R^2\,(\Omega R)^2 \Big\{ -a\sigma(1-e)\Big[\big((e-3)\beta_{1S} + (1+e)\theta_{1C}\big)\frac{\lambda_i}{8} + (e^2+e+4)\frac{\beta_{1S}\theta_0}{24} \\ -(e^2+e+1)\frac{\beta_0\theta_{1S}}{12} + (e^3+e^2+e+3)\frac{\beta_{1S}\theta_{twist}}{24} + (e^2+e-2)\frac{\beta_0\beta_{1C}}{24}\Big]\Big\} \end{aligned} \quad (3.82)$$

$$F_{RZ} = \rho\pi R^2\,(\Omega R)^2 \Big\{ a\sigma(1-e)\Big[(e^2+e+1)\frac{\theta_0}{6} + (e^3+e^2+e+1)\frac{\theta_{twist}}{8} - (1+e)\frac{\lambda_i}{4}\Big]\Big\} \quad (3.83)$$

$$\begin{aligned} M_{RX} = \rho\pi R^2\, R(\Omega R)^2\sigma(1-e)^4 \Big\{\Big(\frac{e}{6(1-e)} + \frac{e^2}{8(1-e)^2} + \frac{1}{16}\Big)\beta_{1C}C_d + a\Big[\frac{e^2(\beta_{1C}-2\theta_{1S})}{8(1-e)^2} - \frac{e^3\theta_{1S}}{4(1-e)^3} - \\ \frac{e\beta_0\beta_{1S}\theta_{twist}}{120} - \frac{\beta_{1C}\lambda_i^2}{8(1-e)^2} + \frac{\lambda_i}{1-e}\Big(\frac{\beta_{1C}\theta_0}{12} - \frac{\beta_0\theta_{1C}}{12} - \frac{\beta_0\beta_{1S}}{6} + \frac{\beta_{1C}\theta_{twist}}{16} + \Big[\frac{e}{8(1-e)}\big(\beta_{1C}\theta_0 - \beta_0\theta_{1C} + \\ \beta_{1C}\theta_{twist}\big)\Big] - \frac{e\beta_{1C}\theta_{twist}}{48}\Big) + \frac{1}{64}\Big({\beta_{1C}}^2\theta_{1S} - {\beta_{1S}}^2(\beta_{1C}+\theta_{1S}) - {\beta_{1C}}^3 + 4\beta_0\beta_{1S}\theta_0 - \\ 2\beta_{1C}\beta_{1S}\theta_{1C} + \frac{16}{5}\beta_0\beta_{1S}\theta_{twist}\Big) + \frac{e}{48(1-e)}\big(4\beta_{1C} - 4\theta_{1S} + {\beta_{1C}}^2\theta_{1S} - {\beta_{1S}}^2\theta_{1S} + \\ 4\beta_0\beta_{1S}\theta_0 - 2\beta_{1C}\beta_{1S}\theta_{1C} + 4\beta_0\beta_{1S}\theta_{twist}\big)\Big]\Big\} \end{aligned} \quad (3.84)$$

$$\begin{aligned} M_{RY} = \rho\pi R^2\, R(\Omega R)^2\sigma(1-e)^4 \Big\{\Big(\frac{e}{6(1-e)} + \frac{e^2}{8(1-e)^2} + \frac{1}{16}\Big)\beta_{1S}C_d + a\Big[\frac{e^2(\beta_{1S}+2\theta_{1C})}{8(1-e)^2} - \frac{e^3\theta_{1C}}{4(1-e)^3} - \\ \frac{e\beta_0\beta_{1C}\theta_{twist}}{120} - \frac{\beta_{1S}\lambda_i^2}{8(1-e)^2} + \frac{\lambda_i}{1-e}\Big(\frac{\beta_{1S}\theta_0}{12} - \frac{\beta_0\theta_{1S}}{12} - \frac{\beta_0\beta_{1C}}{6} + \frac{\beta_{1S}\theta_{twist}}{16} + \Big[\frac{e}{8(1-e)}\big(\beta_{1S}\theta_0 - \beta_0\theta_{1S} + \\ \beta_{1S}\theta_{twist}\big)\Big] - \frac{e\beta_{1S}\theta_{twist}}{48}\Big) + \frac{1}{64}\Big({\beta_{1C}}^2\theta_{1C} - {\beta_{1C}}^2\beta_{1S} - {\beta_{1s}}^2\theta_{1C} - {\beta_{1S}}^3 - 4\beta_0\beta_{1C}\theta_0 + \\ 2\beta_{1C}\beta_{1S}\theta_{1S} - \frac{16}{5}\beta_0\beta_{1C}\theta_{twist}\Big) + \frac{e}{48(1-e)}\big(4\beta_{1S} + 4\theta_{1C} + {\beta_{1C}}^2\theta_{1C} - {\beta_{1S}}^2\theta_{1C} - \\ 4\beta_0\beta_{1C}\theta_0 + 2\beta_{1C}\beta_{1S}\theta_{1S} - 4\beta_0\beta_{1C}\theta_{twist}\big)\Big]\Big\} \end{aligned} \quad (3.85)$$

$$M_{RZ} = \rho\pi R^2\, R(\Omega R)^2\sigma(1-e)^4\left\{-\left(\frac{e^3}{2(1-e)^3} + \frac{3e^2}{4(1-e)^2} + \frac{e}{2(1-e)} + \frac{1}{8}\right)c_d + a\left[\left(\frac{e}{2(1-e)} + \frac{1}{4}\right)\frac{\lambda_i^2}{(1-e)^2}\right] - \left(\frac{\theta_0}{6} + \theta_{twist}\frac{1+e}{8} + \frac{e(2\theta_0 + \theta_{twist})}{4(1-e)} + \left[\frac{e^2}{2(1-e)^2}(\theta_0 + \theta_{twist})\right]\right)\frac{\lambda_i}{1-e} + \left(\frac{1}{16}\right)\left({\beta_{1C}}^2 - \theta_{1S}\beta_{1C} + {\beta_{1S}}^2 + \theta_{1C}\beta_{1S}\right) + \frac{e}{12(1-e)}(\beta_{1C}^2 - 2\theta_{1S}\beta_{1C} + \beta_{1S}^2 + 2\theta_{1C}\beta_{1S}) - \frac{e^2}{8(1-e)^2}(\beta_{1C}\theta_{1S} - \beta_{1S}\theta_{1C})\right\} \tag{3.86}$$

It is possible that the closed form equations listed above can be simplified further using the relations cyclic flap angle and control inputs with a hinge offset as well as neglecting higher order terms. Table 3.2 shows the case specific parameters values used in this simulation. The blade properties are the same as the earlier cases. Figure 16 shows the rotor force and moment time histories in the shaft frame.

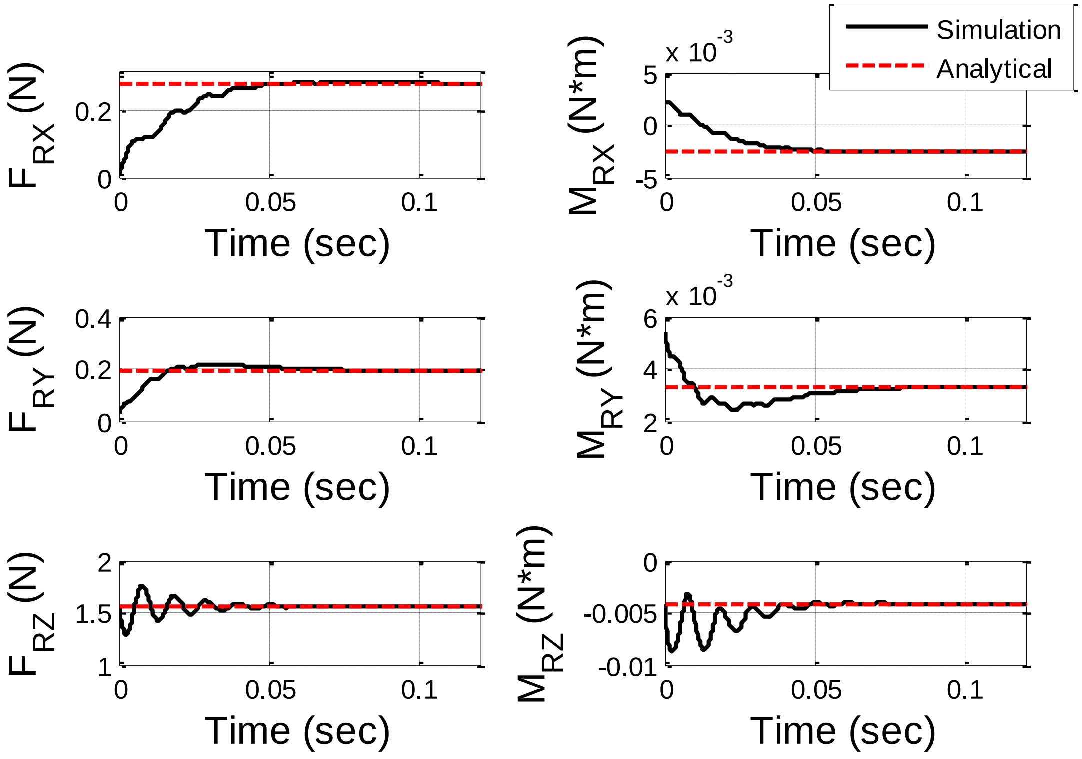

Figure 3.16. Comparison of rotor system model forces and moments to closed form solutions.

Table 3.2. Rotor system model parameters for Case 7.

a	5.7 1/rad	$\mathrm{C_d}$	0.01	θ_{1S}	-5.1 deg
v_i	1.25 m/s	e	0.1	θ_{1C}	12.3 deg
θ_0	21.4 deg	θ_{twist}	-5.2 deg		

3.5 Open Loop Vehicle Simulation

As a check for the entire vehicle model, the response to a series of open loop control inputs is simulated over a fifteen second period. Model parameters are selected to match the experimental platform and yaw rate damping feedback is used to stabilize the vehicle in the same way as the coaxial helicopter used in field experiments. Figure 3.17 shows the sequence of control inputs used to excite the rotorcraft. First, a throttle input increases altitude; this was followed by longitudinal and lateral inputs for forward and side-ward flight respectively, and finally a yaw input to change heading, Fig. 3.18.

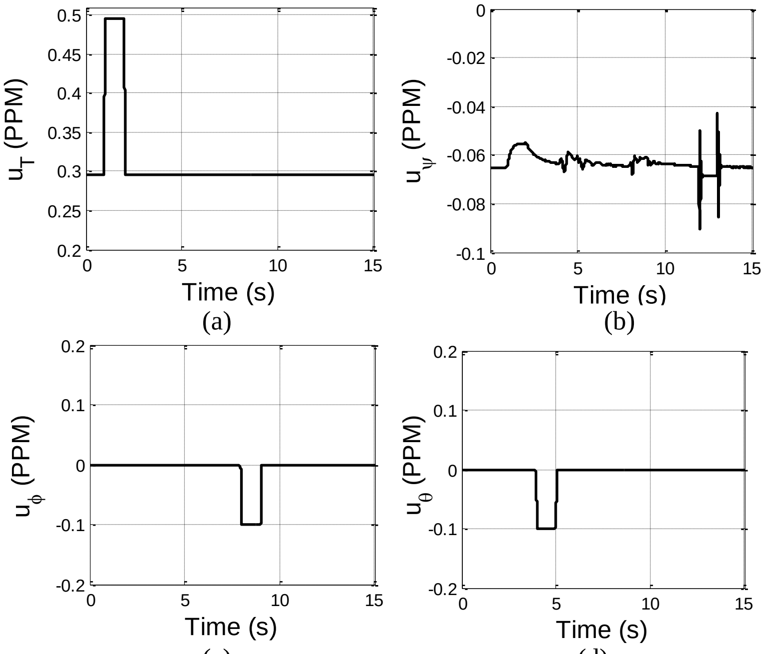

(a) (b) (c) (d)

Figure 3.17. Control input time histories for open loop model simulation. (a) Throttle (b) Yaw Input (c) Lateral Cyclic (d) Longitudinal Cyclic.

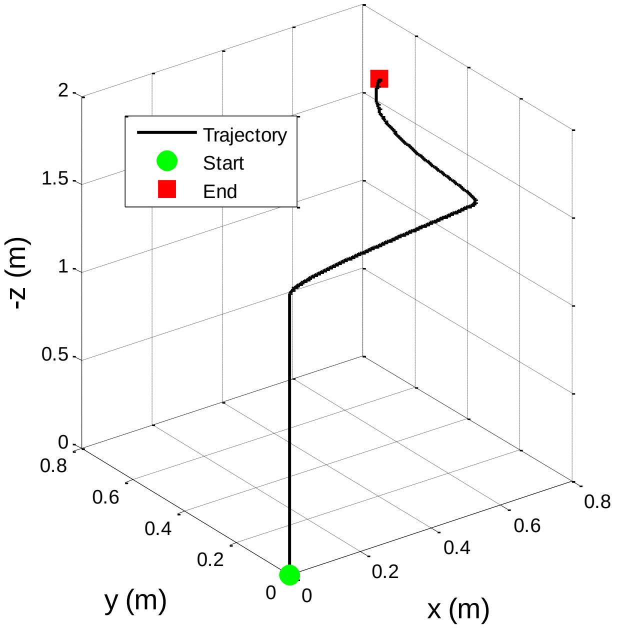

Figure 3.18. Vehicle trajectory of open loop model simulation.

Figures 3.19 and 3.20 show time histories for the rigid body states; the vehicle responds as expected to each of the control inputs—increasing altitude of increasing throttle, pitching forward and moving forward of longitudinal a swashplate input, rolling left and moving left for a lateral swashplate input, and finally changing heading for a yaw input . Figure 3.21 through 3.25 show the rotor speed, rotor flapping, nondimensional inflow, fly bar flapping, and swashplate angle states. The rotor blade hinge offset causes coupling to the longitudinal and lateral flap angles, but it is clear that for a pitch input the lower rotor disk tilts forward (in the body reference frame) and to the right for a roll input. The upper rotor disk tilts the opposite directions to oppose the motion due to fly bar flapping. The inflow decreases during vertical climb before returning closer to the hover value. The effect of forward and side-ward flight on the inflow is a little more difficult to see since the change is not as large, but small dips can be seen in the lower rotor inflow (Fig. 3.23 a) just before 5 s and 10 s corresponding to the spikes in forward and side velocity. The rotor speed and swashplate angles change as the first order systems.

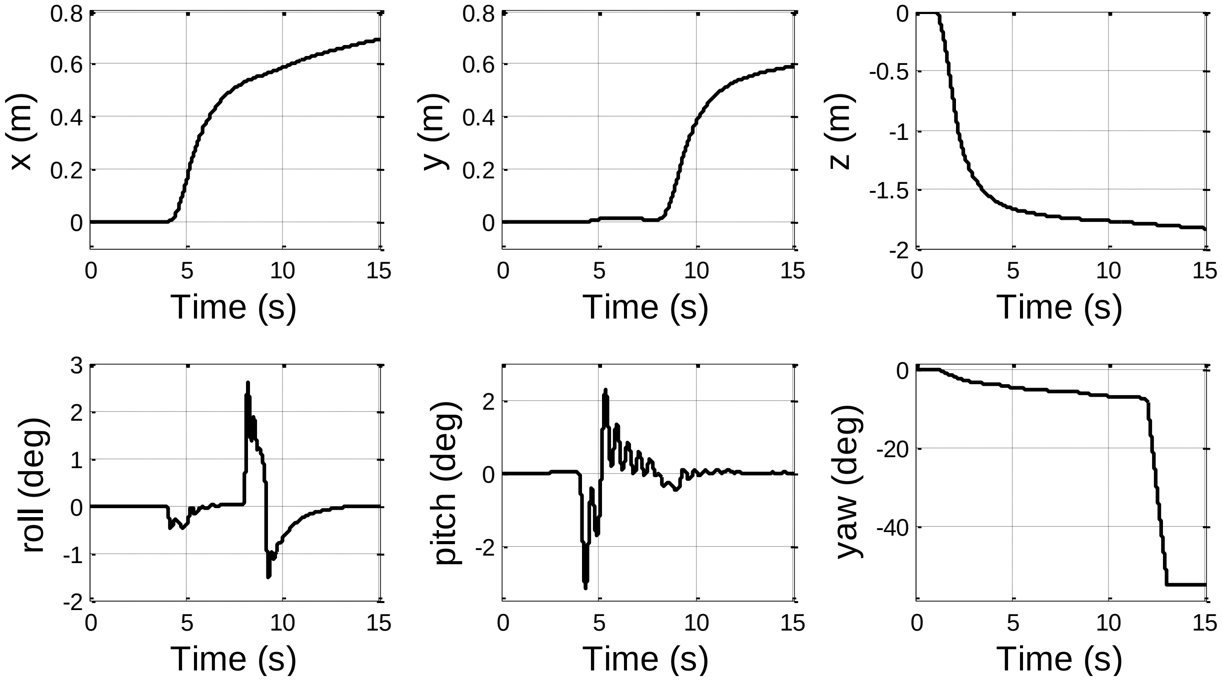

Figure 3.19. Position and attitude time histories of open loop model simulation.

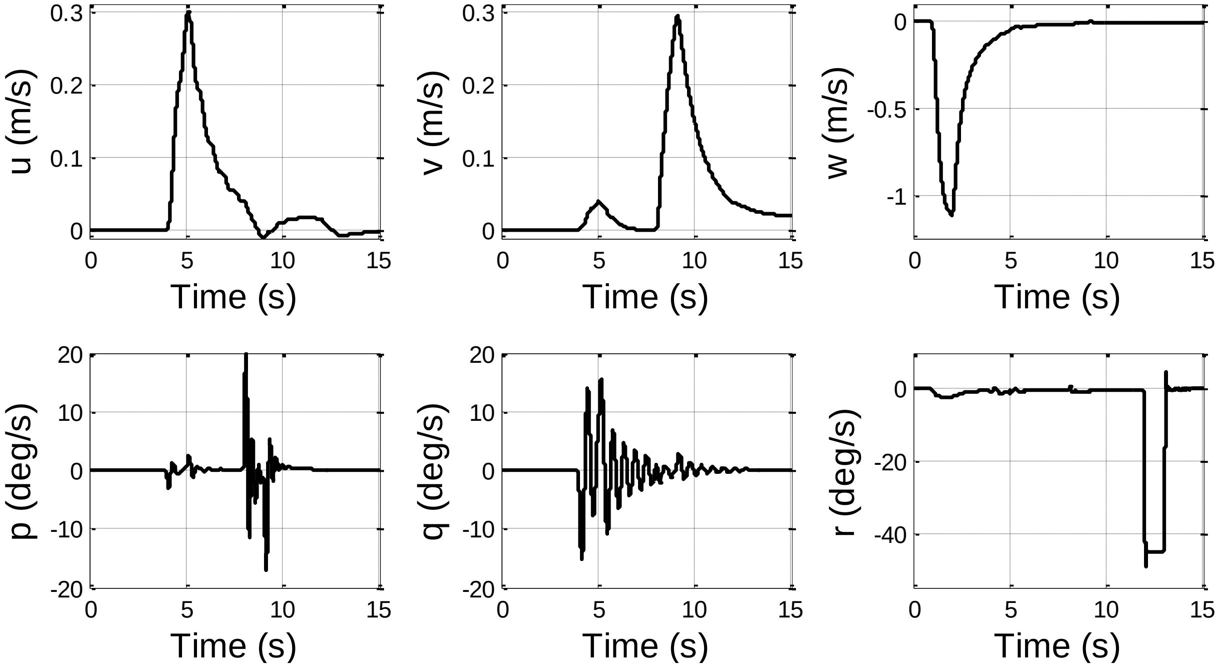

Figure 3.20. Body linear and angular velocities of open loop model simulation.

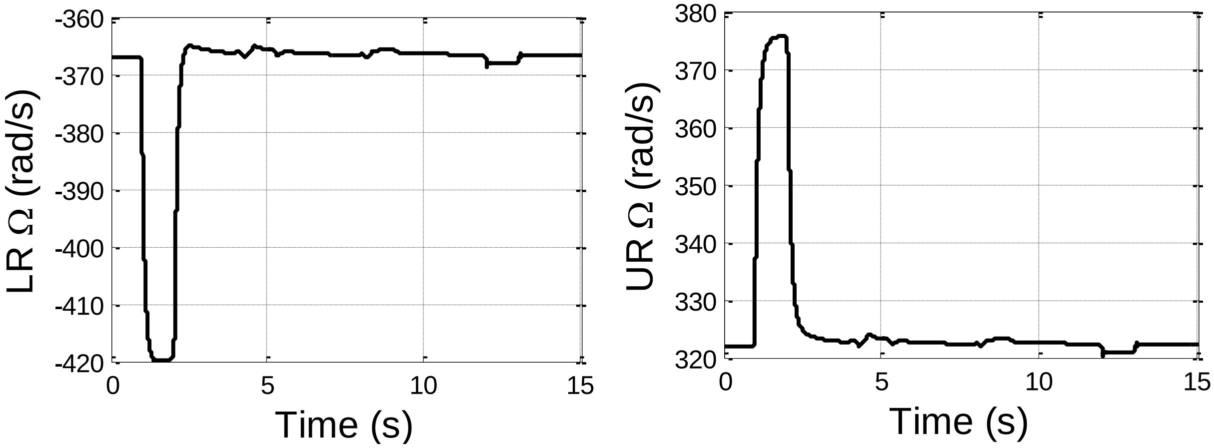

(a) (b)

Figure 3.21. Rotor speeds during open loop model simulation. (a) Lower rotor (b) Upper rotor.

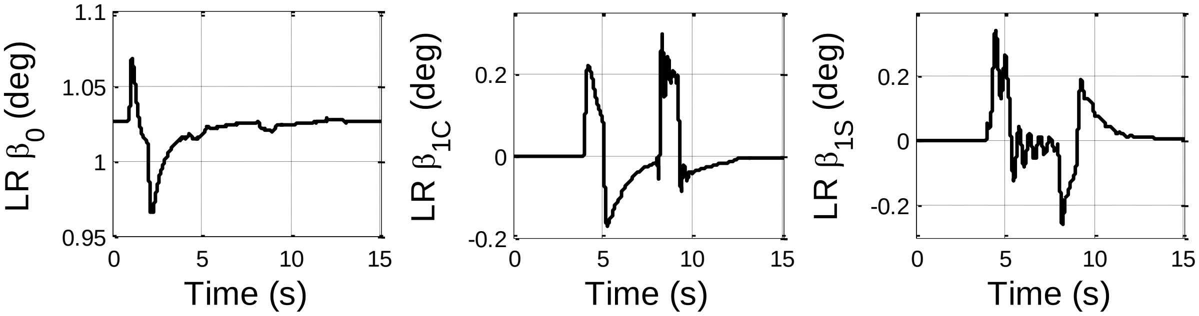

(a)

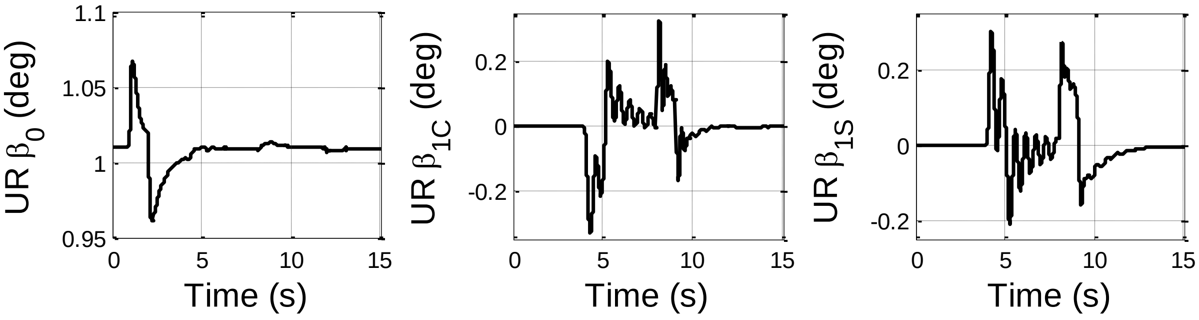

(b)

Figure 3.22. Rotor flapping angles during open loop model simulation. (a) Lower rotor (b) Upper rotor.

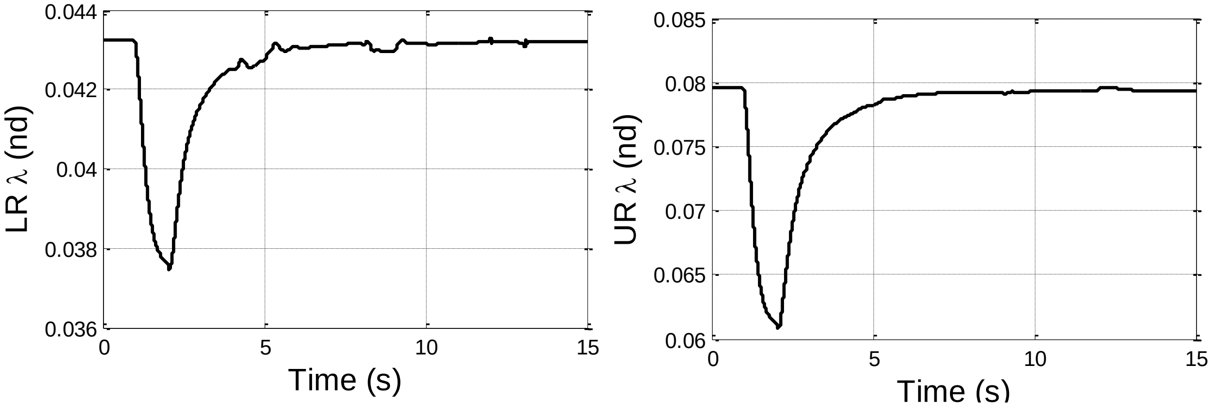

(a) (b)

Figure 3.23. Nondimnesional rotor inflow during open loop model simulation where λ is the dimensional inflow velocity divided the rotor speed and rotor radius. (a) Lower rotor (b) Upper rotor.

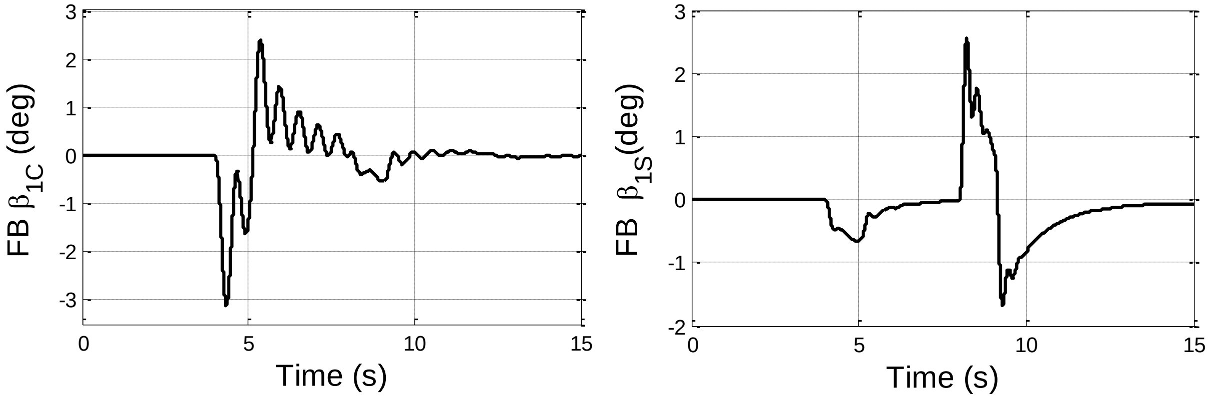

Figure 3.24. Fly bar flap angles.

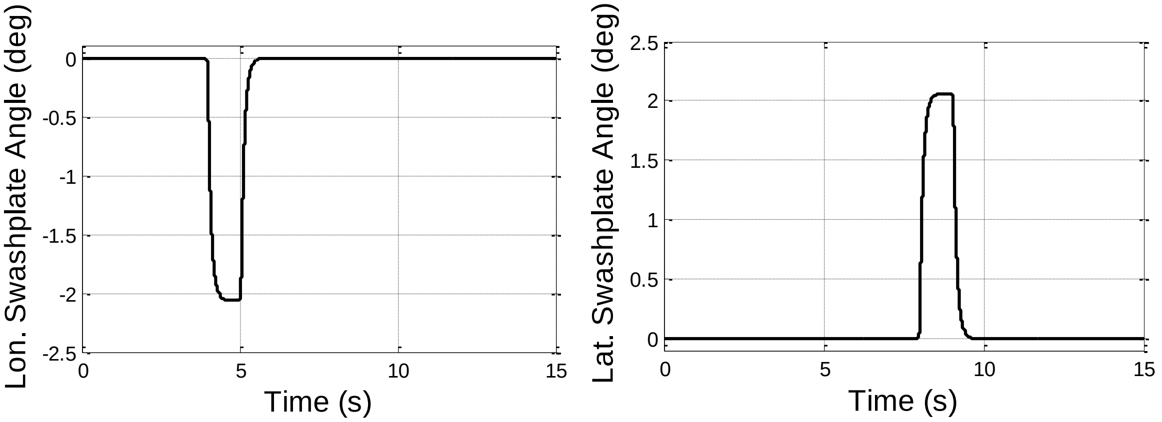

Figure 3.25. Longitudinal and lateral swashplate angles.

CHAPTER 4

COAXIAL HELICOPTER MODEL VALIDATION

This chapter describes the experiments, instrumentation, and procedures used to identify unknown parameters and validate the rotorcraft model developed in Chapter 3. The purpose of the validation process is to assess the accuracy of the dynamic model and consequently the accuracy of the simulation trade studies detailed in later chapters. The system identification procedure involves four steps: direct measurement, estimation from bench top experiments, flight experiments, and fine tuning. After all simulation model parameters are estimated, additional flight tests are used to calculate validation fits for the simulation model, and 95% confidence intervals are estimated for each parameter.

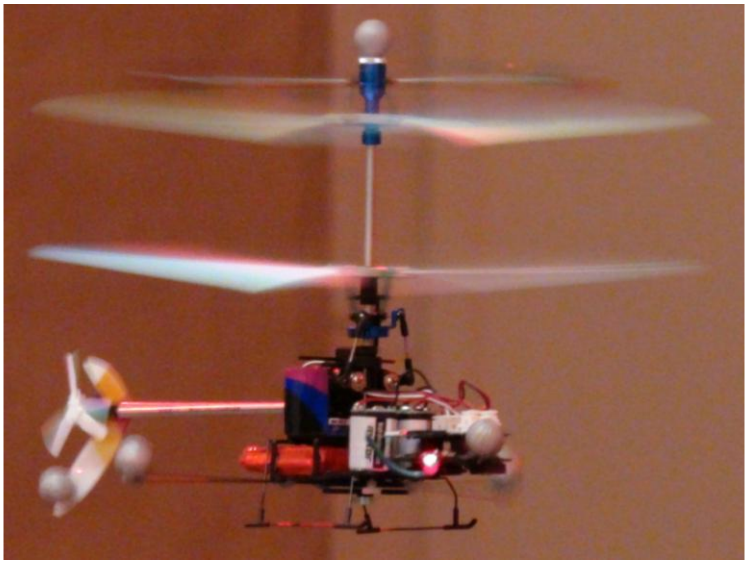

Figure 4.1. Micro coaxial helicopter used to validate the model.

4.1 Direct Measurement

Parameters that can be directly measured through simple means (ruler, scale, etc.) include: vehicle mass, rotor radius and chord, blade mass, blade collective pitch and twist, fly bar mass, fly bar and swashplate phase angles, upper rotor-fly bar linkage lengths, motor coefficients, and distances from the reference point to the rotor hubs. Values for the directly measured parameters are shown in Table 4.3.

4.2 Parameter Estimation from Bench Top Measurements

Simple bench top tests were performed to estimate parameters that could not be directly measured. The goal of these tests is to reduce the number of parameters that must be identified from flight experiments. Parameters identified from bench top tests include rotor blade effective hinge offset and spring constant as well as rotor blade lift and drag coefficients.

As stated in the rotor model development, the flexible rotor blade is approximated as rigid with an effective hinge offset and spring constant (Fig. 3.4b). To estimate both parameters, the tip of the rotor blade is weighted with various known masses and the total deflection is measured, Fig. 4.2.

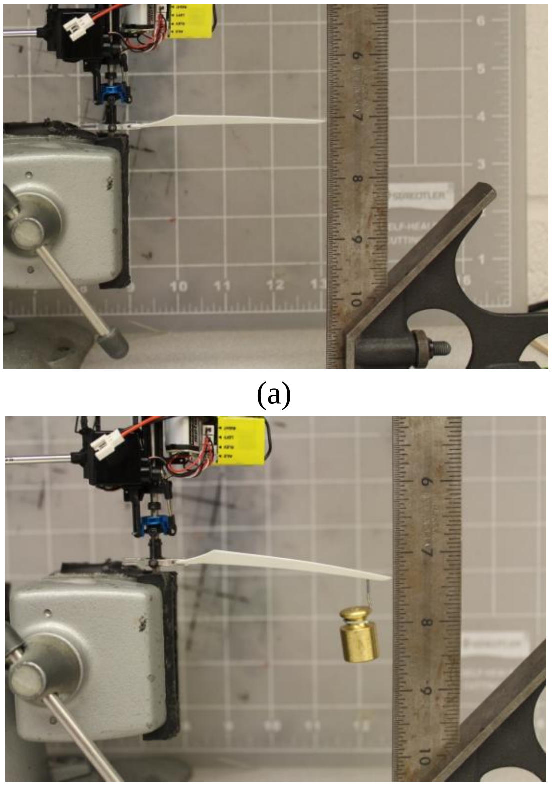

(a)

(b)

Figure 4.2. Effective hinge offset and spring constant test set up. (a) Unloaded (b) Loaded with known mass.

Weights are added to create both positive and negative blade flap angles and repeated to calculate the average deflection for each mass. A simple fit is used to calculate the hinge offset and spring constant by taking the sum of moments about the hinge point and simulating the deflection distance. Figure 4.3 compares the experimental measurements to the simulated results where a positive deflection is the result of a positive flap angle. The estimated parameter values are shown in Table 4.3.

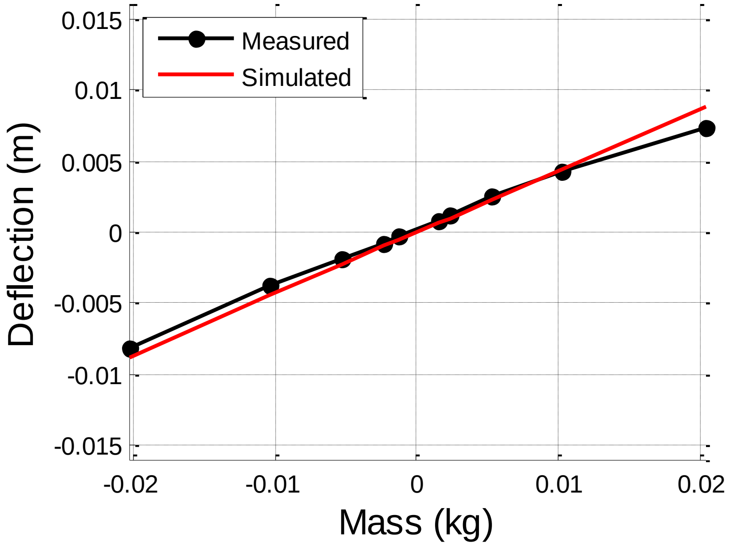

Figure 4.3. Blade deflection with respect to added mass.

Investigation found that the blade cross section is a circular arc air foil for almost the entire length (Fig. 4.4). Based on this shape, the blade sectional lift and drag coefficients are estimated from airfoil theory.

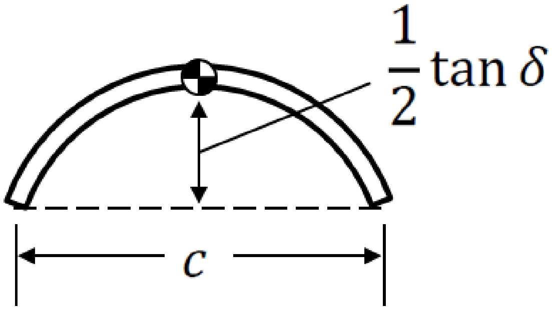

Figure 4.4 . Cross section of circular arc rotor blade.

For low angles of attack, the lift coefficient for a circular arc air foil is calculated using equation 4.1 [71].

$$c_l = \frac{2\pi \sin(\alpha+\delta)}{\cos\delta} \tag{4.1}$$

For high angles of attack, the lift coefficient is approximated using the work of Prouty [72] as

$$c_l = k_{cl}\sin\big(2(\alpha + \alpha_{L0})\big) \tag{4.2}$$

where $\alpha_{L0}$is the zero lift angle of attack. A polynomial fit is used to ensure a smooth transition between the two curves at stall. The drag coefficient has the form:

$$c_d = c_{d0} + c_{d2}\cos(2\alpha) \tag{4.3}$$

where c_{d0} and c_{d2} coefficients are scaled differently for positive and negative angles of attack due to the change in the blade profile as angle of attack changes. Drag coefficients for a thin airfoil, a cylinder, and a cap are used to fit shape c_{d0} and c_{d2} for 0, -90, and 90 degree angles of attack based on the work of Hoerner [73]. For both lift and drag, the stall behavior is approximated from experimental data for circular arc air foils reported by Costello and Beyer [74]. Figures 4.5 and 4.6 show the rotor blade lift and profile drag coefficients versus angle of attack. The values are scaled appropriately to trim the vehicle during fine tuning.

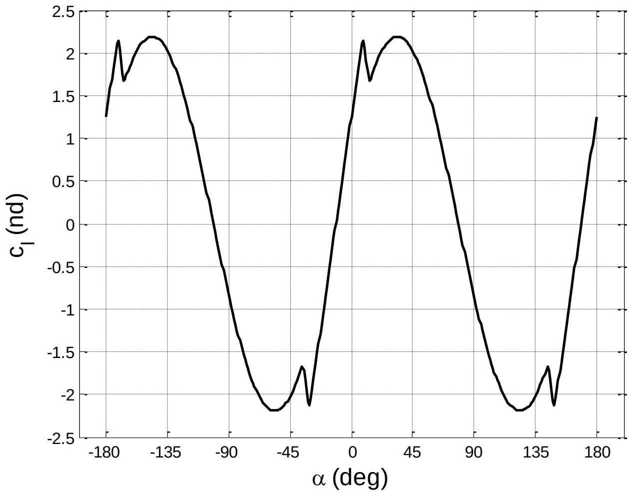

Figure 4.5. Rotor blade aerodynamic lift coefficient with respect to angle of attack.

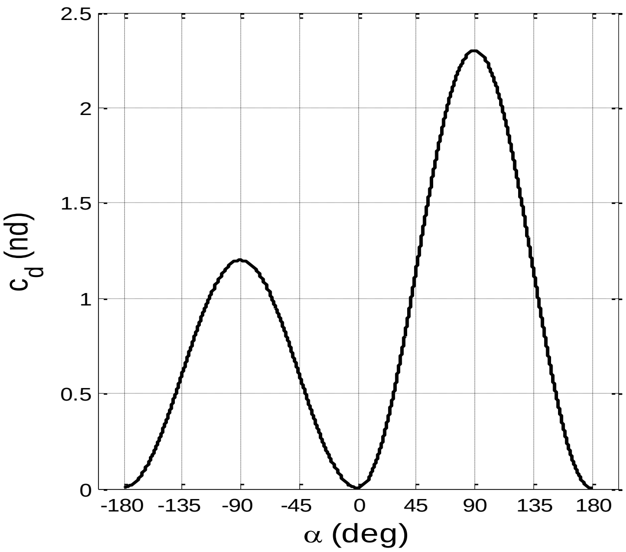

Figure 4.6. Rotor blade aerodynamic drag coefficient with respect to angle of attack.

4.3 Flight Experiments

Piloted flight tests were performed to estimate parameters that could not be directly measured or estimated from bench top tests. The motion capture system in the Indoor Flight Facility (described in Section 2.2) measured vehicle position and attitude during flight, and the onboard electronics recorded control inputs and body angular rates. Flight tests maneuvers are designed to excite the steady state and dynamic response of the platform for each control channel. This includes hover as well as vertical, yaw, roll, and pitch channel maneuvers (Fig. 4.7).

A time domain evaluation of vehicle response is used to estimate model parameters through a numerical optimization method known as meta optimization. Inspired by the idea that an optimization algorithm can work well for certain problems but fail for others, Meta optimization employs a set of optimizers that work collectively to achieve better performance. Each cycle, a basic optimization scheme is randomly chosen. The probability of selecting a particular scheme

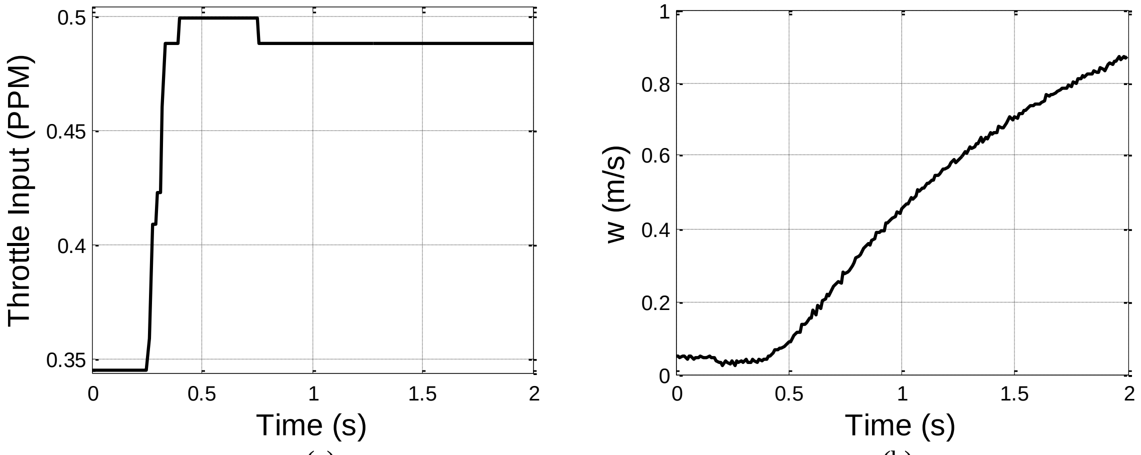

(a) (b)

Figure 4.7. Example flight test time histories for vertical channel response. (a) throttle control input (b) w velocity.

is adjusted by a learning automaton based on performance in previous cycles. By switching between different algorithms, the set can operate more robustly and prevent the solution from "getting stuck" in a region around a local minimum. For the work reported here, the set of optimizers is comprised of: Particle Swarm Optimization, Differential Evolution Optimization, Simplex Optimization, Steepest Descent Optimization, Quasi Newton Optimization and Simulated Annealing.

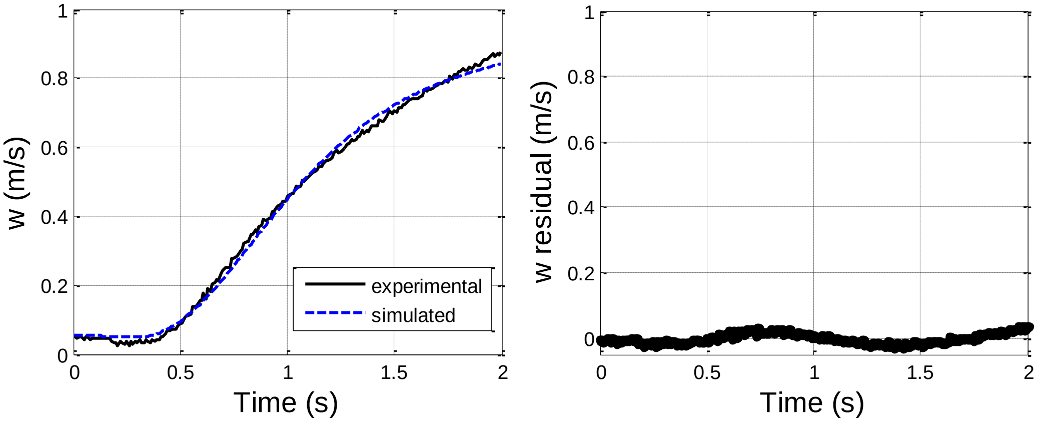

(a) (b)

Figure 4.8. Vertical channel identification. (a) w velocity fit (b) w velocity residual.

Figure 4.8 shows the fit and the residual errors for the vertical channel response—which is used to estimate the motor time constant and z coefficient of vehicle drag. As seen in the w velocity residual, there are some unmodeled higher order dynamics in the response. This could be due to the first order model employed for motor dynamics. However, the effect of the unmolded dynamics is very small, on the order of hundredths of a meter per second.

Since the roll and pitch channels share a subset of the model parameters both maneuvers are fit simultaneously. The parameters fit during roll and pitch channel maneuvers include: x and y components of mass moment of inertia, vertical center of gravity position, swashplate time constant, fly bar center of gravity position, vertical center of pressure position, roll damping coefficient, and pitch damping coefficient. Figures 4.9 and 4.10 show fits and residuals for the roll and pitch maneuvers. During flight tests, the high frequency content measured by the rate gyros was not observed and is believed to be noise. Overall the low frequency motion is captured well. In both simulated maneuvers the peak angular rate achieved was less than the peak achieved during flight tests. This may be due to slight phasing and linkage modeling errors in the flybar-upper rotor connection. Overall, the model fits capture the general pitch and roll motions of the vehicle.

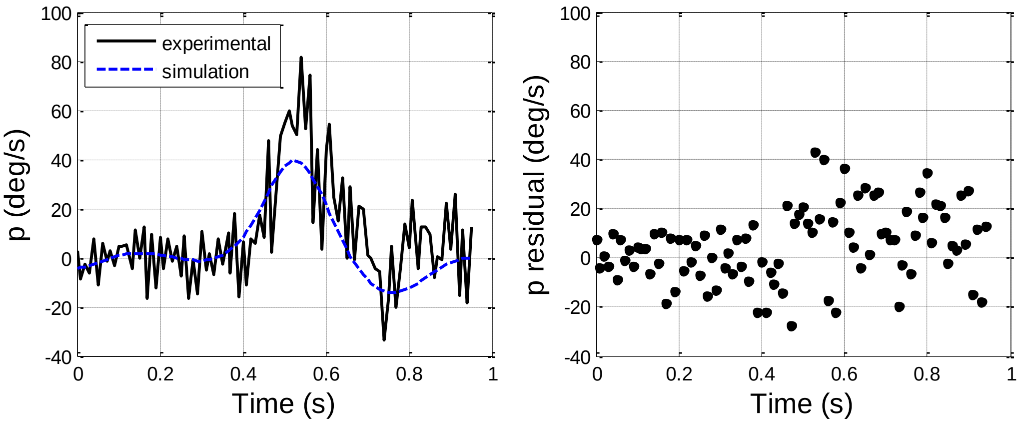

(a) (b)

Figure 4.9. Roll channel identification. (a) p angular velocity fit (b) p angular velocity residual.

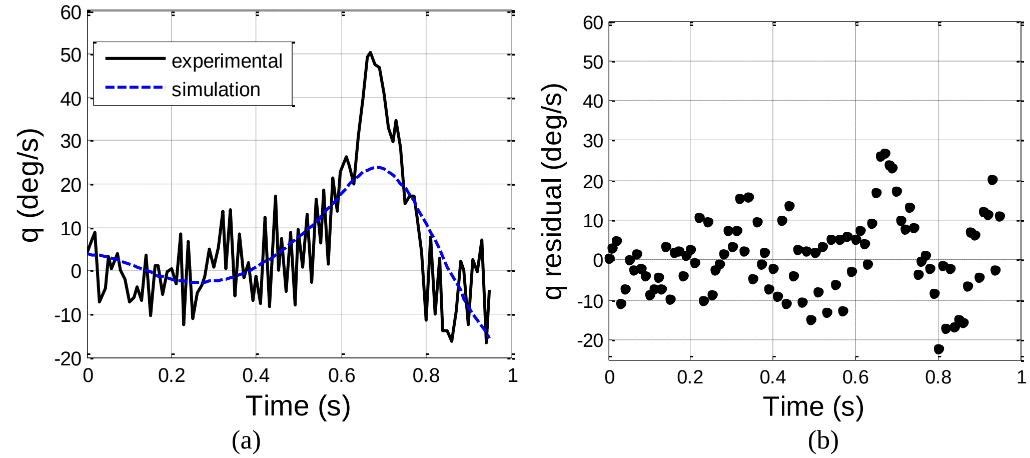

(a) (b)

Figure 4.10. Pitch channel identification. (a) q angular velocity fit (b) q angular velocity residual.

The yaw channel fit and residuals are shown in Figure 4.11. The yaw channel maneuver is used to fit the yaw damping coefficient, z component of mass moment of inertia, longitudinal center of pressure position, and effective tail drag coefficient. Similar to the vertical channel, unmodeled higher order dynamics can be seen in the residual. Since the vertical and yaw channels are controlled by the motors, the source of the unmodeled dynamics could be the same.

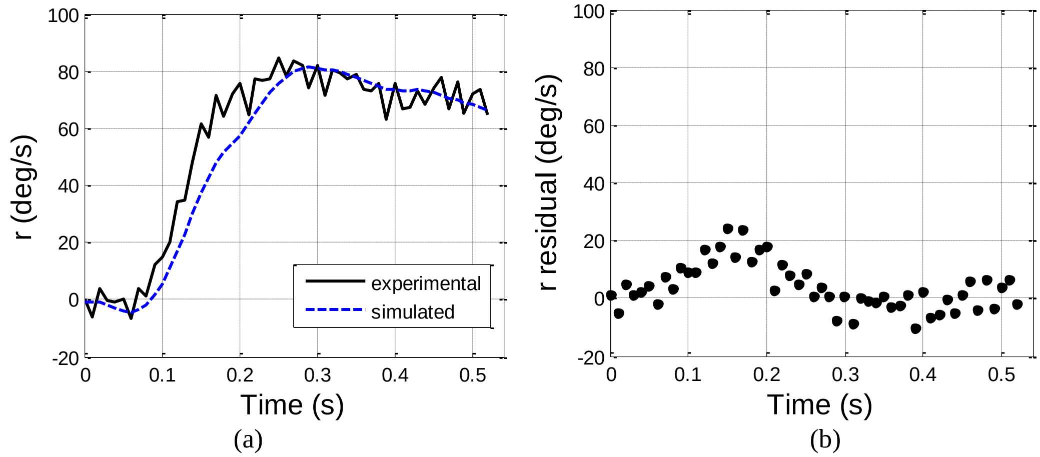

(a) (b)

Figure 4.11. Yaw channel identification. (a) r angular velocity fit (b) r angular velocity residual.

Estimation metrics are calculated to aid in assessing the quality the model fits [75]. The fit error is defined as the standard deviation estimate of the fit error vector

$$S_F^2 = \frac{1}{n_m - 1} \sum_{i=1}^{n_m} (x_i - \bar{x}_i)^2 \quad (4.4)$$

where x_i is the measured state, $\bar{x}_i$ is the estimated state, and n_m is the total number of measurements taken. The coefficient of determination is defined as

$$R^2 = \frac{SS_R}{SS_T} \quad (4.5)$$

where SS_T is the total sum of squares

$$SS_T = \sum_{i=1}^{n_m} (x_i - \tilde{x})^2 \quad (4.6)$$

SS_R is the regression sum of squares

$$SS_R = \sum_{i=1}^{n_m} (\bar{x}_i - \tilde{x})^2 \quad (4.7)$$

and $\tilde{x}$ is the mean of the measurements

$$\tilde{x} = \frac{1}{n_m} \sum_{i=1}^{n_m} x_i \quad (4.8)$$

The coefficient of determination represents the proportion of variation in the measurements explained by model motion. The parameter varies from 0 to 1 where 1 represents a perfect fit. Table 4.1 shows the fit error and coefficient of determination of each channel. The vertical and yaw channel fits are both very accurate, above 0.9, and the roll and pitch fit reasonably well, above 0.5.

Table 4.1. Fit metrics for each channel.

	z (m)	p (deg/s)	q (deg/s)	r (deg/s)
Fit Error (S_F)	0.016	15.546	9.984	8.968
R^2	0.987	0.502	0.578	0.911

To validate the model estimation, additional flight maneuvers were performed and the response simulated using the identified parameters. Figures 4.11 through 4.14 compare the simulated results with the experimental measurements as well as the residual errors. The vertical and yaw channel response residuals exhibit the same higher order dynamics as the fit flight tests with some additional mean error as shown in Figs. 4.12 and 4.13. Figures 4.14 and 4.15 show the response which is also similar for the roll and pitch channels. The estimation metrics for the validation cases are shown in Table 4.2. As expected, the coefficients of determination are smaller for each channel though the vertical fit is close to one. The roll and pitch channel coefficients of determination are smaller than expected but the fit error is only slightly larger than previous cases.

Table 4.2. Validation metrics for each channel.

	z (m)	p (deg/s)	q (deg/s)	r (deg/s)
Fit Error (S_F)	0.049	12.683	9.510	9.328
R^2	0.848	0.281	0.281	0.458

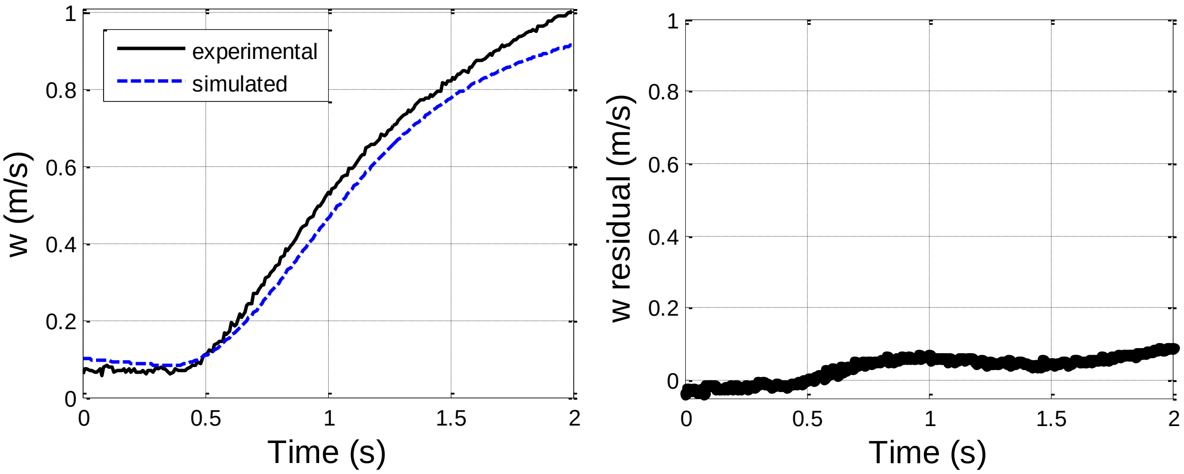

(a) (b)

Figure 4.12. Vertical channel validation. (a) w velocity fit (b) w velocity residual.

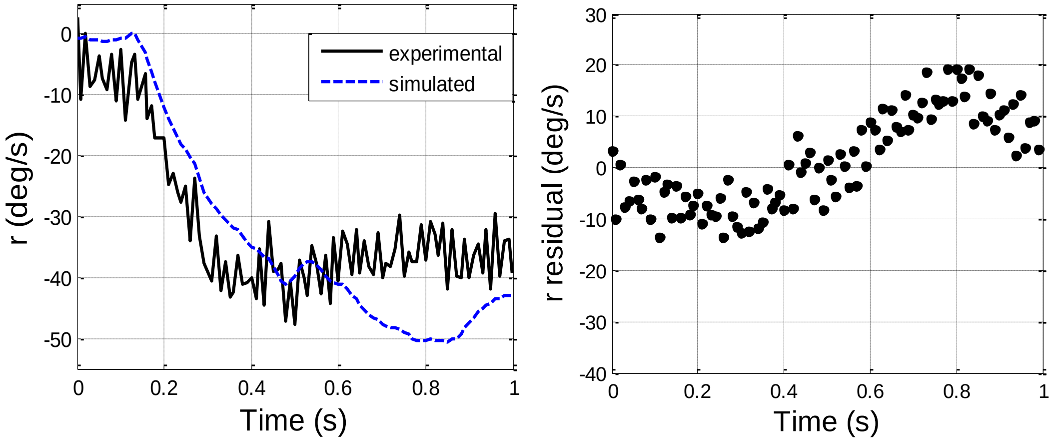

(a) (b)

Figure 4.13. Yaw channel validation. (a) r angular velocity fit (b) r angular velocity residual.

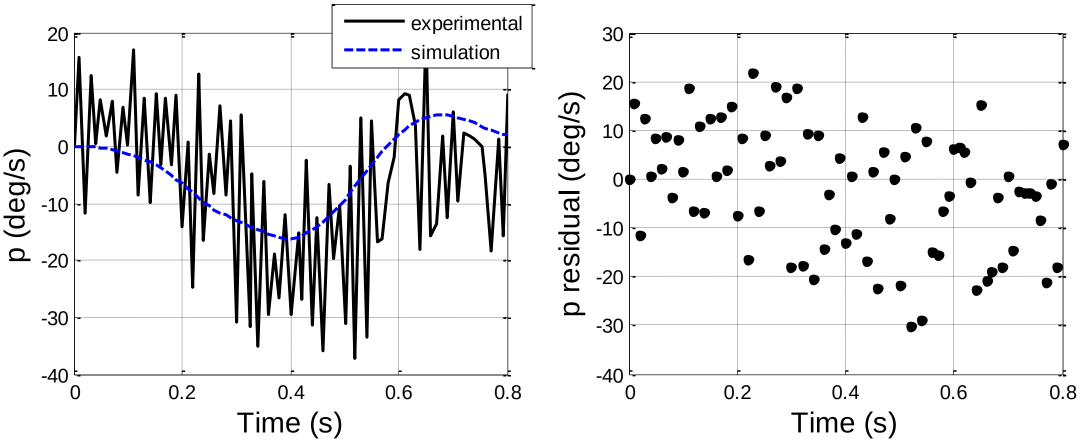

(a) (b)

Figure 4.14. Roll channel validation. (a) p angular velocity fit (b) p angular velocity residual.

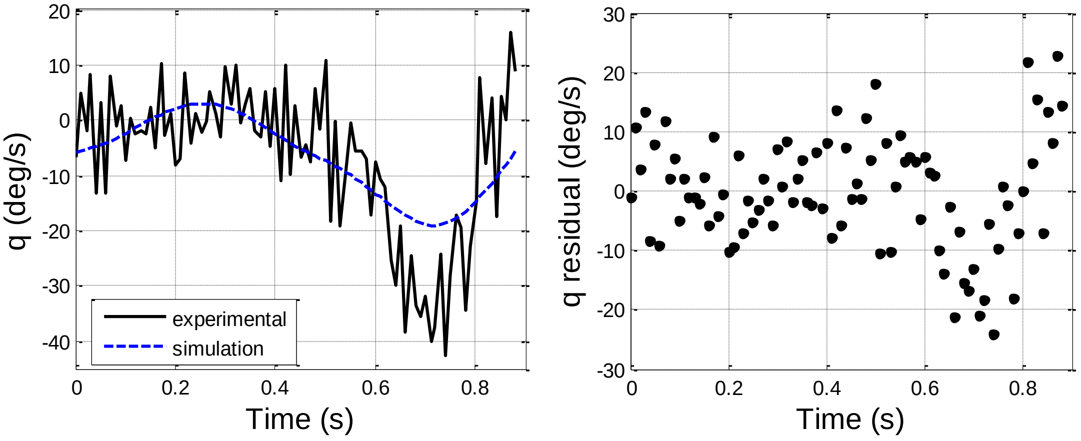

(a) (b)

Figure 4.15. Pitch channel validation. (a) q angular velocity fit (b) q angular velocity residual.

4.4 Fine Tuning

After flight experiments a few final parameters including center of gravity location, fly bar drag coefficient, and blade lift and drag coefficients are fine tuned to ensure the vehicle trimmed properly in hover. Additionally, the fuselage drag coefficients are tuned so the predicted maximum flight speeds matched the coaxial vehicle.

4.5 Confidence Intervals

Bounds for all parameters are estimated for confidence intervals of 95%. For direct measurement parameters, measurements were repeated to calculate confidence intervals using the Student’s t distribution method [76]. For all other parameters, confidence intervals were estimated by inverting the “extra sum of squares” [77]. Given the vector of estimated model parameters

$$\bar{\theta} = (\theta_1, \bar{\theta}_2)^T \tag{4.9}$$

one parameter is fixed at a perturbed value.

$$\theta_{10} = \theta_1 + \Delta\theta \tag{4.10}$$

Then the system identification routine is performed again and remaining model parameters are optimized. Next, a test statistic is calculated from the residual sum of squares for the perturbed model and the original model.

$$F(\theta_{10}) = \frac{RSS\{\overline{\theta}(\theta_{10})\} - RSS\{\overline{\theta}\}}{s^2} \tag{4.10}$$

Where RSS is the residual sum of squares and s is an approximation of the standard deviation. Using the test statistic, the signed square root is found.

$$\tau(\theta_{10}) = \mathrm{sign}(\theta_{10} - \theta_1)\sqrt{\mathrm{F}(\theta_{10})} \tag{4.11}$$

The signed square root is an approximation of the t-statistic with a distribution of $t_{n_m - n_p}$ where $n_p$is the number of model parameters. Therefore, each parameter is fixed at a series of values above and below the estimated value and the t-statistic for 95% confidence and the associated parameter bounds can found through interpolation. Table 4.3 shows the model parameters and bounds with 95% confidence where ΔBounds/Mean is the difference between the parameters lower and upper bounds normalized by the mean value.

Table 4.3. Model Parameters and bounds.

Parameter	Mean Value	Lower Bound	Upper Bound	ΔBounds /Mean (%)	Units	Source of Bounds
M	6.038E-02	6.037E-02	6.038E-02	0.0166	kg	Measured
I_{xx}	4.952E-05	3.878E-05	6.570E-05	54.0	kg m^2	Inverting sum of squares
I_{yy}	1.603E-04	1.347E-04	2.060E-04	44.5	kg m^2	Inverting sum of squares
I_{zz}	1.028E-06	5.138E-07	1.541E-06	100.0	kg m^2	Inverting sum of squares
$C_{A\phi}$	0.3597	0.0873	0.4363	97.0	rad/PPM	Inverting sum of squares
$C_{B\theta}$	0.3597	0.0873	0.4363	97.0	rad/PPM	Inverting sum of squares
C_{dx}	0.5501	0.4859	0.6143	23.3	nd	Inverting sum of squares
C_{dy}	0.2979	0.2532	0.3426	30.0	nd	Inverting sum of squares
C_{dz}	7.880	7.670	8.091	5.3	nd	Inverting sum of squares
r_{COPx}	0.0	-0.02214	0.02214	NA	m	Inverting sum of squares
r_{COPy}	0.0	-0.0089	0.0089	NA	m	Inverting sum of squares
r_{COPz}	0.0514	0.0366	0.0661	57.4	m	Inverting sum of squares
τ_{SW}	0.0999	0.0499	0.1499	100.0	s	Inverting sum of squares
ϕ_{SW}	0.8387	0.7978	0.8796	1.0	rad	Measured

Table 4.3. Continued.

Parameter	Mean Value	Lower Bound	Upper Bound	ΔBounds /Mean (%)	Units	Source of Bounds
ϕ_{FB}	0.8519	0.8110	0.8928	9.6	rad	Measured
$f_{download}$	9.41E-04	7.532E-04	1.130E-03	40.0	m^2	Inverting sum of squares
C_{lp}	-9.595	-13.400	-5.790	79.3	nd	Inverting sum of squares
C_{mq}	-10.325	-14.130	-6.520	73.0	nd	Inverting sum of squares
C_{nr}	-6.234	-6.764	-5.659	17.0	nd	Inverting sum of squares
m_b	9.600E-04	9.031E-04	1.017E-03	11.9	kg	Measured
i_{bxx}	1.400E-08	1.300E-08	1.500E-08	14.3	kg m^2	Inverting sum of squares
i_{byy}	6.300E-07	5.300E-07	7.300E-07	31.7	kg m^2	Inverting sum of squares
i_{bzz}	6.440E-07	6.430E-07	6.450E-07	0.311	kg m^2	Inverting sum of squares
R	8.858E-02	8.824E-02	8.892E-02	0.768	m	Measured
e	0.2178	0.1956	0.2400	20.4	nd	Inverting sum of squares
k_B	0.0950	0.0800	0.1100	31.6	N m/rad	Inverting sum of squares
θ_{twist}	-0.2614	-0.2963	-0.2265	26.7	rad	Measured
θ_0	0.3749	0.3400	0.4098	18.6	rad	Measured
C_{LR}	-531.74	-542.38	-521.11	4.0	rad/s/ PPM	Inverting sum of squares
C_{UR}	531.74	521.11	542.38	4.0	rad/s/ PPM	Inverting sum of squares
τ_M	0.100	0.083	0.117	34.0	s	Inverting sum of squares
m_{FB}	0.001	9.9990E-04	1.0010E-03	0.110	kg	Inverting sum of squares
i_{fbxx}	5.059E-10	5.059E-10	6.059E-10	19.8	kg m^2	Inverting sum of squares
i_{fbyy}	1.368E-08	1.268E-08	1.468E-08	14.6	kg m^2	Inverting sum of squares
i_{fbzz}	1.368E-08	1.268E-08	1.468E-08	14.6	kg m^2	Inverting sum of squares

Table 4.3. Continued.

Parameter	Mean Value	Lower Bound	Upper Bound	ΔBounds /Mean (%)	Units	Source of Bounds
c_{dFB}	0.10	0.05	0.50	450.0	nd	Inverting sum of squares
C_{dTailx}	0.0	0.0	2.000E-07	NA	nd	Inverting sum of squares
C_{dTaily}	2.847E-04	2.56E-04	3.132E-04	20.0	nd	Inverting sum of squares
C_{dTailz}	0.0	0.0	2.000E-07	NA	nd	Inverting sum of squares
r_{Tailx}	-0.1018	-0.1028	-0.1008	1.96	m	Inverting sum of squares
r_{Taily}	0.0	-1.0E-03	1.00E-03	NA	m	Inverting sum of squares
r_{Tailz}	0.0	-1.0E-03	1.00E-03	NA	m	Inverting sum of squares
r_{LRz}	0.0668	0.0666	0.0670	0.5988	m	Measured
r_{URz}	0.1065	0.1062	0.1068	0.5634	m	Measured
r_{FBz}	0.1161	0.1154	0.1167	1.1197	m	Measured
r_{CGx}	0.0	-1.35E-03	1.350E-03	NA	m	Measured
r_{CGy}	0.0	-1.350E-03	1.350E-03	NA	m	Measured
r_{CGz}	4.834E-03	2.417E-03	7.252E-03	100.0	m	Measured
l_{FB}	5.870E-03	5.858E-03	5.882E-03	0.4089	m	Measured
l_{UR}	6.426E-03	6.414E-03	6.439E-03	0.389	m	Measured
lt_{FB}	6.508E-02	6.408E-02	6.608E-02	3.07	m	Measured
ls_{FB}	5.177E-02	2.392E-02	6.443E-02	78.25	m	Measured

4.6 Discussion

A nonlinear rotorcraft model was developed and validated using time domain flight maneuvers in the four control channels. Though some unmodeled higher order dynamics were noted during the fit and validation process; overall the identified model captures general motion of the rotorcraft platform. It represents a high fidelity model that is valid over a large range of operating conditions. The limits of model validity result from some base assumptions, specifically: steady state aerodynamics, rotor stall dynamics, and operation in the vortex ring and turbulent wake states. The rotor blade lift and drag profiles were estimated from circular arc airfoil theory and motion above blade stall is approximated by general stall trends. Additionally, the inflow and wake model during vertical descent is also approximated from experimental trends. In both cases, reasonable approximations were made and the model still simulates response over most of the vehicle flight envelope, specifically accounting for spatial wind gradients and nonlinear rotor effects. The model is very useful for analysis in urban environments.

CHAPTER 5

GUST REJECTION CONTROL ARCHITECTURE

Control algorithms face many challenges in urban gust fields where they must be able to handle the nonlinear changes in control response and vehicle dynamics associated with movement through different regions of the vehicle flight envelope as well as frequently encounter wind magnitudes that exceed the micro rotorcraft platform's maximum flight speed. Thus the control architecture must be robust enough to prevent control saturation and maintain stable flight even in extreme wind fields. As described in Chapter 1, including the wind speeds in the control law—whether through direct measurement and a feedfoward structure or by estimating disturbances and using them as feedback—can improve controller performance. It is assumed that micro rotorcraft will not have the payload capacity to directly measure the wind field, thus a disturbance estimate must be part of the control architecture.

The Gust Rejection Control (GRC) architecture is a control strategy to operate micro rotorcraft in urban environments. Based on the requirements detailed here, an active disturbance rejection control (ADRC) algorithm is selected as the foundation of the GRC. Developed by Han [78], ADRC combines the nonlinear feedback of a dynamic inversion tracking controller with an extended state observer (ESO) for estimation of model uncertainty and external disturbances. It has been applied in a variety of engineering fields including tension controls for industrial web tension regulation by Hou, Gao, Jiang, and Bolter [79] and precise motion control of robotic platforms by Su, Duan, Zheng, et al. [80] as well as aircraft flight control by Huang, Kekang, Jingqing, and Lam [81] and rejection of vertical and yaw channel gusts for an unmanned rotorcraft by Martini, Lénoard, and Abba [33, 34]. A novel estimation algorithm is developed which utilizes the bounded converging estimations of the ESO to provide in-flight estimation of the local wind velocity. To the author's knowledge, an ESO framework has not been applied to parameter estimation in this way for any previous work. The wind estimates are used to improve controller dynamic inversion and to create a flight envelope protection scheme (FEPS) which acts as a safe guard when the micro rotorcraft platform experiences wind magnitudes that exceed the vehicle's maximum flight speed. Similar envelope protection systems have been developed for larger (71.2 kg) unmanned rotorcraft by Yayruck, Prasad, and Unnikrishnan [82], where an adaptive neural network was used to generate dynamic models of helicopter load factor and blade stall. These models were used to estimate envelope limits which were mapped to state command limits. Similar to previous envelope protection systems, the FEPS developed here modifies state trajectory commands to prevent dangerous flight conditions using a link between the vehicle's maximum flight speed and the local wind conditions to prevent control saturation and ensure safe vehicle operation. Figure 5.1 shows a block diagram of the overall structure of the GRC architecture. This chapter details the derivations and stability proofs of the ESO and feedback linearization tracking controller as well as the development of the wind estimation and FEPS algorithms.

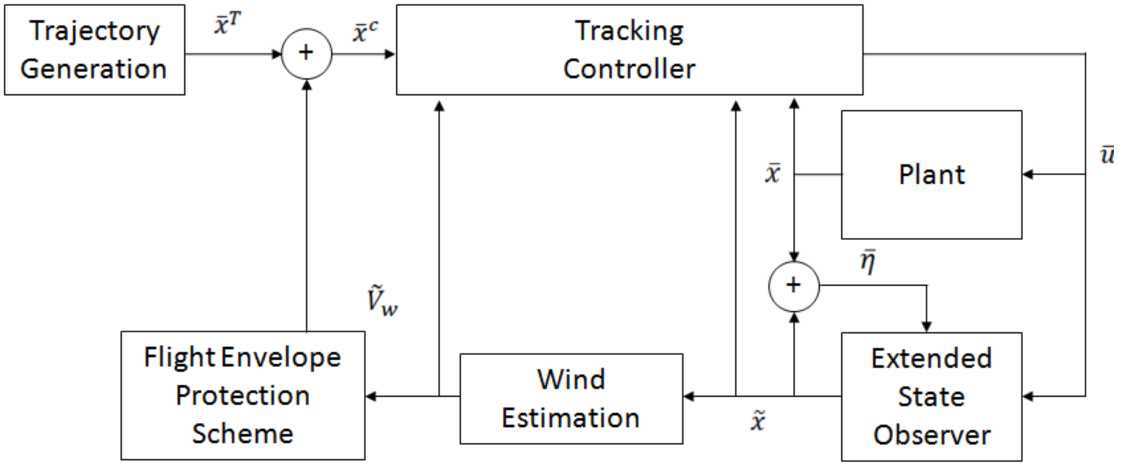

Figure 5.1. Block diagram of overall Gust Rejection Control Architecture.

5.1 Extended State Observer

Consider a dynamic system of the form

$$\begin{Bmatrix} \dot{x}_1 \\ \dot{x}_2 \end{Bmatrix} = \begin{Bmatrix} x_2 \\ \tilde{F} + \tilde{G} + \Delta \end{Bmatrix} \tag{5.1}$$

where $\tilde{F} = \tilde{F}(x)$, $\tilde{G} = \tilde{G}(x, u)$, and Δ is the uncertainty caused by both model error and unknown external disturbances. An observer is proposed with an extended state

$$\begin{Bmatrix} \dot{\tilde{x}}_1 \\ \dot{\tilde{x}}_2 \\ \dot{\tilde{x}}_3 \end{Bmatrix} = \begin{Bmatrix} \tilde{x}_2 + \epsilon \ell_1 \\ \tilde{F} + \tilde{G} + \tilde{x}_3 + \ell_2 \\ \left({}^{1}/_{\epsilon}\right) \ell_3 \end{Bmatrix} \tag{5.2}$$

where the purpose of the extended states ($\tilde{x}_3$) is to estimate the unknown disturbances and uncertainty and ϵ is a tuning parameter of the observer. It should be noted that the term $\tilde{x}_3$ is not truly a state of the system but an estimate of the time varying uncertainty. The ESO functions ℓ_1, ℓ_2, and ℓ_3 are included to guide the dynamics of the estimation error. The estimation error can be defined as η where

$$\eta_1 = \frac{x_1 - \tilde{x}_1}{\epsilon^2},\ \eta_2 = \frac{x_2 - \tilde{x}_2}{\epsilon},\ \eta_3 = \Delta - \tilde{x}_3, \text{ and } \bar{\eta}^T = [\eta_1\ \eta_2\ \eta_3] \tag{5.3}$$

Then the error dynamics can be expressed as

$$\dot{\eta}_1 = \frac{\dot{x}_1 - \dot{\tilde{x}}_1}{\epsilon^2} = \frac{x_2 - \tilde{x}_2 - \epsilon \ell_1}{\epsilon^2} = \frac{\eta_2 - \ell_1}{\epsilon} \tag{5.4}$$

$$\dot{\eta}_2 = \frac{\dot{x}_2 - \dot{\tilde{x}}_2}{\epsilon} = \frac{\Delta - \tilde{x}_3 - \ell_2}{\epsilon} = \frac{\eta_3 - \ell_2}{\epsilon} \tag{5.5}$$

$$\dot{\eta}_3 = \dot{\Delta} - \frac{\ell_3}{\epsilon} = \frac{\epsilon \dot{\Delta} - \ell_3}{\epsilon} \tag{5.6}$$

or in vector form as

$$\dot{\bar{\eta}} = \begin{Bmatrix} \dot{\eta}_1 \\ \dot{\eta}_2 \\ \dot{\eta}_3 \end{Bmatrix} = \frac{1}{\epsilon} \begin{Bmatrix} \eta_2 - \ell_1 \\ \eta_3 - \ell_2 \\ \epsilon \dot{\Delta} - \ell_3 \end{Bmatrix} \tag{5.7}$$

The objective is to design the observer such that $\bar{\eta}$ is driven to a small value with stable error dynamics. The stability of the error dynamics can be examined through Lyapunov stability theory. Given the Lyapunov function

$$\mathrm{V} = \frac{1}{2}\bar{n}^T\bar{\eta} \tag{5.8}$$

The time derivative of the function is

$$\dot{\mathrm{V}} = \frac{1}{2}\left(\dot{\bar{n}}^T\bar{\eta} + \bar{n}^T\dot{\bar{\eta}}\right) = \bar{n}^T\dot{\bar{\eta}} \tag{5.9}$$

and substituting in Eqn. 5.6, rearranging, and removing the constant $1/\epsilon$ without the loss of generality

$$\dot{\mathrm{V}} = [\eta_1(\eta_2 - \ell_1) - \eta_2\ell_2] + \eta_3\big(\eta_2 + \epsilon\dot{\Delta} - \ell_3\big) \tag{5.10}$$

For the GRC architecture it is assumed there is full state feedback and the ESO functions are

$$\ell_1 = \eta_2 + k_1\mathrm{sat}(\eta_1, \delta_1),\ \ell_2 = k_2\mathrm{sat}(\eta_2, \delta_2),\ \ \ell_3 = k_3\eta_2 \tag{5.11}$$

where $\mathrm{sat}(\eta, \delta)$ is a saturation function with a boundary layer

$$\mathrm{sat}(\eta, \delta) = \begin{cases} \eta/\delta & \text{if } |\eta/\delta| \le 1 \\ \mathrm{sign}(\eta) & \text{if } |\eta/\delta| > 1 \end{cases} \tag{5.12}$$

Eqn. 5.10 can then be rewritten as

$$\dot{\mathrm{V}} = [-k_1\eta_1\mathrm{sat}(\eta_1, \delta_1) - k_2\eta_2\mathrm{sat}(\eta_2, \delta_2)] + \eta_3\left(\epsilon\dot{\Delta} - \eta_2(k_3 - 1)\right) \tag{5.13}$$

It is reasonable to assume that the uncertainty and external disturbances are bounded thus $\eta_3 \le \mathrm{M}$, and $\dot{\Delta}$ is also bounded, $|\dot{\Delta}| \le \mathrm{N}$.

$$\dot{\mathrm{V}} \le [-k_1\eta_1\mathrm{sat}(\eta_1, \delta_1) - k_2\eta_2\mathrm{sat}(\eta_2, \delta_2)]\ - \eta_2 M(k_3 - 1) + M\epsilon\mathrm{N} \tag{5.14}$$

Then ϵ, k_1, k_2, and k_3 can be selected so $\dot{\mathrm{V}} \le 0$ and therefore the error dynamics are bounded and stable.

For most work using ADRC, the uncertainty estimate is used to capture all model errors and external disturbances indiscriminately. This feature is seen as an advantage as extremely accurate models for both the vehicle and disturbances are not required. However, in the GRC, estimates of the wind speed are employed to specifically reject the effects of wind on the vehicle, improve tracking performance, and for use in the FEPS. The ESO disturbance estimates are filtered to estimate the local wind conditions as

$$\dot{\hat{V}}_w = f_w(\tilde{x}_{3O}) \tag{5.15}$$

where $\tilde{x}_{3O}$ is the outer loop disturbance estimates for x, y, and z, and f_w is a mapping between the disturbances and the associated wind components. For this work, the mapping f_w is developed as a low pass filter using test flight simulations in known winds. Figures 5.2 through 5.6 show time histories for the ESO states, wind estimates, and Lyapunov function for a hover flight maneuver in an engulfing head wind with a 5 second ramp time and 1.0 m/s steady state magnitude, (Fig. 5.2).

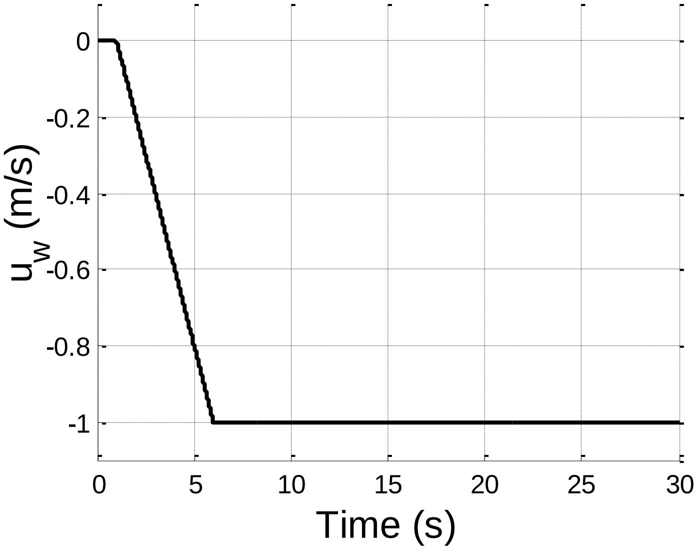

Figure 5.2. Example engulfing head wind profile.

The estimated states are initialized with some errors but most quickly converge to the actual state within 5 seconds as shown in Fig. 5.3. The yaw estimate converges slower, on the order of 15 seconds. The uncertainty estimates also converge, Fig. 5.4, as well as the wind estimates which have a maximum error of just over 0.1 m/s, Fig 5.5.

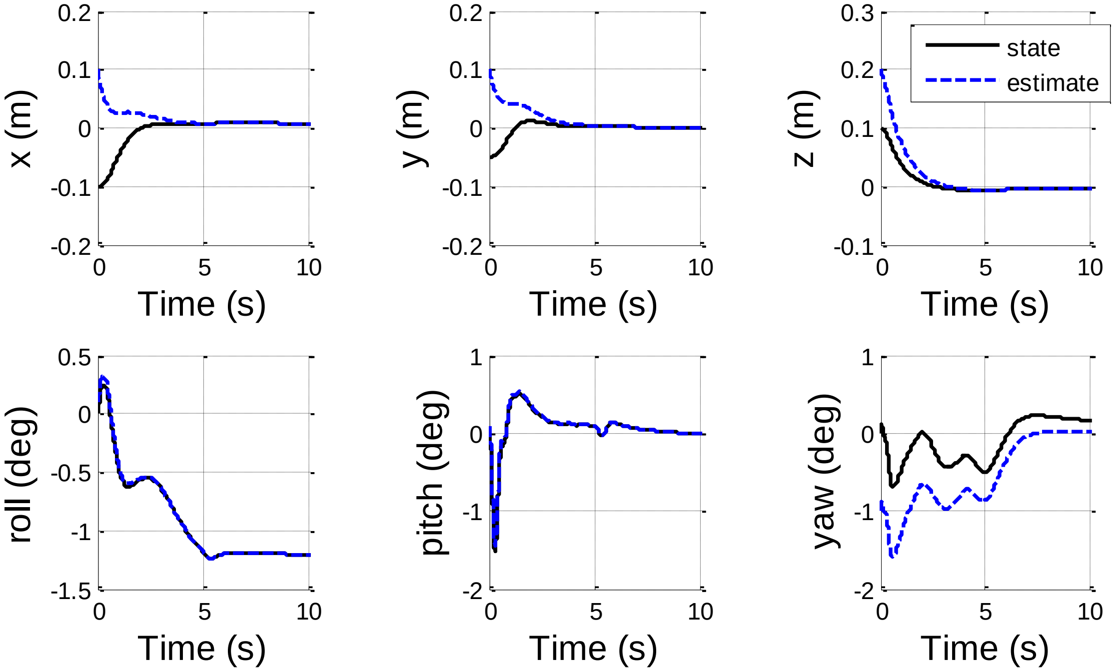

Figure 5.3. Example time histories for position and attitude truth states and the states from the ESO.

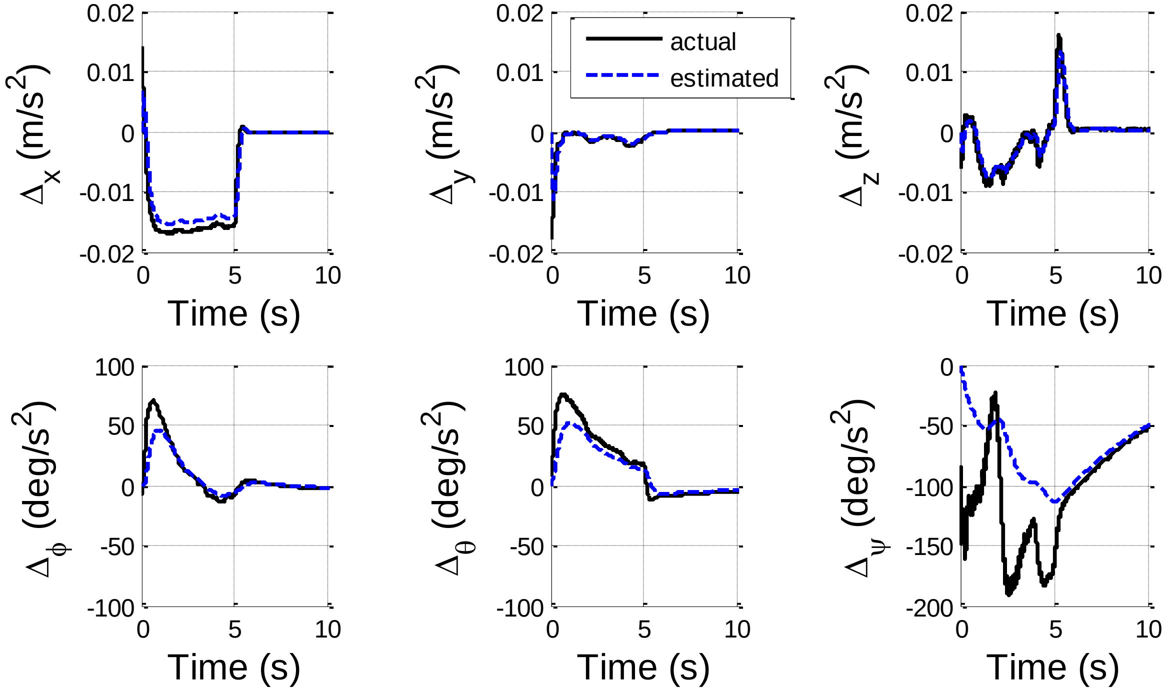

Figure 5.4. Example time histories for model uncertainties for each channel during an engulfing head wind.

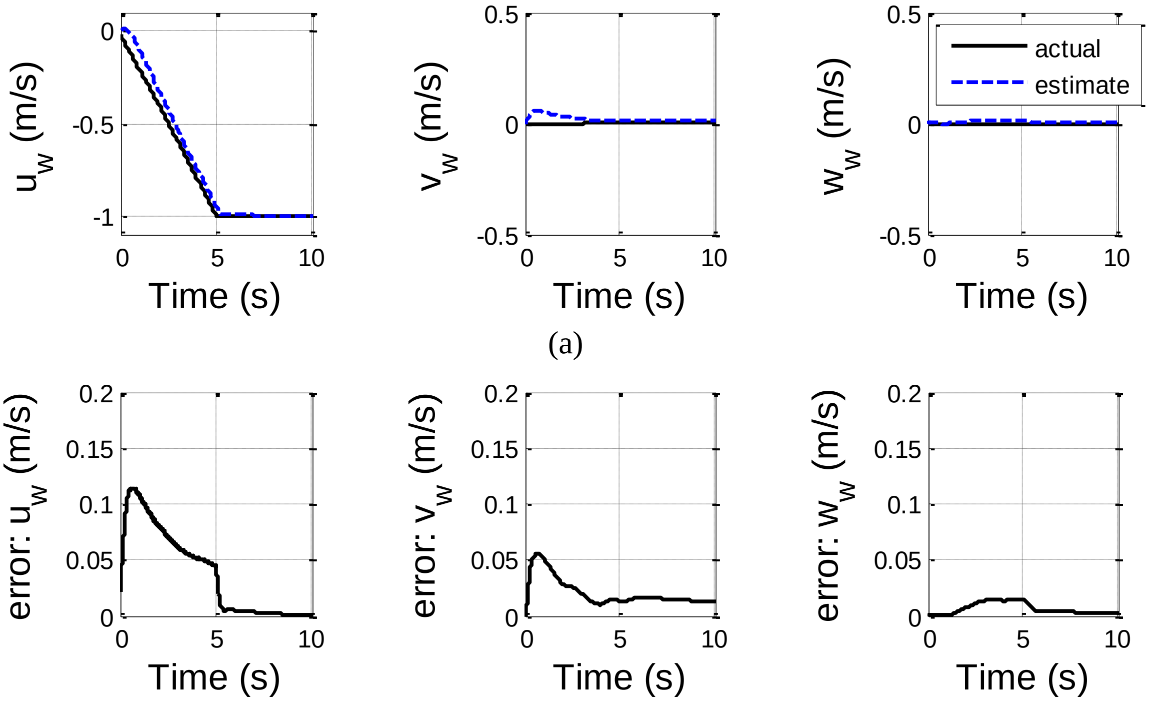

(a)

(b)

Figure 5.5. Wind estimation and error for an example head wind. (a) Wind histories (b) estimation error.

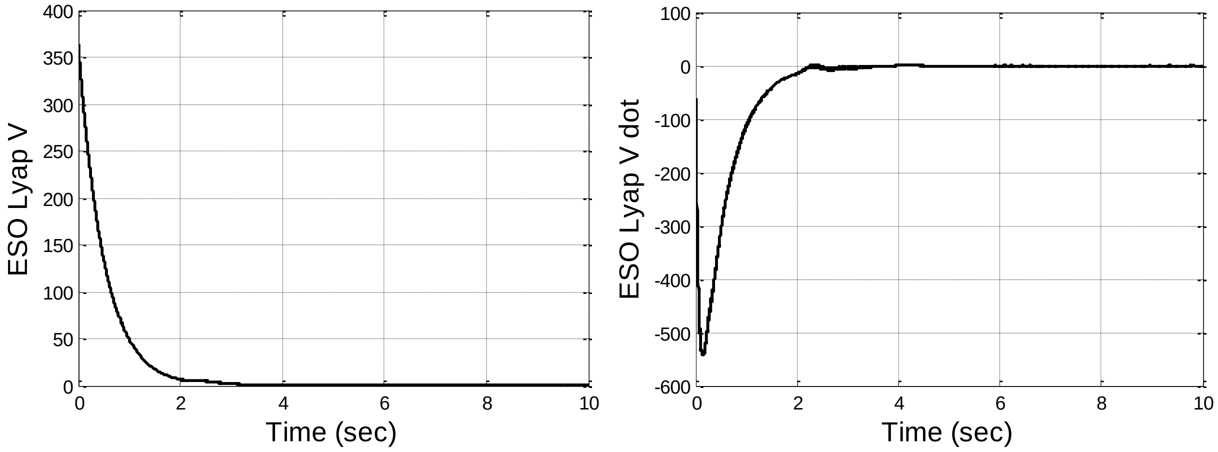

(a) (b)

Figure 5.6. ESO Lyapunov function time histories in an example head wind. (a) Lyapunov function (b) Lyapunov function time derivative.

The Lyapunov function is calculated for this example and shown to steadily decrease over the first five seconds before converging closely to zero (Fig. 5.6a) while the function derivative stays less than or equal to zero (Fig. 5.6b).

5.2 Tracking Controller

The tracking controller employs dynamic inversion to feedback linearize the system to follow position and heading commands and reject external disturbances. Figure 5.7 shows a block diagram of the tracking control algorithm. An inner loop-outer loop structure is used to convert inertial position commands into attitude commands thereby tilting the thrust and achieving the desired inertial accelerations.

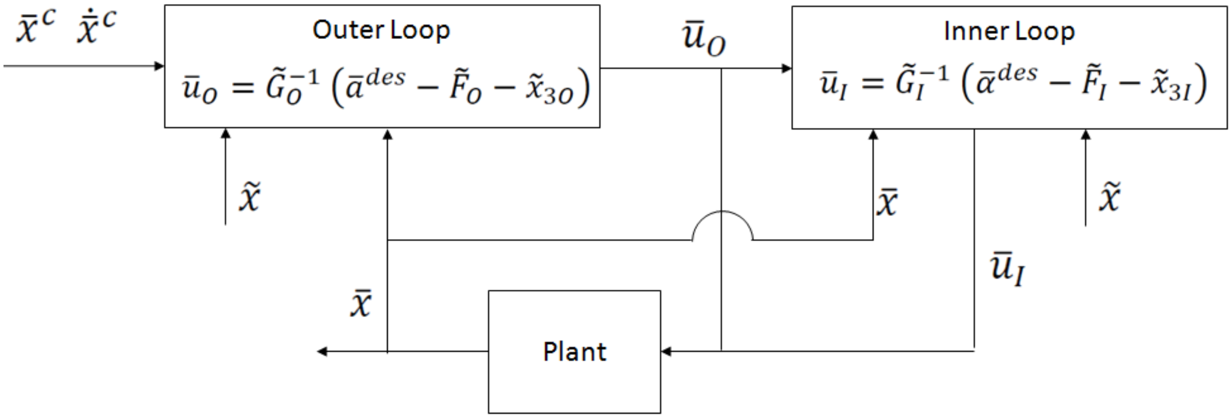

Figure 5.7. Block diagram of detail of tracking controller.

Casting the system in a similar form to the ESO, the outer loop and inner loop systems are

$$\bar{x} = \begin{Bmatrix} \bar{x}_O \\ \bar{x}_I \end{Bmatrix} \tag{5.16}$$

$$\dot{\bar{x}}_{1O} = \bar{x}_{2O} \tag{5.17}$$

$$\dot{\bar{x}}_{2O} = \tilde{F}_O(\bar{x}) + \tilde{G}_O(\bar{x},\bar{u}) + \bar{\Delta}_O \tag{5.18}$$

$$\dot{\bar{x}}_{1I} = \bar{x}_{2I} \tag{5.19}$$

$$\dot{\bar{x}}_{2I} = \tilde{F}_I(\bar{x}) + \tilde{G}_I(\bar{x},\bar{u}) + \bar{\Delta}_I \tag{5.20}$$

where $\bar{x}_{1O} = (x, y, z)^T$, $\bar{x}_{2O} = (\dot{x}, \dot{y}, \dot{z})^T$, $\bar{x}_{1I} = (\phi, \theta, \psi)^T$, and $\bar{x}_{2I} = \left(\dot{\phi}, \dot{\theta}, \dot{\psi}\right)^T$. The outer loop control inputs are the throttle input which controls the mean speeds of the upper and lower rotors as well as the roll and pitch commands which are fed to the inner loop, $\bar{u}_O = (u_T, \phi^c, \theta^c)^T$. The inner loop control inputs are the lateral and longitudinal cyclic swashplate inputs and the heading input which controls the differential speed between the rotors, $\bar{u}_I = \left(u_\phi, u_\theta, u_\psi\right)^T$. Both the outer and inner control inputs are calculated through dynamic inversion as

$$\bar{u}_O = \tilde{G}_O^{-1}\left(\bar{a}^{des} - \tilde{F}_O - \tilde{x}_{3O}\right) \tag{5.21}$$

$$\bar{u}_I = \tilde{G}_I^{-1}\left(\bar{\alpha}^{des} - \tilde{F}_I - \tilde{x}_{3I}\right) \tag{5.22}$$

where $\bar{a}^{des}$is the desired linear acceleration and $\bar{\alpha}^{des}$ is the desired angular acceleration.

$$\bar{a}^{des} = \dot{\bar{x}}_{2O}^c + K_p(\bar{x}_{1O}^c - \bar{x}_{1O}) + K_d(\bar{x}_{2O}^c - \bar{x}_{2O}) \tag{5.23}$$

$$\bar{\alpha}^{des} = \dot{\bar{x}}_{2I}^c + R_p(\bar{x}_{1I}^c - \bar{x}_{1I}) + R_d(\bar{x}_{2I}^c - \bar{x}_{2I}) \tag{5.24}$$

The desired acceleration PD gains $\left(K_p, K_d, R_p, R_d\right)$ are set to give the system the desired error dynamics. Substituting the control inputs back into Eqns. 5.18 and 5.19

$$\dot{\bar{x}}_{2O} = \dot{\bar{x}}_{2O}^c + K_p(\bar{x}_{1O}^c - \bar{x}_{1O}) + K_d(\bar{x}_{2O}^c - \bar{x}_{2O}) + \mathit{\Delta}_O - \tilde{x}_{3O} \tag{5.25}$$

$$\dot{\bar{x}}_{2I} = \dot{\bar{x}}_{2I}^c + R_p(\bar{x}_{1I}^c - \bar{x}_{1I}) + R_d(\bar{x}_{2I}^c - \bar{x}_{2I}) + \mathit{\Delta}_I - \tilde{x}_{3I} \tag{5.26}$$

Then the tracking error can be defined as

$$E = \begin{Bmatrix} \bar{x}_{1O}^c - \bar{x}_{1O} \\ \bar{x}_{2O}^c - \bar{x}_{2O} \\ \bar{x}_{1I}^c - \bar{x}_{1I} \\ \bar{x}_{2I}^c - \bar{x}_{2I} \end{Bmatrix} \tag{5.27}$$

and the time derivative can be expressed as

$$\dot{E} = \begin{Bmatrix} \bar{x}_{2O}^c - \bar{x}_{2O} \\ \dot{\bar{x}}_{2O}^c - \dot{\bar{x}}_{2O} \\ \bar{x}_{2I}^c - \bar{x}_{2I} \\ \dot{\bar{x}}_{2O}^c - \dot{\bar{x}}_{2O} \end{Bmatrix} = \begin{bmatrix} 0 & \mathrm{I} & 0 & 0 \\ -K_p & -K_d & 0 & 0 \\ 0 & 0 & 0 & \mathrm{I} \\ 0 & 0 & -R_p & -R_d \end{bmatrix} E + \begin{bmatrix} 0 & 0 \\ \mathrm{I} & 0 \\ 0 & 0 \\ 0 & \mathrm{I} \end{bmatrix} (\tilde{x}_3 - \bar{\Delta}) \tag{5.28}$$

Equation 5.28 can be written in a more compact form as

$$\dot{E} = AE + B(\tilde{x}_3 - \overline{\Delta}) \tag{5.29}$$

The PD gains are chosen so A is Hurwitz, thus

$$A^T P + PA = -Q \tag{5.30}$$

As with the ESO, the stability of the tracking error can be examined through Lyapunov stability theory by defining a candidate Lyapunov function.

$$\mathrm{V}(t) = \frac{1}{2}\begin{cases} E^T PE & \text{if } \sqrt{E^T PE} > E_0 \\ E_0^T PE_0 & \text{if } \sqrt{E^T PE} \leq E_0 \end{cases} \tag{5.31}$$

First, considering if $\sqrt{E^T PE} > E_0$, the derivative of the Lyapunov function is

$$\dot{\mathrm{V}}(t) = \frac{1}{2}\dot{E}^T PE + \frac{1}{2}E^T P\dot{E} \tag{5.32}$$

$$= \frac{1}{2}\left(AE + B(\tilde{x}_3 - \overline{\Delta})\right)^T PE + \frac{1}{2}E^T P\left(AE + B(\tilde{x}_3 - \overline{\Delta})\right) \tag{5.33}$$

Rearranging

$$\dot{\mathrm{V}}(t) = \frac{1}{2}E^T(A^T P + PA)E + E^T PB(\tilde{x}_3 - \overline{\Delta}) \tag{5.34}$$

and substituting in Eqn. 5.30

$$\dot{\mathrm{V}}(t) = -\frac{1}{2}E^T QE + E^T PB(\tilde{x}_3 - \overline{\Delta}) \tag{5.35}$$

From Section 5.1, it is assumed $\overline{\Delta}$ is bounded and since $\tilde{x}_3$ is part of the ESO as long as the observer is has stable error dynamics, the term $(\tilde{x}_3 - \overline{\Delta})$ is also bounded $\|\tilde{x}_3 - \overline{\Delta}\| \leq M$. Then Eqn. 5.35 becomes

$$\dot{\mathrm{V}}(t) \leq -\frac{1}{2}E^T QE + E^T PBM \tag{5.36}$$

Using the matrix theory for quadratic functions, the derivative of the Lyapunov function can be rewritten as

$$\dot{V}(t) \le -\frac{\lambda_{max}(Q)}{2\lambda_{min}(P)} E^T PE + M\sqrt{E^T PE}\sqrt{\lambda_{max}(P)} \tag{5.37}$$

Thus $\dot{V}(t) < 0$ if $\sqrt{E^T PE} > 2M\,\frac{\lambda_{max}(P)^{3/2}}{\lambda_{min}(Q)}$, so by setting $E_0 = 2M\,\frac{\lambda_{max}(P)^{3/2}}{\lambda_{min}(Q)}$ then $\dot{V}(t) < 0$ if $\sqrt{E^T PE} > E_0$ and $\dot{V}(t) = 0$ if $\sqrt{E^T PE} \le E_0$. Since the tracking controller does not feedback into the ESO, the tracking error will be bounded if the ESO is bounded. This is true as long as the uncertainty remains within the set bounds for the ESO gains. Therefore the GRC architecture is bounded.

Figures 5.8 and 5.9 show example time histories of vehicle response and control input in the same 1.0 m/s head wind as in Section 5.1. The tracking controller uses the ESO wind estimates to reject the disturbance and settle to the commanded hover position of (0.0, 0.0, 0.0 m) while keeping the commanded heading of zero degrees, Fig. 5.8.

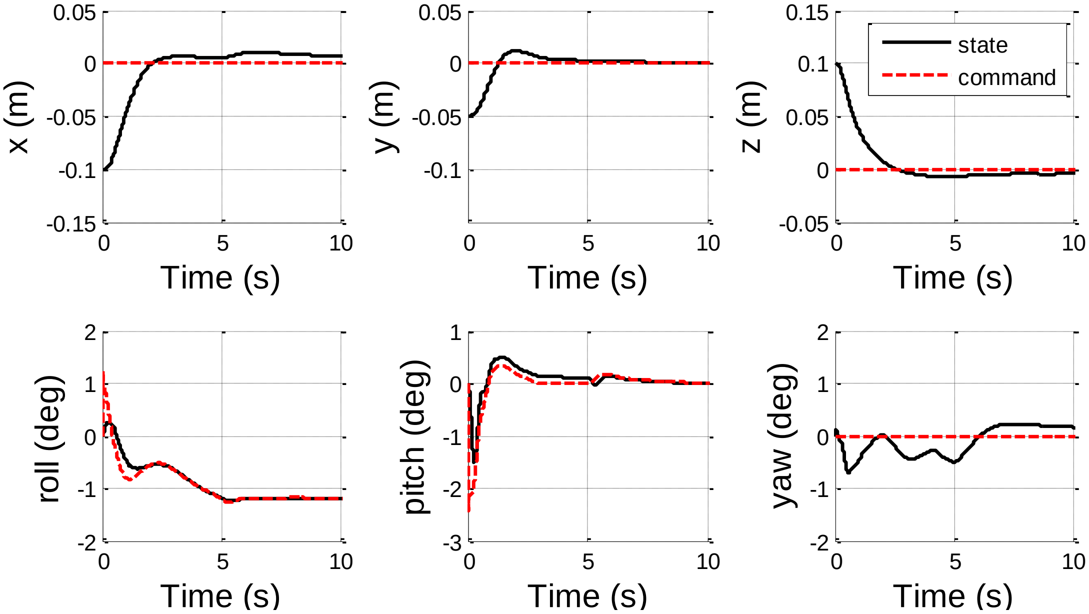

Figure 5.8. Example time histories for position and attitude response to 1.0 m/s engulfing head wind.

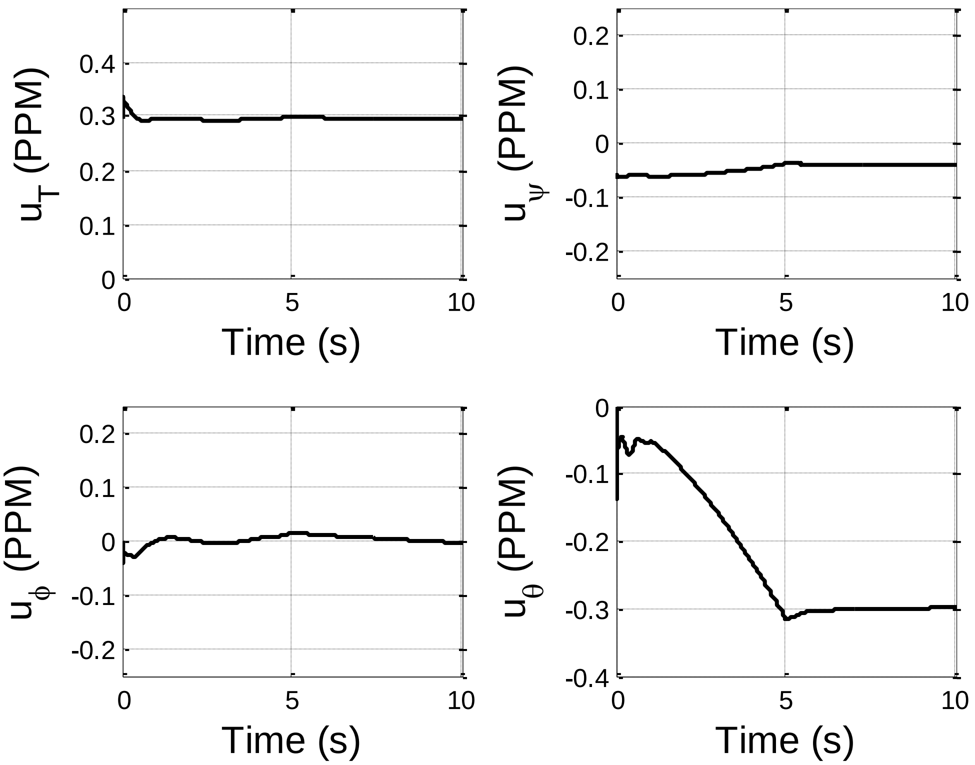

Figure 5.9. Example time histories of control inputs for 1.0 m/s engulfing head wind.

Figure 5.10 shows the time histories of the tracking controller Lyanpov function for 1.0 m/s engulfing head wind. As expected from the stability proof, the function derivative is always less than or equal to zero and the function is bounded.

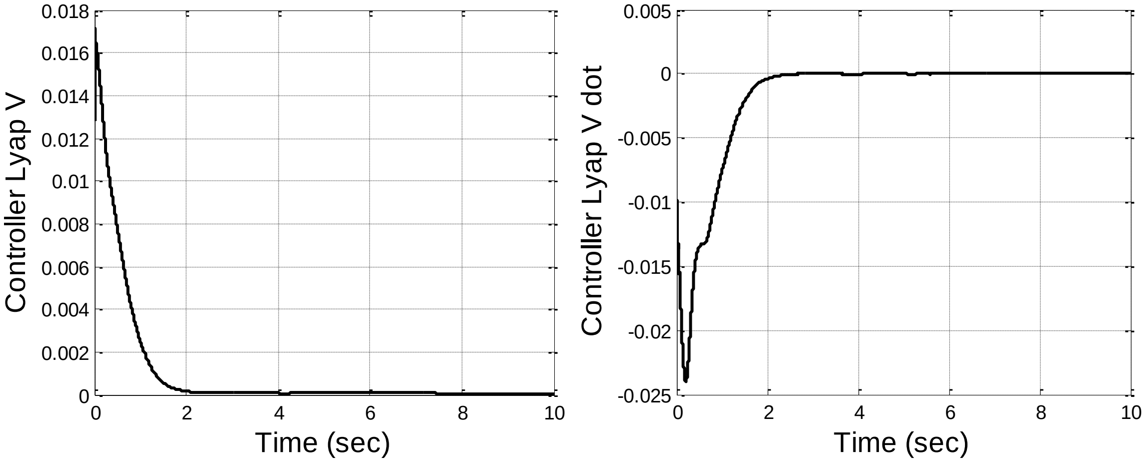

(a) (b)

Figure 5.10. Example time histories of the tracking controller (a) Lyanpov function (b) Lyanpov function derivative.

5.3 Flight Envelope Protection Scheme

The feedback linearization tracking controller does not account for control limits. Saturation causes the system to become open loop as the desired accelerations are not achieved; which can result in vehicle instability. In the application of micro rotorcraft operating in urban wind environments, the main cause of control saturation is due to the wind magnitude exceeding the platform's maximum flight speed. In order to ensure the GRC does not demand control beyond the system limits, a Flight Envelope Protection Scheme (FEPS) is constructed to modify the state commands to account for the vehicle maximum flight speed relative to the local wind velocity.

Two reference frames are defined to construct the FEPS. The vehicle frame (F_V) is fixed the vehicle center of gravity with a yaw rotation from the inertial.

$$\begin{Bmatrix} \bar{I}_V \\ \bar{J}_V \\ \bar{K}_V \end{Bmatrix} = \begin{bmatrix} c_\psi & s_\psi & 0 \\ -s_\psi & c_\psi & 0 \\ 0 & 0 & 1 \end{bmatrix} \begin{Bmatrix} \bar{I}_I \\ \bar{J}_I \\ \bar{K}_I \end{Bmatrix} = T_{VI} \begin{Bmatrix} \bar{I}_I \\ \bar{J}_I \\ \bar{K}_I \end{Bmatrix} \tag{5.37}$$

Thus $\bar{I}_V$ is in the horizontal plane pointing out the nose, $\bar{K}_V$ points down in the direction of gravity, and $\bar{J}_V$ completes the right hand rule—Fig. 5.11a. The airmass (F_A) frame is fixed to the vehicle center of gravity with $\bar{I}_A$ pointing along the body's velocity vector and $\bar{K}_A$ pointing downward, Fig. 5.11b. It is derived as a two angle rotation from the vehicle frame.

$$\begin{Bmatrix} \bar{I}_A \\ \bar{J}_A \\ \bar{K}_A \end{Bmatrix} = \begin{bmatrix} c_{\psi_A} c_{\alpha_A} & s_{\psi_A} c_{\alpha A} & -s_{\alpha_A} \\ -s_{\psi_A} & c_{\psi_A} & 0 \\ c_{\psi_A} s_{\alpha_A} & s_{\psi_A} s_{\alpha_A} & 1 \end{bmatrix} \begin{Bmatrix} \bar{I}_V \\ \bar{J}_V \\ \bar{K}_V \end{Bmatrix} = T_{AV} \begin{Bmatrix} \bar{I}_I \\ \bar{J}_I \\ \bar{K}_I \end{Bmatrix} \tag{5.38}$$

The vehicle's velocity vector can be expressed in the inertial, vehicle, and airmass frames as

$$\bar{V}_{B/I} = \dot{x}\bar{I}_I + \dot{y}\bar{J}_I + \dot{w}\bar{K}_I = \left(c_\psi \dot{x} + s_\psi \dot{y}\right)\bar{I}_V + \left(-s_\psi \dot{x} + c_\psi \dot{y}\right)\bar{J}_V + \dot{w}\bar{K}_V = V\bar{I}_A \tag{5.39}$$

where *V* is the scalar magnitude of the velocity vector.

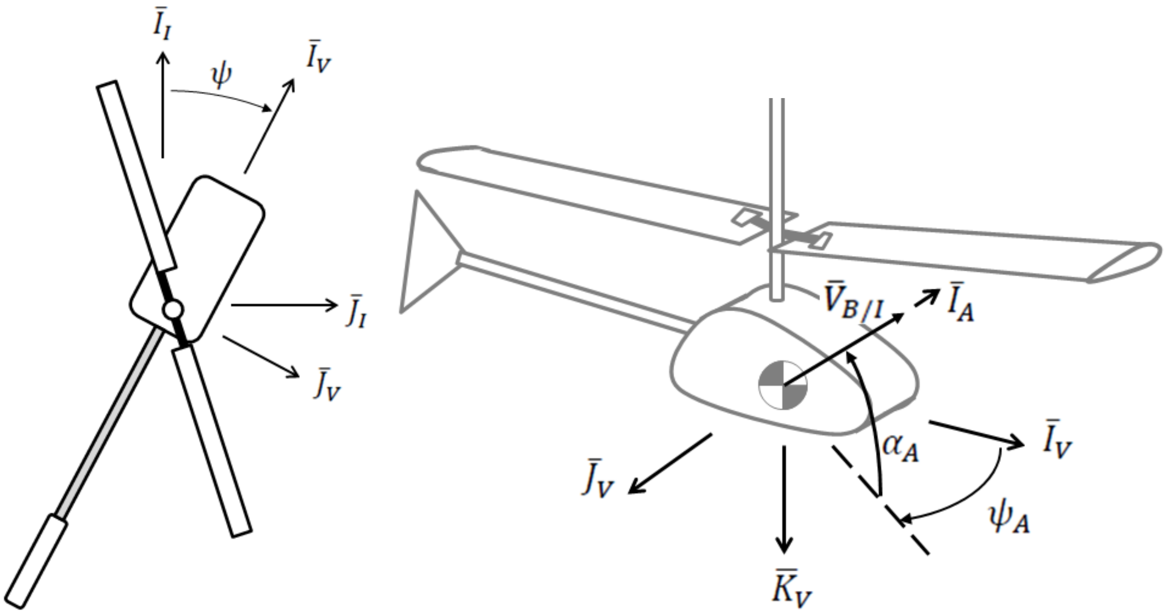

(a) (b)

Figure 5.11. Illustration of FEPS reference frames. (a) Vehicle frame (b) Airmass frame.

The rotorcraft's steady state maximum flight speed in a given direction is the balance the control and aerodynamic contributions to the body forces and moments. The velocity terms enter the equations of motion as the velocity of the body relative to the airmass.

$$\bar{V}_{B/A} = (u - u_w)\bar{I}_B + (v - v_w)\bar{J}_B + (w - w_w)\bar{k}_B \tag{5.40}$$

Thus the maximum achievable inertial velocity is a function of the maximum body velocity with respect to the airmass frame ($\bar{V}_{B/A_{max}}$) and the current wind vector ($\bar{V}_w$).

$$\bar{V}_{\mathrm{max}} = \bar{V}_{B/A_{\mathrm{max}}} + \bar{V}_w \tag{5.41}$$

The maximum body velocity with respect to the airmass is a function of the physical vehicle properties—fuselage drag, blade lift and drag, swashplate pitch limits, etc.—and therefore a constant vehicle property. The maximum flight speed envelope is defined as $\left|\bar{V}_{B/A_{\mathrm{max}}}(\psi_A, \alpha_A)\right|$ in all directions relative to the vehicle frame (F_V). Additionally, since maximum body velocity with respect to the airmass is a constant, the maximum flight speed envelope can be determined a priori during training flights in still air.

Given the relation between maximum achievable flight speed and the current wind vector, a simple protection scheme can be employed to ensure the body velocity with respect to the airmass does not exceed the maximum flight speed envelope. At any given time, the GRC is tracking a commanded inertial position—either a commanded hover point or part of a flight trajectory. If the wind exceeds the maximum flight speed, the platform cannot overcome the disturbance to track the commanded position. Thus the commanded position is convected in the direction of the wind vector at prescribed rate so the vehicle rejects as much as the disturbance as possible—Fig. 5.12. The FEPS can be expressed as

$$\dot{\bar{x}}^C = \begin{cases} \dot{\bar{x}}^T + f_R(\bar{x}^T - \bar{x}^C) \text{ if } \left|\bar{V}_{B/A}\right| < \left|\bar{V}_{B/A_{\max}}(\psi_A, \alpha_A)\right| \\ T_{VI}^T T_{AV}^T \bar{V}_{B/A_{max}} + \tilde{V}_w \qquad \text{if } \left|\bar{V}_{B/A}\right| \geq \left|\bar{V}_{B/A_{\max}}(\psi_A, \alpha_A)\right| \end{cases} \tag{5.42}$$

where $\bar{x}^T$ is the vector of reference trajectory states from the trajectory generator. A return function, $f_R(\bar{x}^T - \bar{x}^C)$, is added to the FEPS to smoothly pull the commanded position back to the original trajectory if the wind magnitude falls below the maximum flight speed.

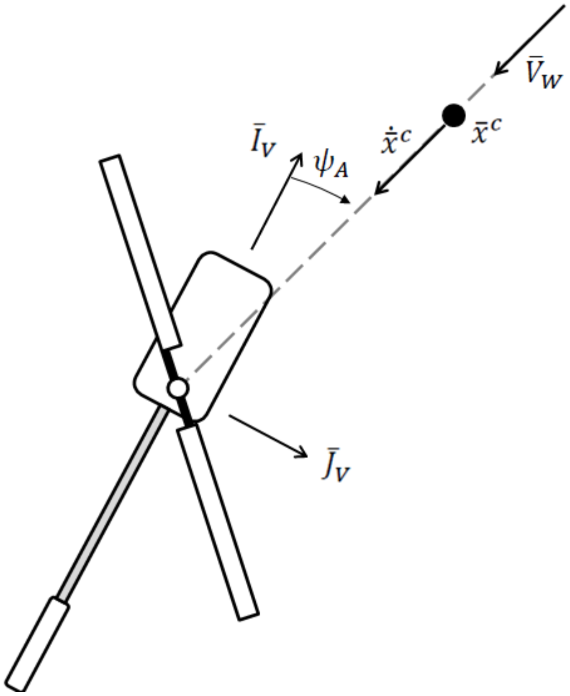

Figure 5.12. Illustration of FEPS command point modification in the presence of high wind.

A small safety margin is added to ensure controls do not saturate during transient dynamics. This does reduced the maximum safe flight speed of the vehicle, but it was discovered that adequate margin could be obtained without sacrificing much control authority

Figures 5.13-5.17 show an example time history for flight in an engulfing head wind with a magnitude of 3.0 m/s and 5 second ramp time, Fig. 5.13. The maximum forward flight speed of the micro rotorcraft platform is 2.08 m/s, with the additional safety margin making the safe flight envelope 1.8 m/s. The vehicle maintains the commanded hover position until the wind magnitude exceeds the maximum flight speed at 4.25 s. After that, the commanded position begins to move with the wind in the negative $\bar{I}_I$ direction ending up with a steady state velocity of 1.2 m/s. The kinematic states are shown in Fig. 5.14 and the velocity states are shown in Fig. 5.15. As seen in Fig. 5.16, the velocity with respect to the airmass settles the maximum safe value after some transient motion preventing control saturation—which can be seen in the tim history of the control input in Fig. 5.17.

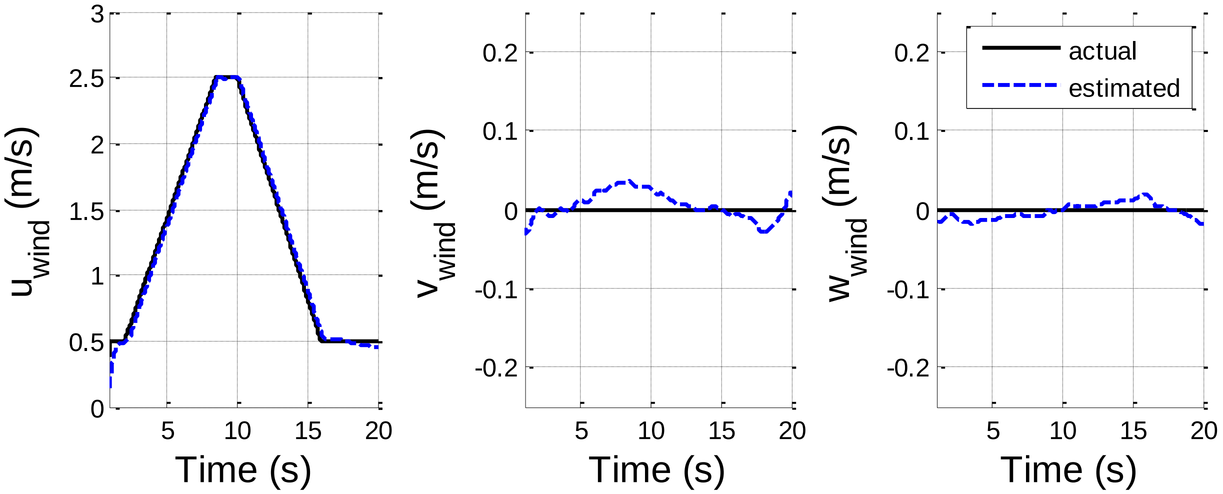

Figure 5.13. Time histories of wind components and estimate values.

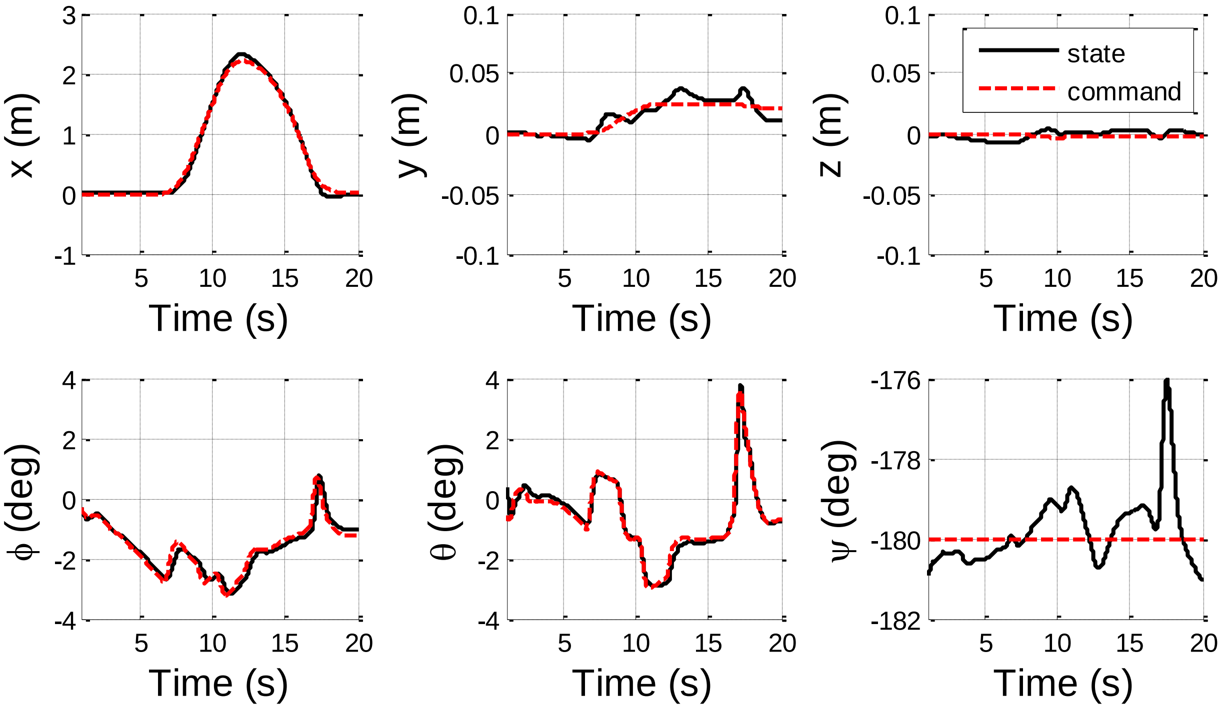

Figure 5.14. Position and attitude time histories with commanded values.

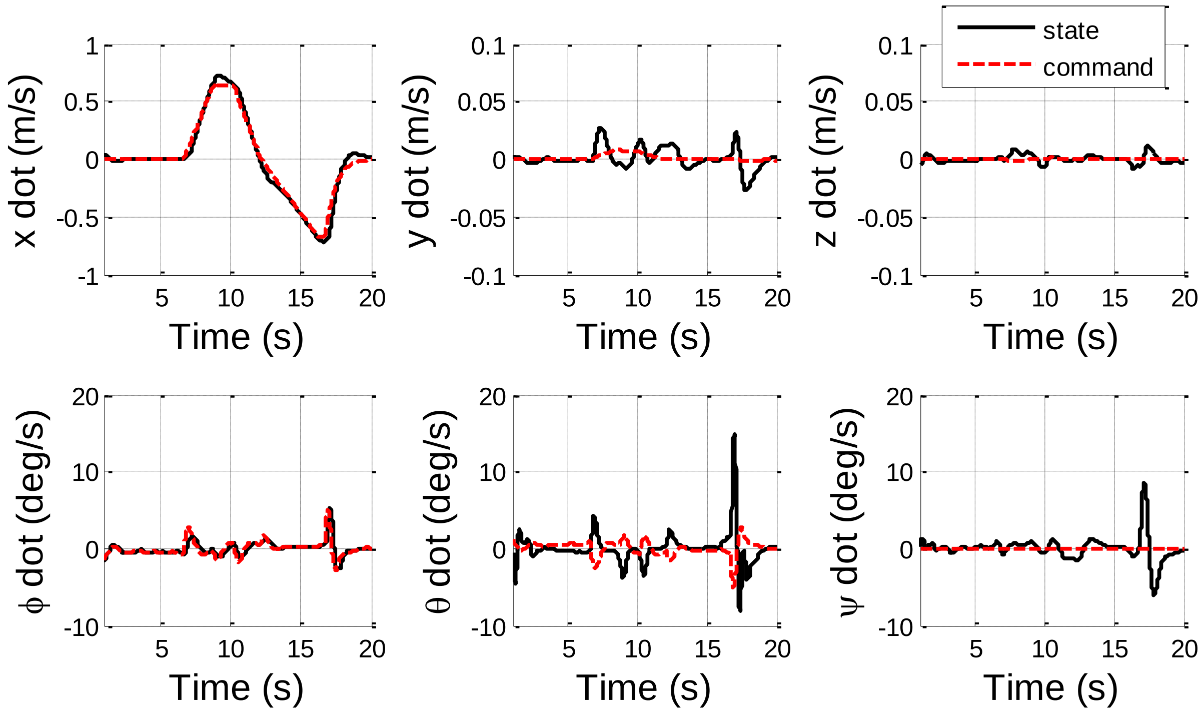

Figure 5.15. Position and attitude derivative time histories with commanded values.

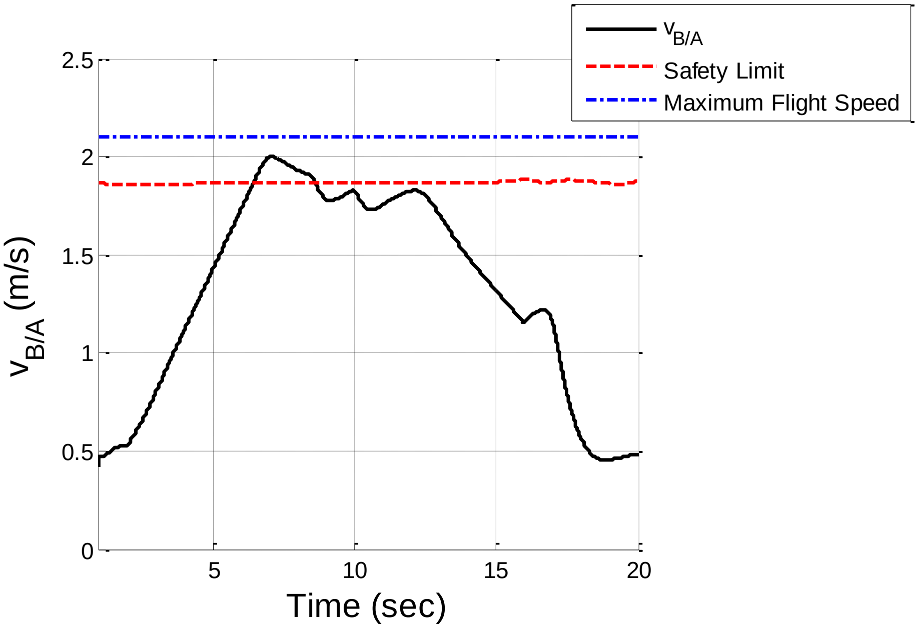

Figure 5.16. Velocity of body with respect to airmass with limits overlaid.

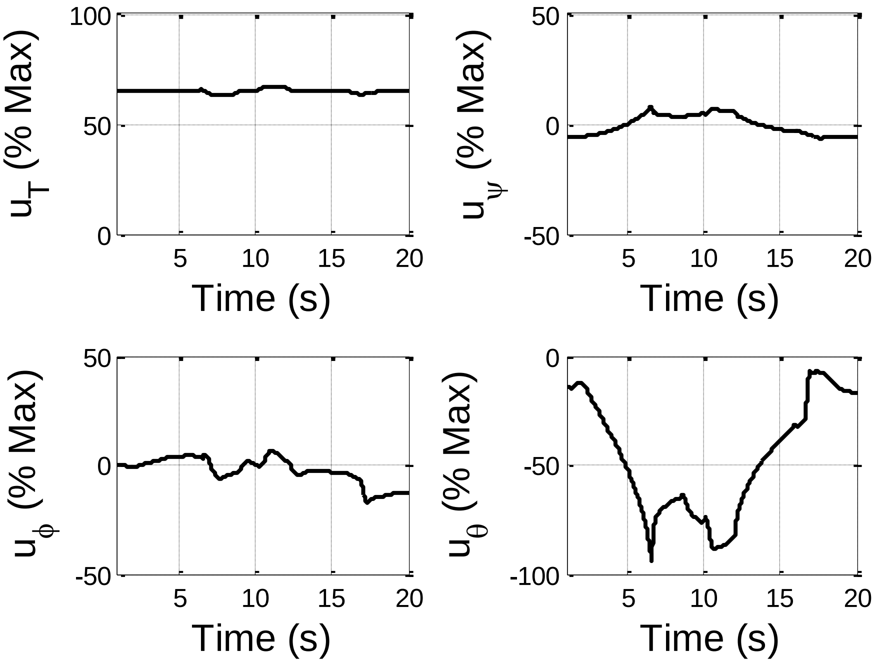

Figure 5.17. Time histories of control inputs for engulfing wind. The control limits are for throttle are 0% to 100% while control limits for yaw, roll, and pitch are ±100%.

CHAPTER 6

MICRO ROTOCRAFT-GUST TRADE STUDIES

A series of simulation trade studies are performed to investigate many key aspects of micro rotorcraft operation in urban wind disturbances including: response of a baseline coaxial helicopter to basic wind kernels, analysis of simulation model fidelity to adequately capture rotorcraft response to spatially and temporally varying urban wind disturbances, the importance of wind estimation to controller tracking performance, and the impact of vehicle design parameters on platform gust rejection capabilities. Employing the validated nonlinear dynamic model and the Gust Rejection Controller each trade study conforms to the same basic set up. Given a set of values for the parameter of interest, Monte Carlo simulations are executed varying initial vehicle states, model error, and measurement error to obtain the average rotorcraft performance in a given urban wind field kernel.

Initial vehicle states are varied using probability distributions to randomize initial attitude, body rates, and initial state of the gust field. The body roll and pitch angles, velocities, and angular rates are randomized using Gaussian distributions to start simulations in off-nominal but expect states. The vehicle position in the gust field, initial heading, and wind inclination angle are randomized using uniform distributions to subject the vehicle to disturbances from all directions and parts of the wind field. Tables 6.1 and 6.2 show the ranges for the normally and uniformly distributed initial states.

Model error is added to the GRC to represent the uncertainty that is inherent in system identification. The confidence intervals calculated during model validation (Table 4.3) are used to derive mean and standard derivations for Gaussian distributions of each model parameter, and each Monte Carlo simulation initializes the control model parameters based on these distributions. Model error ensures the GRC gains have not been overtuned to a specific case and the control architecture is robust to uncertainty. This is done for all parameters expect in trade studies where a model parameter was the focus of the investigation. For those cases a design of experiments was done on for the parameter of interest.

Table 6.1. Normally distributed initial vehicle state parameters.

Parameter	Mean	Standard Deviation
ϕ (deg)	0.0	0.333
θ (deg)	0.0	0.333
u (m/s)	0.0	0.0167
v (m/s)	0.0	0.0167
w (m/s)	0.0	0.0167
p (deg/s)	0.0	0.0333
q (deg/s)	0.0	0.0333
r (deg/s)	0.0	0.0333

State measurements for the feedback to the GRC include measurement error from sensor noise and bias. Errors are modeled as exponentially correlated Gaussian noise where measurement signals take the form

$$y_k = x_k + n_k$$

$$n_k = e^{-\Delta t/\tau} n_{k-1} + \xi_k \sqrt{1 - e^{-2\Delta t/\tau}} \tag{6.1}$$

$$\xi_k \sim N(0, \sigma_N)$$

where x_k is the actual value, y_k is the measurement value, $n_k$is the measurement noise, and Δt is the time between measurements. The measurement error parameters (σ_N, τ) are tuned based on realistic sensor signals from the VICON motion capture system for position, attitude, and linear velocity and from low cost MEMS rate gyros for angular velocity. Measurement error parameter values for the trade study simulations are shown in Table 6.3.

Table 6.2. Uniformly distributed initial vehicle state parameters.

Parameter	Lower Bound	Upper Bound
x (m)	-1.0	2.0
y (m)	-0.5	0.5
z (m)	0.0	1.1
ψ (deg)	0.0	360.0
α_{wind} (deg)	-90.0	90.0
t_{wind} (s)	0.0	15.0

Table 6.3. Measurement error parameters.

Signal	σ_N	Units	τ (s)
x	1.01E-04	m	0.01
y	6.2E-05	m	0.01
z	5.6E-05	m	0.01
φ	0.02634	deg	0.01
θ	0.02434	deg	0.01
ψ	0.04126	deg	0.01
u	0.01	m/s	0.01
v	0.01	m/s	0.01
w	0.01	m/s	0.01
p	5.0	deg/s	0.001
q	5.0	deg/s	0.001
r	2.5	deg/s	0.001

The trade studies performed are:

- Micro rotorcraft performance in prototypical gust environments
  - Engulfing
  - Sinusoidal
  - Discrete shutter
  - Turbulent engulfing
- Simulation model fidelity in urban gusts
- Investigations of the Gust Rejection controller
  - Wind estimation in the controller architecture
  - Tracking controller gains
- Vehicle design parameters and gusts
  - Motor time constant
  - Swashplate time constant
  - Swashplate control margin
  - Rotor blade stall angle
  - Lift coefficient
  - Vehicle stability
  - Rotor dynamic response time
  - Direct force vehicles

All trade studies are performed using a hover maneuver as the mission task element. The vehicle is commanded to hover at the initial position and heading in the presence of various wind disturbances, and simulations are run until the vehicle reaches steady state. Performance metrics are calculated for the transient response—over the entire simulation—and for the steady state response—over the last 10 seconds. Statistics of the metrics are calculated for all Monte Carlo simulations to understand the trends in vehicle performance.

6.1 Micro Rotorcraft Performance in Prototypical Gust Environments

An array of trade studies are carried out to assess micro rotorcraft performance in prototypical wind kernels. The simulations capture baseline capabilities and vehicle response as well as highlight wind features that are most detrimental to mission operation. The results can aid in the design of vehicle guidance algorithms to avoid urban areas where the most dangerous wind features occur, and help identify vehicle response characteristics that should be investigated further in vehicle design parameter trade studies. Wind kernels simulated include engulfing, sinusoidal, discrete shutter, and turbulent engulfing winds, and kernel parameters are varied to subject the vehicle to a range of conditions for study.

Engulfing Wind: Magnitude and Ramp Time

The engulfing wind kernel simulates a gradually changing gust which convects downstream creating a spatially and temporally varying disturbance. This model represents a wind field feature that exists in a many urban areas such as coming around the corner of a building, crossing a doorway or window, and ascending a wind shear. The kernel parameters varied in this trade study are the wind magnitude—the final wind speed the disturbances ramps to—and the ramp time—the time it takes for the wind to change from zero to the wind magnitude, Fig. 6.1. The wind magnitude and ramp time parameters are varied in a two dimensional matrix and Monte Carlo simulations are performed for 30 seconds to allow the vehicle to reach steady state.

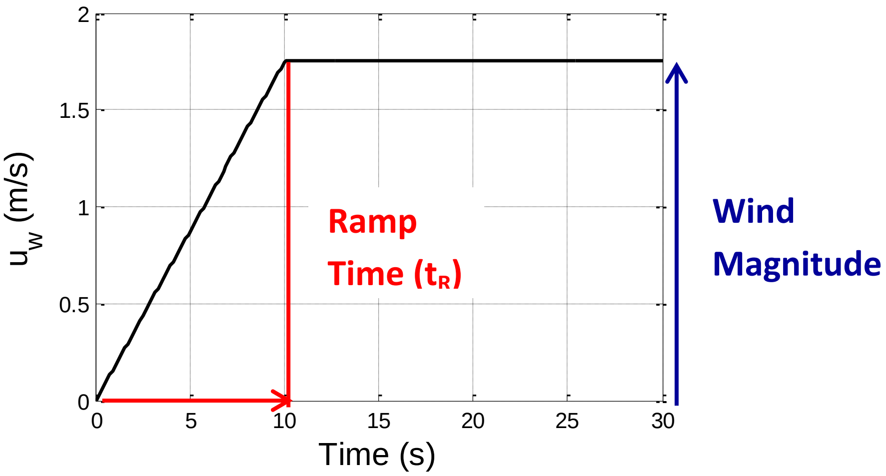

Figure 6.1. Illustration of engulfing wind kernel parameters.

Figure 6.2 shows the mean transient and steady state SEP calculations for varying mean wind speed and ramp time with the maximum safe operating flight speed (1.81 m/s) drawn as a red grid. For wind speeds greater than the safe operating flight speed, the vehicle convects downstream leading to very large SEP values. The flight envelope protection scheme prevents the rotorcraft from going unstable even in mean wind speeds of 3.0 m/s and 2 second ramp times.

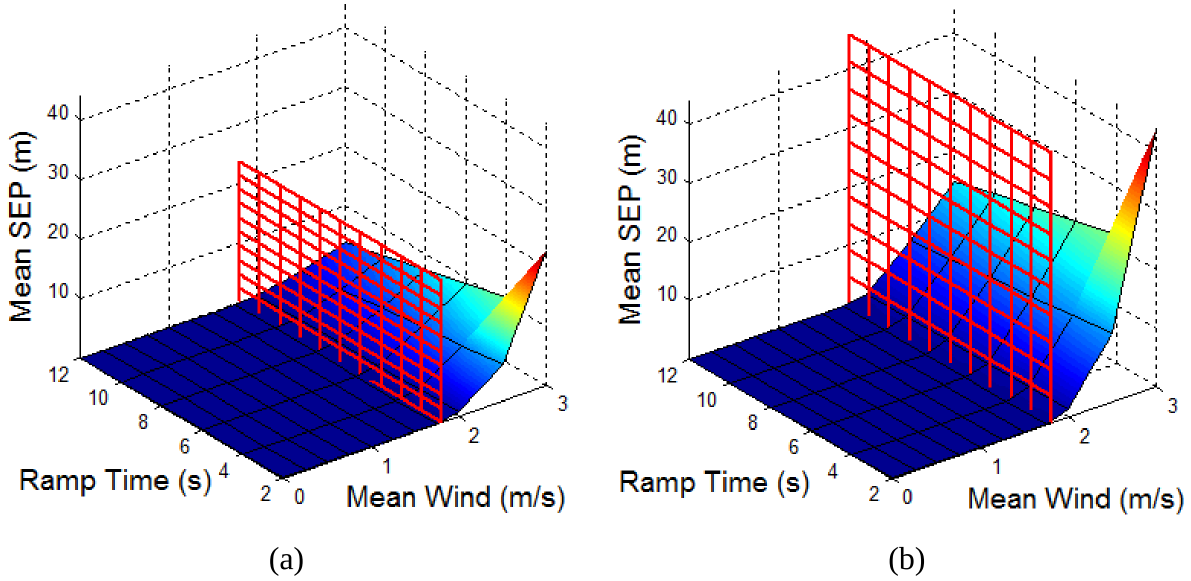

Figure 6.2. Mean SEP for engulfing wind. (a) Transient (b) Steady state. The red lined grid denotes the safe flight speed envelope limit of 1.81 m/s.

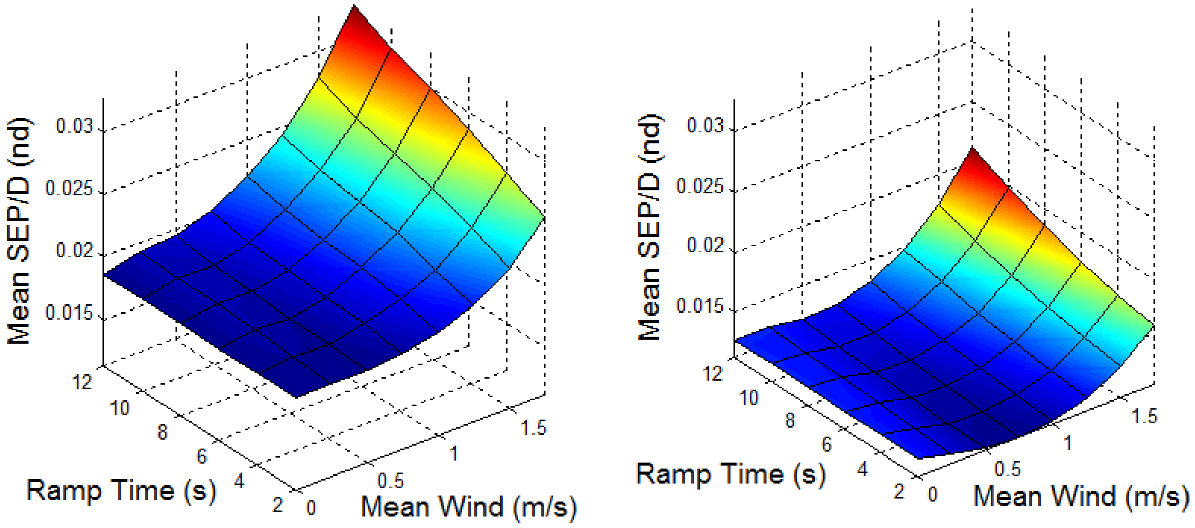

(a) (b)

Figure 6.3. Mean SEP below maximum flight speed nondimensionalized by rotor diameter. (a) Transient (b) Steady state.

Figure 6.3 zooms in on the mean SEP for engulfing winds below the safe flight speed to show response to winds the vehicle could overcome. The results were nondimensionalized by rotor diameter to convey the vehicle positional tracking capability relative to the rotorcraft's size. The results show good disturbance rejection for winds under the maximum flight speed. Unexpectedly, SEP performance is worse for slower varying winds as both transient and steady state SEP increase with increasing ramp time. The reason for this trend can be seen by looking at example time histories of vehicle response and state uncertainty for wind kernel ramps times of 12 and 2 seconds with a mean wind speed of 1.75 m/s, Fig. 6.4. Initially the positional error is much larger for the 2 second ramp time wind kernel (Fig. 6.4a), however because the disturbance reaches a constant state quicker the GRC is able to compensate and drive the uncertainty and position error to zero quicker.

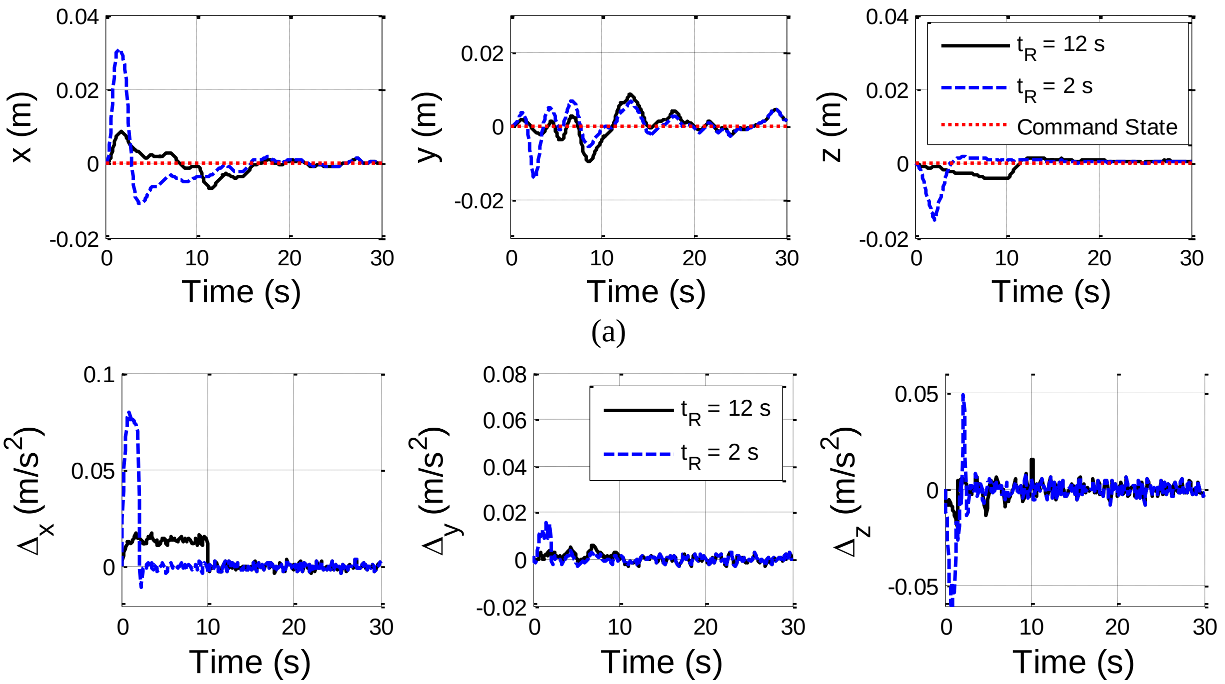

(a)

(b)

Figure 6.4. Example state time histories for 12 s (solid) and 2 s (dashed) ramp times for 1.75 m/s wind magnitude. (a) vehicle position including commanded states (dotted line) (b) state uncertainty.

The wind with the 12 second ramp time has a smaller uncertainty but the ESO takes longer to drive it to zero, Fig. 6.4b. This is a result of the ESO architecture which estimates all uncertainty as constant, thus the quicker ramp time to a longer constant disturbance is easier to estimate. It also shows that since SEP encircles 50 % of the trajectory, that the ill effects of faster ramps times is somewhat averaged out. Therefore, the detrimental effects of rapidly changing wind conditions can be seen more clearly by looking at the maximum tracking errors, Fig. 6.5. Rotorcraft operating in confined spaces will be in greater danger of hitting walls or other obstacles in the presence of quickly changing wind disturbances.

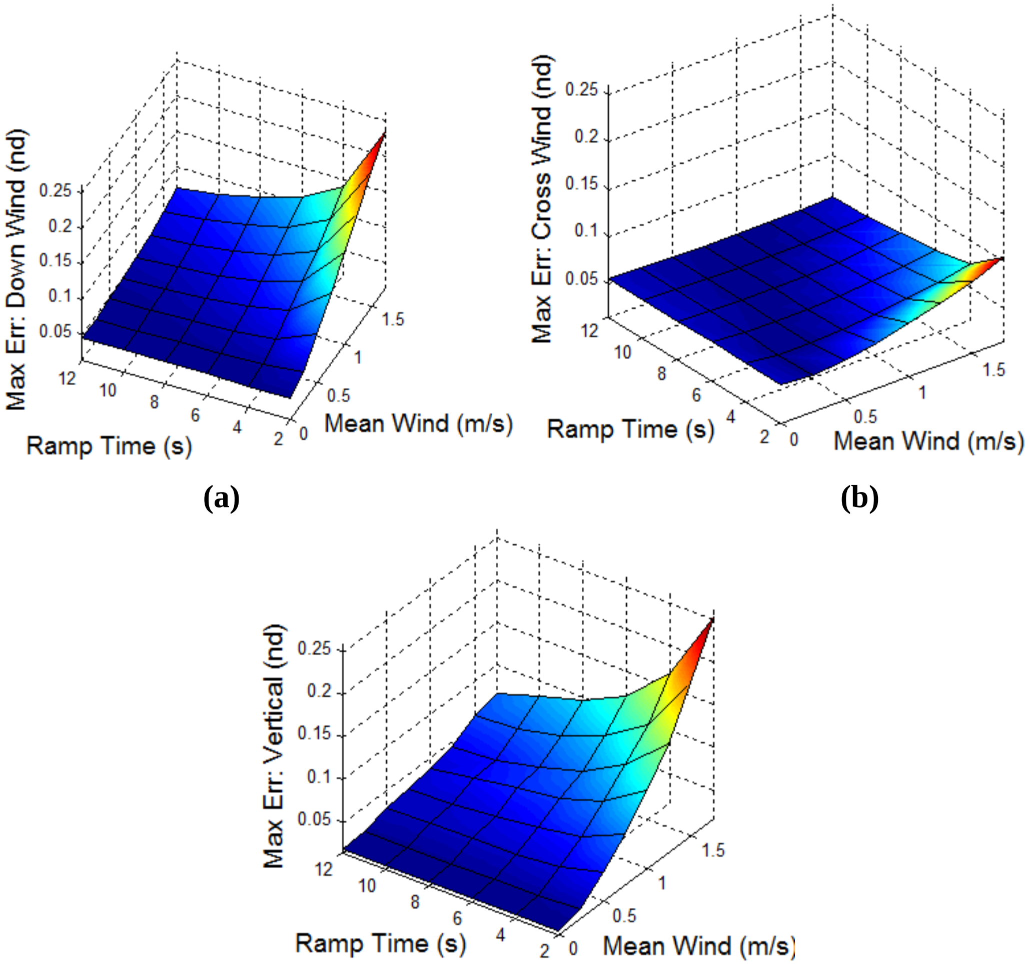

(a) **(b)**

(c)

Figure 6.5. Mean max position tracking error nondimensionalized by rotor diameter. (a) Downwind (b) cross wind (c) vertical.

Figures 6.6 and 6.7 show the mean and maximum AVRMS respectively during engulfing wind kernel trade studies. Both the mean and maximum values stay relatively small and constant for wind speeds under the maximum safe flight speed with the largest peaks occurring for the smallest ramp times.

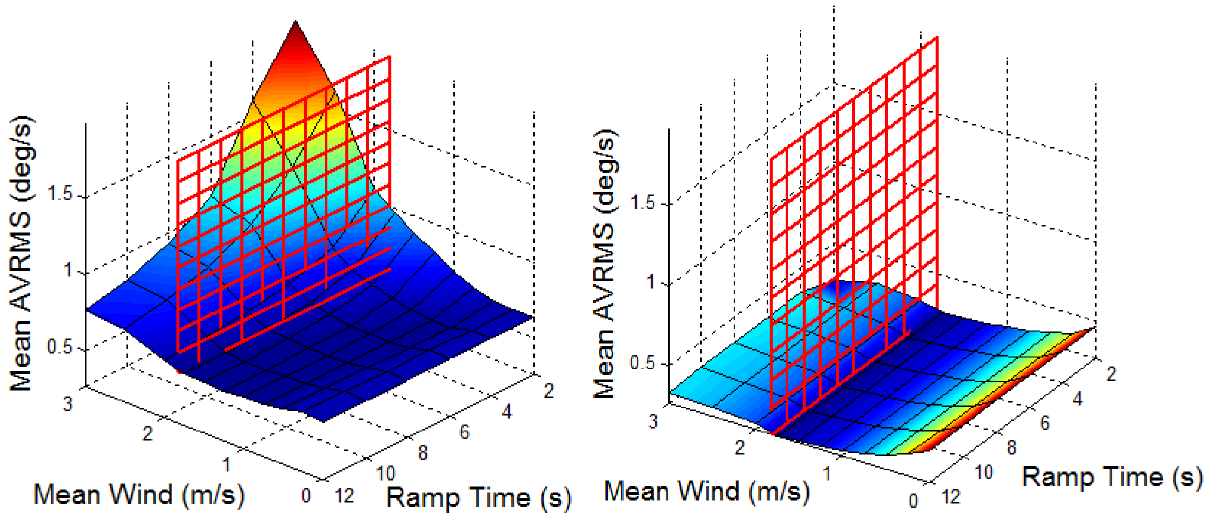

(a) (b)

Figure 6.6. Mean angular velocity root mean square. (a) Transient (b) Steady state.

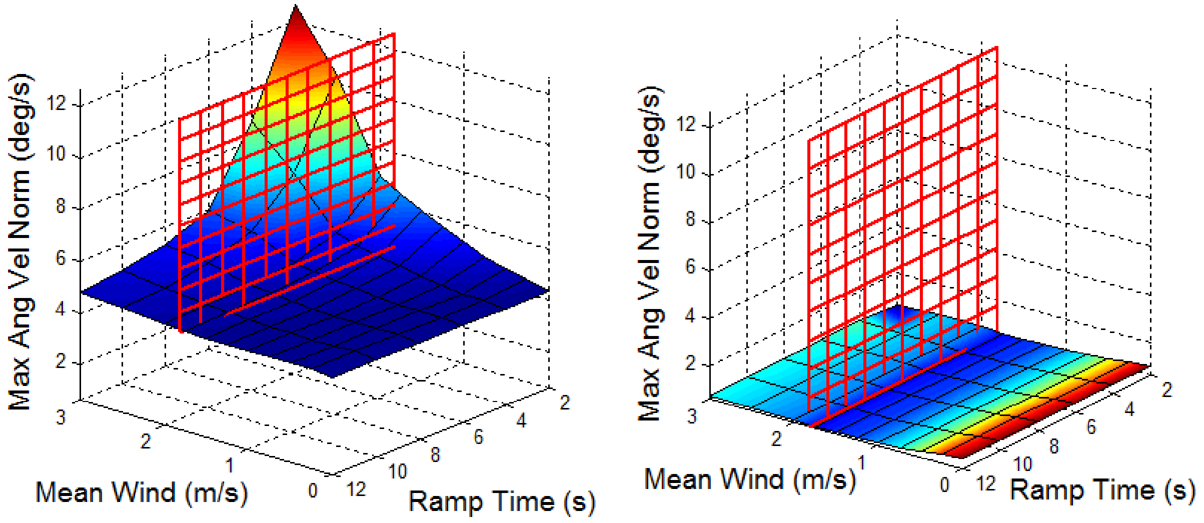

(a) (b)

Figure 6.7. Average maximum angular velocity excursion during flight. (a) Transient (b) Steady state.

Figure 6.8 shows the mean AERMS for both transient and steady state portions of the engulfing simulations. Overall the attitude errors are quite small, especially in steady state. This also highlights the ability of the FEPS scheme to maintain controllability in winds that exceed the maximum vehicle flight speed. While AERMS trends larger as mean wind speed increases, the mean values are still quite small—less than 2 degrees.

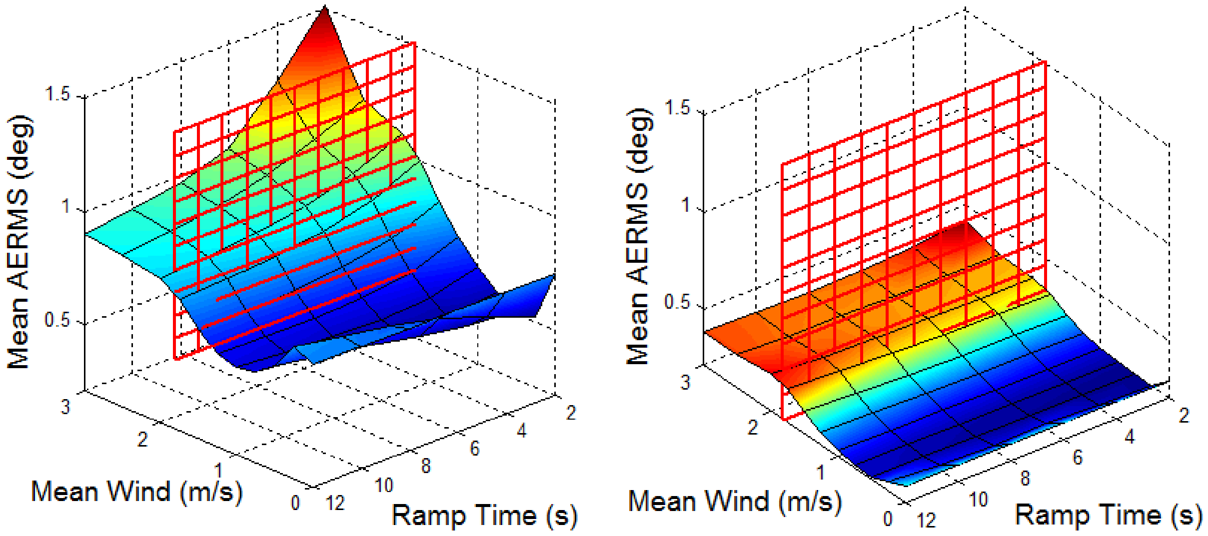

(a) (b)

Figure 6.8. Mean attitude error root mean square. (a) Transient (b) Steady state.

Figure 6.9 shows the mean control standard deviation of each control channel, which steadily increase with mean wind speed. Roll and pitch standard deviation are much larger than other inputs with pitch being the largest and yaw being extremely small. The larger pitch control standard deviation is most likely due to the larger inertia (I_{yy}) while yaw is smallest because of large yaw control authority generated by differential rotor speed. It is interesting that all control standard deviations very clearly trend with mean wind speed but not with ramp time. Another metric to aid in understanding in control effort is the average control margin, however it was discovered that averaging control margin over all cases reduced the average results since unless the wind was acting mostly along one control axis, the inputs to the vehicle were small.

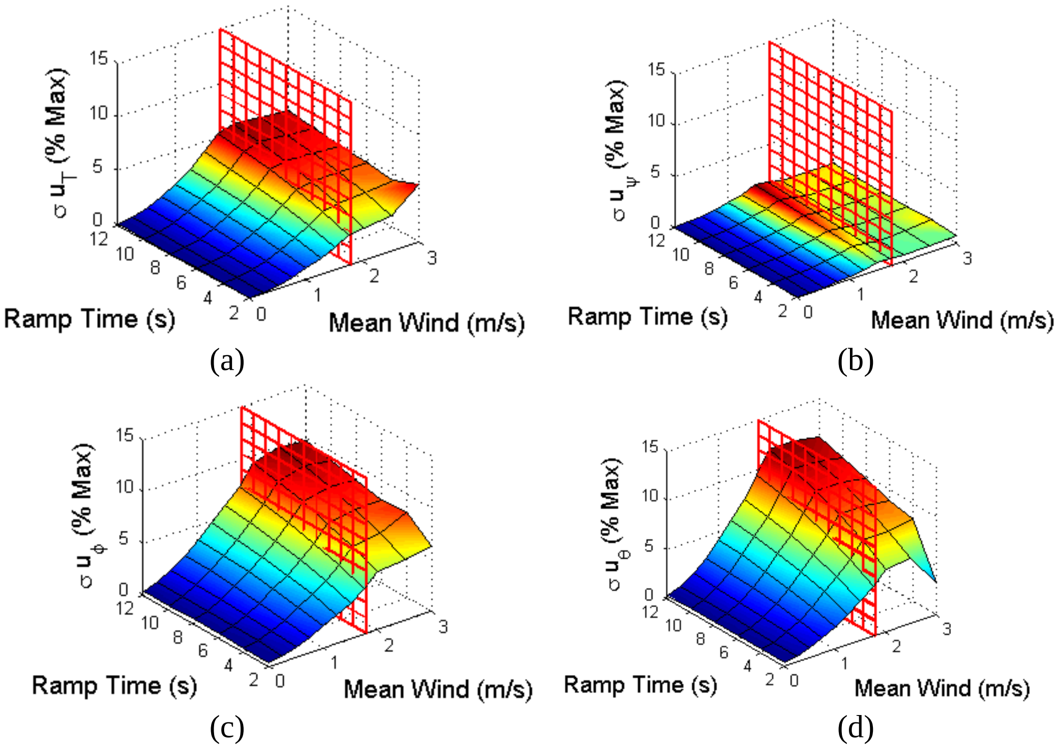

(a) (b)

(c) (d)

Figure 6.9. Mean control standard deviation for engulfing wind kernels. (a) throttle (b) yaw input (c) roll input (d) pitch input.

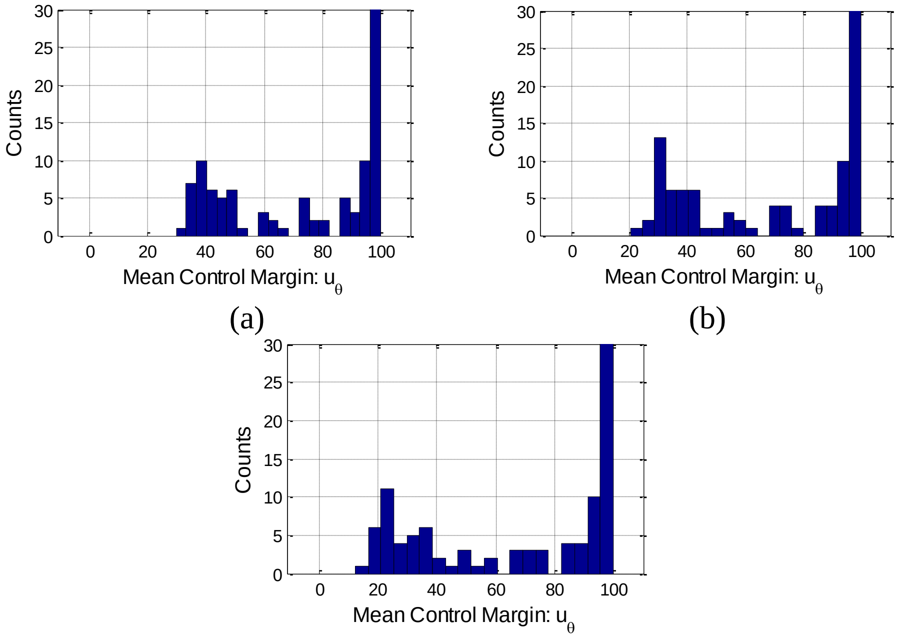

(a) (b)

(c)

Figure 6.10. Mean pitch control margin for 1.75 m/s wind for decreasing ramp times. (a) 12.0 seconds (b) 6.0 seconds (c) 2.0 seconds.

Therefore it is more insightful to look at results in the form of histograms. Figure 6.10 shows histograms of pitch control margin for ramp times of 12.0, 6.0, and 2.0 seconds. All three figures show a large number of simulations with mean control margin close to one, which are the cases where the wind vector was perpendicular to $\hat{I}_B$ axis. For cases where the wind vector was mostly in the body x-direction, Figure 6.10 shows the steady decrease in mean control margin as ramp time decreases, therefore more control effort is required to reject faster varying wind disturbances.

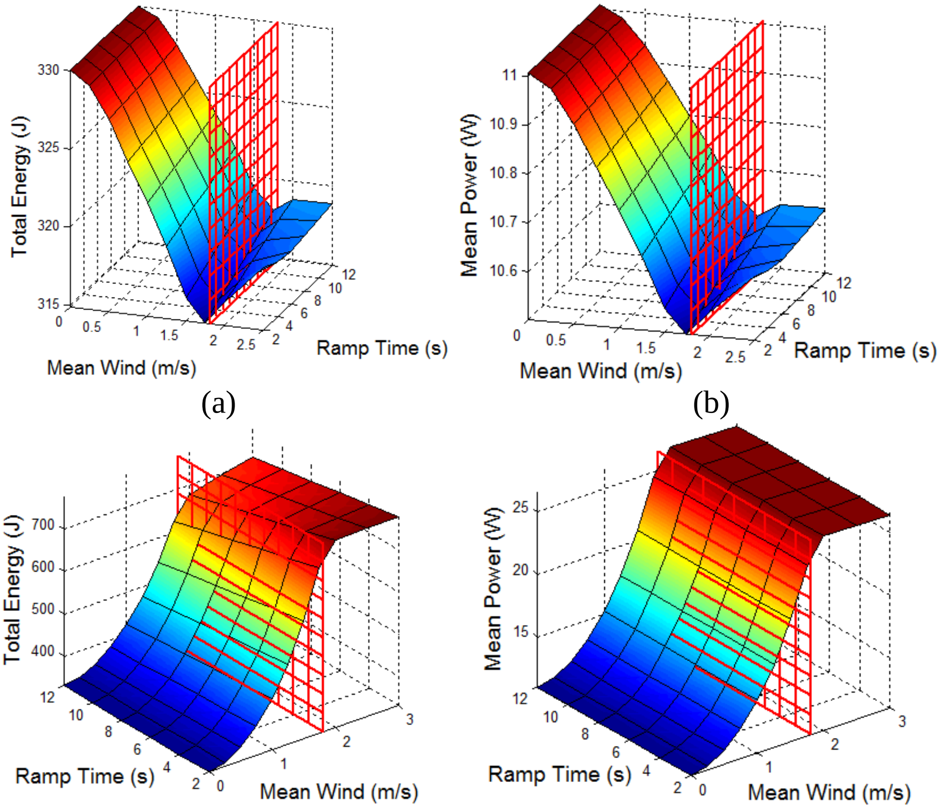

(a) (b)

(c) (d)

Figure 6.11. Mean transient energy and power for engulfing wind simulations. (a) Total energy in horizontal winds (b) Power in horizontal winds (c) Total energy in vertical winds (d) Power in vertical winds.

Histograms for roll, throttle, and yaw control inputs follow similar trends. Taking a look at control standard deviation and mean control margin, we can begin to understand the trends in control effort for rotorcraft for different wind disturbances.

Figure 6.11a and Figure 6.11b shows the total energy and mean power over all simulation cases with a mostly horizontal wind disturbance. As expected, the power required initially drops similar to a rotorcraft power curve in forward flight. However it is clear that the power curve is not balanced for this vehicle. It is general design practice for the operational forward flight speed to require the same power as hover. It is clear from Figure 6.11 that the power consumed at the safe FEPS speed of 1.83 m/s and at the maximum flight speed of 2.03 m/s are well below the hover power required. Figure 6.11c and Figure 6.11d shows the total energy and power for vertical downwind simulation cases. As expected, the power increases as if the vehicle was in a climb.

Sinusoidal Wind: Frequency and Amplitude

Urban wind environments contain a large variety of disturbances with repetitive structures and a wide range of frequency content. The sinusoidal wind kernel provides a pure sine wave wind to study the effect of frequency and amplitude from a continuous disturbance on a micro rotorcraft vehicle, Fig. 6.12. Frequency and amplitude are varied in a two dimensional matrix; however a boundary is established for high winds to maintain controller stability. Beyond 1.5 m/s amplitude and 0.4 Hz frequency the ESO limits on $\tilde{x}_3 - \bar{\Delta}$ and $\dot{\Delta}$ are violated. Thus in order to keep $|\tilde{x}_3 - \bar{\Delta}| \leq 38.0$ and $\left|\dot{\bar{\Delta}}\right| \leq 50.0$, the frequency and amplitude ranges studied are 0.03 Hz to 1.0 Hz for 0.0 m/s to 1.0 m/s amplitude and 0.03 Hz to 0.4 Hz for 1.5 m/s amplitude winds. Responses are simulated for 15 seconds.

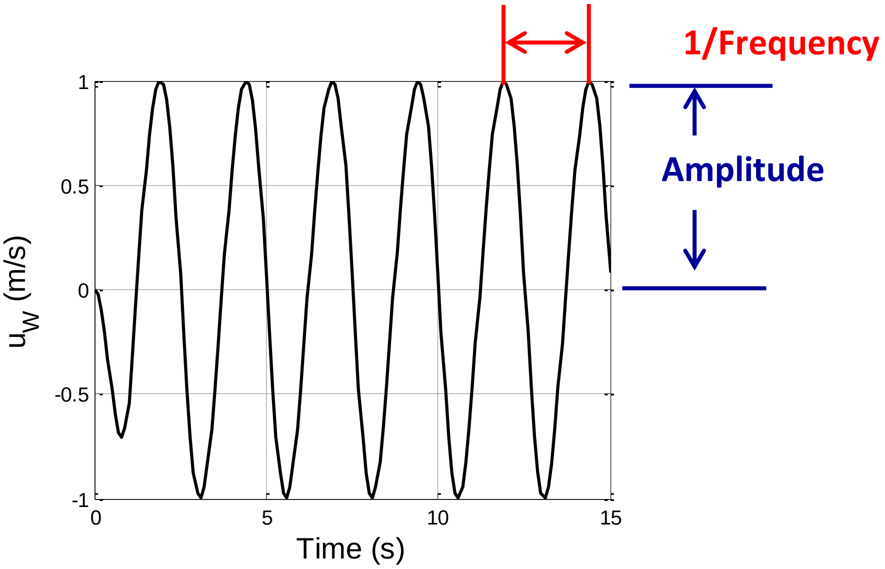

Figure 6.12. Illustration of sinusoidal wind kernel parameters.

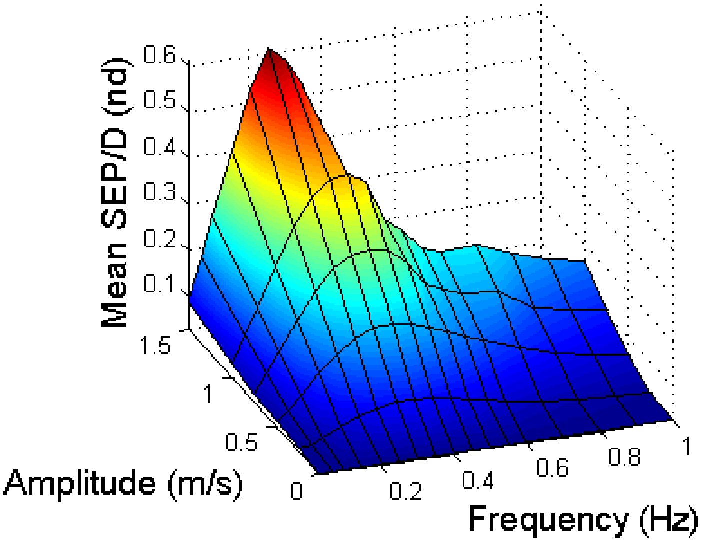

Figure 6.13. Mean nondimensional SEP for sinusoidal wind kernel.

Figure 6.13 shows the mean nondimensional SEP for vehicle response to sinusoidal wind kernels. Interestingly, there is a peak response between 0.3 Hz and 0.35 Hz which becomes sharper with increasing amplitude. The main cause of the peak response is to the time required to tilt the helicopter thrust vector for horizontal control of the underactuated system. At the peak disturbance frequency, the time the vehicle tilts the thrust vector in phase with the changing wind vector. This can be seen in Figure 6.14a where the wind vector peaks and starts changing direction just as the helicopter has tilted to enough to start rejecting the disturbance. On the other hand, for higher frequency sinusoidal winds the vehicle response is out of sync with the changing wind conditions resulting in less positional displacement—Fig. 6.14b. This can also be seen in example time histories of rotor flapping states, Fig. 6.15.

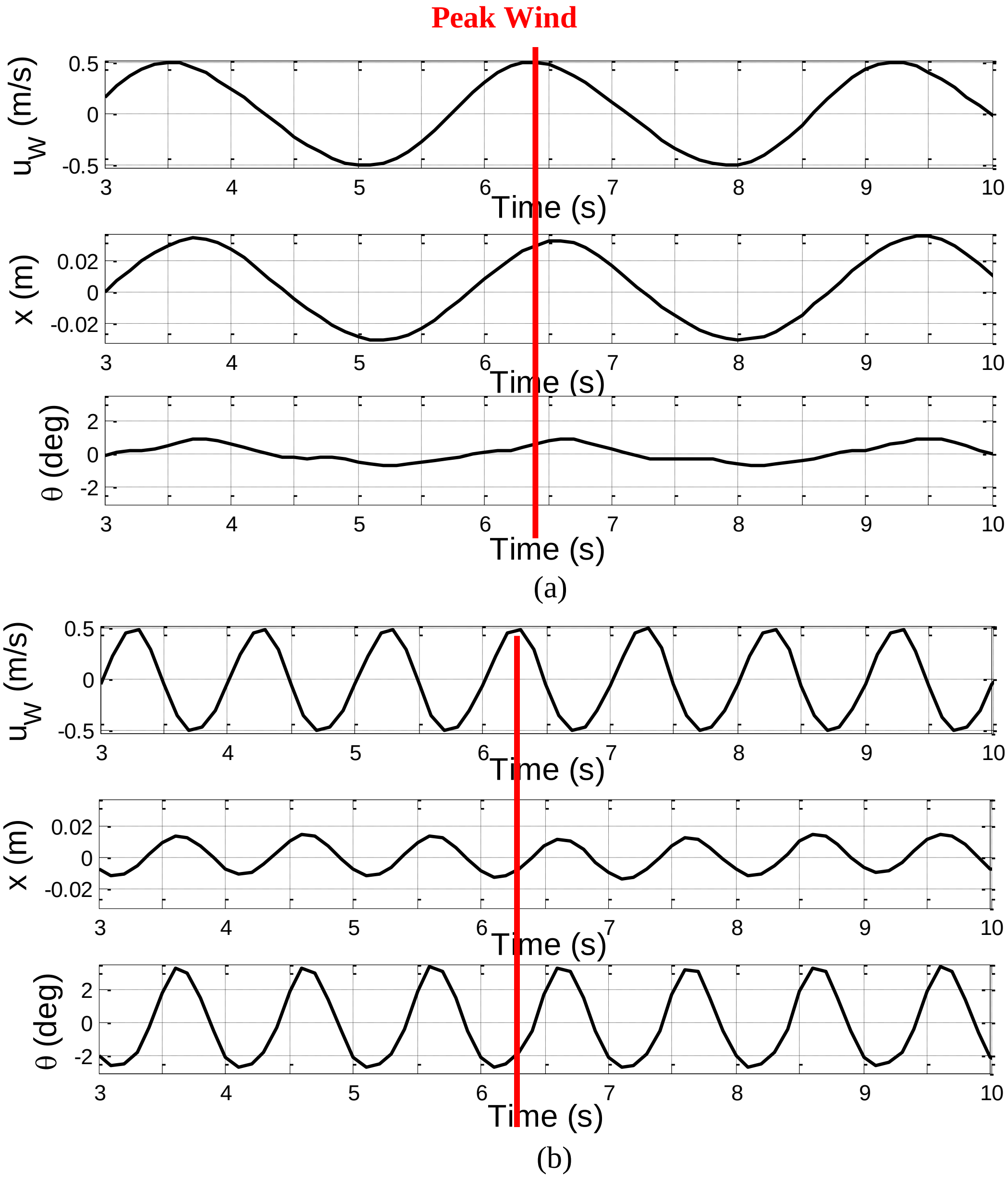

Figure 6.14. Example partial time histories for x position and pitch angle for sinusoidal winds with red lines representing a wind peak. (a) 0.35 Hz frequency wind (b) 1.0 Hz frequency wind.

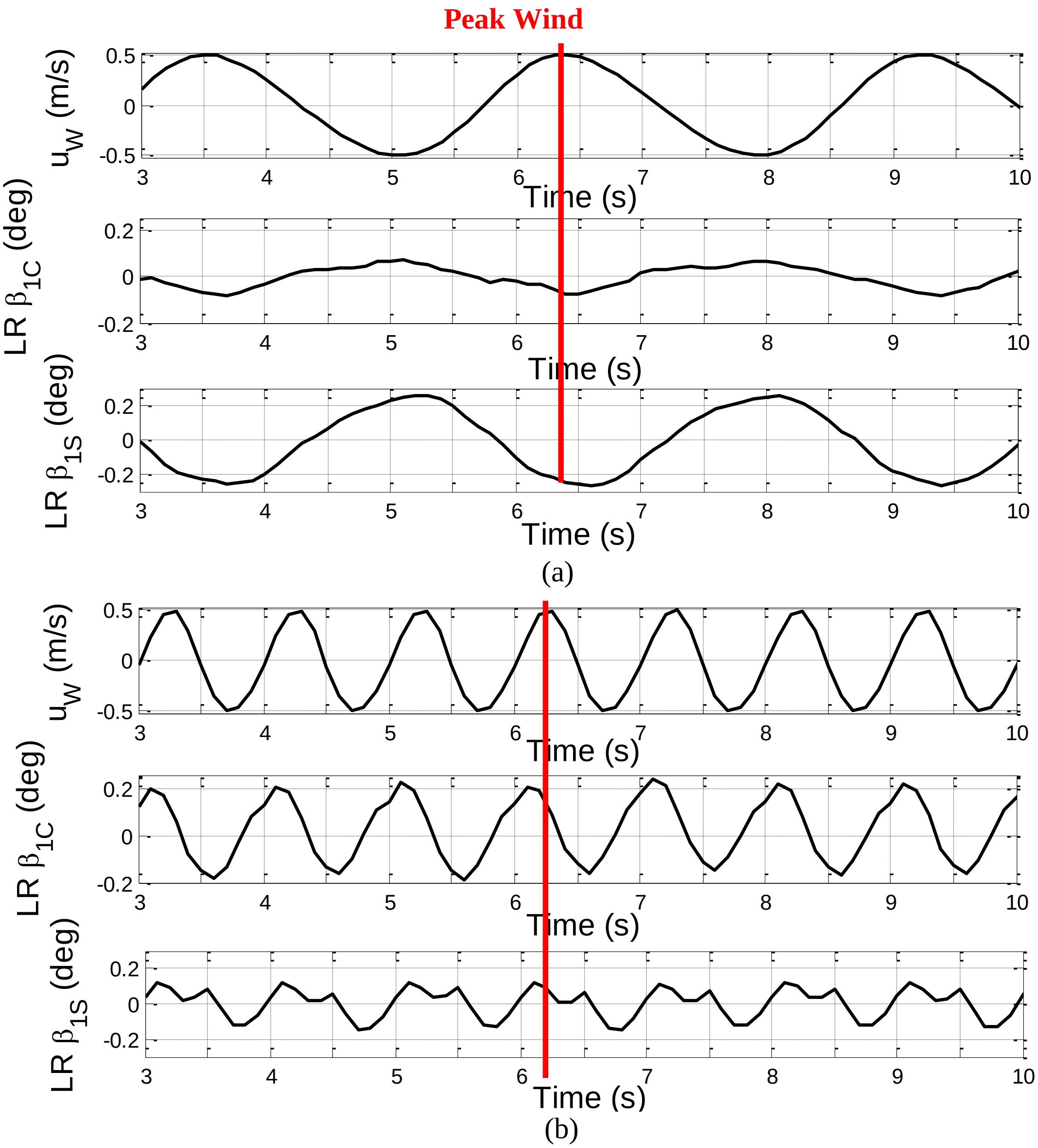

Figure 6.15. Example partial time histories for lower rotor cyclic flap angles for sinusoidal winds with red lines representing a wind peak. (a) 0.35 Hz frequency wind (b) 1.0 Hz frequency wind.

Figures 6.16 and 6.17 show mean AVRMS and AERMS for sinusoidal wind kernels. Both metrics are affected significantly by amplitude while AVRMS, as expected, is also extremely sensitive to disturbance frequency. Neither metric shows the same peak response as SEP.

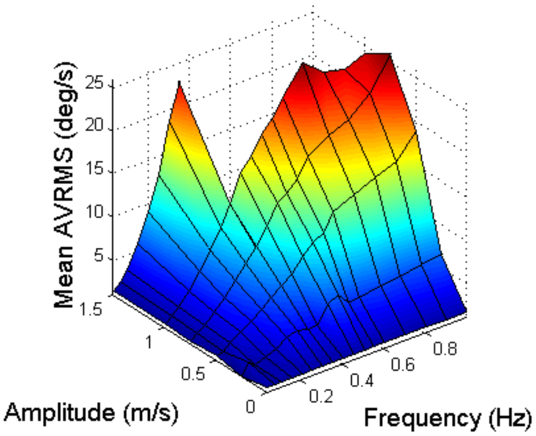

Figure 6.16. Mean AVRMS for sinusoidal wind kernel.

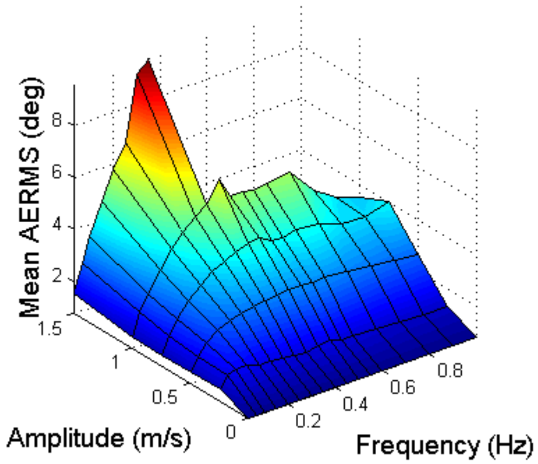

Figure 6.17. Mean AERMS for sinusoidal wind kernel.

The average control input standard deviations for roll and pitch inputs show a similar but smaller peak in the same frequency range as SEP, Fig. 6.18. While throttle and yaw input show dependence on wind amplitude, the peak exhibited by roll and pitch support the theory that the peak response behavior is associated with horizontal control.

The micro rotorcraft's peak response to sinusoidal winds could endanger platform safety during operation and limit the number of feasible flight trajectories in an urban environment. A vehicle could be excited by a region of turbulence with a critical length scale or by a common structure such as shedding vortices. While the exact flow conditions a micro rotorcraft will experience are highly dependent on the local conditions discussed in Chapter 1, it is possible to bound some of the expected parameters.

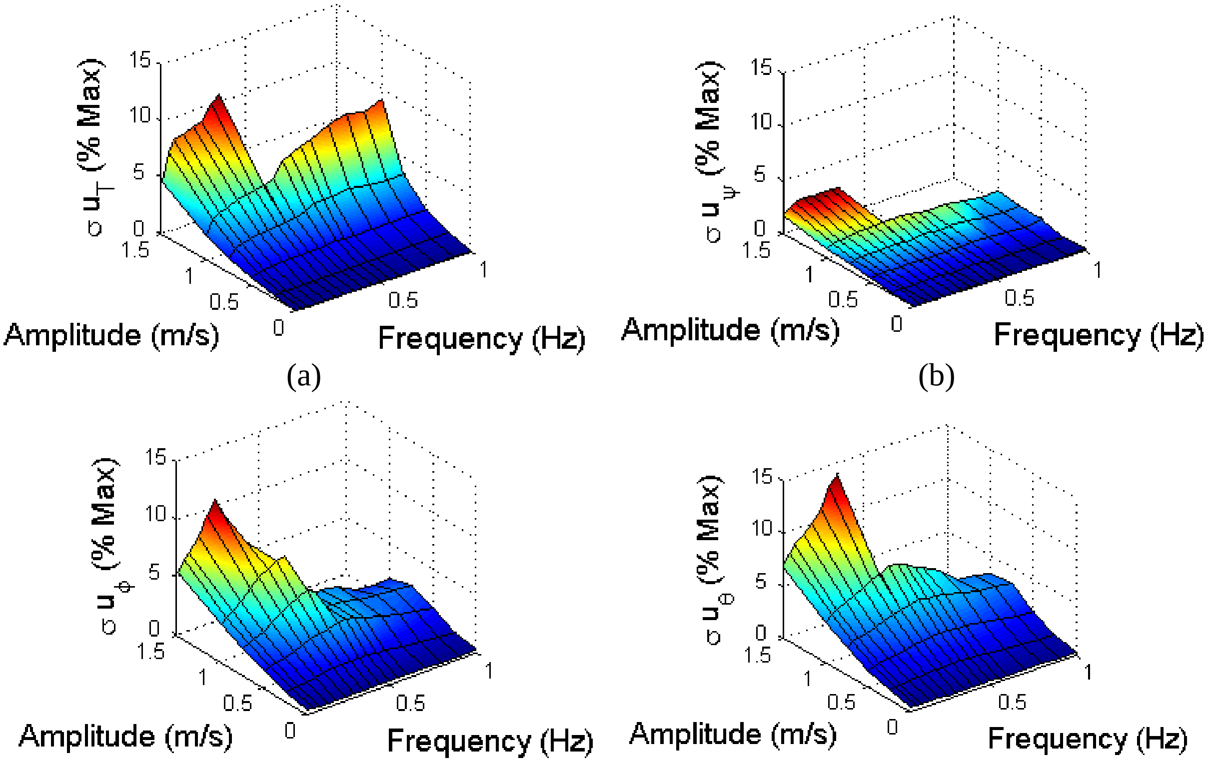

(a) (b)

(c) (d)

Figure 6.18. Mean control standard deviations for a sinusoidal wind kernel. (a) throttle (b) yaw input (c) roll input and (d) pitch input.

Strouhal number is the dimensionless quantity that describes the oscillation of shed vortices from a Kármán vortex sheet [83]

$$St = \frac{fL}{V} \tag{6.2}$$

where f is the frequency of vortex shedding, L is the characteristic length, and V, is the velocity of the flow. Experimental and simulation based studies have documented the ranges of Strouhal numbers in urban environments with respect to Reynolds number, Table 6.4 shows some expected ranges based on the work of Frank and Mauch [60] and Tamai, Okuda, and Katsura [63].

Based on the reported ranges for Strouhal number, the expected vortex shedding frequencies around different obstacles can be estimated for the reasonable range of flow velocities. Figure 6.19 shows estimated vortex shedding frequencies for expected Strouhal numbers and flow velocities for obstacles of different sizes: a building, car, small tree, and lamp post.

Table 6.4. Strouhal number ranges for Reynolds numbers in urban environments.

Reynolds number	Strouhal number
10^2-10^4	0.1 – 0.175 [60]
$2x10^4 – 1x10^5$	0.03 – 0.15 [63]
$1x10^5 – 4x10^5$	0.05 – 0.3 [63]
$1x10^6 – 1.2x10^6$	0.05 – 0.45 [63]

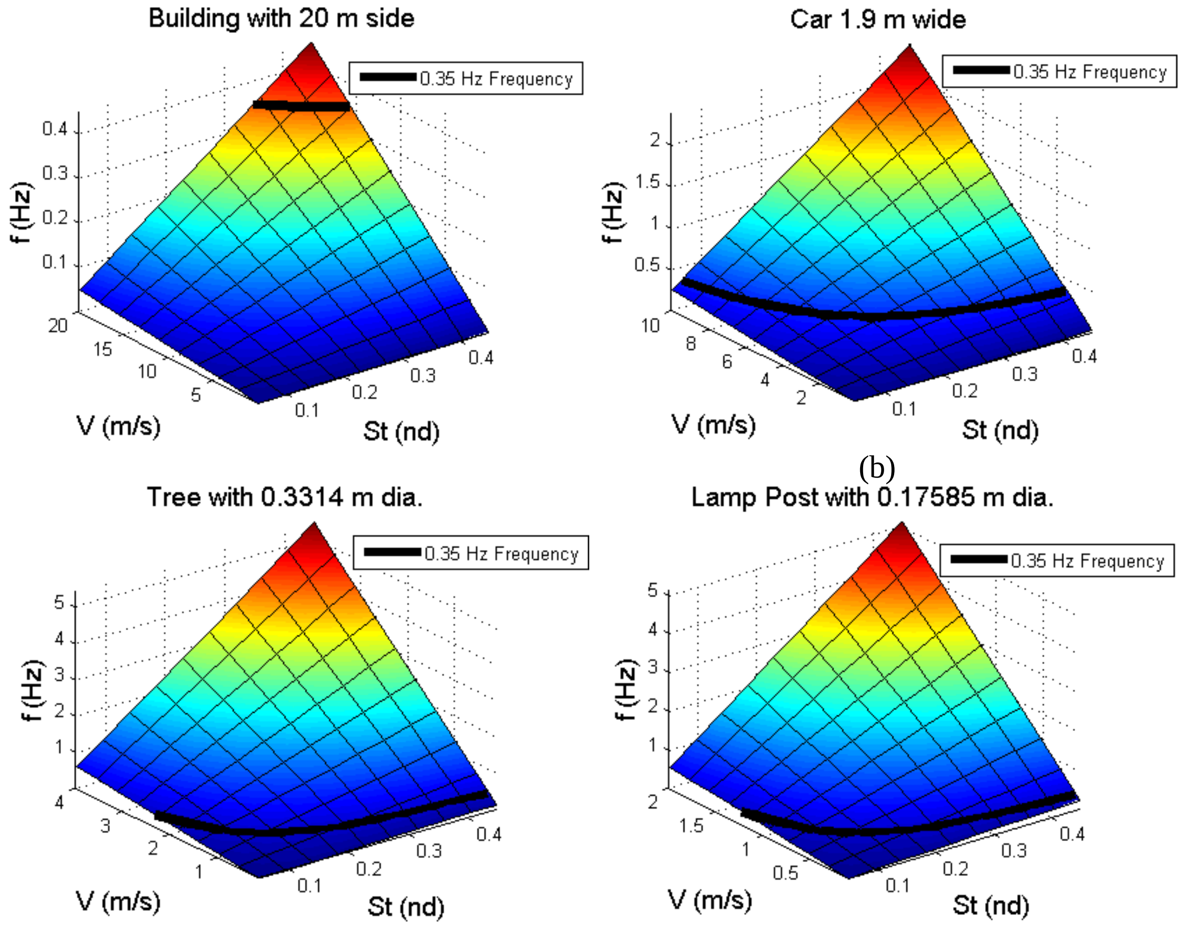

(b)

(c) (d)

Figure 6.19. Vortex shedding frequencies for expected Strouhal number and flow velocities around urban obstacles. (a) a building with a 20 m side (b) an average 4 door car that is 1.9 m wide (c) a small tree with 0.33 m diameter (d) a common street lamp post with 0.175 m diameter.

Of the four obstacles, the 18-20 m/s wind speed required to create the appropriate shedding off a building is least likely. However, it is very likely that that flow field conditions capable of producing low frequency disturbances for the smaller obstacles can reasonably happen at street level. Therefore, based on the mission scenarios expected for a micro rotorcraft, it may be important to consider the peak response frequency throughout the design process. Additionally, care should be taken to tune control gains to not excite this frequency with feedback.

Discrete Shutter Wind: Frequency and Wind Strength

As seen in the engulfing wind kernel trade study, rapidly changing wind velocities can degrade rotorcraft tracking performance. Discrete changes in the local flow velocities, such as the turning on or off of a fan or HVAC system or flying through the separated flow in an obstacles wake, can be especially challenging. The discrete shutter wind kernel is described by the parameters frequency, mean wind speed, maximum wind speed, and amplitude from the mean – Fig. 6.20. As with sinusoidal wind kernel, vehicle response is simulated for 15 seconds and the wind frequency and amplitude parameters are varied in a two dimensional matrix. The relations between maximum wind speed, mean wind speed, and wind amplitude parameters for test cases simulated are shown in Table 6.5.

Table 6.5. Discrete shutter wind kernel wind speed parameters.

Max (m/s)	Mean (m/s)	Amplitude (m/s)
0.25	0.1654	0.0847
0.5	0.3307	0.1693
0.75	0.4961	0.254
1.0001	0.6614	0.3386

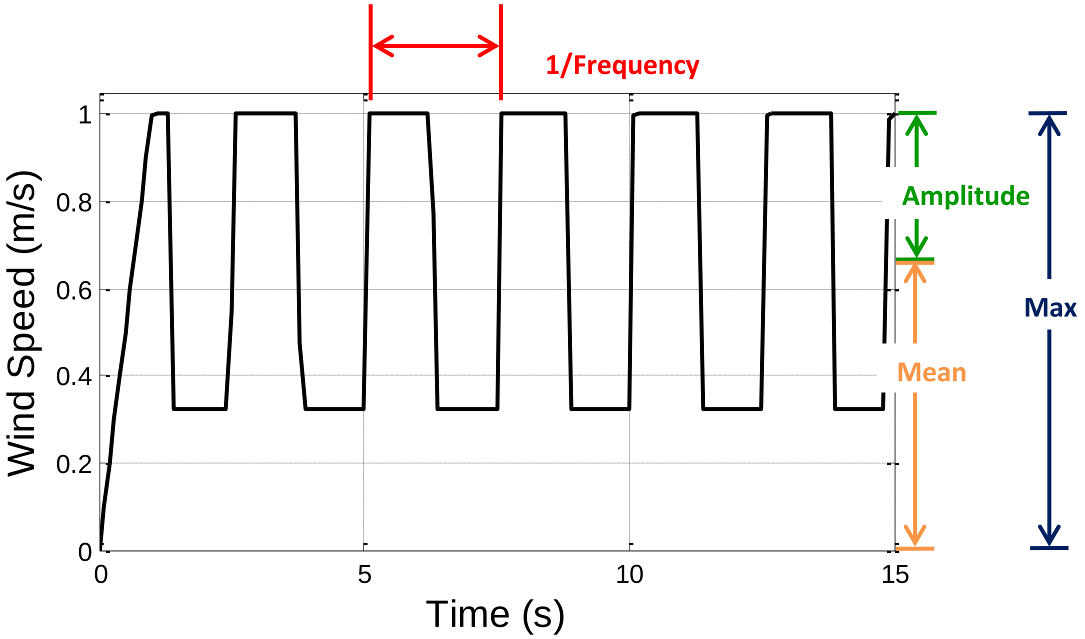

Figure 6.20. Illustration of discrete shutter wind kernel parameters.

The nondimensional mean SEP, Fig. 6.21, shows a comparable peak response in the same frequency range as the sinusoidal wind kernel results though the peak magnitude is a little less. Also similar to the sinusoidal wind kernel results, the mean AVRMS and AERMS increase with both wind speed and frequency, Figs 6.22 and 6.23. This confirms that the peak response frequency is an issue for micro rotorcraft regardless of the shape of the disturbance.

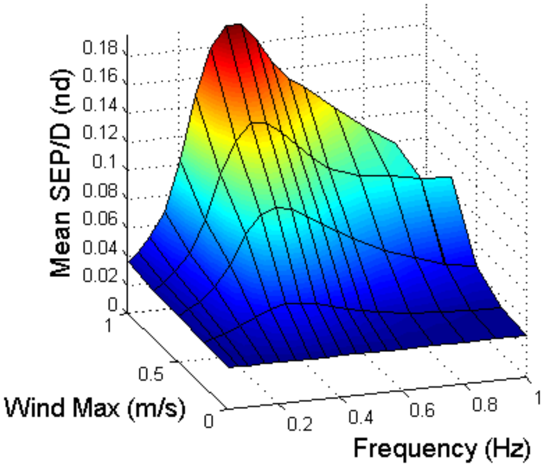

Figure 6.21. Steady state mean nondimensional SEP for discrete shutter wind kernel.

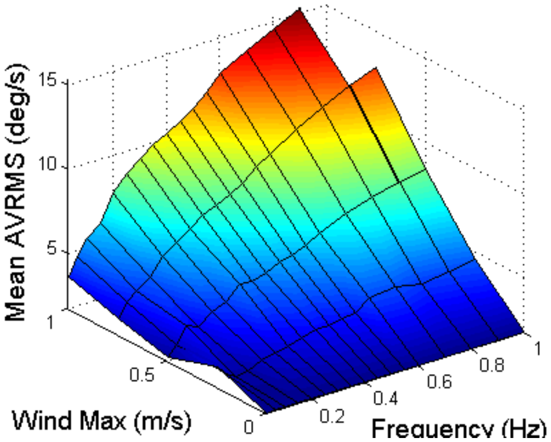

Figure 6.22. Steady state mean AVRMS for discrete shutter wind kernel.

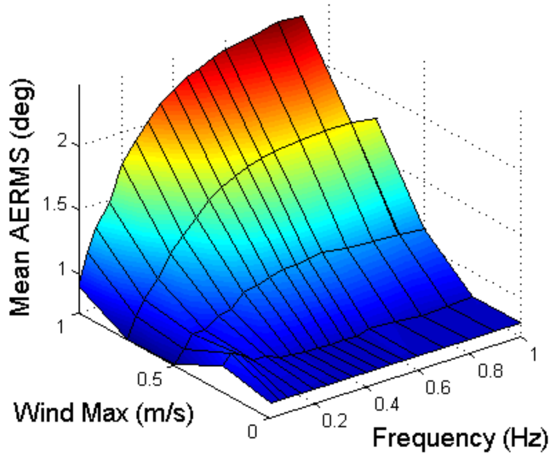

Figure 6.23. Steady state mean AERMS for discrete shutter wind kernel.

Turbulent Engulfing Wind: Turbulence Intensity and Mean Wind

While structured wind flows are common in urban environments, it is also expected that flows will be messy, turbulent winds. The engulfing wind kernel with 10 second ramp is used to study vehicle response to turbulent winds. Experimentally derived turbulence is added to the mean wind vector as a turbulence intensity parameter (σ). For the work reported here, turbulence intensity is defined as the standard deviation of the wind velocity during final 20 seconds of the simulation—Fig. 6.24. This definition is used over the alternative nondimensional turbulence intensity, where the standard deviation is divided by the mean wind, to allow flows with zero mean wind to be simulated as well. The turbulent wind kernel parameters mean wind speed and turbulence intensity are varied in a 2D matrix to investigate the effects of both on system response. Simulations are performed for 30 seconds with steady state metrics calculated over the last 20 seconds after the mean wind speed has reached a constant value.

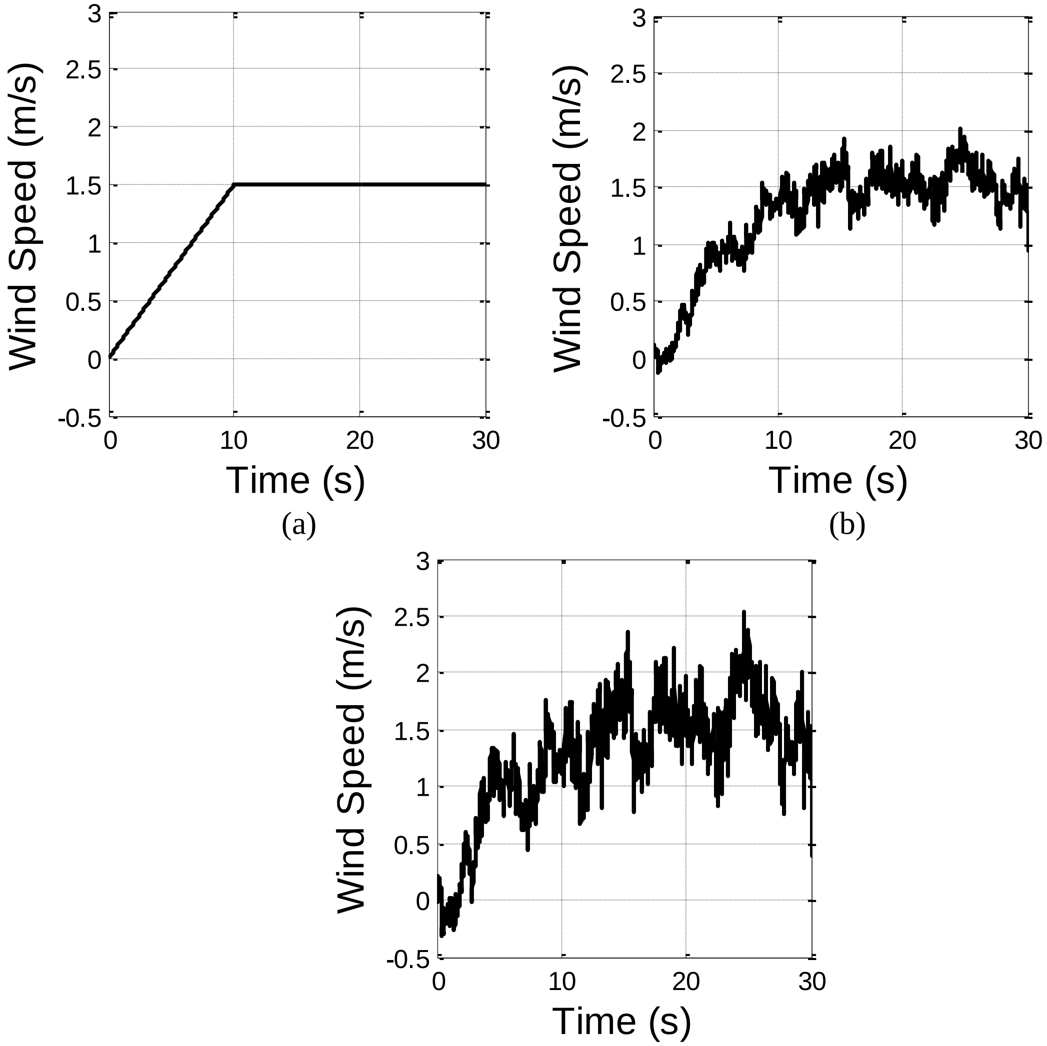

(a)

(b)

(c)

Figure 6.24. Example turbulent engulfing wind kernels. (a) σ_I = 0.0 m/s (b) σ_I = 0.158 m/s (c) σ_I = 0.315 m/s.

Figure 6.25 shows the mean nondimensional SEP for turbulent wind kernels. The effect of rapidly changing wind conditions on performance is even more pronounced than in earlier trade studies as vehicle is much more sensitive to turbulence intensity than mean wind speed. The combination of higher mean wind speed near 1.5 m/s and large turbulence intensities near 0.25 m/s appears to be a level where tracking becomes very difficult. Mean AVRMS also shows sensitivity to turbulence intensity though the angular excursions of the vehicle increase as mean wind decreases, Fig. 6.26. This is most likely due to the reversal of wind direction which occurs for turbulent wind flows with a small mean. Figure 6.27 shows the mean AERMS which exhibits behavior similar to both AVRMS and SEP. Like AVRMS, the AERMS is very high for low mean speeds, and attitude tracking performance starts to degrade as well as for high mean wind-large turbulence intensity combinations like SEP.

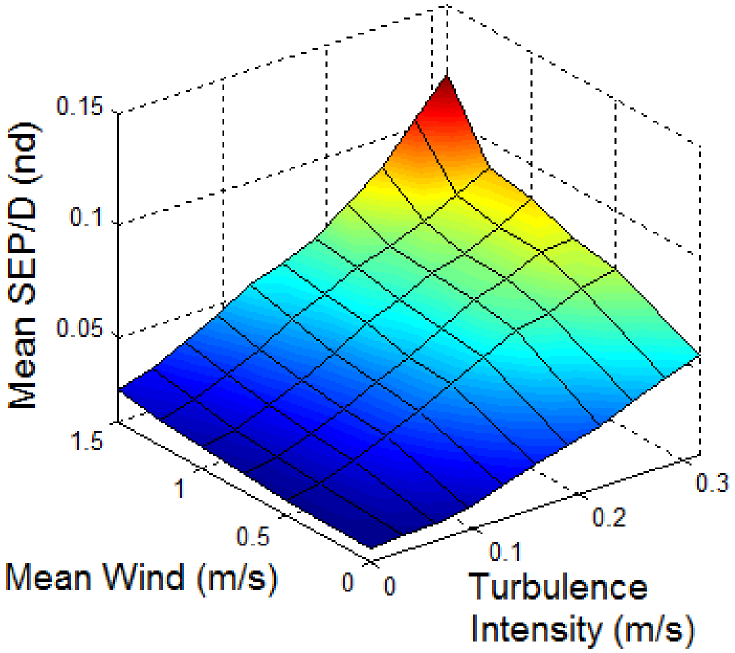

Figure 6.25. Mean nondimensional steady state SEP in turbulent engulfing wind kernel.

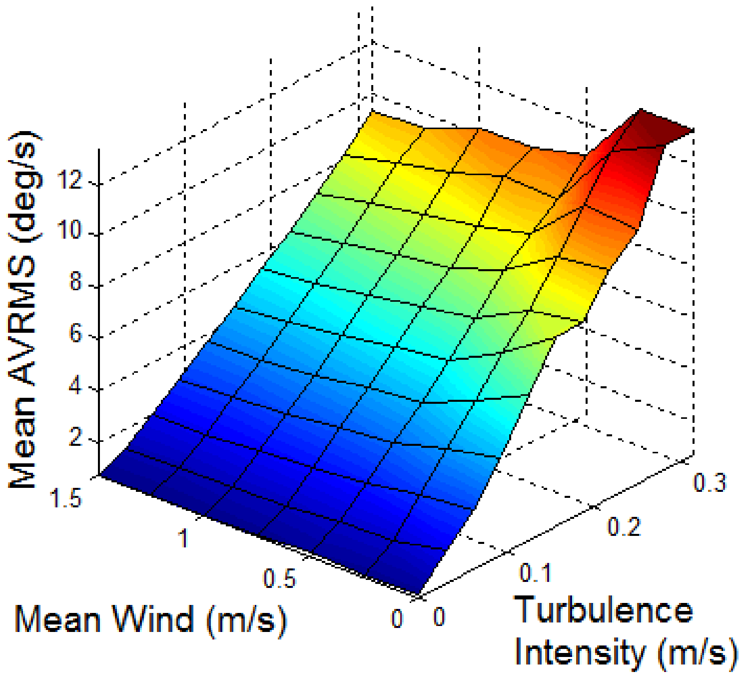

Figure 6.26. Steady state mean AVRMS in turbulent engulfing wind kernel.

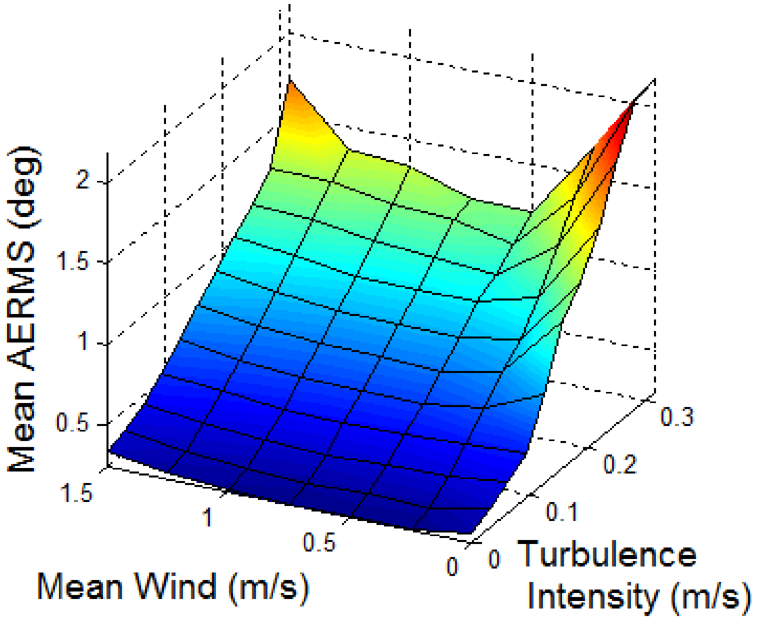

Figure 6.27 Steady state mean AERMS in turbulent engulfing wind kernel.

Figure 6.28 show the average control input standard deviations for turbulent wind kernels. Mean wind speed and turbulence intensity both have a significant effect control effort for throttle, roll, and pitch inputs. Steady energy and power are shown in Figure 6.29, and while mean wind speed has a much greater effect on power required and total energy, increasing turbulence does increase power required and energy consumed. This can also be seen for purely horizontal winds, the drop in power and energy for increasing wind mean as a much larger effect, but increasing turbulence does increase power required and total energy, Fig. 30.

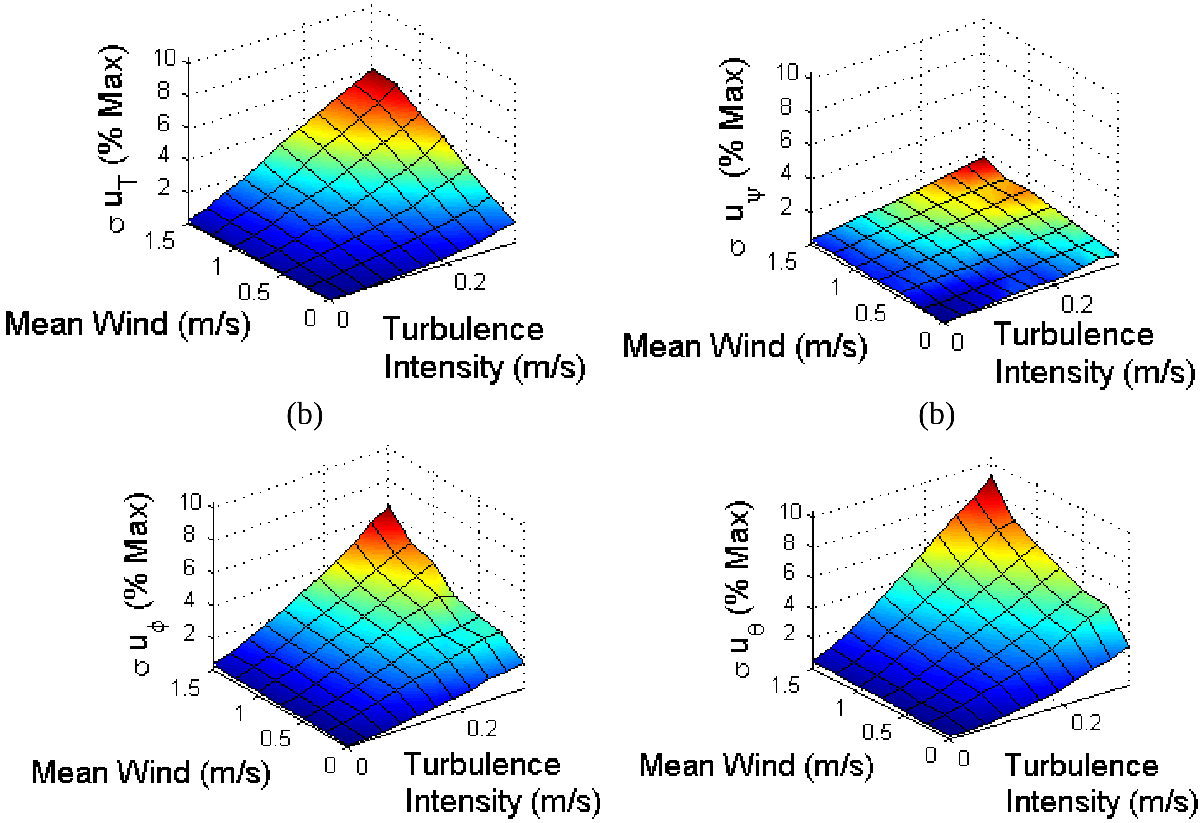

(b) (b)

(c) (d)

Figure 6.28 Steady state mean control standard deviations for a turbulent engulfing wind kernel. (a) throttle (b) yaw heading (c) roll (d) pitch.

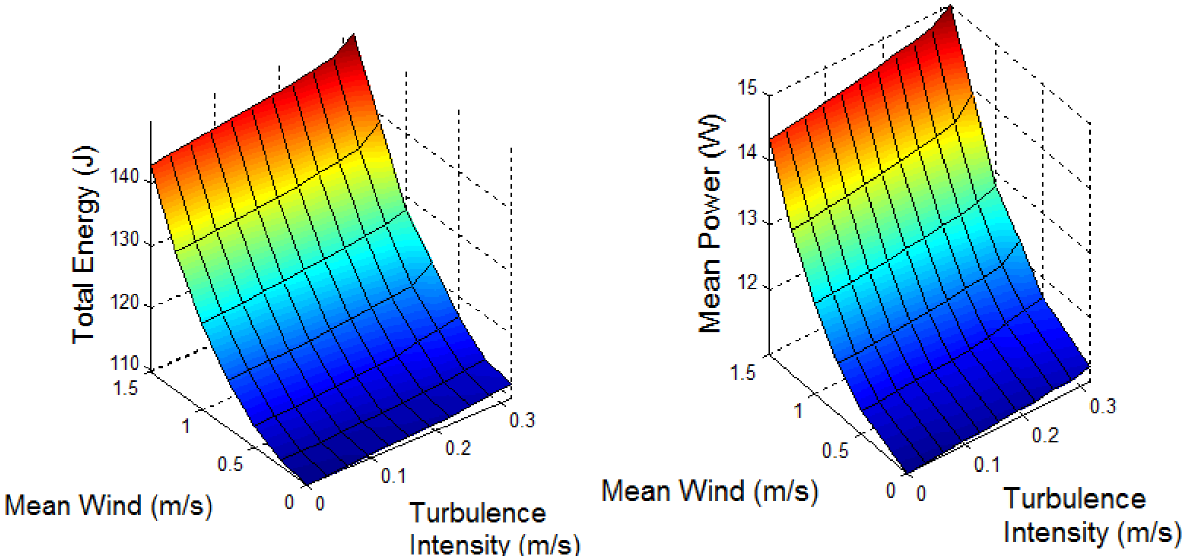

(a) (b)

Figure 6.29. Steady state mean transient energy and power for turbulent engulfing wind simulations. (a) Total energy (b) Power.

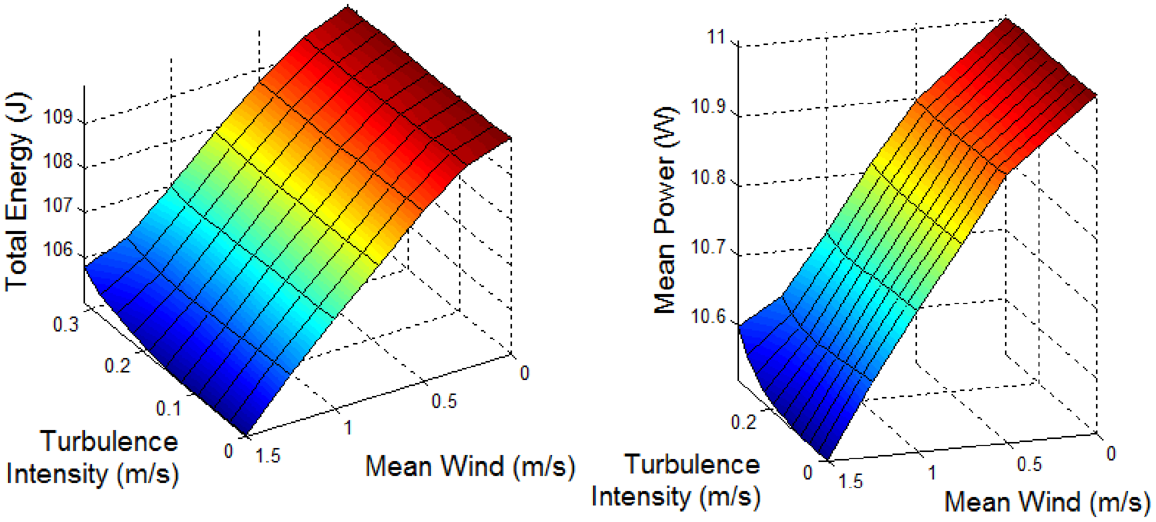

(a) (b)

Figure 6.30. Steady state mean transient energy and power for horizontal turbulent engulfing wind simulations. (a) Total energy (b) Power.

Measurements take outdoors by Oikawa and Meng [84] and Rotach [59] as well as in wind tunnel experiments by Ricciardelli and Polimeno [85] and Peterka, Meroney, and Kothari [86] report nondimensional turbulence intensities between 0.1 and 0.4 for urban environments. Even though mean wind speeds are highly depend on local environment conditions, turbulence intensities in this range would result in dimensional variations as high as 1.0 m/s in urban flows. Clearly for safe operate in urban environments micro rotorcraft platforms and control laws must be robust to highly turbulent disturbances.

6.2 Simulation Model Fidelity in Urban Gusts

During design and development of new micro rotorcraft, modeling and simulation will be a key part of the engineering process. Flow fields in urban environment are very complex and can vary over the rotor blade which creates large aerodynamic moments and high frequency inputs to the vehicle airframe. It is important for models to accurately simulate response to wind disturbances to be effective tools. This trade study investigates the model fidelity necessary to capture vehicle response to different spatially varying wind kernels. Model fidelity is varied by changing how wind is modeled in the rotor system. Models simulated are:

- Fuselage drag only—wind is “turned off” in the rotor system and only generates fuselage aerodynamic drag on the airframe.
- Constant over rotor—the wind components at the rotor hub are applied to all blade elements in the rotor system.
- Linear interpolation—a two-dimensional linear interpolation is used to calculate the wind components for the blade elements. The interpolation is based on the distance from rotor hub and azimuth angle, and the wind components at the rotor hub and the rotor tips at azimuth angles 0, 90, 180, and 270 degrees are used to interpolate.
- Blade element—the local wind components at each lade element center are calculated.

The rotor models are simulated in kernels for spatially varying winds: linear, sinusoidal longitudinal turbulence spectra, and vertical turbulence spectra. As with the trade studies reported in section 6.1, Monte Carlo simulations are performed varying initial states, model error, and measurement error.

The linear wind disturbance is prescribed as

$$v_{atx} = v_{mean} + 0.5\Delta_{wind} y \hat{J}_I \tag{6.1}$$

where y is the inertial position component of the blade element in the J_I direction and Δ_{wind} is the linear variation of the wind over the rotor disk. Response is simulated in horizontal and vertical linear winds, Fig. 6.31, for a mean wind speed of 1.0 m/s and increasing linear variations from 0.0 m/s to 2.0 m/s.

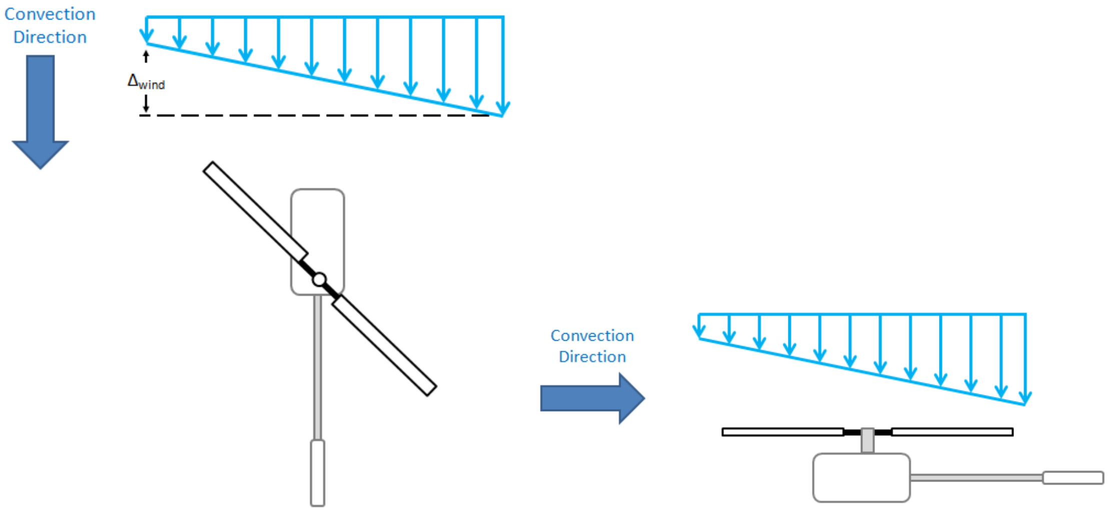

(a) (b)

Figure 6.31. Illustration of the linear wind kernel. (a) horizontal (b) vertical.

Figures 6.32 through 6.34 show the nondimensional SEP, AVRMS, and AERMS for each model in linear winds of increasing Δ_{wind}. Linear variation over the rotor disk results in increasing variation between the models in all metrics. The linear interpolation model results are close to those for the blade element model but do not match exactly since only four azimuth points are used for interpolation, Fig. 6.35.

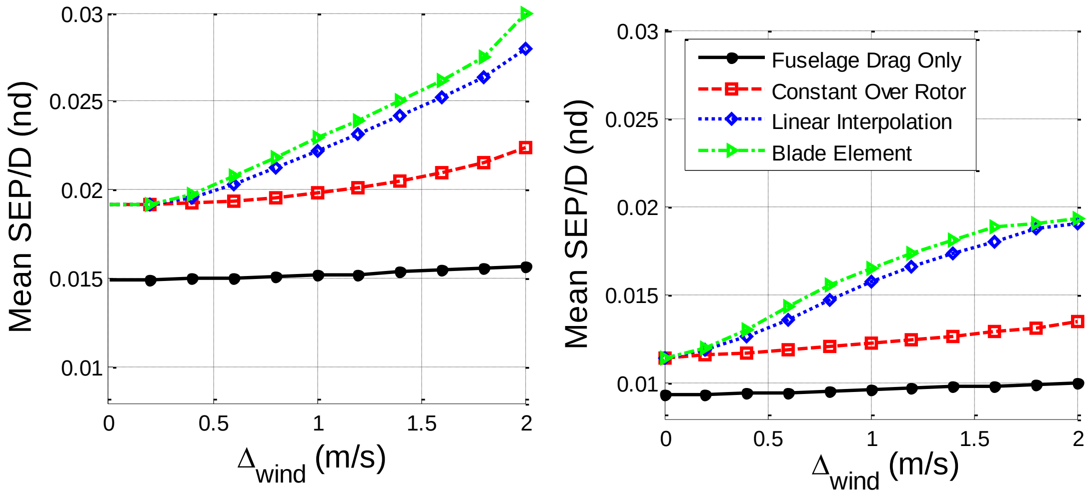

(a) (b)

Figure 6.32. Comparison of model mean nondimensional SEP for linear wind kernels. (a) Transient (b) Steady state.

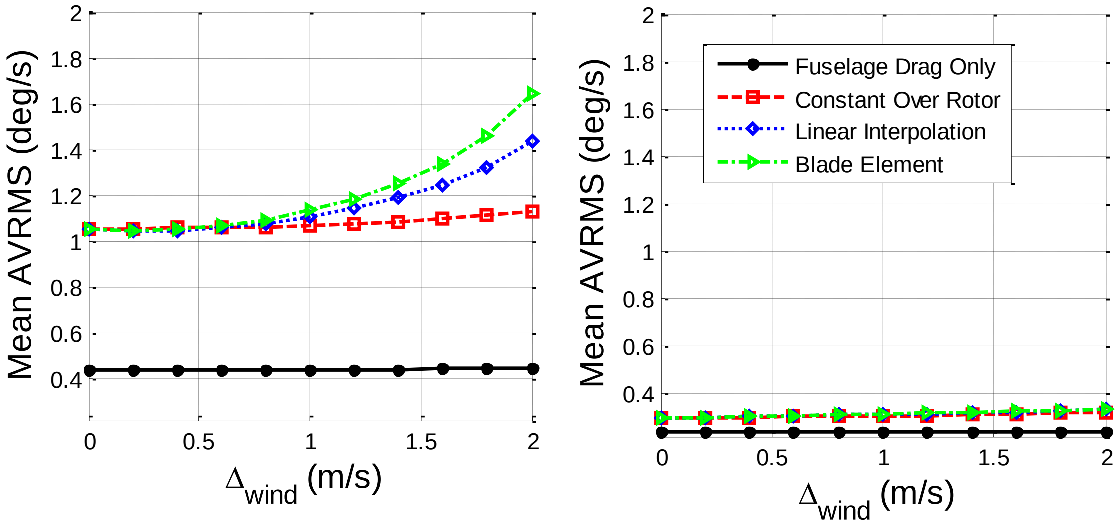

(a) (b)

Figure 6.33. Comparison of model mean AVRMS for linear wind kernels. (a) Transient (b) Steady state.

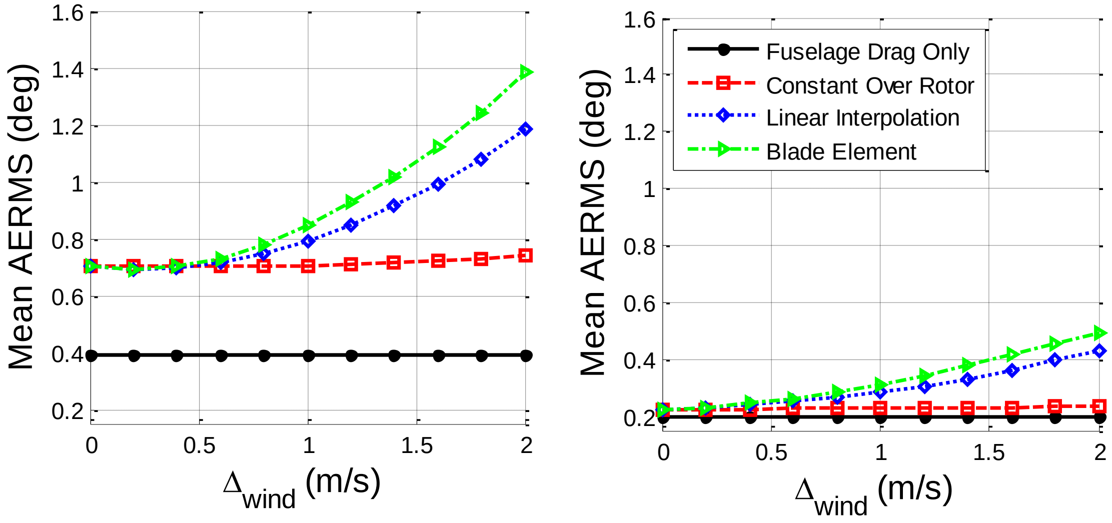

(a) (b)

Figure 6.34. Comparison of model mean AERMS for linear wind kernels. (a) Transient (b) Steady state.

Clearly, if the expected wind fields contain spatial variation large enough (on the order of 0.5 m/s over the rotor disk) a higher fidelity model using blade elements or an interpolation with many azimuthal points is required; however for fields with less severe variation, a faster low fidelity model will produce adequate response.

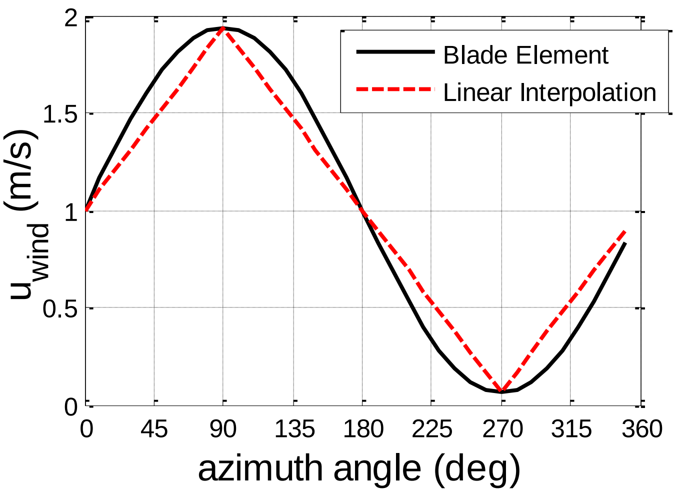

Figure 6.35. Linear wind component at the blade tip for the blade element model (solid) and the linear interpolation model (dashed).

The sinusoidal wind kernel is employed to simulate a disturbance which spatially varies multiple cycles over the rotor disk. As with the linear wind kernel, spatial variation is based on inertial y position and both horizontal and vertical winds are modeled, Fig. 6.36. The amplitude of the sinusioindal wind is 0.5 m/s and the frequencies are chosen so the wind disturbance varies between 2 and 10 cycles over the rotor disk

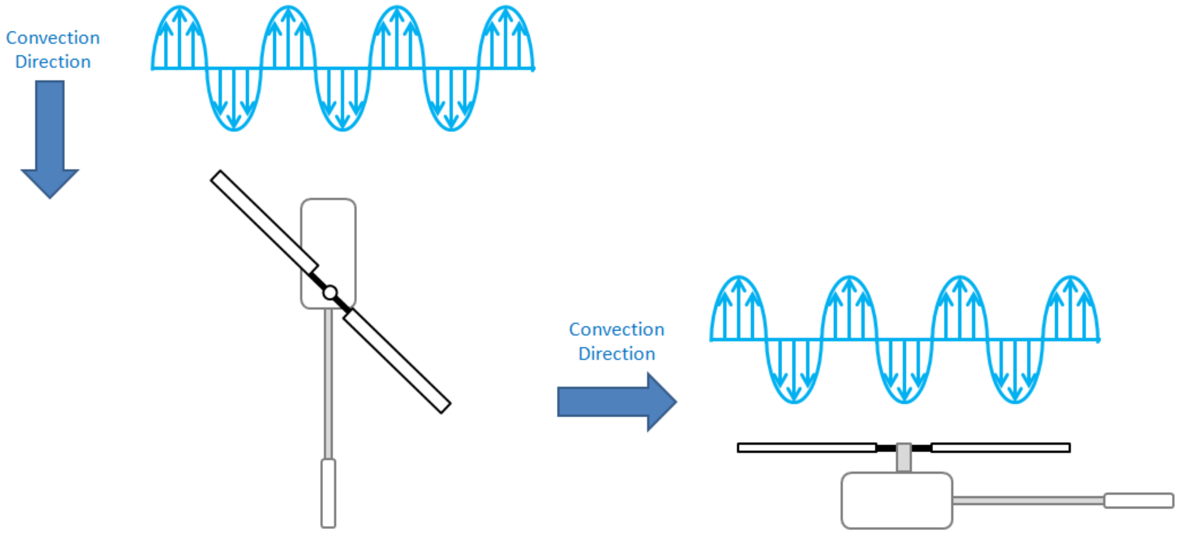

(a) (b)

Figure 6.36. Illustration of sinusoidal wind kernel used in model fidelity trade studies. (a) horizontal (b) vertical.

Figuress 6.37 through 3.39 show nondimensional SEP, AVRMS, and AERMS metrics for all models in the sinusoidal wind kernel. Though there are differences for different cycles, the trends aren’t as clear cut as for linear variation. This may be use to the rigid rotor and first-order flapping assumptions of the rotor system module. If urban wind frequencies were expected to be very high, a flexible rotor model will be required to capture the high frequencies effects.

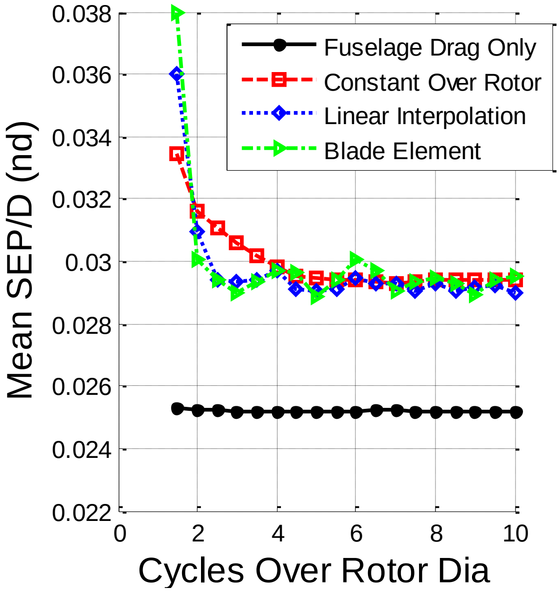

Figure 6.37. Comparison of model mean SEP for sinusiodal wind kernels.

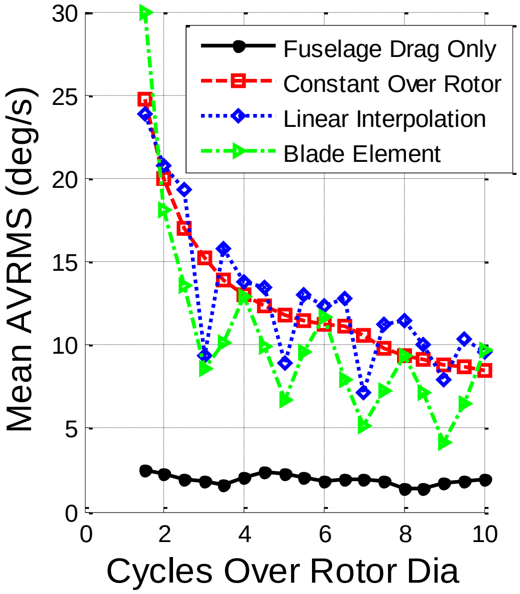

Figure 6.38. Comparison of model mean AVRMS for sinusiodal wind kernels.

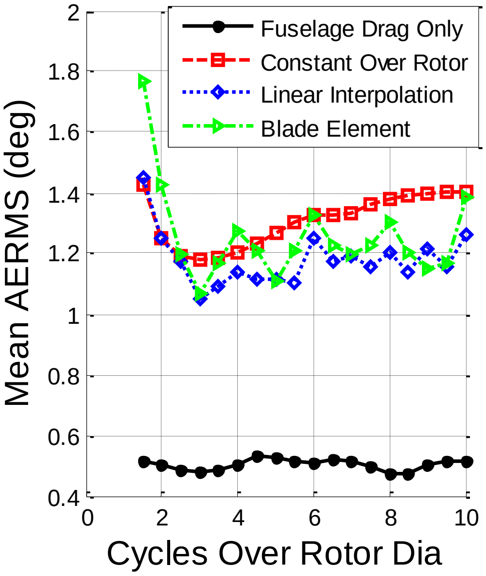

Figure 6.39. Comparison of model mean AERMS for sinusiodal wind kernels.

Experimental measurements of urban turbulence spectra such as the work of Rotach [59], Geurts, Rutten and Wisse [87], and Oikawa and Meng [84] report significant content for nondimensional frequencies between 10^{-2} and 10, Fig. 6.40.

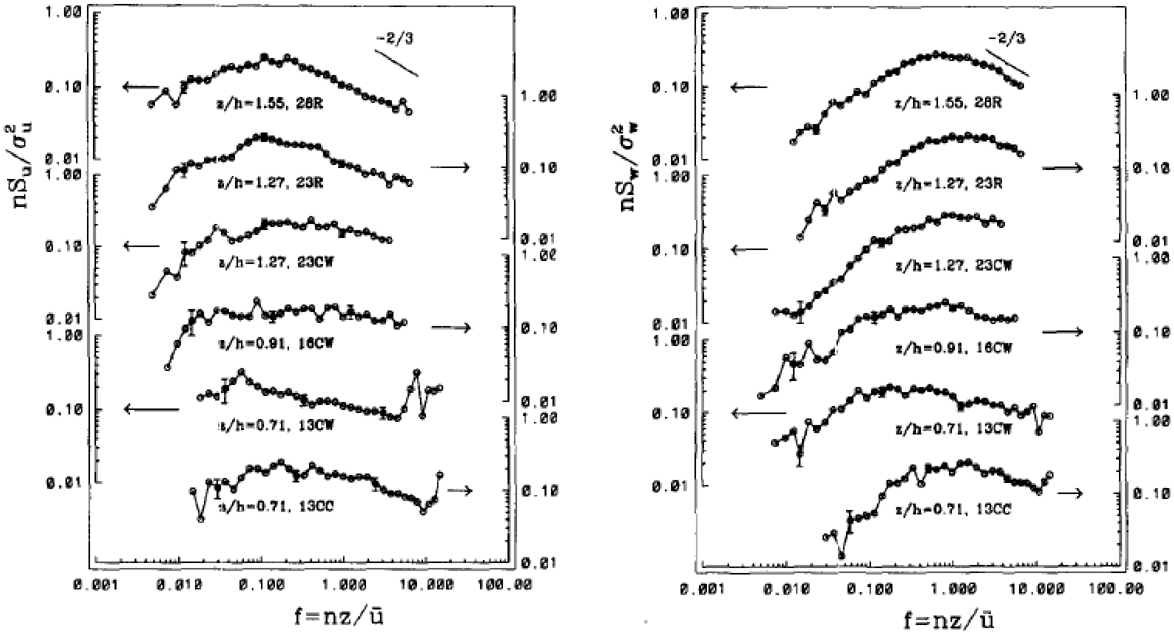

(a) (b)

Figure 6.40. Composite spectra of velocity at non-dimensional height from Rotach [59]. (a) longitudinal (b) vertical.

Using approximate shapes of the spectra in Figure 6.40, a one dimensional digital simulation of the turbulence is created employing the methodology described in chapter 2 summing cosines and integrating the spectra curve.

$$f(t) = \sqrt{2}\sum_{k=1}^{N}[S_0(\omega_k)\Delta\omega]^{1/2}\cos(\omega_k' t + \phi_k) \quad (6.3)$$

Where $\delta\omega$ is a small random frequency introduced to avoid the periodicity of the simulated process and ϕ_k independent random phase uniformity distributed between 0 and 2π. Table 6.6 shows the wind parameters selected to dimensionalize the spectra curves, which were chosen to represent a disturbance close to the ground in an urban canyon. The turbulent wind generated from the spectra is added to the mean wind speed to create the complete urban wind disturbance, Fig. 6.41.

Table 6.6. Wind parameter values to dimensionalize spectra curves.

Parameter	Value
$\sigma_{u/w}$ (m/s)	0.0 to 0.3333
z (m)	4.5
$\bar{u}$ (m/s)	1.0

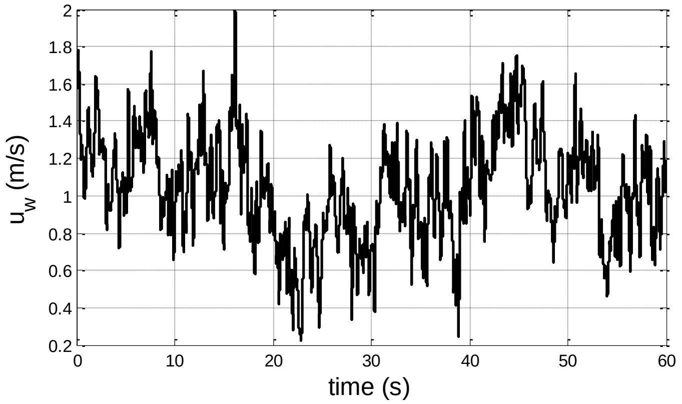

Figure 6.41. Time history of simulated longitudinal wind based on experimental spectra.

Figures 6.42 through 6.4 show the SEP, AVRMS, and AERMS of each model in longitudinal turbulence spectra winds for increasing turbulence intensity, where all three metrics start to see differences in blade element, linear interpolation, and constant over rotor models after turbulence intensities of 0.2 m/s.

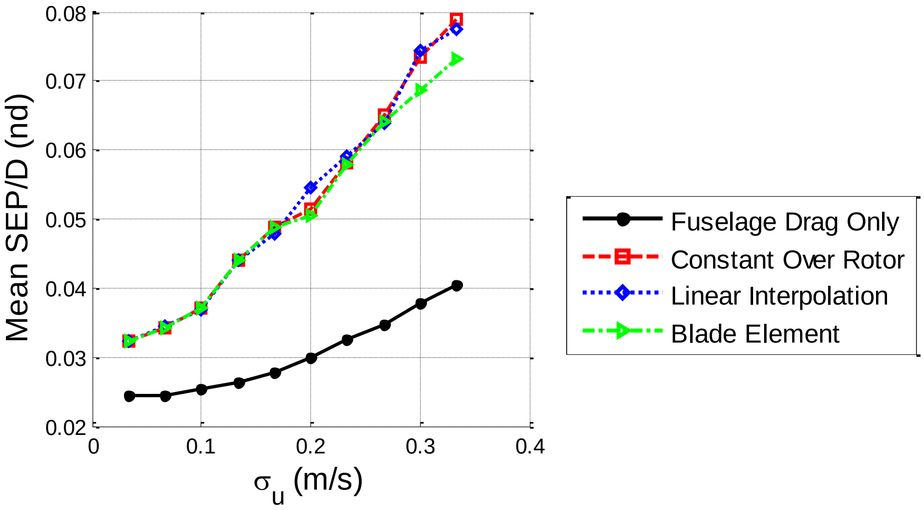

Figure 6.42. Comparison of model mean SEP for longitudinal wind spectra.

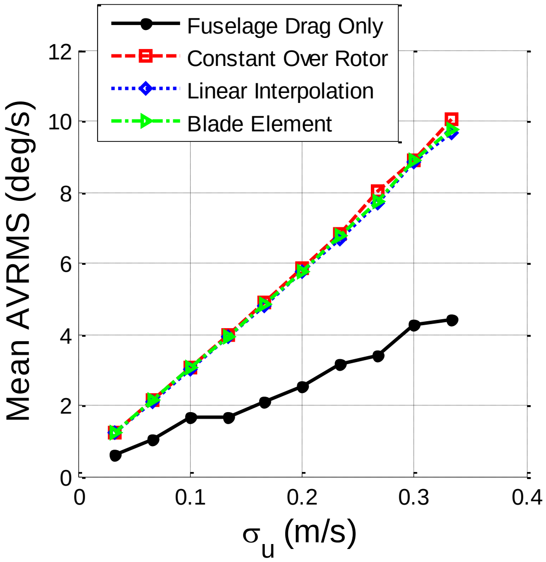

Figure 6.43. Comparison of model mean AVRMS for longitudinal wind spectra.

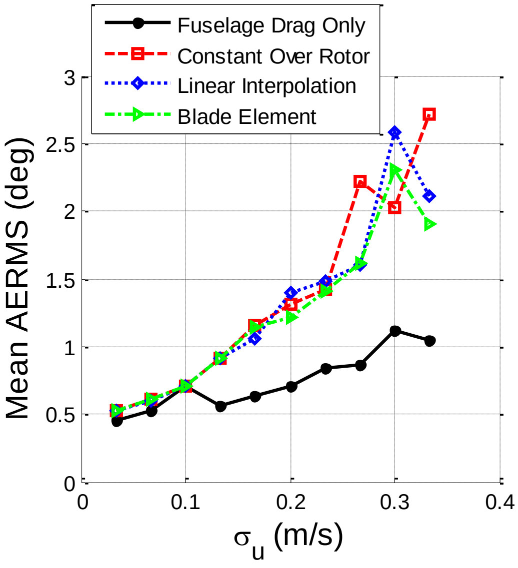

Figure 6.44. Comparison of model mean AERMS for longitudinal wind spectra.

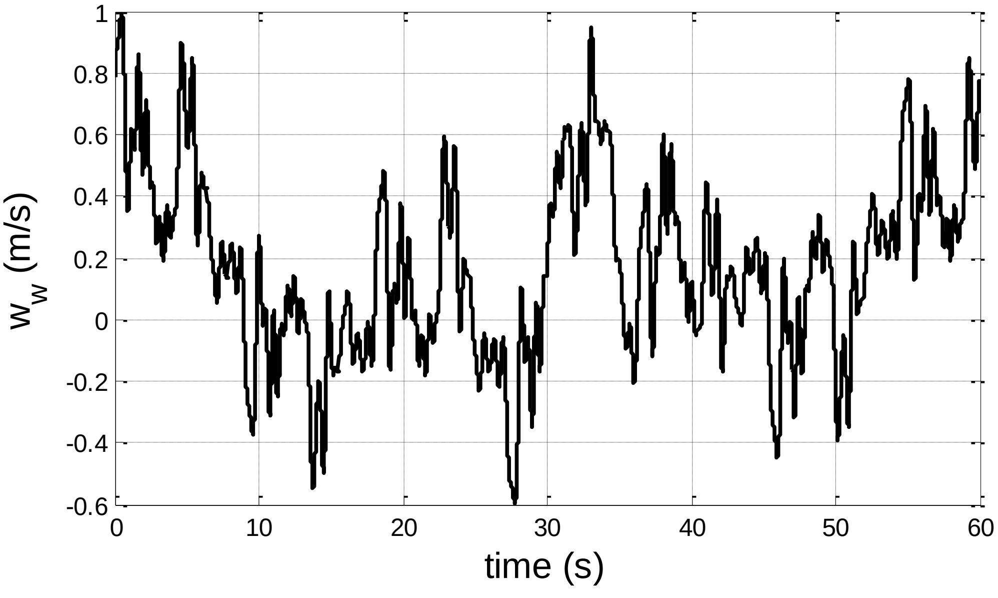

Figure 6.45. Time history of simulated vertical wind based on experimental spectra.

A vertical turbulent wind based on the experimentally measured urban spectra is also simulated, Fig. 6.45. The spectra is dimensionalized using the parameters in Table 6.6 and convects horizontally with a velocity $\bar{u}$. Figures 6.46 through 6.48 show the SEP, AVRMS, and AERMS of each model in vertical turbulence winds for increasing turbulence intensity. The differences between the simulated models become noticeable for even lower turbulence intensities than the longitudinal spectra, particularly for AVRMS and AERMS which show differences for all wind kernels. This may be due to the larger effect vertical air flows have on blade angle of attack; whereas horizontal disturbances are added to the flow velocity due to rotor angular rotation. As reported in section 6.1, expect nondimensional turbulence intensities ranging from 0 to 0.4 thus it is reasonable to expect large intensities that will be required to be captured with blade element models.

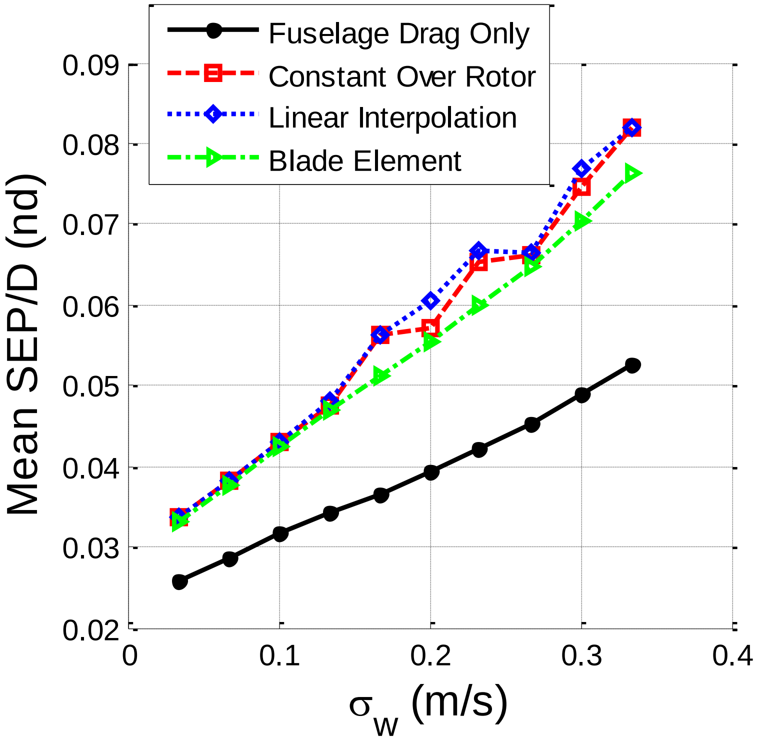

Figure 6.46. Comparison of model mean SEP for vertical wind spectra.

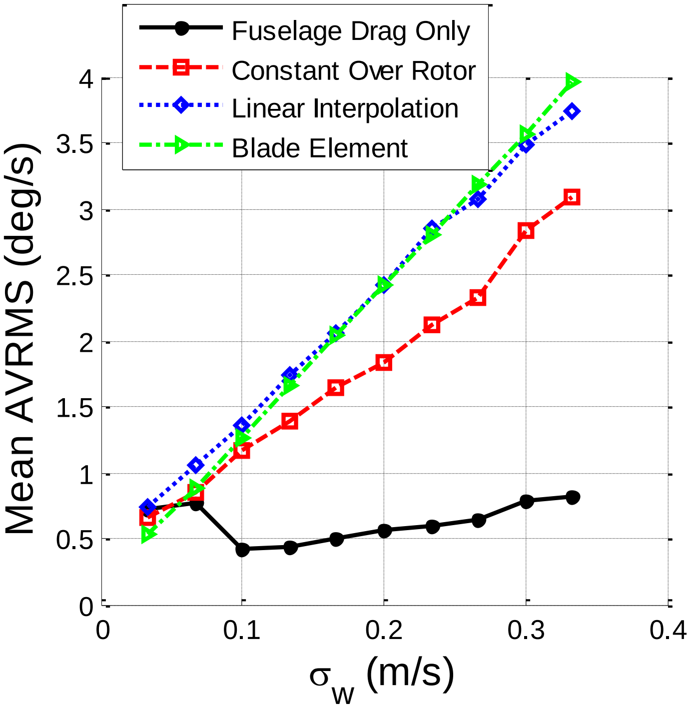

Figure 6.47. Comparison of model mean AVRMS for vertical wind spectra.

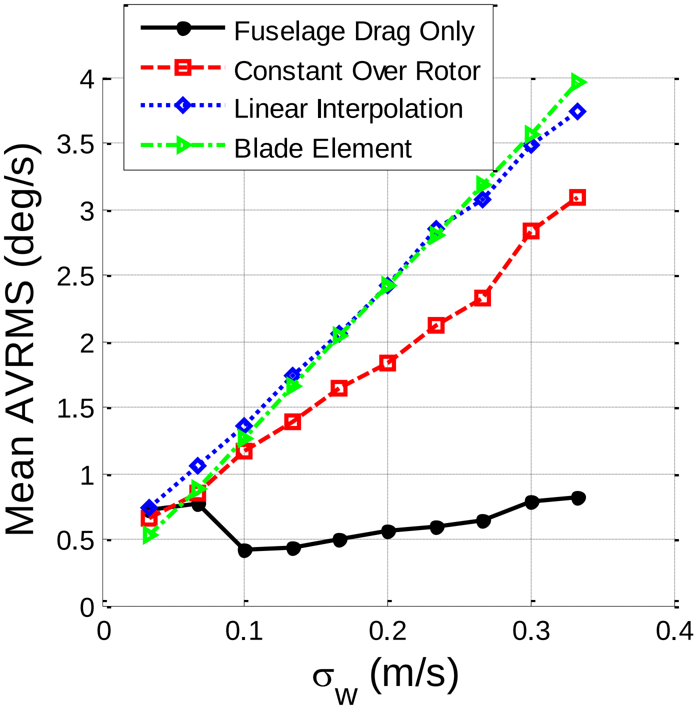

Figure 6.48. Comparison of model mean AERMS for vertical wind spectra.

6.3 Gust Rejection Controller Trade Studies

Two trade studies are performed to investigate different aspects of the GRC and the associated effects on vehicle performance in urban environments. First, a study is performed to assess the importance of the ESO and the wind estimation algorithm to controller capabilities. Second, a study is performed to understand the robustness of the controller to varying tracking controller gains. This is achieved by scaling all the control gains by ±10% of the nominal values. Both trade studies are performed in the same manner as earlier simulations, varying initial conditions and model error while including measurement noise and running cases over a variety of wind kernels.

Wind Estimation in Controller Architecture

While the GRC architecture has been developed using previously established literature and logical choices, it is still useful to study how the controller performs compared to similar alternatives. However it is difficult to create an “apples to apples” comparison of different control techniques. Campbell, Kaneshige, Nguyen, Krishnakumar proposed a tuning and test methodology to evaluate seven different model reference adaptive control (MRAC) based adaptive control technologies [88, 89]. Since most MRAC based adaptive controls technologies are comprised of modifications to adaptive algorithms for model parameter estimation, the same baseline dynamic inversion controller was employed with each MRAC technology augmenting it. Tuning metrics based on transient and steady state performance along with design requirements such as robustness to time delay and having constant gains (no gain scheduling) were developed to coarsely tune the free design parameters of each technology to improve control performance with respect to the baseline controller. Therefore different MRAC adaptive control technologies could be evaluated in simulation on common ground.

A similar approach is employed here to evaluate the importance of the ESO and wind estimation in the GRC. Using the dynamic inversion controller as a baseline, two control architectures are developed. The GRC includes an ESO for uncertainty and disturbance estimation, and the other has a basic integral gain to compensate for steady state errors. By keeping the same baseline architecture and switching the ESO with an integral gain, a common architecture is maintained allowing evaluation and comparison of the two controllers. The integral gain is tuned to provide good transient and steady state tracking performance while preserving vehicle stability. The integral only controller is tested in engulfing and sinusoidal wind kernels to assess performance, and Monte Carlo simulations randomize case initial states, model error, and measurement noise.

Figure 6.49 shows the mean nondimensional SEP for GRC and integral only controllers in engulfing wind kernels. It is clear that increasing mean wind speeds drastically degrade the performance of the integral only controller. It can be seen from Figure 6.50 that the integral controller takes much longer to build up enough feedback to reject the wind disturbance. While tuning the integral controller, there was a tradeoff between quicker response and stability which is much less of an issue for the GRC.

Figure 6.51 shows the mean SEP for sinusoidal wind kernels. The integral only controller has a much higher peak response near 0.1 Hz, but actually performs slightly better than the GRC for frequencies near 0.5 Hz. This response is the result of the integral gain controller being too slow to react and the quickly changing wind having little effect on vehicle position, Fig. 6.52. The trade study shows that overall estimating local wind components drastically improves disturbance rejection capabilities, but care must be taken to tune gains so frequency inputs don’t excite peak response.

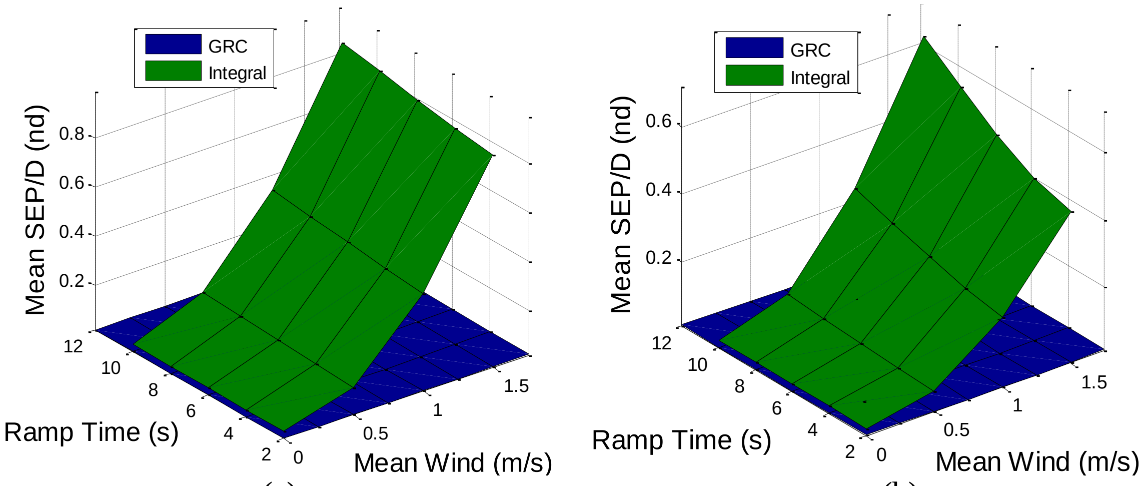

(a) (b)

Figure 6.49. Comparison of mean nondimensional SEP for GRC architecture and controller with integral gains only in an engulfing wind kernel. (a) Transient (b) Steady state.

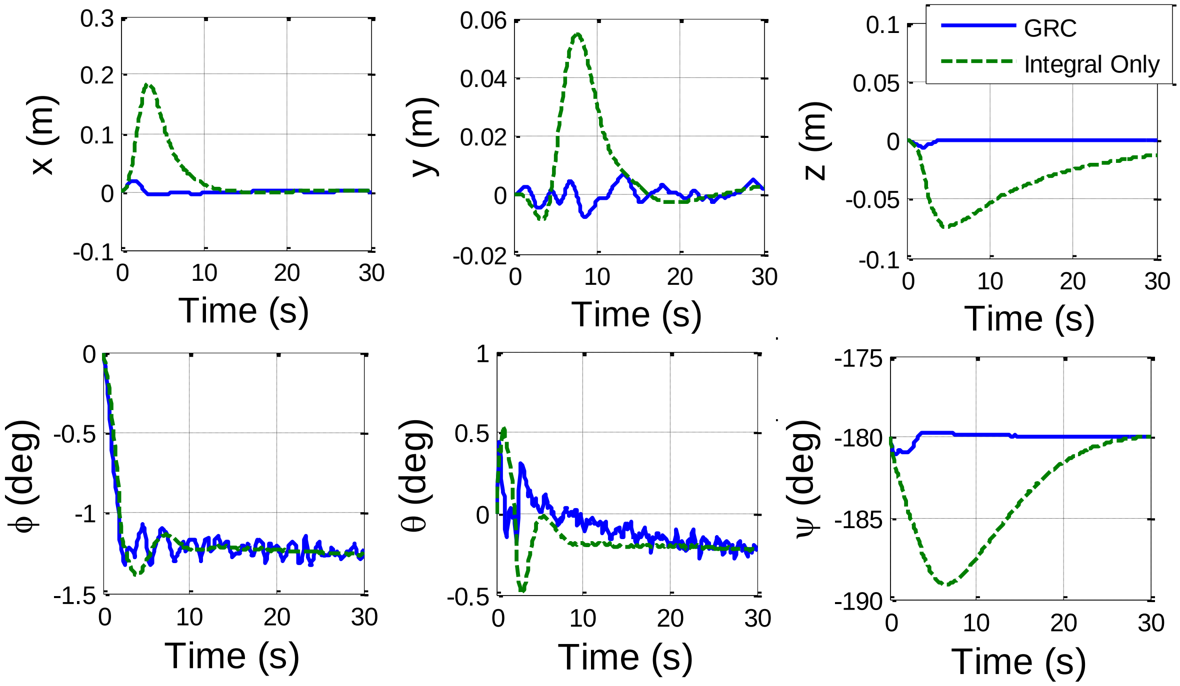

Figure 6.50. Example time histories comparing GRC architecture and controller with integral gains only in an engulfing wind kernel.

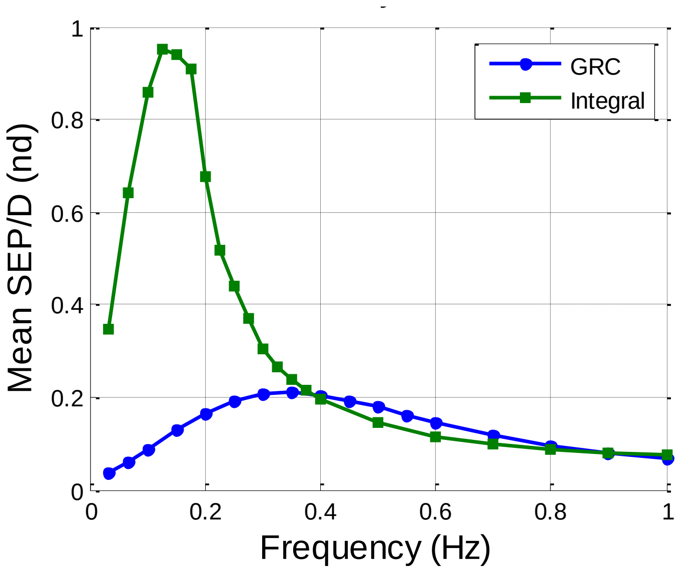

Figure 6.51. Comparison of mean nondimensional SEP for GRC architecture and controller with integral gains only in a sinusoidal wind kernel with 0.5 m/s amplitude.

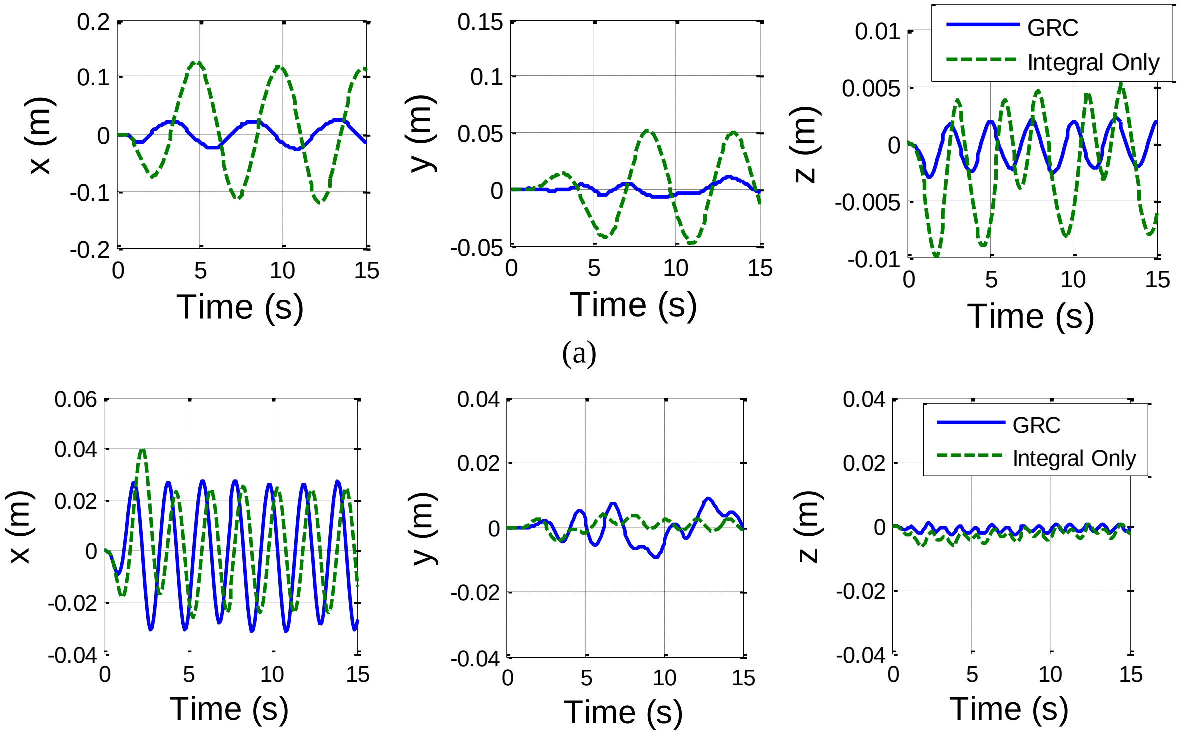

(a)

(b)

Figure 6.52. Example time histories comparing GRC architecture and controller with integral gains only in sinusoidal wind kernels. (a) 0.2 Hz (b) 0.5 Hz

Tracking Controller Gains

The tracking controller gains feedback linearize the system to cancel the vehicle's nonlinear dynamics and enforce chosen error dynamics. In order the assess the robustness of the controller and investigate the affect of controller gains on the platform's sensitivity to low frequency winds, the feedback gains are varied ±10% from the nominal values in sinusoidal wind kernels of increasing frequency. The amplitude of the sinusoidal wind kernels was kept constant at 0.5 m/s.

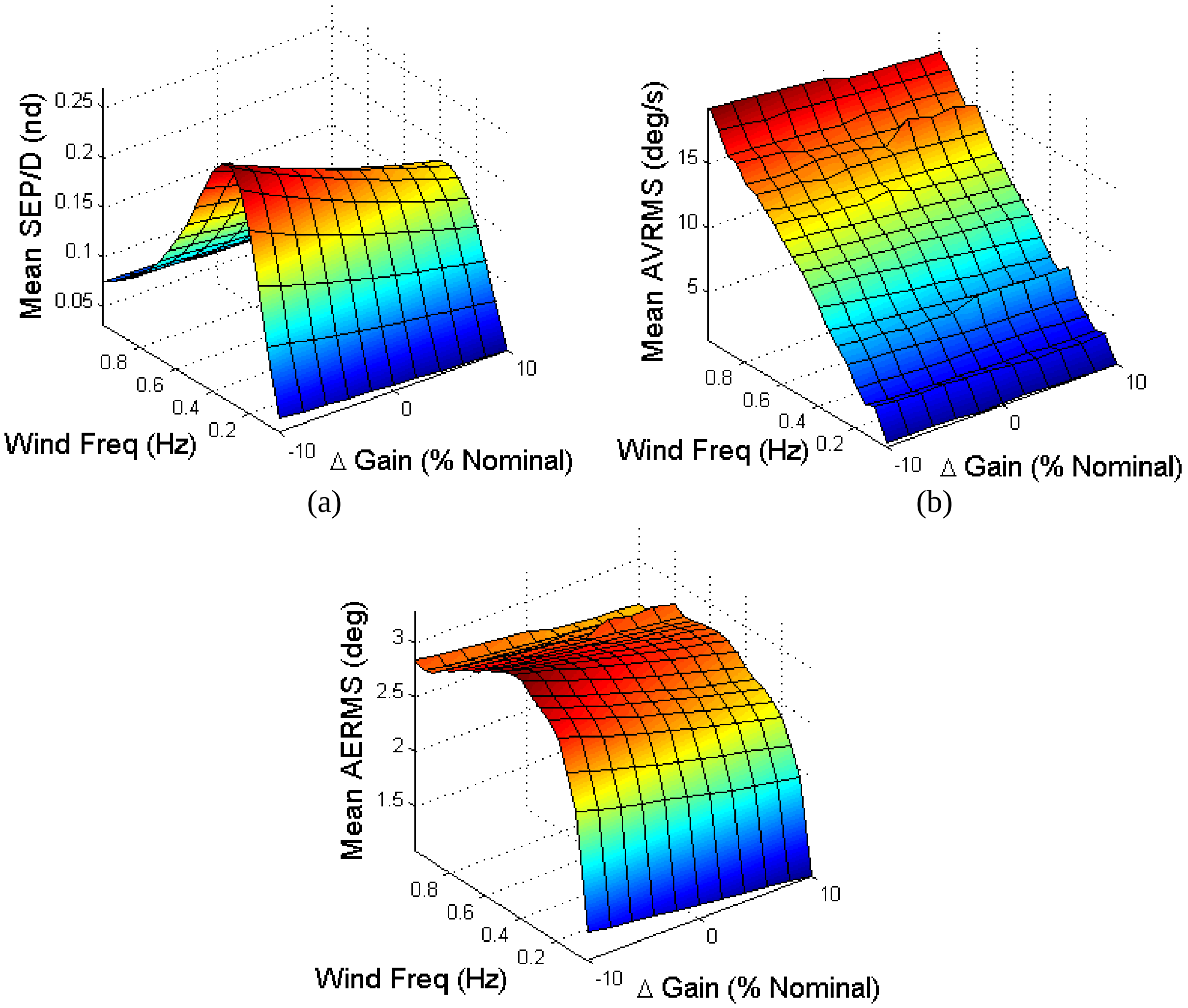

(a) (b)

(c)

Figure 6.53. Mean steady state performance metrics for controller gain study. (a) nondimensional SEP (b) AVRMS (c) AERMS.

Figure 6.53 shows the mean SEP, AVRMS, and AERMS for changing controller gains and wind kernel frequency. All three metrics show similar trends as the nominal gains: the SEP shows a peak response on 0.35 Hz, the AVRMS increases with increasing frequency, and the AERMS shows almost constant attitude error for frequencies larger than 0.2 Hz. Performance does slightly improve the higher gains for SEP and AERMS but not significantly.

After the results of controller gain trade study showed the chosen gains were not responsible for low frequency sensitivity, it is logical to analyze the dynamics of closed loop system. This is accomplished two ways. First, the impulse response of the vehicles is investigated by simulating the time history off the vehicle from an initial non-trim attitude, and second, the transfer functions of the feedback linearized system are examined. Figure 6.54 shows the impulse response of the micro coaxial helicopter to an initial non-trim attitude.

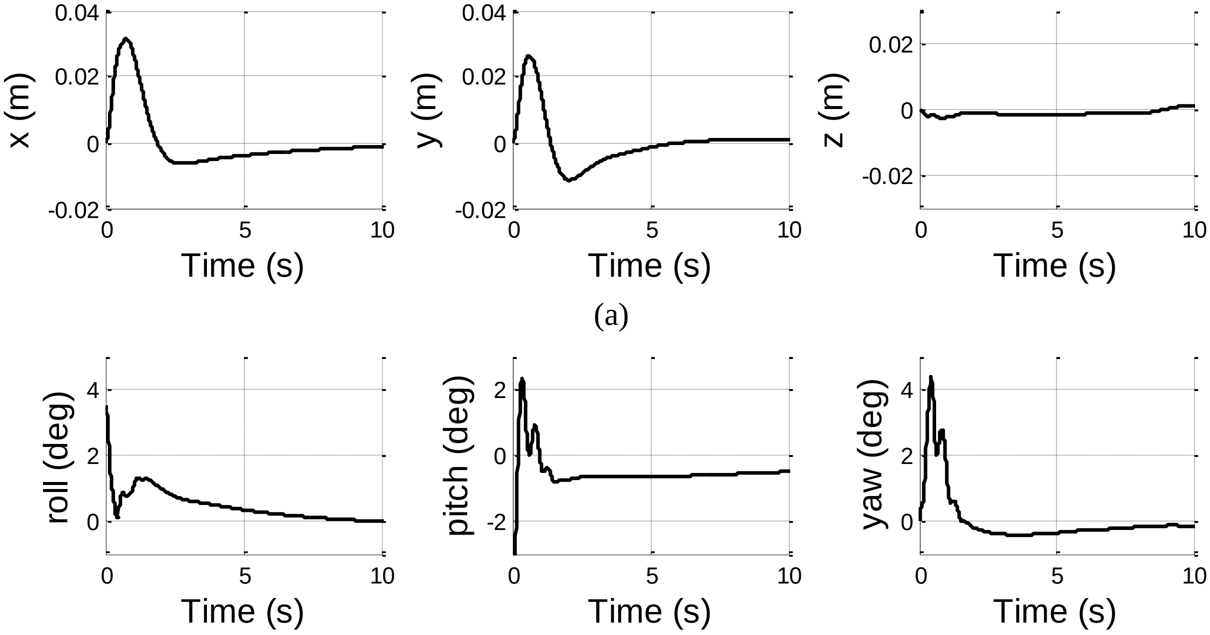

(a)

(b)

Figure 6.54. Time history of vehicle impulse response. (a) positional states (b) attitude states.

The time histories of the position states show very little oscillation with neither the x-position nor y-position exhibiting any motion at 0.2-0.4 Hz.

Therefore to more clearly investigate frequency response, the transfer functions of the feedback linearized system can also be calculated. Since the micro rotorcraft exhibits a peak response to low frequency winds even for low amplitude disturbances of 0.25 m/ s and 0.5 m/s, the system can be considered near hover where the dynamic inversion can cancel system response to achieve the desired accelerations as show in Eqns. 5.21-5.24. Johnson and Kannan proposed a method for selecting inner loop-outer loop gains for a helicopter by treating the outer loop as a point mass model [90]. Therefore the combined x-position and pitch transfer function can be expressed as

$$\frac{x(s)}{x^c(s)} = \frac{K_{p_\theta} s^2 + K_{p_\theta} R_{d_x} s + K_{p_\theta} R_{p_x}}{s^4 + K_{d_\theta} s^3 + K_{p_\theta} s^2 + K_{p_\theta} R_{d_x} s + K_{p_\theta} R_{p_x}} \tag{6.4}$$

with the y-position and roll transfer function taking the same form. The z-position and yaw heading transfer functions are not combined functions and can be expressed as

$$\frac{z(s)}{z^C(s)} = \frac{R_{p_z}}{s^2 + R_{d_z} s + R_{p_z}} \tag{6.5}$$

$$\frac{\psi(s)}{\psi^C(s)} = \frac{K_{p_\psi}}{s^2 + K_{d_\psi} s + K_{p_\psi}} \tag{6.6}$$

Figure 6.55 shows the bode plots for the x, z, and yaw transfer functions for the nominal controller gains—the y bode plot matches the x. The x transfer function shows an amplification of the input with a peak at 0.7 Hz. While there is a small amplification for low frequencies near 0.35 Hz, the sinusoidal wind kernel trade study does not show similar amplification as there is no peak response for 0.7 Hz frequency winds. Overall the investigate of tracking controller gains on vehicle performance—through the gain trade study, impulse response, and closed loop transfer functions—show while the selected gains may slightly contribute the sensitivity to low frequency wind inputs, they are not the main source the issue.

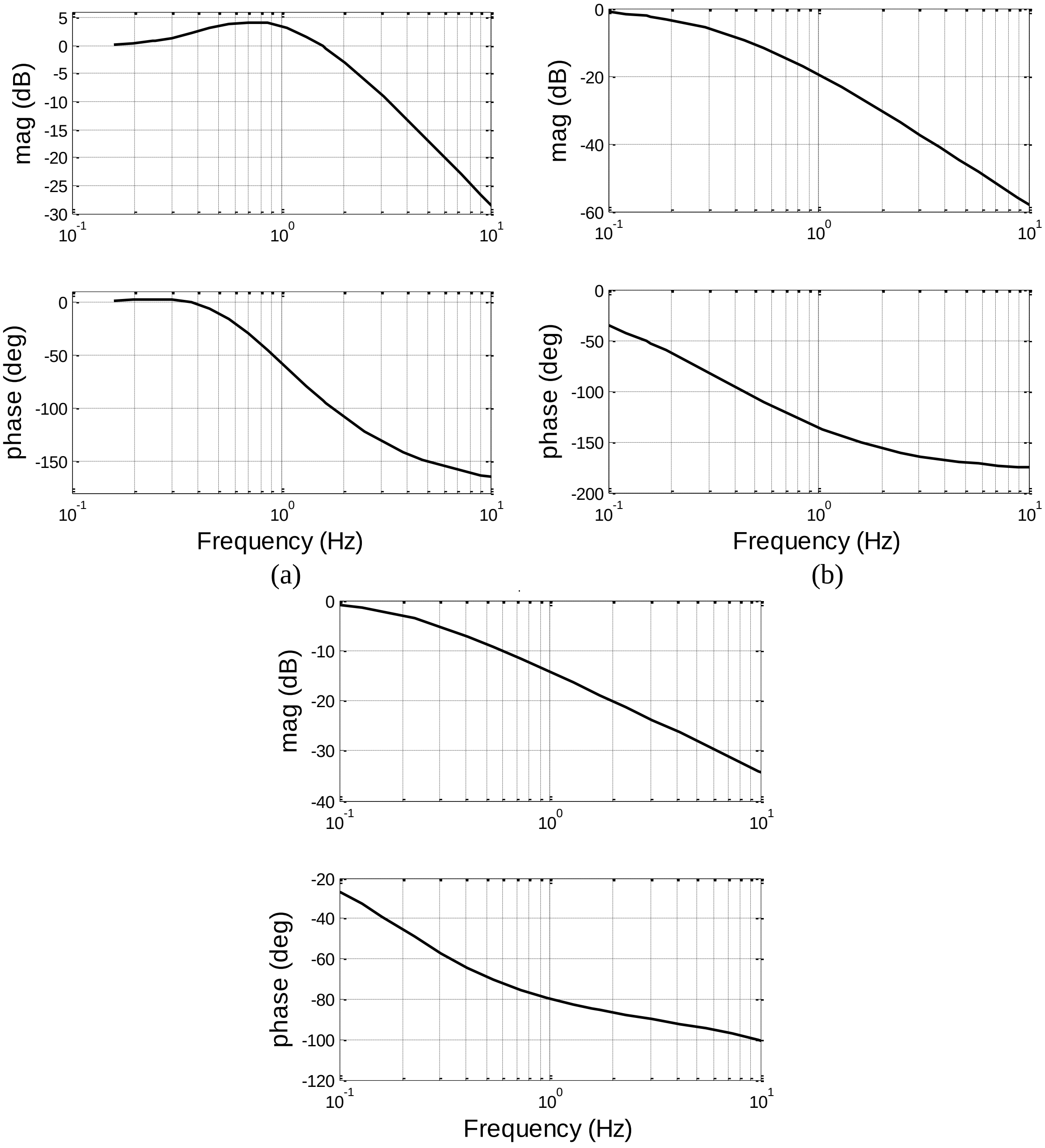

(a) (b)

(c)

Figure 6.55. Transfer functions for the feedback linearized system. (a) x/x_c (b) z/z_c (c) ψ/ψ_c.

6.4 Vehicle Design Parameters and Gusts

The goal of this set of trade studies is to identify key platform design trends that are important for gust rejection. Design trends can be useful for defining requirements of new micro rotorcraft, analyzing tradeoffs, and estimating platform gust rejection capabilities. Parameters investigated include actuator dynamics, swashplate control margin and maximum flight speed limitations, and rotor response. The trade studies follow the same form as all previous studies. Platform design parameters are varied one dimensionally and vehicle response is simulated in a few prototypical winds. Monte Carlo simulations vary initial conditions, model error, and measurement noise to capture the overall impact of each design parameter.

Actuator Response Time

Rotorcraft actuators—brushless motors that drive the rotors and servo motors that tilt the swashplate—will always have some dynamics and response time associated with their motion. While its better for control law design if new actuators have smaller response times, it is useful to understand how performance trends with actuator time constants and the minimum actuator response times required to operate in urban wind gusts. As described the Chapter 3, the actuators are modeled as first order systems:

$$\dot{\Omega}_{LR} = \frac{1}{\tau_M} C_{LR} u_{LR} - \Omega_{LR} \tag{6.7}$$

$$\dot{\theta}_{1C} = \frac{1}{\tau_{SW}} C_{lon} u_{lon} - \theta_{1C} \tag{6.8}$$

Motor and swashplate time constants are varied in one dimensional trade studies, and for each parameter the vehicle is simulated in engulfing, turbulent, and sinusoidal wind kernels.

Figure 6.56 shows mean nondimensional SEP as a function of motor time constant for engulfing, turbulent, and sinusoidal wind kernels (Figs 6.56a, 6.56b, and 6.56c respectively). As expected, performance in all winds decreases for increasing motor time constant—except for a sinusoidal wind kernel with a frequency of 1.0 Hz which plateaus for motor time constants over 0.2 seconds, Fig. 6.56c. An upper limit to motor time constant starts to emerge in high wind speed-fast changing wind kernels. Simulation cases for time constants greater than 0.75 seconds go unstable in engulfing winds with a mean wind speed of 1.5 m/s and ramp time of 2 seconds—Fig. 6.56a, due to the tracking error induced by the delay in control actuation driving the controller unstable. However, the system identification of the micro coaxial helicopter described in Chapter 4 estimated motor time constants of 0.1 seconds. For all wind kernels, the improvements below 0.1seconds are very small, and therefore design and engineering efforts may be better served focusing on other areas for improvement.

Figure 6.57 shows platform performance and stability are much more sensitive to swashplate time constant for all wind kernels. The micro helicopter experiences a dramatic decrease in performance for swashplate time constants near 0.25 seconds as seen from simulation cases in engulfing and sinusoidal wind kernels (Figs. 6.57a and 6.57c). With an estimated parameter value of 0.099 seconds, improvements to the swashplate time constant will improve performance more than similar changes in motor time constant however gains are still small

Overall, actuator time constants are shown to be key factors to micro rotorcraft gust rejection, particularly in rapidly changing flow fields. However current motor response characteristics are relatively close to the point of diminishing returns in the wind kernels tested. Trends suggest that more important design parameters may be how quickly a vehicle is able to generate meaningful accelerations in a desired direction. For underactuated micro rotorcraft, the inherit delay in applying horizontal control forces seems more important than the physical control actuators. Therefore, vehicle design parameters which affect the overall response time to tilt the thrust vectors must be considered carefully.

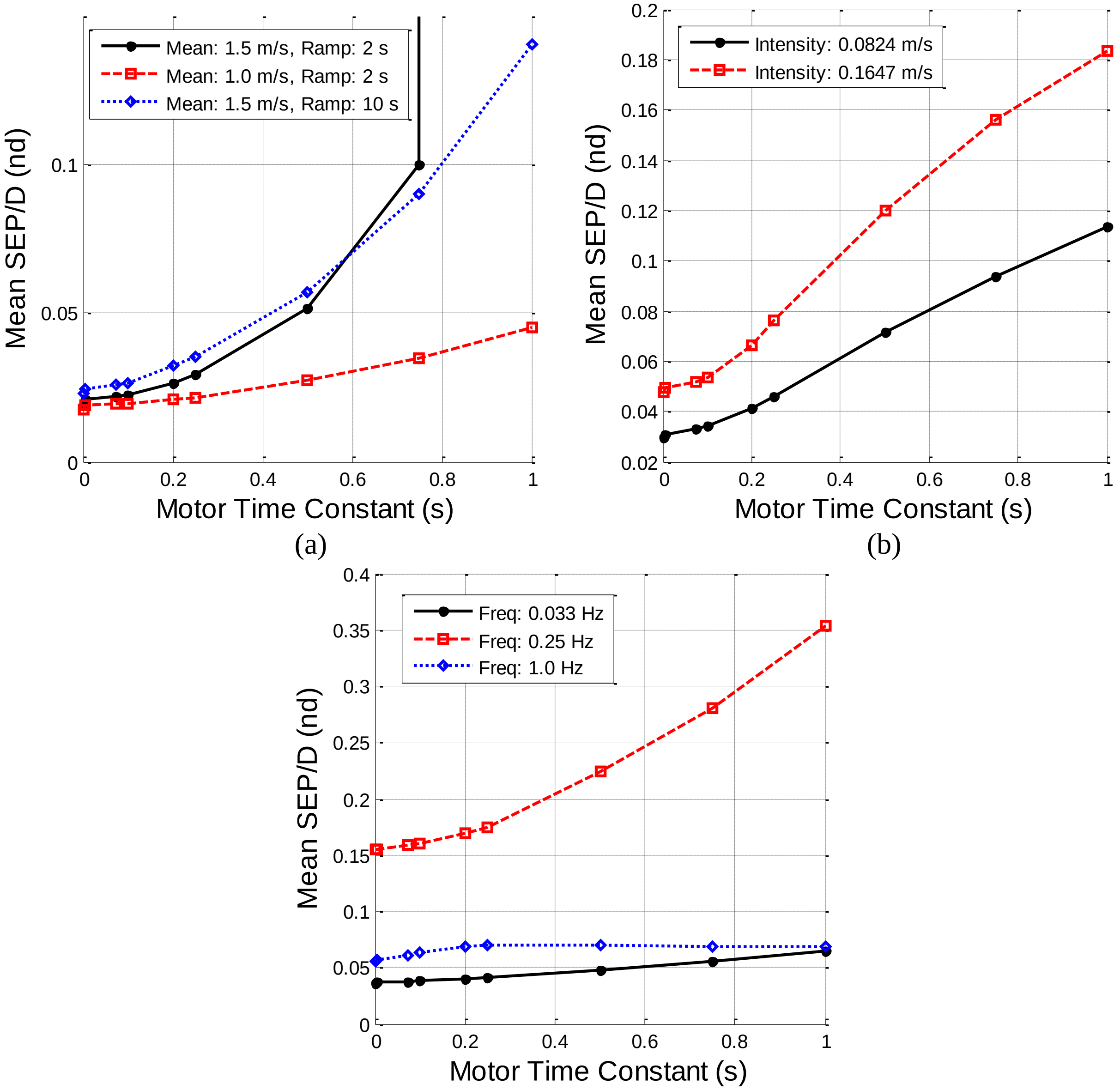

(a) (b)

(c)

Figure 6.56. Mean nondimensional transient SEP with respect to motor time constant in various wind kernels. (a) engulfing wind kernels (b) turbulent wind kernels with 1.0 m/s mean wind and 10 second ramp time (c) sinusoidal wind kernels with 0.5 m/s amplitude .

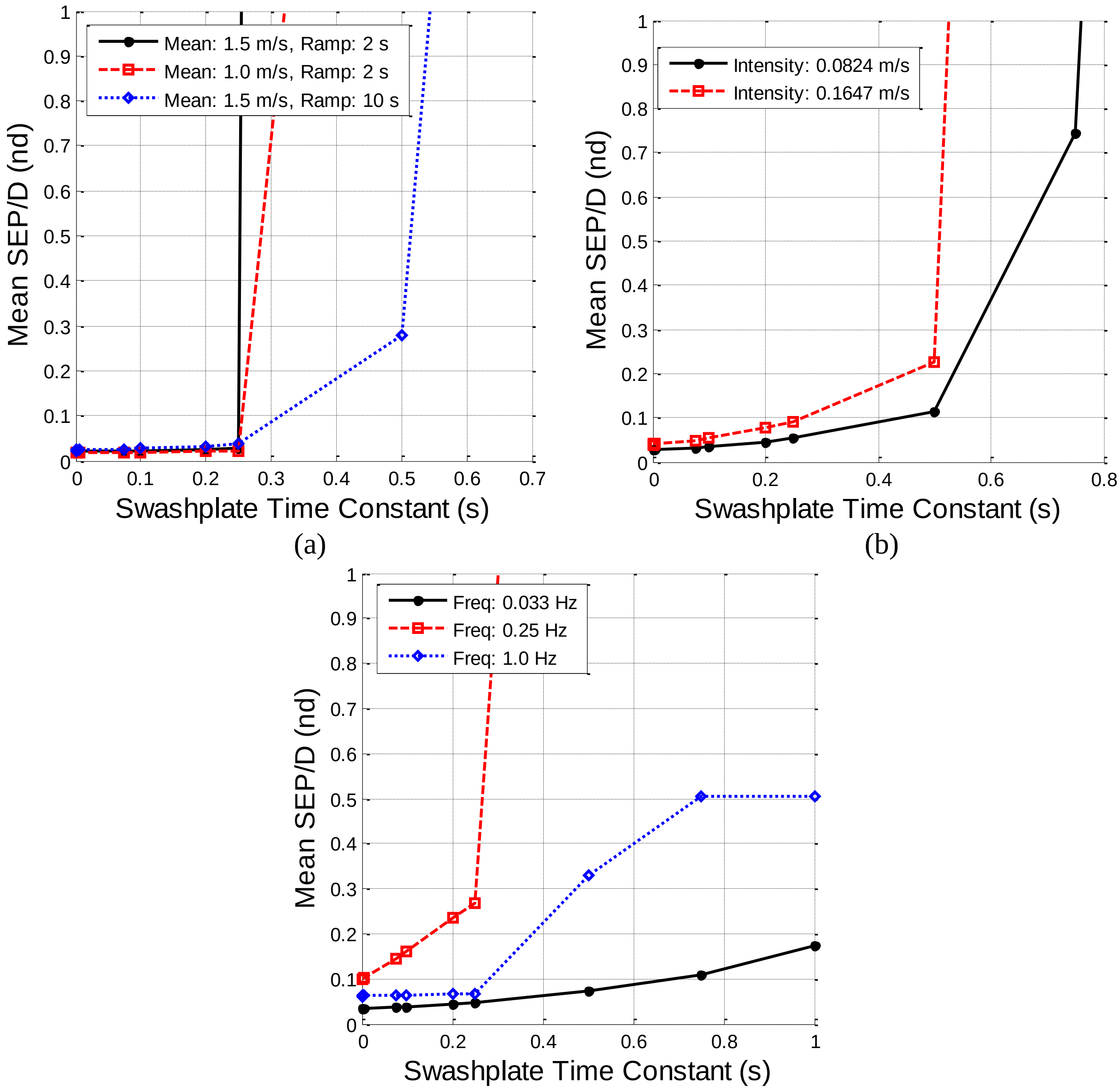

(a)

(b)

(c)

Figure 6.57. Mean nondimensional transient SEP with respect to swashplate time constant in various wind kernels. (a) engulfing wind kernels (b) turbulent wind kernels with 1.0 m/s mean wind and 10 second ramp time (c) sinusoidal wind kernels with 0.5 m/s amplitude .

Maximum Flight Speed Limitations

Response time to changing wind conditions is one of the main issues for micro rotorcraft operation in urban environments. The other main challenge is the large magnitudes of disturbances. Power and energy metrics from engulfing wind trade studies and subsequent power curve analysis show the maximum flight speed of the micro coaxial helicopter tested does not utilize all the power available or balance the power required in hover and operational forward flight, Fig. 6.58.

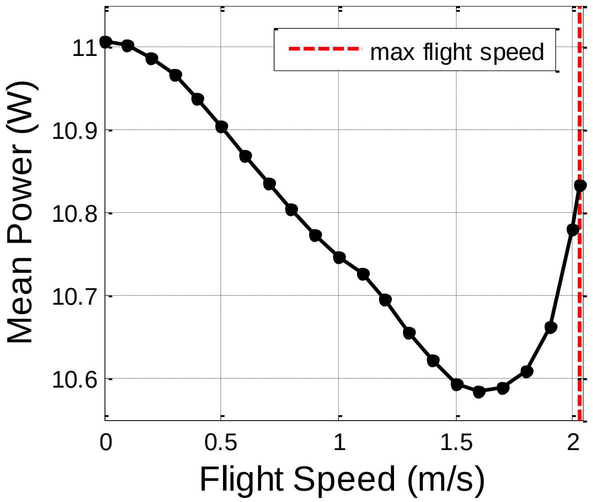

Figure 6.58. Mean steady state power curve for the coaxial helicopter calculated through simulation.

Therefore the goal of this trade study is to investigate different ways to increase flight speed including: increasing swashplate control margin, increasing blade stall angle, and increasing rotor blade section lift coefficient. Monte Carlo cases are performed varying model parameters over the measured confidence intervals as in other trade studies and a simulation model with a modified control law is employed to calculate the maximum flight speed in no wind.

Increasing swashplate control margin increases the maximum angle the swashplate can tilt. The experimental swashplate control margin for the coaxial helicopter is ±1 PPM which corresponds to a cyclic pitch angle of ±20 degrees. The average maximum flight speed calculated from Monte Carlo simulations for increasing swashplate control margin is shown in Figure 6.59a, where maximum achievable flight speed is shown to quickly plateau after a control margin of 1.2 PPM. The total increase in maximum flight speed from the experimental platform is only 0.1 m/s.

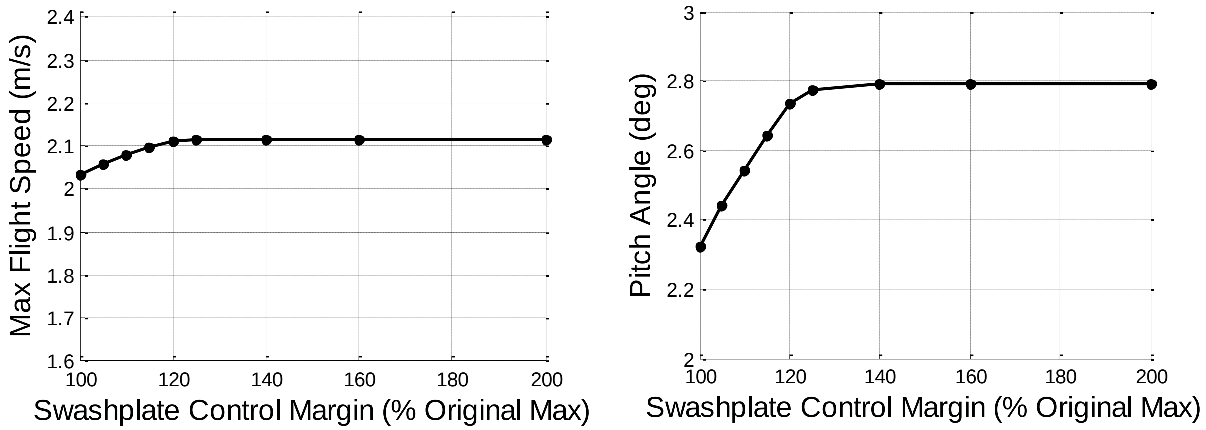

(a) (b)

Figure 6.59. Maximum flight speed and steady state pitch angle with respect to swashplate control margin. (a) Maximum flight speed (b) steady state pitch angle.

It is clear that the swashplate control margin is not the only factor contributing to a low maximum flight speed. Other limiting factors are inhibiting the maximum angle the vehicle's thrust vector can be tilted to achieve horizontal flight speed. This can be seen from the small increase in trim body pitch angle achieved, Fig. 6.59b, only about 0.5 degrees for increasing control margin. One possible limiter could blade stall caused by the increased cyclic pitch angles. This would result in only marginal increases to the aerodynamic forces and moments being generated by the rotor thus limiting the achievable body pitch angles. Therefore increasing the rotor blade stall angle may increase maximum flight speed.

As described in Chapter 4, the airfoil stall angles are prescribed as a combination of a circular arc airfoil for low angles of attack and a high angle of attack sinusoid. Increasing the stall angle increases the linear lift region described through circular airfoil theory as

$$c_l = \frac{2\pi\sin(\alpha+\delta)}{\cos\delta} \tag{6.9}$$

resulting in higher lift generation capability, Fig. 6.60.

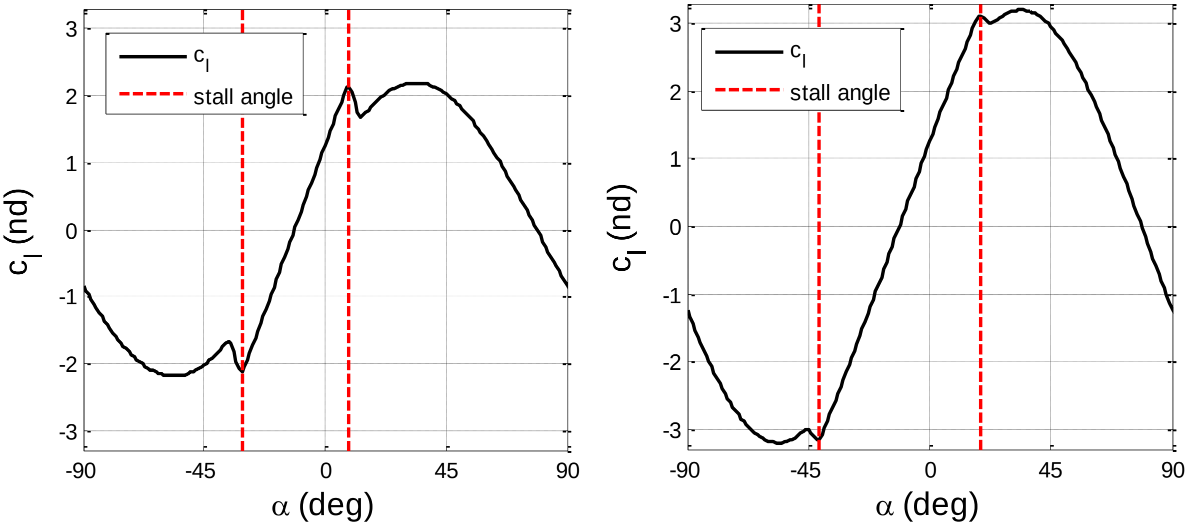

Figure 6.60. Rotor blade lift coefficient versus angle of attack. (a) 20 degree stall angle (b) 30 degree stall angle.

Figure 6.61 shows that while the achievable maximum flight speed and pitch angle do increase for higher stall angles, the improvements are still small, plateauing at 2.3 m/s and 3.5 degrees respectively. Based on the results stall angle is not a key limiting factor for vehicle flight speed, however it still seems reasonable to hypothesize that if the platform can tilt more it can achieve high maximum flight speeds.

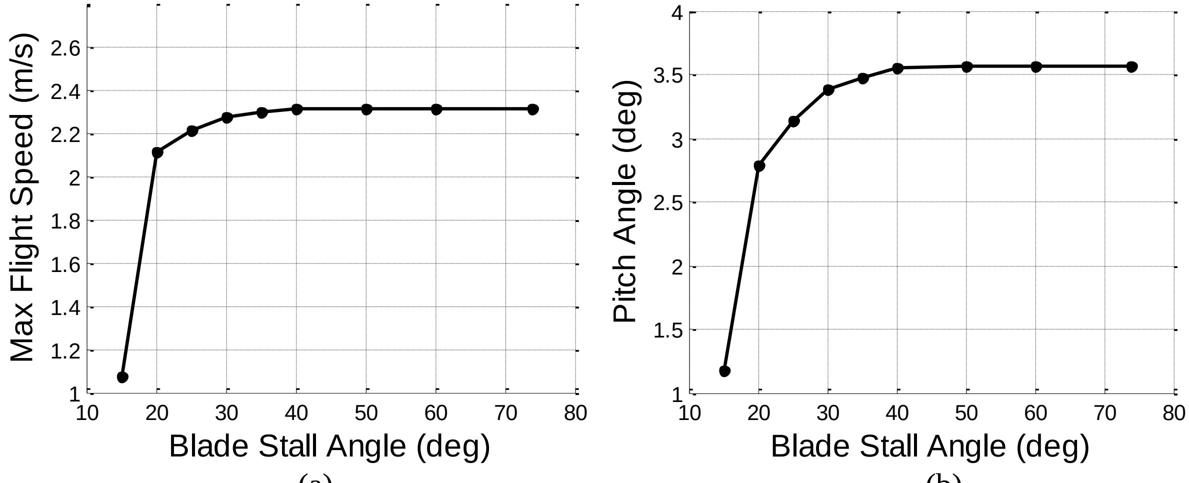

(a) (b)

Figure 6.61. Maximum flight speed and steady state pitch angle with respect to stall angle. (a) Maximum flight speed (b) steady state pitch angle.

To further test this hypothesis that the rotorcraft power available will allow for a higher maximum flight speed if the vehicle can tilt the thrust vector more, the control authority of the vehicle is increased by scaling lift generation directly. This is achieved by multiplying the coefficient of lift functions by a factor K_{cl}:

$$c_l = K_{cl} c_l(\alpha) \tag{6.10}$$

Employing a scaling factor results in a more drastic increase to rotor blade section lift than increasing stall angle, and can more clearly isolate the effect of achievable rotor forces and moments on maximum flight speed. Figure 6.62 shows the average maximum flight speeds and trim body pitch angles for increase lift coefficient scalar. As expected, increase the lift generation capability has much larger effect than control margin or blade stall angle, with the maximum flight increasing by 35% to 2.7 m/s and the trim body pitch angle doubling to 6 degrees. This confirms the hypothesis that if the helicopter can tilt the thrust vector more, the motors still have a large amount of power available to achieve higher flight speeds.

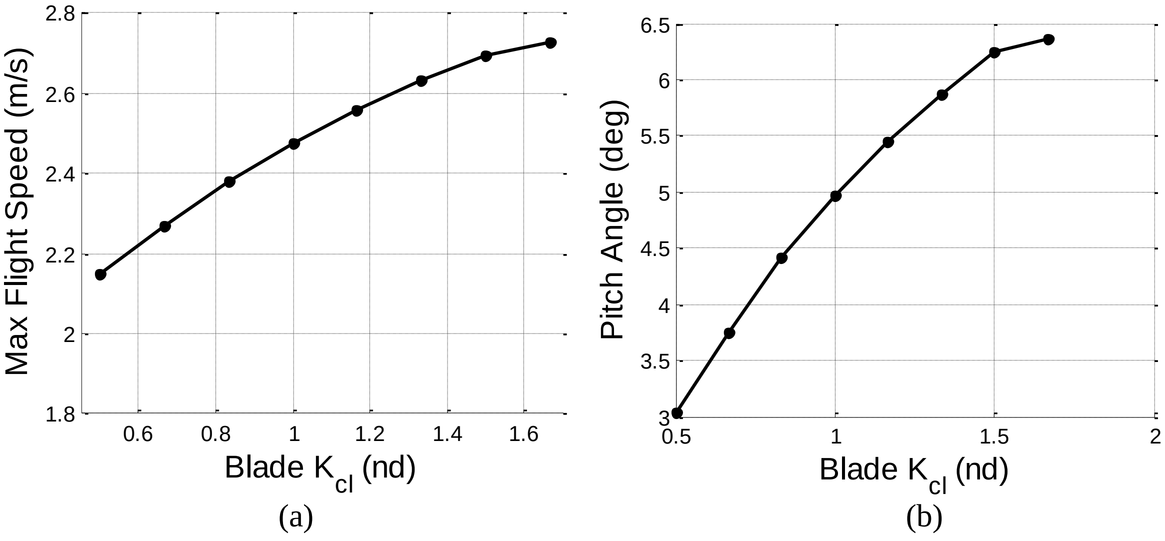

(a) (b)

Figure 6.62. Maximum flight speed and steady state pitch angle with respect to lift coefficient scaling. (a) Maximum flight speed (b) steady state pitch angle.

Results from trade studies for swashplate control margin, stall angle, and lift coefficient lead to the conclusion the coaxial helicopter configuration is possibly too stable to achieve maximum body pitch and utilize the power available. This conclusion can be investigated by calculating the flight speeds of less stable configurations. Rotorcraft configurations simulated include:

- Coaxial helicopter with no fly bar: the cyclic pitch angle of the upper is fixed to zero but both rotors are still allowed to flap.
- Coaxial helicopter with no fly bar and completely rigid rotors: fixes rotor flapping states to zero so the rotors cannot to oppose the forward flight speed.
- Single main rotor helicopter: the upper rotor is not simulated and a simple tail rotor is modeled to cancel main rotor torque. The rotor radius and collective pitch input are adjusted to generate the required lift to trim the vehicle.

The validated coaxial helicopter simulation model is used as a baseline vehicle and small modifications to the model are made to create the less stable configurations. The largest model changes are for the single main rotor helicopter where the rotor radius and collective pitch are scaled to generate the required thrust while keeping as many similar model properties as possible. Additionally a simple tail rotor is added trim the yaw moment. As with previous trade studies, Monte Carlo simulations varying model parameters are run to calculate average maximum flight speed. Figure 6.63 shows the maximum flight speed and trim body pitch angle for the baseline coaxial platform and the less stable configurations. As expected, the less stable coaxial helicopter configurations show improvement over the baseline but it is still small—0.05 m/s and 0.13 m/s increases in flight speed for the no fly bar and no rotor flapping configurations respectively. The single main rotor configuration shows a drastic increase in maximum flight speed up to 4.1 m/s. These results indicate that the poor power curve design and small maximum flight speed of the coaxial platform are due to the influence of drag on the upper rotor and the reduced control authority inherent in splitting the thrust generation between two rotors. While the coaxial helicopter platform has always been viewed as a less maneuverable configuration than other rotorcraft, these results clearly show the deficiencies are not only in response time and dynamic stability but also in the maximum achievable flight speeds.

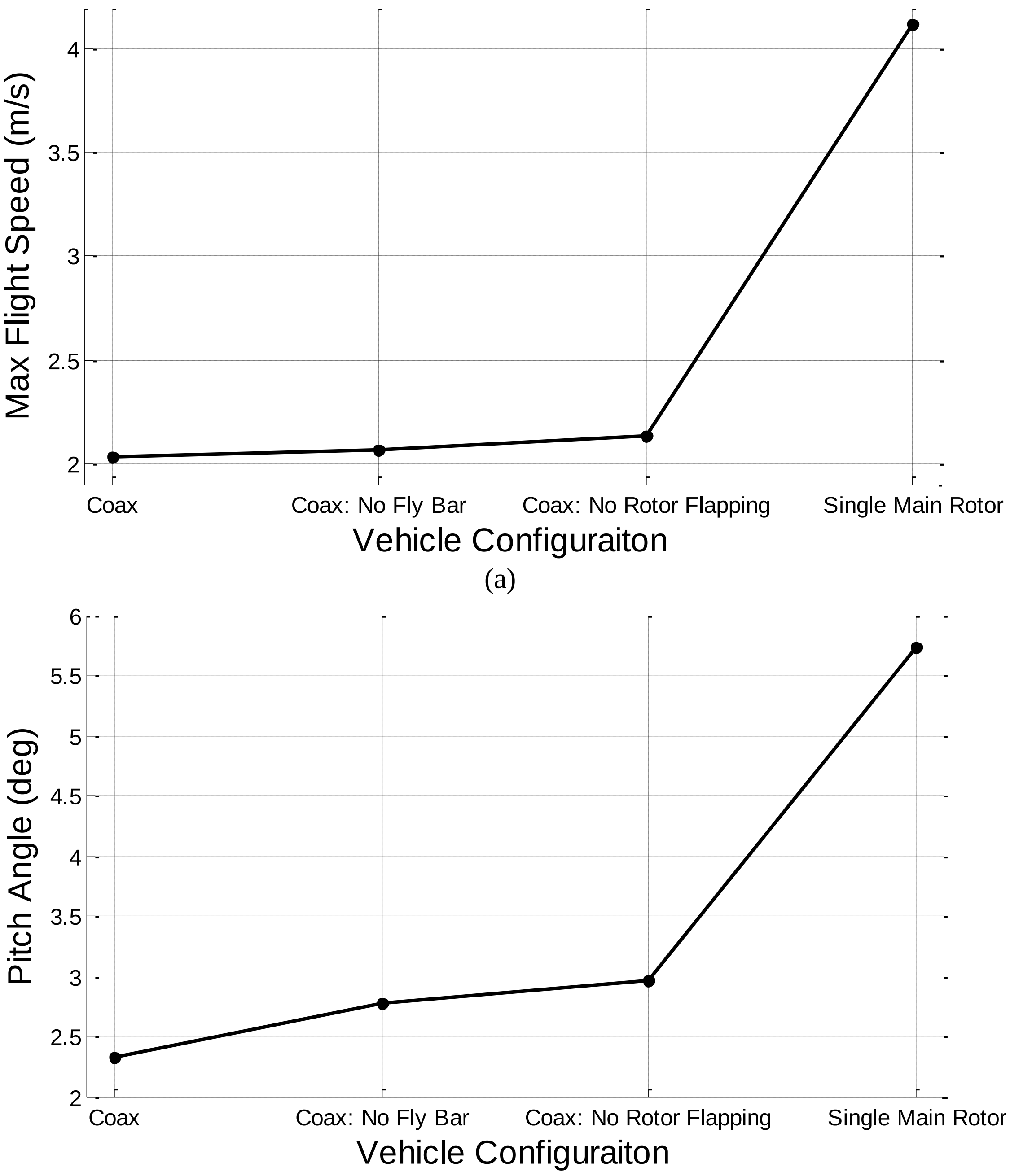

(a)

(b)

Figure 6.63. Maximum flight speed and steady state pitch angle with respect to vehicle configuration. (a) Maximum flight speed (b) steady state pitch angle.

Rotor Dynamic Response Time

Wind kernel trade studies revealed a peak response in sinusoidal and discrete shutter wind kernels around 0.35 Hz due to the time required for the coaxial helicopter to tilt its thrust vector and reject horizontal disturbances. One factor that dictates the time required to tilt the thrust vector is the rotor dynamic response time, thus a trade study is performed to investigate if changing rotor response behavior has an impact on peak response frequency. If rotor response is determined to be a key factor, future design of micro rotorcraft can incorporate the resulting trends to minimize peak response for specific disturbances expected to occur in the planned mission environments. However it is difficult to isolate rotor response time from the rotor system model parameters. Therefore a first pass binary trade study is performed comparing the baseline vehicle and a platform with best case rotor response where the rotor instantly flaps to steady state, thus minimizing the time required to tilt the thrust vector.

To create a coaxial helicopter with instant rotor flap, the first harmonic flapping equations of motions—Eqns. 3.24, 3.25, and 3.26—are solved for substituting in the steady state conditions:

$$\ddot{\beta}_0 = \ddot{\beta}_{1C} = \ddot{\beta}_{1S} = \dot{\beta}_0 = \dot{\beta}_{1C} = \dot{\beta}_{1S} = 0 \tag{6.11}$$

which simplify the equations of motion to

$$\frac{1}{2\pi}\int_0^{2\pi} \ddot{\beta}\, d\psi_R = 0 \tag{6.12}$$

$$\beta_{1C}\Omega^2 + \frac{1}{\pi}\int_0^{2\pi} \ddot{\beta}\cos(\psi_R)\ d\psi_R = 0 \tag{6.13}$$

$$\beta_{1S}\Omega^2 + \frac{1}{\pi}\int_0^{2\pi} \ddot{\beta}\ \sin(\psi_R)\, d\psi_R = 0 \tag{6.14}$$

The numerical blade element rotor model is used to calculate $\ddot{\beta}$ from Eqn. 3.14 and a nonlinear least squares solver is implemented to solve for the steady state rotor flap angles at each model integration time step, Fig. 6.64.

To gain fuller picture of the effect rotor response, the baseline coaxial platform and a coaxial helicopter with instant rotor flapping are compared to a coaxial helicopter with instant rotor flapping and no actuator dynamics as well as a simple model of a hex rotor vehicle. A coaxial helicopter with instant rotor flapping and no actuator dynamics represents an underactuated platform that is applying control forces and moments as quickly as possible. The hex rotor vehicle, Fig. 6.65, is a representative model of rotorcraft configuration that has full six degree of freedom control authority [91]. For this simple hex configuration, the rotors are modeled as force and moment generators where thrust and torque generated by the i^{th} rotor are calculated in Eqns. 6.12 and 6.13. All hex rotor model parameters are set to match the coaxial platform as closely as possible.

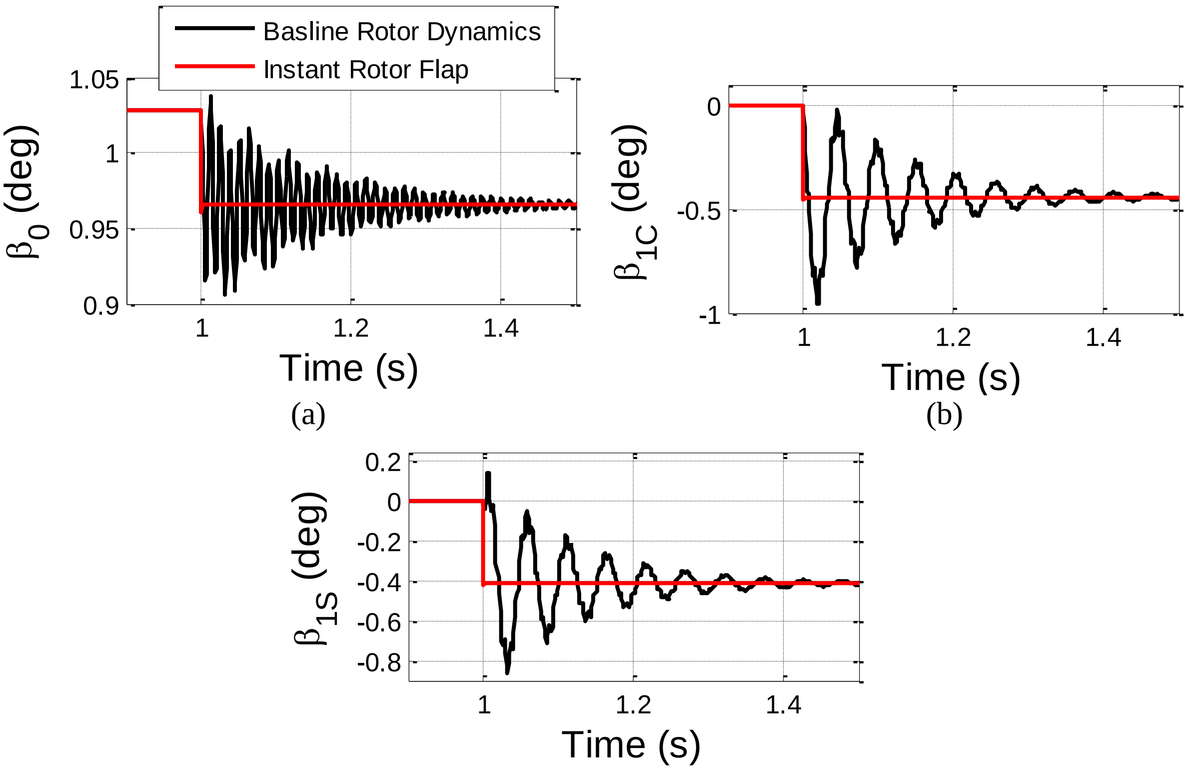

(a) (b)

(c)

Figure 6.64. Comparison of baseline rotor system response and instant rotor response to step inputs. (a) Coning angle (b) Longitudinal flap angle (c) Lateral flap angle.

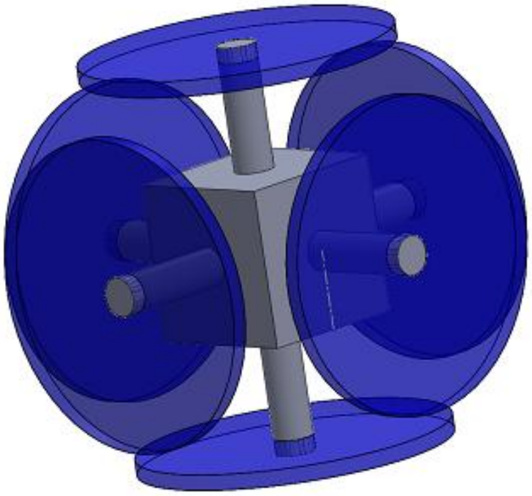

Figure 6.65. Simple hex rotor configuration.

$$T_i = \rho \pi R^2 \Omega^2 sign(\Omega) C_{T_i} \quad (6.15)$$

$$Q_i = C_{Q_i} T_i \quad (6.16)$$

Where the coefficients of thrust and torque ($C_{T_i}$and C_{Q_i}) are constant, and rotor angular rate response modeled as a 1st order system,

$$\dot{\Omega}_i = \frac{1}{\tau_\Omega} \left(C_\Omega u_{T_i} - \Omega_i \right) \quad (6.17)$$

The hex rotor is a very simple model which does not account for wind on the rotors, flexible rotor blades, or rotor inflow. The purpose of including this model is to give an idea of how underactuated rotorcraft response compares to a different type of rotorcraft vehicle.

Figure 6.66 shows the nondimensional SEP of each rotorcraft platform as a function of sinusoidal wind frequency. Surprisingly, the coaxial helicopter with instant rotor flapping has only marginally improved positional tracking compared to the baseline coax. This is a result of rotor flapping response for the baseline coaxial being fast enough to keep up with the swashplate control inputs for wind disturbances within the frequency range simulated, Fig. 6.67.

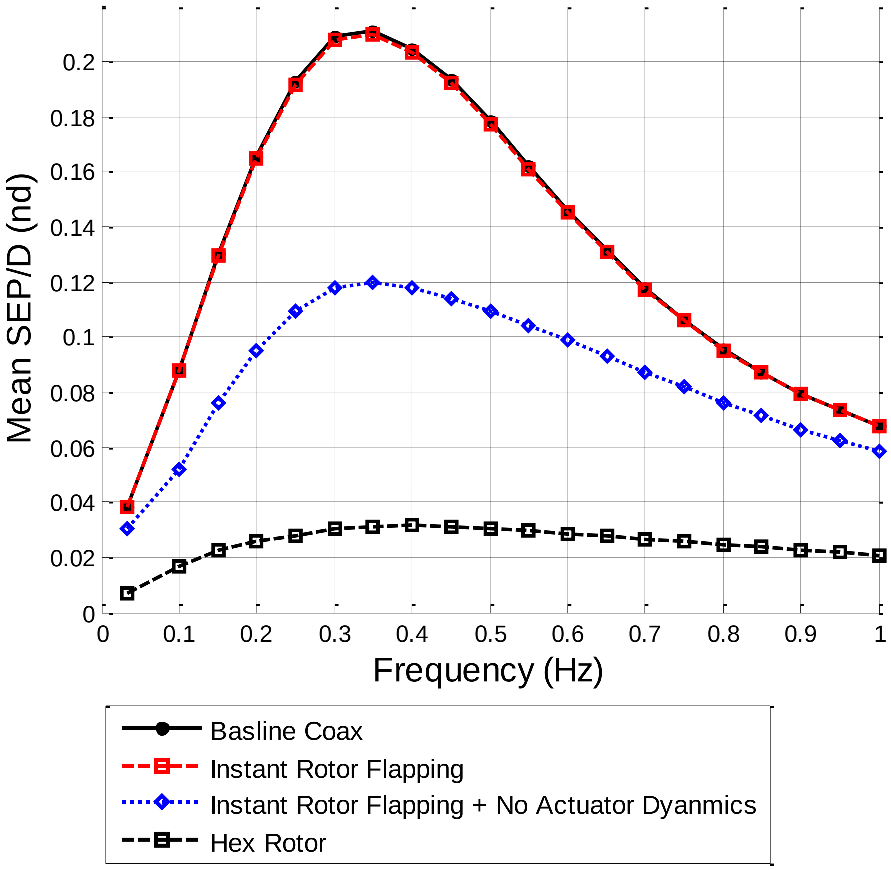

Figure 6.66. Mean nondimensional steady state SEP for rotor response models in sinusoidal wind kernels with 0.5 m/s amplitude.

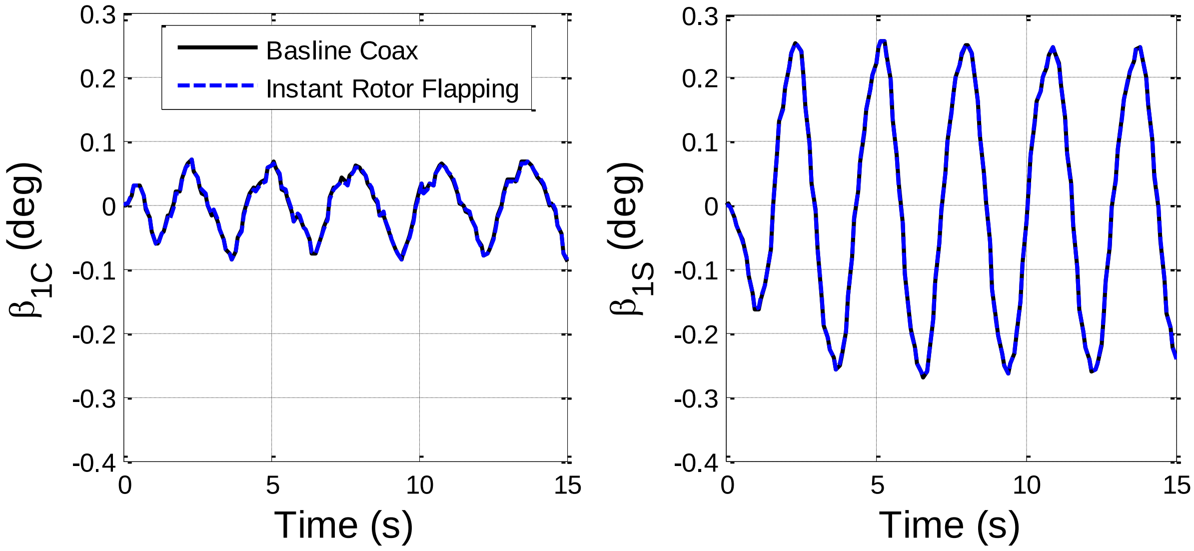

(a) (b)

Figure 6.67. Example time histories of lower rotor flap angles for the baseline original coaxial platform and the instant rotor model. (a) longitudinal flap angle (b) later flap angle.

This trade study shows that the time required to tilt the rotor plane is a partial contributor to the peak response frequency, as seen by the performance improvements for the instant rotor with no actuator dynamics, but that platform still showed a peak response at about 0.4 Hz. Therefore, the main cause of the peak response frequency is the time required to tilt the thrust vector of an underactuated rotorcraft system, which has implications not just for the coaxial helicopter analyzed here but also for the other common micro rotorcraft platforms—the single main rotor helicopter and the quadrotor. Novel concepts which can apply direct forces in all dimensions may be required in environments where the critical disturbance frequencies are expected to occur.

Following the results of the instant rotor dynamics trade study, it is valuable to isolate rotor response time as a model parameter, and to understand how peak response frequency changes for varying rotor response time. Therefore a simple model of a coaxial helicopter is developed with force and moment generators representing the rotors and first order flapping to represent the tilt of the thrust vector. Thrust, torque, and rotor angular rate are modeled employing the same methods as the simple hex rotor platform (Eqns 6.15-6.17). The first order flapping include the effects of swashplate control inputs and aerodynamic velocity

$$\dot{\beta}_{1C} = \frac{1}{\tau_{\mathrm{R}}}\left(C_{\theta}u_{\theta} - \beta_{1C} + C_{vx}(v_{ox} - v_{atx})\right) \tag{6.18}$$

$$\dot{\beta}_{1S} = \frac{1}{\tau_{\mathrm{R}}}\left(C_{\phi}u_{\phi} - \beta_{1S} + C_{vy}\left(v_{oy} - v_{aty}\right)\right) \tag{6.19}$$

where the flapping model coefficient are fit from the nonlinear rotor system model employed in trade studies so far. It is clear this simple model does not account for spatially varying wind fields or the effects of inflow, wake, and angular rate on rotor flap. The main propose of this model is to study the effect of the rotor flapping time constant (τ_{R}) on vehicle response.

The simple coaxial helicopter model and the hex rotor platform model are both simulated in sinusoidal wind kernels employing the a Monte Carlo approach similar to the previous trade studies. The coaxial rotor time constant and the hex rotor motor time constant are varied in a 2D matrix with wind frequency and the nondimeisional SEP results are shown in Figure 6.68. The simple coaxial helicopter show a large peak response between 0.2 and 0.3 Hz for rotor time constants greater than 0.5 seconds and a much smaller peak response at 0.1 Hz for rotor time constants below 0.5 seconds. As the instant rotor flapping trade study showed, even for an extremely small time constant the underactuated system exhibits a peak response frequency. On the other hand, the hex rotor shows no significant peak response frequency but does exhibit a large increase of SEP for motor time constants above 0.2 seconds.

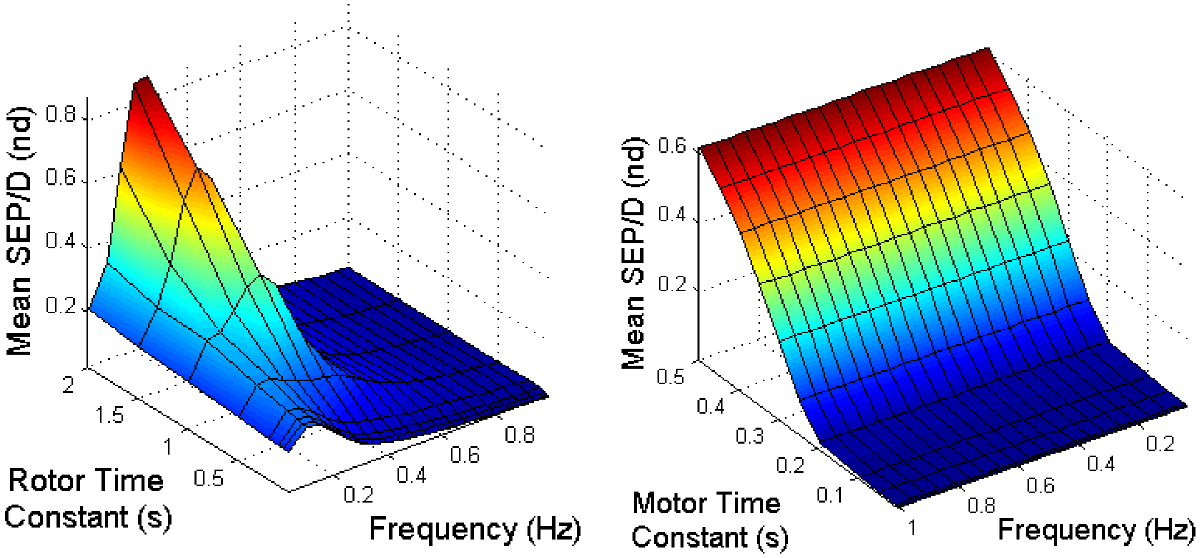

(a) (b)

Figure 6.68. Mean nondimensional steady state SEP for rotor and motor time constants verses sinusoidal wind kernels with 0.5 m/s amplitude. (a) Coaxial helicopter (b) Hex rotor.

Overall, response time for the rotorcraft to tilt the thrust vector and apply forces in the horizontal plane is a key design parameter for micro rotorcraft to reject changing wind disturbances—especially for low frequencies winds on the order of 0.1 to 0.4 Hz.

6.5 Discussion of Performance Metrics

After employing the performance metrics for both experimental flight tests and simulation trade studies, it is clear that not every metric is useful at accurately capturing vehicle performance in all situations. Spherical error probable is useful for capturing micro rotorcraft transient response to almost all wind kernels for short duration flights. However, SEP does not adequately capture performance for longer duration maneuvers that include a significant time spent at one position. The longer data is collected, the more the large excursions are averaged out which reduces the usefulness of the metric. As seen in the engulfing wind trade study, for longer duration hover maneuvers it is more instructive to look at the maximum tracking errors instead. Attitude error RMS is effective for measuring attitude tracking performance, particularly in the turbulent, engulfing, and low frequency sinusoidal and discrete shutter winds. Though as seen in the sinusoidal wind trade study, for high frequency disturbances the AERMS is essentially constant for wind frequencies above 0.4 Hz making it not very useful. Additionally, attitude tracking is tied to positional tracking so there is a balance; there may be times when a vehicle has high attitude error but low positional errors and vice versa. The tradeoff and weighting between SEP and AERMS will vary depending on mission objectives. Angular velocity RMS has been shown to be suitable for assessing performance in most winds including: sinusoidal, discrete shutter, and turbulent. A micro rotorcraft's AVRMS is misleading when the platform is required to tilt quickly to reject a horizontal disturbance—such as a sharp or discrete change in wind—resulting in high AVRMS but low SEP and positional tracking errors. Similar to AERMS the tradeoff is dependent on the mission objectives as well as payload sensor requirements. The control input standard deviations are good for evaluating controller workload in sinusoidal, discrete shutter, and engulfing wins but rapidly changing winds, such as high intensity turbulent winds, required constant control corrections thus control STD trends due to other parameters become difficult to identify. It is still possible to use relative changes in control STD to assess vehicle perform but it is not as straightforward. On the other hand average control margin is helpful for turbulent and high magnitude winds; however as seen in engulfing wind trade study, if the average is being taken over caess with winds in orthogonal directions, the effect due to wind is averaged out and trends are much more difficult to see. It is important to isolate control for a given direction with winds for same direction either through limiting the runs or using histograms. Average power and total energy consumed were both useful for analyzing platform endurance in engulfing, sinusoidal, and discrete shutter winds. Although average power trends are difficult to see in high intensity turbulent winds, and total energy consumed difficult to calculate when the flight enveloped protection scheme was engaged for winds the exceed the vehicle's maximum flight speed. Table 6.7 shows an overview of the winds for which each metric was good at capturing vehicle performance and for which winds each metric was bad.

Table 6.7. Overview of the winds for which each performance metric is useful for accurately capturing micro rotorcraft performance.

Metrics	Good For	Bad For
SEP	Sinusoidal winds	Long constant winds
	Turbulent winds	Winds that change between two steady states over long periods
	Shutter winds	
	Short maneuvers	
AERMS	Low frequency sinusoidal winds	High frequency sinusoidal winds
	Turbulent winds	
	Engulfing winds	
AVRMS	Sinusoidal winds	Engulfing winds times with small ramp times
	Shutter winds	
	Turbulent winds	
Control STD	Sinusoidal winds	Turbulent winds
	Shutter winds	
	Engulfing winds	
Control Margin	Turbulent winds	Engulfing winds from many different directions
	High magnitude winds	Low magnitude winds
	Sinusoidal winds	
Average Power	Engulfing winds	Turbulent winds
	Sinusoidal winds	Winds that exceed the platform maximum flight speed
	Shutter winds	
Total Energy	Engulfing winds	Winds that exceed the platform maximum flight speed
	Sinusoidal winds	
	Shutter winds	
	Turbulent winds	

CHAPTER 7

ADDITIONAL APPLICATIONS OF EXTENDED STATE OBSERVERS FOR PARMAETER ESTIMATION

The Gust Rejection Controller utilizes disturbance states from the ESO to estimate the wind acting on the micro coaxial helicopter improving the feedback linearization model and enabling the flight envelop protection scheme. This is a novel use of an ESO, which has been mainly applied to strictly disturbance estimation as part of the Active Disturbance Rejection Controller framework. However, an algorithm with provable stability can be extremely usefully many applications where parameter estimation of a nonlinear system is required. This chapter describes another area where the estimation framework developed in Chapter 5 is a potential solution, helicopter mass properties.

In-flight estimations of helicopter mass and center of gravity (CG) are critical for health and life cycle estimation, flight control system feedback, and mission planning. A common method for rotorcraft mass property estimation is the extended Kalman filter (EKF). First employed for helicopter mass and CG estimation by Abraham and Costello [92], an EKF fuses sensor data and a system model for accurate state estimation in the presence of measurement error such as bias and noise. However there are two main difficulties with an EKF based mass properties estimation algorithm. Extended Kalman filters are extremely sensitive to model error which results in poor estimation of mass and CG location. Secondly, the linearization of the system plant that is required for EKF propagation and update means the filter is not necessarily stable and can diverge [93]. This is especially true for highly nonlinear plants. An alternative estimation method is a neural network such as the works by Morales and Haas [94] and Idan, Iosilevskii, and Nazarov [95]. Neural networks are straightforward and can efficiently solve for the most significant parameters, but require intensive training with sufficient data. Apetre, Sarkar, Iyyer, and Phan combined a neural network with an EKF to create a hybrid approach that leverages both methods to combat the issues of model error and lack of sufficient data [96]. However this approach still doesn't account for EKF divergence. As helicopters are used more and more for aggressive maneuvering such as nap of the earth flight, estimate algorithms will be required that can handle the nonlinear flight regimes of modern helicopters and have proven stability. Extended state observers provide a potential solution to this issue.

Employing the methodology developed to estimate wind states, filters are designed to use the ESO disturbance signals as feedback to update mass parameter estimates.

$$\begin{Bmatrix} \dot{\tilde{m}} \\ \dot{\tilde{r}}_{CG_x} \\ \dot{\tilde{r}}_{CG_y} \\ \dot{\tilde{r}}_{CG_z} \end{Bmatrix} = \begin{Bmatrix} f_m\left(\tilde{x}, \dot{\tilde{x}}\right) \\ f_{CG_x}\left(\tilde{x}, \dot{\tilde{x}}\right) \\ f_{CG_y}\left(\tilde{x}, \dot{\tilde{x}}\right) \\ f_{CG_z}\left(\tilde{x}, \dot{\tilde{x}}\right) \end{Bmatrix} \tag{7.1}$$

where $\tilde{x} = [\tilde{x}_1 \; \tilde{x}_2 \; \tilde{x}_3]^T$. Model errors in mass and horizontal center of gravity primarily produce large low frequency disturbances, and Eqn. 7.2 shows the simple filters employed for mass and horizontal CG as functions of z, roll, and pitch disturbance states respectively.

$$\begin{aligned} f_m &= k_{p_m}\tilde{x}_{3_z} + k_{d_m}\dot{\tilde{x}}_{3_z} \\ f_{CG_x} &= k_{p_{CG_x}}\tilde{x}_{3_\theta} + k_{d_{CG_x}}\dot{\tilde{x}}_{3_\theta} \\ f_{CG_y} &= k_{p_{CG_y}}\tilde{x}_{3_\phi} + k_{d_{CG_y}}\dot{\tilde{x}}_{3_\phi} \end{aligned} \tag{7.2}$$

The vertical CG location is almost always dominated by other uncertainties, but test simulations identified a pattern which is clearer during roll and pitch maneuvers after horizontal CG location estimates have settled out:

$$f_{CG_z} = k_{z1}\mathrm{f}_{DB}\left(\dot{\tilde{x}}_{3_\phi}, \alpha_\phi\right)\dot{\tilde{\phi}} + \; k_{z2}\mathrm{f}_{DB}\left(\dot{\tilde{x}}_{3_\theta}, \alpha_\theta\right)\dot{\tilde{\theta}} \tag{7.3}$$

where $\mathrm{f}_{DB}$is a deadband function

$$f_{DB}(x,\alpha) = \begin{cases} x, & |x| \leq \alpha \\ 0, & |x| > \alpha \end{cases} \qquad (7.4)$$

Figure 7.1 shows example time histories of estimations for vehicle mass and longitudinal, lateral, and vertical CG locations for a helicopter in hover with a discrete change in mass properties after 1 second. The discrete change is meant to simulate a rotorcraft performing payload drop off. Mass, longitudinal CG, and lateral CG estimates all converge quickly, within 3 to 5 seconds. With very little excitation during hover, the vertical CG estimate converges to within 1 mm but not much more.

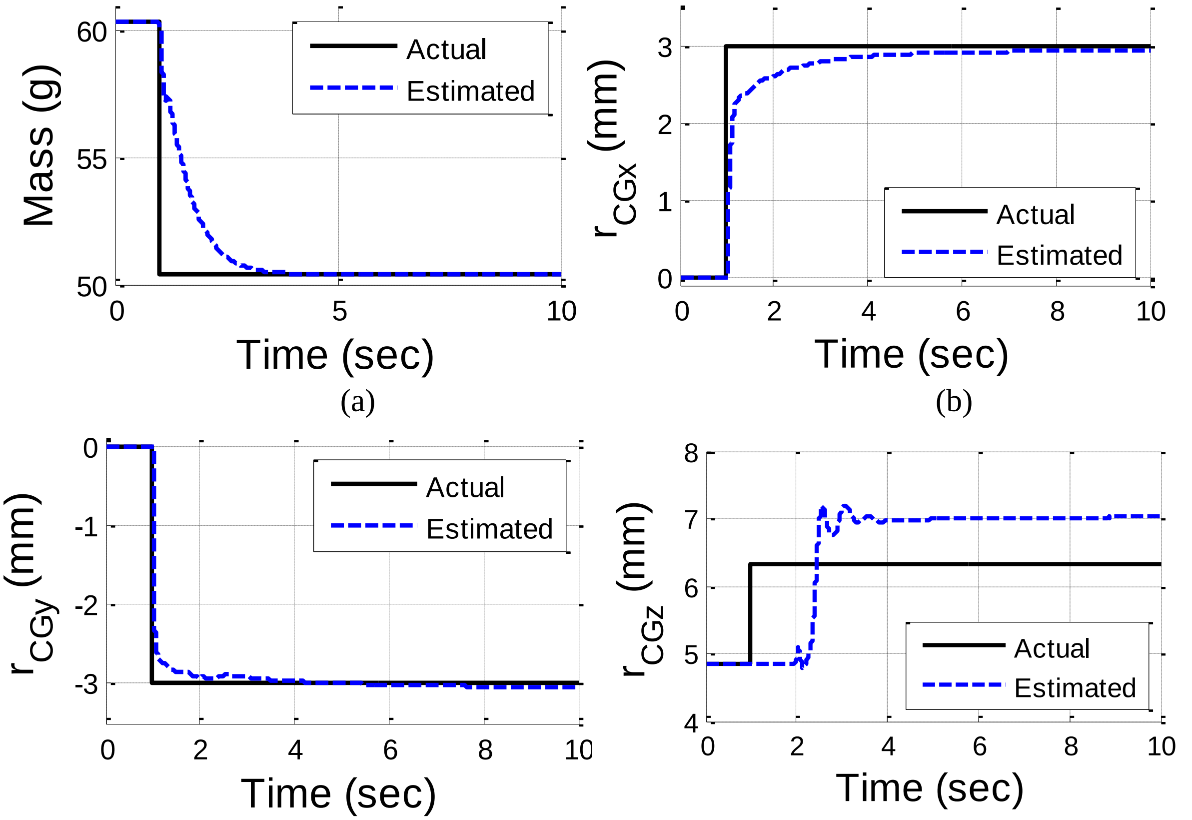

(a) (b)

(c) (d)

Figure 7.1. Estimation of mass during a payload drop off in hover.

To make vertical CG more observable, a roll maneuver during forward flight is simulated to excite the system, Fig. 7.2, where a forward flight speed of 1.0 m/s is maintained while the body roll angle varies between -4 and 1 degrees.

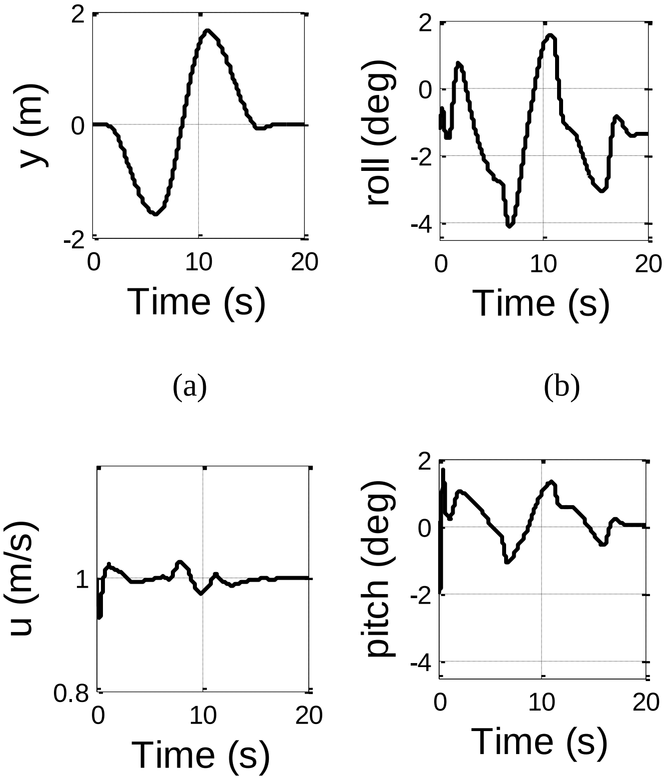

(a) (b)

(c) (d)

Figure 7.2. Forward flight maneuver. (a) y position (b) roll attitude (c) body forward flight velocity (d) pitch attitude.

Figure 7.3 shows time history examples of the mass property estimates during the forward flight maneuver. As expected, estimation of the vertical CG is improved while all other mass property estimates remain very accurate. While Figure 7.3d shows good estimation, it is clear vertical CG position will become even harder to isolate when model mismatch and measurement noise are added to the simulation.

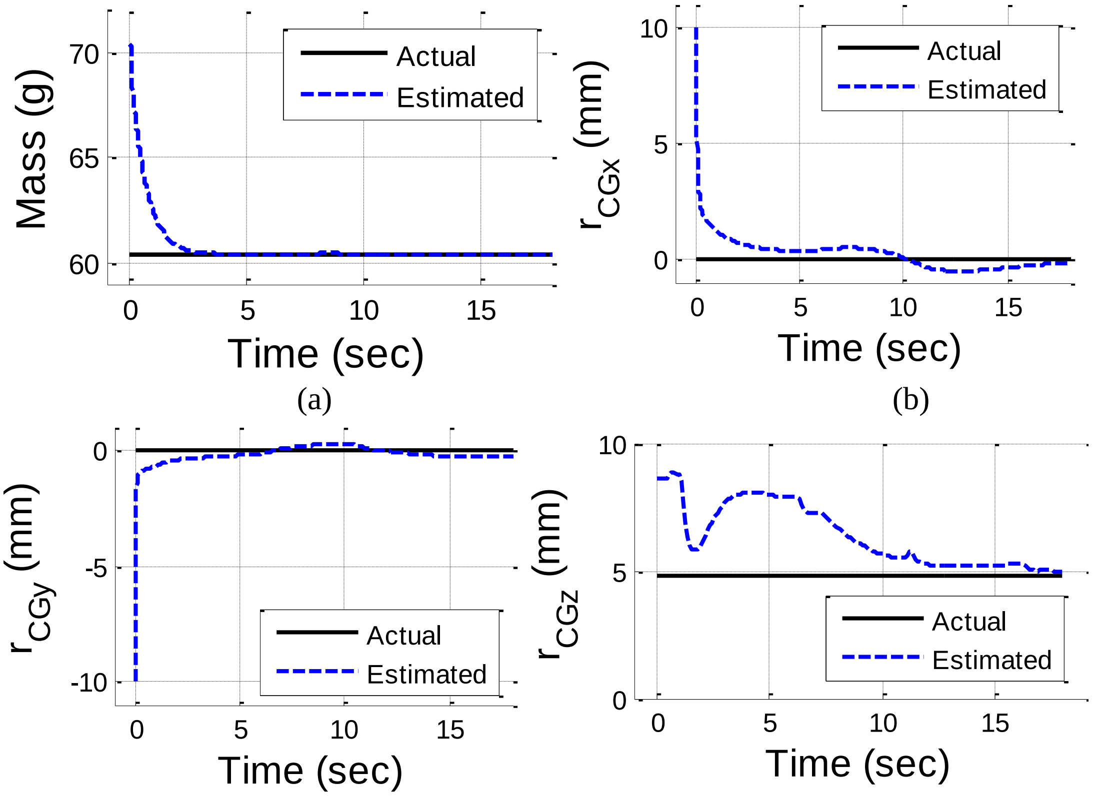

(a) (b)

(c) (d)

Figure 7.3. Estimation of mass properties during forward flight maneuver. (a) mass (b) longitudinal CG location (c) lateral CG location (d) vertical CG location.

A metric of goodness for the vertical CG filter is proposed based on the number of observer updates for which the observer states satisfy the expected conditions to isolate the error signal. The satisfactory update number (SUN) employs a series of logical checks to determine if the vehicle is currently experiencing sufficient pitch and roll excitations with steady horizontal CG estimates to observe the uncertainty due to vertical CG error. The larger the SUN, the more confidence there is in the filter estimate—Fig. 7.4.

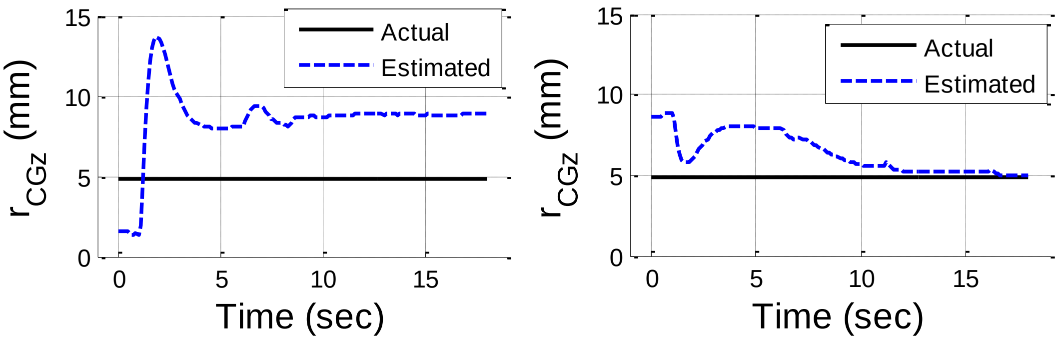

(a)

(b)

Figure 7.4. Example estimations of vertical center of gravity position during a forward flight maneuver for different SUN values. (a) 940 SUN (b) 2256 SUN.

While changing model parameters in flight does feedback into the ESO, as long as the time derivative of the uncertainty $(\dot{\Delta})$ remains within the prescribed bounds the observer will remain stable. This can be ensured by setting the filter gains and update rate appropriately.

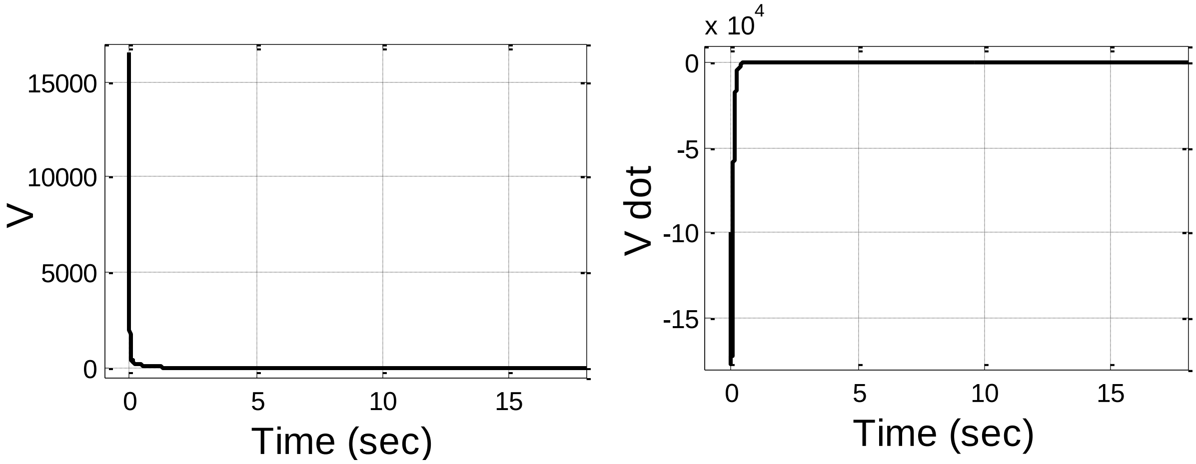

(a)

(b)

Figure 7.5. Example time history of a candidate Lyapunov function for an extended state observer with mass property estimation. (a) Lyapunov function (b) Lyapunov function time derivative.

Thus the helicopter model errors due to mass and CG can be driven to zero as part of the observers designed convergence and stability. Figure 7.5 shows the Lyapunov function and its time derivative for the example forward flight maneuver. After starting with large initial errors, the function is driven to zero with a negative derivative.

The mass and CG estimation algorithm is assessed through Monte Carlo simulations for the forward flight maneuver described above. Simulations are performed for 250 cases and model and measurement errors are varied in the same manner as the gust trade studies in Chapter 6.

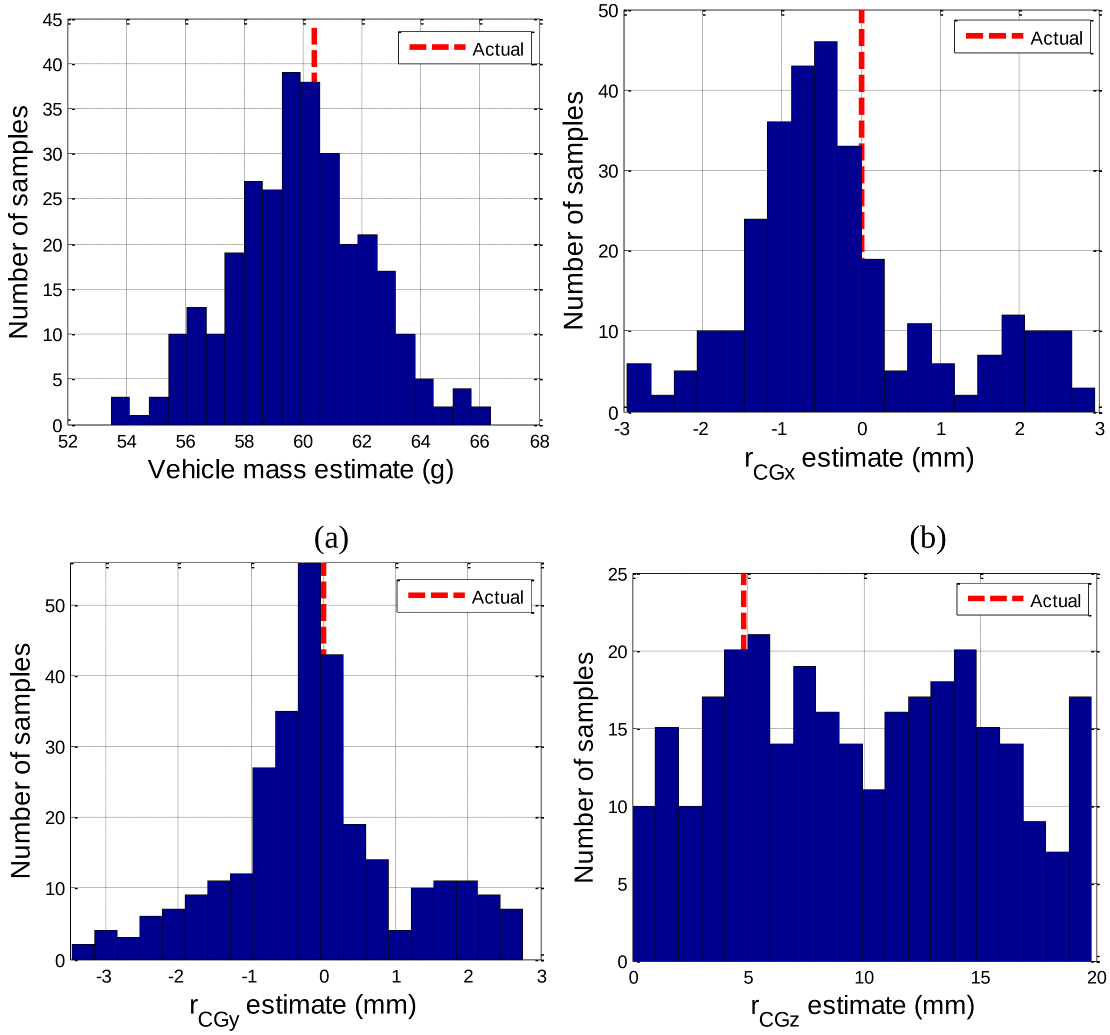

(a) (b)

(c) (d)

Figure 7.6. Histograms of helicopter mass properties estimation. (a) mass (b) longitudinal CG location (c) lateral CG location (d) vertical CG location.

Figure 6 shows histograms of the mass parameter estimations for Monte Carlo simulations with baseline model error and measurement noise. Mean estimates for vehicle mass, longitudinal CG position, and lateral CG are all accurate with small standard deviations, Table 7.1. Vertical CG estimates are very poor with a large mean error and standard deviation. The cause of poor vertical CG estimation is the much smaller uncertainty caused by vertical CG mismatch being dominated by the other sources of uncertainty for certain combinations of model errors. The filter goodness metric described earlier clearly shows a connection between the SUN and the final estimation error as shown in Fig. 7.7. Figure 7.8 shows vertical CG estimates for samples with filter metrics greater than 2180 SUN. For Figures 7.7 and 7.8, the SUN is calculated for each controller update step if the roll or pitch rate is above 0.5 deg/s and if $\dot{\hat{x}}_{3\phi}$ and $\dot{\hat{x}}_{3\theta}$ are less than 1 rad/s^2. The result is the removal of many of the higher error estimates which improves the mean estimate, but the standard deviation is still quite larger (4.67 mm).

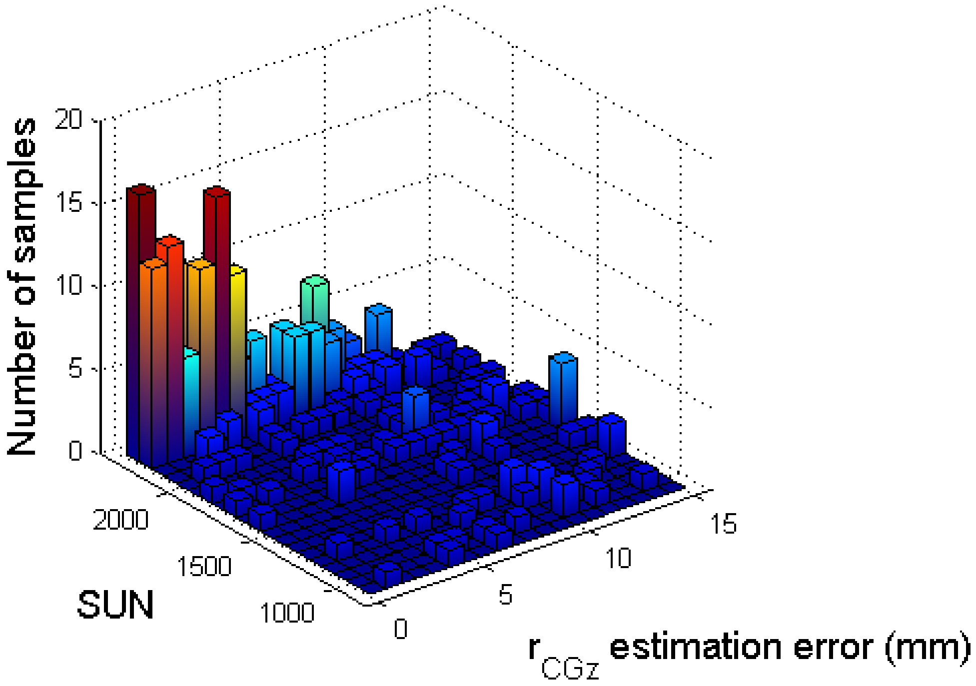

Figure 7.7. Histogram of vertical center of gravity location estimation error and number of good updates for the estimation filter.

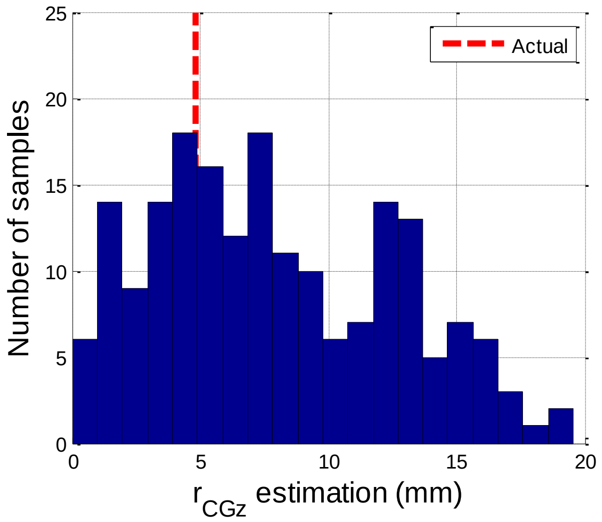

Figure 7.8. Histogram of vertical center of gravity location for good updates > 2180.

Table 7.1. Trade study mean and standard deviations of estimated mass properties with baseline model error and measurement noise.

Parameter	Mean	Standard Deviation	Actual Value
Vehicle mass (g)	59.90	2.33	60.38
r_{CG_x} (mm)	-0.27	1.23	0.00
r_{CG_y} (mm)	-0.11	1.22	0.00
r_{CG_z} (mm) (All)	9.74	5.44	4.83
r_{CG_z} (mm) (Good Updates Only)	7.91	4.67	4.83

The millimeter accuracy of the longitudinal and lateral CG estimates is difficult to place in context. Pilot observations during experimental flight testing with the commercial micro helicopter estimated the horizontal variation in the platform CG to be approximately 12 mm. Given this possible range, 1 mm errors in horizontal CG are accurate estimations representing 1.4% of the rotor radius while the possible CG range is 13%. Projecting the algorithm's accuracy to manned helicopters, Table 7.2 shows reported longitudinal CG ranges for the UH-1, AH-64, and UH-60 helicopters. Even though the larger rotorcraft have considerably less CG travel than the estimated micro coaxial helicopter, assuming similar algorithm performance, the ESO framework would perform adequately for the UH-1 and UH-60 while the very small range of the AH-64 would be difficult. The known CG bounds could also be incorporated in the filters which may improve estimation accuracy.

In addition to Monte Carlo simulations with baseline model error, two other sets of cases are run to assess the affect of model error on algorithm performance. Given the baseline confidence intervals, cases are performed for half model error and double model error by scaling the bounds for all parameters appropriately. Table 7.3 shows the helicopter mass property estimate means and standard deviations for half, baseline and double model error. As expected, accuracy decreases for increasing model error which can particularly be seen by the large increases in estimate standard deviations.

Overall, the novel approach to parameter estimation developed for the GRC shows promise in other applications for nonlinear systems. As long as the disturbance due error in the desired parameters can isolated and extract, the ESO framework provides accurate estimation with guaranteed stability.

Table 7.2. Expected longitudinal center of gravity ranges for manned and unmanned helicopters.

	CG Range (mm)	Rotor Radius (mm)	CG Range as % of Rotor Radius
Micro Coax	12	88	13.64
	CG Range (in)	Rotor Radius (ft)	CG Range as % of Rotor Radius
Bell UH-1 Iroquois [97]	14	24	4.86
Boeing AH-64 Apache [98]	6	24	2.08
Sikorsky UH-60 Black Hawk [99]	23	26.83	7.14

Table 73. Model error trade study mean and standard deviation for mass properties.

Parameter	Model Error	Mean	Standard Deviation	Actual Value
Vehicle mass estimate (g)	Half	59.98	1.33	60.38
	Baseline	59.90	2.33	
	Double	59.76	4.06	
r_{CG_x}estimate (mm)	Half	-0.32	1.14	0.00
	Baseline	-0.27	1.23	
	Double	-0.26	1.33	
r_{CG_y} estimate (mm)	Half	-0.06	1.08	0.00
	Baseline	-0.11	1.22	
	Double	-0.26	1.33	
r_{CG_z} estimate (mm) (All)	Half	9.60	5.41	4.83
	Baseline	9.74	5.44	
	Double	10.29	5.78	
r_{CG_z} estimate (mm) (Good Updates)	Half	7.47	4.53	4.83
	Baseline	7.91	4.67	
	Double	9.39	5.06	

CHAPTER 8

CONCLUSIONS AND FUTURE WORK

With wind speeds multiple times larger than vehicle maximum flight speeds and rapidly changing flow conditions that contain many different continuous and discrete frequencies, urban wind environments pose a significant challenge to the operation of micro rotorcraft. Studying and understanding vehicle response in such environments creates a very large and complex trade space. Therefore, the problem must be attacked from many different approaches. In this thesis, this is achieved through experimental testing and trade studies using a high fidelity dynamic simulation in order to begin to understand how to improve the performance and reliability of micro rotorcraft in urban winds.

The performance metrics and testing methodology developed were shown to provide a valuable framework to assess mission-level performance of micro rotorcraft in both flight experiments and simulation trade studies. Inspired by established handling qualities specifications for manned rotorcraft, the metrics give a common comparison for rotorcraft in different wind features, for changes to the control architecture, and for analyzing vehicle design changes. The metrics can be used for cross platform comparisons for different rotorcraft platforms which will be even more important as novel platform designs are proposed to tackle the challenges of urban winds. Both simulated and experimental flights tested demonstrated that the metrics are useful building blocks for evaluation but it is clear that no one metric can individually capture total vehicle performance and capabilities. The metrics must be taken together to gain the most insight. Future work with the performance metrics includes continued assessment of which wind kernels and scenarios each metric is effective for as well as investigations to see if there any useful ways to describe wind speeds in terms of nondimensional parameters in order to generalize the descriptions of wind velocities in relation to size or maximum speed of a vehicle.

Trade studies employing the performance metrics and a high fidelity dynamic simulation produced a variety of interesting results and trends. Logical hypotheses such as the effects of high winds and turbulence were validated; however the peak response behavior of the micro coaxial helicopter to low frequency wind disturbances was unexpected. Trade studies into rotor flapping response further confirmed that the main cause of the peak response is the time required to tilt the helicopter thrust vector to generate horizontal forces, which will be an issue for not only the coaxial helicopter simulated but all underactuated rotorcraft. The peak response drastically increased trajectory tracking errors which could be dangerous in confined spaces or near obstacles, such as at street level. Even though mean wind speeds are relatively small close to the ground, the low frequency wind disturbances generated by shed vortices and recirculating flows could excite the peak vehicle response making operation in these areas more difficult.

Limitations due to the time required to generate horizontal forces are also apparent in other trade studies including the swashplate time constant trade study. The additional time required to generate horizontal forces make the vehicle and control law much more sensitive to increasing swashplate time constant than to increases in motor constant, which mostly affects the vertical direction—where the vehicle can generate direct forces.

Based on these results, vehicles would improve performance by generating horizontal forces as quickly as possible, which is difficult for common underactuated rotorcraft since there will always be an inherent time required to tilt the thrust vector associated with the platform’s mass moment of inertia. Therefore, novel direct force vehicles may be required in urban environments. Direct force vehicles are fully actuated systems which generate forces in all directions. In addition to minimizing the time required to generate control forces, vehicles of this nature won’t exhibit the peak response behavior to low frequency winds as the time constants for motors and other force generation mechanisms are much faster than the sensitive range of 0.2-0.4 Hz shown to be an issue in these trade studies. Future work should include more in depth design and analysis for direct force vehicles as the additional hardware required will likely reduce efficiency and control margins as well as increase the complexity of the control algorithms.

More research must also be done to understand which control architectures are best suited for operation in urban winds. Based on the trade study results, the control algorithm will benefit from including an estimation of the local wind components to improve control model fidelity and provide flight envelope protection. The ESO based estimation algorithm developed here was shown to be very useful not only for the estimation of wind states, but also for other applications where estimation of parameters for a nonlinear system is required. Also, as it is clear micro rotorcraft can expect to see larger flow magnitude, the development and analysis of guidance and control strategies for flight in winds that exceed the platform maximum flight speeds is critical, practically in the areas of obstacle avoidance and alternative trajectory generation.

Additional future work on this topic includes the continued testing of micro rotorcraft platforms in more expected urban wind fields. Specifically two scenarios that were not tested in this work were the re-ingestion the rotor wake and the composite effect of multiple prototypical wind kernels. The re-ingestion of the wake back into the rotors is expected to occur indoors in confined spaces when the vehicle flies in multiple times around the same area and can have a negative effect on platform control. The addition of multiple prototypical wind kernels starts to recreate a more generalized “messy” wind flow that is expected in urban environments. Continued testing of different disturbances in urban environments will improve the understanding vehicle performance and refine feasible mission scenarios. This will help to reduce the design trade space to the most mission critical cases which can then be studied to identify more vehicle design parameters that are important gust rejection. For future testing done in simulation, trade studies of model fidelity demonstrated that the rotor system modeling required to capture vehicle response is highly dependent on the wind fields being test. Results show that high fidelity models which include the local wind components at each blade element are only required if the spatial wind gradient over the rotor disk is quite large, greater than 0.5 m/s. Urban areas with such large gradients are most likely low to the ground, close to obstacles which create regions of detached or dead flow very close to regions of high speed flow such as eddies or vortices. Indoors, flow regions with high spatial gradients include areas around HVAC vents and open windows or doors. For all other areas where spatial wind gradients are less serve, lower fidelity models the interpolate the local wind conditions or even assume constant wind over the rotor disk capture the overall trends in performance very well.

Urban environments present a great challenge for micro rotorcraft, and thus it is imperative to continue to test and validate even the most basic assumptions and hypotheses in a trade space where performance is dependent on so many variables—all while searching for novel solutions to make micro rotorcraft even more useful.

APPENDIX A

ROTOR SYSTEM DEVELOPMENT

Rotor Dynamics

The single degree of flapping equation (equation 3.6) is a result of summing moments about the blade hinge point (equation 3.5). To detail a full expression for equation 3.6, a few parameters must be defined. The position vectors from the rotor hub center (*0*) to the hinge point (*F*) and from the hinge point to the blade center of gravity (cg) are:

$$\bar{r}_{0\rightarrow F} = \epsilon \bar{I}_H \qquad \text{and} \qquad \bar{r}_{F\rightarrow cg} = \ell^* \bar{I}_{BL} \tag{A.1}$$

The vehicle body angular velocity vector can be written as:

$$\bar{\omega}_{B/I} = p\bar{I}_B + q\bar{J}_B + r\bar{K}_B = \Omega_{xS}\bar{I}_S + \Omega_{yS}\bar{J}_S + \Omega_{zS}\bar{K}_S \tag{A.2}$$

The total blade angular velocity includes the body angular velocity as well as the rotor angular rate (Ω) and blade flapping rate ($\dot{\beta}$) as shown in equation A.3, the blade velocity in the hub frame.

$${}^{H}\bar{\omega}_{BL/I} = \left(c_{\psi_R}\Omega_{XS} + s_{\psi_R}\Omega_{YS}\right)\bar{I}_H + \left(-\dot{\beta} - s_{\psi_R}\Omega_{XS} + c_{\psi_R}\Omega_{YS}\right)\bar{J}_H + (\Omega_{ZS} + \Omega)\bar{K}_H \tag{A.3}$$

The angular momentum of the blade in the blade frame is

$${}^{BL}\bar{H}_{BL/I} = \begin{bmatrix} I_{Rxx} & 0 & 0 \\ 0 & I_{Ryy} & 0 \\ 0 & 0 & I_{Ryy} \end{bmatrix} \left[T_\beta\right] {}^{H}\bar{\omega}_{BL/I} \tag{A.4}$$

and the inertia moment can be expressed using the vector transport theorem

$$\frac{{}^{I}d\bar{H}_{BL/I}}{dt} = \frac{{}^{BL}d\bar{H}_{BL/I}}{dt} + \mathbb{S}_I(\bar{\omega}_{BL/I})\bar{H}_{BL/I} \tag{A.5}$$

where $\frac{{}^{I}d\bar{H}_{BL/I}}{dt}$ represents the inertial frame derivative and $\frac{{}^{BL}d\bar{H}_{BL/I}}{dt}$ represents the blade frame derivative. Equation A.5 can be rearranged into terms containing $\ddot{\beta}$ and those without as

$$\frac{{}^{I}d\bar{H}_{BL/I}}{dt} = \bar{H}_{\ddot{\beta}}\ddot{\beta} + \bar{H}_0 \tag{A.6}$$

The acceleration of the blade center of gravity can be expressed as

$$\begin{aligned} \bar{a}_{cg/I} = {} & \mathbb{S}_I(\bar{\alpha}_{H/I})\bar{r}_{0\to F} + \mathbb{S}_I(\bar{\omega}_{H/I})\mathbb{S}_I(\bar{\omega}_{H/I})\bar{r}_{0\to F} + \mathbb{S}_I(\bar{\alpha}_{BL/I})\bar{r}_{F\to cg} \\ & + \mathbb{S}_I(\bar{\omega}_{BL/I})\mathbb{S}_I(\bar{\omega}_{BL/I})\bar{r}_{F\to cg} \end{aligned} \tag{A.7}$$

where $\bar{\alpha}_{H/I}$ and $\bar{\alpha}_{BL/I}$ are the angular accelerations of the hub and blade frames and the angular velocity of the hub frame is

$$\bar{\omega}_{H/I} = \bar{\omega}_{B/I} + \Omega\bar{K}_H \tag{A.8}$$

As with equation A.6, the linear acceleration can separated into parts containing $\ddot{\beta}$and those without:

$$\bar{a}_{cg} = \bar{A}_{\ddot{\beta}}\ddot{\beta} + \bar{A}_0 \tag{A.9}$$

Thus, in equation 3.6 H_0 and A_0 can be expanded as

$$\begin{aligned} H_0 = {} & I_{Rxx}\Omega\Omega_{xS}c_\beta^2 c_{\psi_R} - I_{Ryy}\Omega\Omega_{xS}c_{\psi_R} - I_{Rzz}\Omega\Omega_{xS}c_\beta^2 c_{\psi_R} + I_{Rxx}\Omega_{xS}\Omega_{zS}c_\beta^2 c_{\psi_R} - \\ & I_{Rzz}\Omega_{xS}\Omega_{zS}c_\beta^2 c_{\psi_R} + I_{Rxx}\Omega^2 c_\beta s_\beta + I_{Rzz}\Omega^2 c_\beta s_\beta + 2I_{Rxx}\Omega\Omega_{zS}c_\beta s_\beta - 2I_{Rzz}\Omega\Omega_{zS}c_\beta s_\beta + \\ & I_{Rxx}\Omega_{zS}^2 c_\beta s_\beta - I_{Rzz}\Omega_{zS}^2 c_\beta s_\beta - I_{Rxx}\Omega_{xS}^2 c_\beta c_{\psi_R}^2 s_\beta + I_{Rzz}\Omega_{xS}^2 c_\beta c_{\psi_R}^2 s_\beta - \\ & I_{Rxx}\Omega_{xS}\Omega_{zS}c_{\psi_R}s_\beta^2 + I_{Rzz}\Omega_{xS}\Omega_{zS}c_{\psi_R}s_\beta^2 - I_{Ryy}\Omega\Omega_{yS}s_{\psi_R} + I_{Rxx}\Omega\Omega_{yS}c_\beta^2 s_{\psi_R} - \\ & I_{Rzz}\Omega\Omega_{yS}c_\beta^2 s_{\psi_R} + I_{Rxx}\Omega_{yS}\Omega_{zS}c_\beta^2 s_{\psi_R} - I_{Rzz}\Omega_{yS}\Omega_{zS}c_\beta^2 s_{\psi_R} - \\ & 2I_{Rxx}\Omega_{xS}\Omega_{yS}c_\beta c_{\psi_R}s_\beta s_{\psi_R} + 2I_{Rzz}\Omega_{xS}\Omega_{yS}c_\beta c_{\psi_R}s_\beta s_{\psi_R} - I_{Rxx}\Omega\Omega_{yS}s_\beta^2 s_{\psi_R} + \end{aligned}$$

$$I_{Rzz}\Omega\Omega_{yS}s_\beta^2 s_{\psi_R} - I_{Rxx}\Omega_{yS}\Omega_{zS}s_\beta^2 s_{\psi_R} + I_{Rzz}\Omega_{yS}\Omega_{zS}s_\beta^2 s_{\psi_R} - I_{Rxx}\Omega_{yS}^2 c_\beta s_\beta s_{\psi_R}^2 + I_{Rzz}\Omega_{yS}^2 c_\beta s_\beta s_{\psi_R}^2 \tag{A.10}$$

$$A_0 = l^*\Omega\Omega_{xS}c_{\psi_R} + 2\epsilon\Omega\Omega_{xS}c_\beta c_{\psi_R} + \epsilon\Omega_{xS}\Omega_{zS}c_\beta c_{\psi_R} + l^*\Omega\Omega_{xS}c_\beta^2 c_{\psi_R} + l^*\Omega_{xS}\Omega_{zS}c_\beta^2 c_{\psi_R} + \epsilon\Omega^2 s_\beta + 2\epsilon\Omega\Omega_{zS}s_\beta + \epsilon\Omega_{zS}^2 s_\beta + l^*\Omega^2 c_\beta s_\beta + 2l^*\Omega\Omega_{zS}c_\beta s_\beta + l^*\Omega_{zS}^2 c_\beta s_\beta + \epsilon\Omega_{yS}^2 c_{\psi_R}^2 s_\beta - l^*\Omega_{xS}^2 c_\beta c_{\psi_R}^2 s_\beta - l^*\Omega\Omega_{xS}c_{\psi_R} s_\beta^2 - l^*\Omega_{xS}\Omega_{zS}c_{\psi_R}s_\beta^2 + l^*\Omega\Omega_{yS}s_{\psi_R} + 2\epsilon\Omega\Omega_{yS}c_\beta s_{\psi_R} + \epsilon\Omega_{yS}\Omega_{zS}c_\beta s_{\psi_R} + l^*\Omega\Omega_{yS}c_\beta^2 s_{\psi_R} + l^*\Omega_{yS}\Omega_{zS}c_\beta^2 s_{\psi_R} - 2\epsilon\Omega_{xS}\Omega_{yS}c_{\psi_R}s_\beta s_{\psi_R} - 2l^*\Omega_{xS}\Omega_{yS}c_\beta c_{\psi_R}s_\beta s_{\psi_R} - l^*\Omega\Omega_{yS}s_\beta^2 s_{\psi_R} - l^*\Omega_{yS}\Omega_{zS}s_\beta^2 s_{\psi_R} + \epsilon\Omega_{xS}^2 s_\beta s_{\psi_R}^2 - l^*\Omega_{yS}^2 c_\beta s_\beta s_{\psi_R}^2 \tag{A.11}$$

Rotor Forces and Moments

The blade element section aerodynamic forces are calculated used the local aerodynamic velocity components in the blade frame (Fig. 3.3). The position vector from the blade hinge point to the center of blade element section (p) is

$$\bar{r}_{F\to p} = r_x\bar{I}_{BL} + r_y\bar{J}_{BL} + r_z\bar{K}_{BL} \tag{A.12}$$

The local aerodynamic velocity vector is shown in equation A.13.

$$\bar{V}_p = \bar{V}_0 + \mathbb{S}_I(\bar{\omega}_{H/I})\bar{r}_{0\to F} + \mathbb{S}_I(\bar{\omega}_{BL/I})\bar{r}_{F\to p} - \bar{V}_{atm} - v_i\bar{K}_S \tag{A.13}$$

where $\bar{V}_0$ is body velocity, $\bar{V}_{atm}$ is the atmospheric wind disturbance, and v_i is the induced rotor inflow velocity.

$$\bar{V}_0 = V_{0x}\bar{I}_S + V_{0y}\bar{J}_S + V_{0z}\bar{K}_S \tag{A.14}$$

$$\bar{V}_{atm} = V_{atmx}\bar{I}_S + V_{atmy}\bar{J}_S + V_{atmz}\bar{K}_S \tag{A.15}$$

Thus the tangential and perpendicular velocity components are:

$$u_T = \epsilon\Omega + \epsilon\Omega_{zS} + \Omega r_x c_\beta + \Omega_{zS} r_x c_\beta - V_{atmy} c_\psi + V_{oy} c_\psi - \Omega_{xS} r_z c_\beta c_\psi - \Omega r_z s_\beta - \Omega_{zS} r_z s_\beta - \Omega_{xS} r_x c_\psi s_\beta + V_{atmx} s_\psi - V_{ox} s_\psi - \Omega_{yS} r_z c_\beta s_\psi - \Omega_{yS} r_x s_\beta s_\psi + c_\psi v_{iy} - s_\psi v_{ix} \tag{A.16}$$

$$u_P = \dot{\beta} r_x - V_{atmz} c_\beta + v_i c_\beta - c_\psi s_\beta v_{ix} - s_\beta s_\psi v_{iy} + V_{oz} c_\beta - \Omega_{yS} r_x c_\psi - \epsilon\Omega_{yS} c_\beta c_\psi + \Omega_{xS} r_y c_\beta c_\psi + \Omega r_y s_\beta + \Omega_{zS} r_y s_\beta + V_{Gx} c_\psi s_\beta - V_{ox} c_\psi s_\beta + \Omega_{xS} r_x s_\psi + \epsilon\Omega_{xS} c_\beta s_\psi + \Omega_{yS} r_y c_\beta s_\psi + V_{atmy} s_\beta s_\psi - V_{oy} s_\beta s_\psi \tag{A.17}$$

REFERENCES

[1] M. Costello, "Challenges Facing Micro Air Vehicle Flight Dynamics and Controls Engineers," *46th AIAA Aerospace Sciences Meeting and Exhibit,* January 2008.

[2] G. Cai, B. M. Chen and T. H. Lee, "An Overview on Development of Miniature Unmanned Rotorcraft Systems," *Frontiers of Electrical and Electronic Engineering in China,* vol. 5, no. 1, 2010.

[3] C. Galinkski and R. Zbikowski, "Some Problems of Micro Air Vehicles Development," *Bulletin of the Polish Academy of Sciences: Technical Sciences,* vol. 55, no. 1, 2007.

[4] V. Kumar and N. Michael, "Opportunities and Challenges with Autonomous Micro Aerial Vehicles," *Proceedings of the International Symposium of Robotic Research*, 2011.

[5] Y. Ketema and Y. Zhao, "Micro Air Vehicle Trajectory Planning in Winds," *Journal of Aircraft*, vol. 47, no. 4, 2010.

[6] Anon., "Journal of Wind Engineering & Industrial Aerodynamics: Aims and Scope," Elsevier, 2013. [Online]. Available: http://www.journals.elsevier.com/journal-of-wind-engineering-and-industrial-aerodynamics/. [Accessed June 2013].

[7] Anon., "International Association of Wind Engineering: Purpose," IAWE, July 2011. [Online]. Available: http://www.iawe.org/purp.html. [Accessed June 2013].

[8] S. Lane, J. Barlow and C. Wood, "An assessment of a three-beam Doppler lidar wind profiling method for use in urban areas," *Journal of Wind Engineering and Industrial Aerodynamics,* vol. 119, pp. 53-59, August 2013.

[9] H. Wang, A. Li, J. Nui, Z. Zong and J. Li, "Long-term monitoring of wind characteristics at Sutong Bridge site," *Journal of Wind Engineering and Industrial Aerodynamics,* vol. 115, pp. 39-47, April 2013.

[10] G. Kopp and D. Banks, "Use of the Wind Tunnel Test Method for Obtaining Design Wind Loads on Roof-Mounted Solar Arrays," *Journal of Structural Engineering,* vol. 139, no. 2, p. 284–287, 2013.

[11] S. K. Au and P. To, "Full-Scale Validation of Dynamic Wind Load on a Super-Tall Building under Strong Wind," *Journal of Structural Engineering,* vol. 138, no. 9, pp. 1161-1172, 2012.

[12] T. Uffinger, I. Ali and S. Becker, "Experimental and numerical investigations of the flow around three different wall-mounted cylinder geometries of finite length," *Journal of Wind Engineering and Industrial Aerodynamics,* vol. 119, pp. 13-27, August 2013.

[13] F. Brusiani, S. de Miranda, L. Patruno, F. Ubertini and P. Vaona, "On the evaluation of bridge deck flutter derivatives using RANS turbulence models," *Journal of Wind Engineering and Industrial Aerodynamics,* vol. 119, pp. 39-47, August 2013.

[14] D. Galway, J. Etele and G. Fusina, "Modeling of Urban Wind Field Effects on Unmanned Rotorcraft Flight," *Journal of Aircraft*, vol. 48, no. 5, 2011.

[15] W. Frost and A. Shahabi, "A Field Study of Wind Over a Simulated Block Building," *NASA Technical Report, NASA CR-2804*, March 1977.

[16] H. Nagib and T. Corke, "Wind Microclimate Around Buildings: Characteristics and Control," *Journal of Wind Engineering and Industrial Aerodynamics,* vol. 16, pp. 1-15, 1984.

[17] Anon., "Framers Alamanc Weather History Results for Atlanta, GA," August 2011. [Online]. Available: http://www.farmersalmanac.com/weather-history/30328/2011/08/11/. [Accessed 6 January 2013].

[18] Anon., "NOAA Climate Data Online Daily Averages: Fulton County Airport, Atlanta GA," August 2011. [Online]. Available: http://www.ncdc.noaa.gov/cdo-web/search. [Accessed 6 January 2013].

[19] J. Straube, "Building Sciences Digest: Air Flow Control in Buildings," 5 May 2008. [Online]. Available: http://www.buildingscience.com/documents/digests/bsd-014-air-flow-control-in-buildings?topic=doctypes/digests.

[20] E. Johnson and J. Jacob, "Development and Testing of a Gust and Shear Tunnel for NAVs and MAVs," *47th AIAA Aerospace Sciences Meeting Including The New Horizons Forum and Aerospace Exposition,* January 2009.

[21] T. Hasma, S. Kato and R. Ooka, "Analysis of wind-induced inflow and outflow through a single opening using LES & DES," *Journal of Wind Engineering and Industrial Aerodynamics,* vol. 96, no. 10, pp. 1678-1691, 2008.

[22] E. Conceição, V. Vicentea and M. Lúciob, "Airflow Inside School Building Office Compartments with Moderate Environments," *HVAC&R Research,* vol. 14, no. 2, March 2008.

[23] D. Pines and F. Bohorquez, "Challenges Facing Future Micro-Air-Vehicle Development," *Journal of Aircraft,* vol. 43, no. 2, March-April 2006.

[24] Anon, "PD-100 PRS: Proxdynamics," Proxdynamics, 2013. [Online]. Available: http://www.proxdynamics.com/products/pd_100_prs/. [Accessed July 2013].

[25] B. Mettler, M. Tischler and T. Kanade, "System Identification Modelding of a Small-Sclae Unmanned Rotorcraft for Flight Control Design," *Journal of the American Helicopter Society,* vol. 47, no. 1, 2002.

[26] V. Gavrilets, E. Frazzoli, B. Mettler, M. Piedmonte and E. Feron, "Agressive Maneuvering of Small Autonomous Helicopters:A Human-Centered Approach," *The International Journl of Robotics Research,* vol. 20, no. 10, 2001.

[27] G. Cai, B. Chen, T. Lee and K. Lum, "Comprehensive Nonlinear Modeling of a Miniature Unmanned Helicopter," *Journal of the American Helicopter Society,* vol. 57, no. 1, January 2012.

[28] J. Conroy, J. S. Humbert and D. Pines, "System Identification of a Rotary-Wind Micro Air Vehicle," *Journal of the American Helicopter Society,* vol. 56, no. 2, April 2011.

[29] D. Schafroth, "Aerodynamics, Modeling, and Control of an Autonomous Micro Helicopter," Ph.D Thesis, ETH Zurich, DISS ETH No. 18901, 2010.

[30] M. Costello, G. H. Gaonkar, J. V. R. Prasad and D. P. Schrage, "Some Issues Modeling Atmospheric Turbulence Experienced by Helicopter Rotor Blades," *Journal of the American Helicopter Society,* pp. 71-75, April 1992.

[31] G. Gaonkar, "Review of Turbulence Modeling and Related Applications to Some Problems of Helicopter Flight Dynamics," *Journal of the American Helicopter Society,* 2008.

[32] T. Cheviron, A. Chriette and F. Plestan, "Robust Control of an Autonmouns Reduced Scale Helicopter in Presence of Wind Gusts," *AIAA Guidance, Navigation, and Control Conference and Exhibit,* August 2006.

[33] A. Martini, F. Léonard and G. Abba, "Dynamic Modelling and Stability Analysis of Model-Scale Helicopters Under Wind Gust," *Journal of Intelligent and Robotic Systems,* 2009.

[34] F. Léonard, A. Martini and G. Abba, "Robust Nonlinear Controls of Model-Scale Helicopters Under Lateral and Vertical Wind Gusts," *IEEE Transactions on Control Systems Technology,* vol. 20, no. 1, 2012.

[35] M. Bisgaard, A. la Cour-Harbo and K. Danapalasingam, "Nonlinlear Feedforward Control for Wind Disturbance Rejection on Autonmous Helicopter," in *The 2010 IEEE/RSJ International Conferecne on Intelligent Robots and Systems*, Taipei, Taiwan, 2010.

[36] X. Yang, H. Pota and M. Garratt, "Design of a Gust-Attenuation Controller for Landing Operations of Unmanned Autonmous Helicopters," *18th IEEE International Conference on Control Applications,* July 2009.

[37] K. Alexis, G. Nikolakopoulos and A. Tzes, "Experimental Model Predictive Tracking Control of a Quadrotor Helicopter Subject to Wind-Gusts," *18th Mediterranean Conference on Control & Automation,* June 2010.

[38] V. Hrishikeshavan and I. Chopra, "Aeromechanics and Control of a Shrouded Rotor Micro Air Vehicle in Hover and in Edgewise Flow," *Journal of the American Helicopter Society,* vol. 56, 2011.

[39] D. Rezgui, M. Lowenberg and P. Bunniss, "Design Concept for Stabilising and Controlling Rotary Wing Micro Air Vehicles in Gusts," *21st Bristol International UAV Systems Conference,* 2007.

[40] F. Hoblit, Gust Loads on Aircraft: Concepts and Applications, AIAA Education Series, 1988.

[41] J. Roadman and K. Mohseni, "Gust Characterization and Generation for Wind Tunnel Testing of Micro Aerial Vehicles," in *47th AIAA Aerospace Sciences Meeting Including the New Horizons Forum and Aerospace Exposition*, Orlando, Florida, 2009.

[42] Anon., "Flying Qualities of Piloted Airplanes. Military Specification," *USAF, MIL-F-8785C,* 1980.

[43] Anon., "Flying Qualities of Piloted V/STOL Aircraft. Military Specification," *USA, MIL-F-83300,* 1970.

[44] Anon., "Handling Qualities Requirements for Military Rotorcraft," *Aeronautical Design Standard - 33 (ADS-33E-PRF), US Army Aviation and Missile Command,* March 2000.

[45] S. Labows, "UH-60 Black Hawk Distrubance Rejection Study for Hover/Low Speed Handling Qualities Criteria and Turbulence Modeling," *Master's Thesis, Naval Postgraduate School,* 2000.

[46] R. Hess, "Simplified Technique for Modeling Piloted Rotorcraft Operations Near Ships," *Journal of Guidance, Control, and Dynamics,* vol. 29, no. 6, pp. 1339-1349, 2006.

[47] J. Lusardi, M. Tischler, C. Blanken and S. Labows, "Empirically Derived Helicopter Response Model and Control System Requirements for Flight in Turbulence," *Journal of the American Helicopter Society*, July 2004.

[48] D. Lee and J. Horn, "Simulation of Pilot Workload for a Helicopter Operating in a Turbulent Ship Airwake," *Proceedings of the Institution of Mechanical Engineers, Part G: Journal of Aerospace Engineering,* 2005.

[49] D. Miller, C. Morse and J. Wood, "HACT Flight Control System (HFCS) Control Law Overview," *American Helicopter Society 58th Annual Forum*, June 2002.

[50] D. Miller, E. de Brun, Y. Lu and P. Hagar, "V-22 Roll-on-Deck Control Law Design," *Journal of the American Helicopter Society*, vol. 55, no. 2, April 2010.

[51] J. Horn, D. Bridges and D. Lee, "Flight Control Design for Alleviation of Pilot Workload During Helicopter Shipboard Operations," *the American Helicopter Society 62th Forum,* 2006.

[52] J. Horn and D. Bridges, "A Model Following Controller Optimized for Gust Rejection during Shipboard Operations," *American Helicopter Society 63th Annual Forum,* 2007.

[53] Anon.. [Online]. Available: http://www.sikorsky.com

[54] Anon.. [Online]. Available: http://www.boeing.com/rotorcraft/military/v22/v22spec.htm. [Accessed 6 February 2012].

[55] H. Makita, "Realization of a Large-Scale Turbulence Field in a Small Wind Tunnel," *Fluid Dynamics Research* , vol. 8, pp. 53-94, 1991.

[56] M. Sytsma and L. Ukeiley, "Wind Tunell Generated Turbulence," *49th AIAA Aerospace Sciences Meeting including the New Horizons Forum and Aerospace Exposition*, January 2011.

[57] M. Shinozuka and C. Jan, "Digital Simulation of Random Processes and Its Applications," *Journal of Sound and Vibration*, vol. 25, no. 1, pp. 111-128, 1972.

[58] M. Shinozuka and G. Deodatis, "Simulation of Stochastic Processes by Spectral Representation," *Apple Mech Rev,* vol. 44, no. 4, pp. 191-204, 1991.

[59] M. W. Rotach, "Profiles of Turbulences Statistics in and Above an Urban Street Canyon," *Atmospheric Environment*, vol. 29, no. 13, 1995.

[60] W. Frank and H. Mauch, "Large-Eddy Simulation of the Flow Around Building Models," *Journal of Wind Engineering and Industrial Aerodynamics,* no. 46 & 47, pp. 213-218, 1993.

[61] C. a. I. A. K. S. Farell, "Experiments on the Wind Tunnel Simulation of Atmospheric Boundary Layers," *Journal of Wind Engineering and Industrial Aerodynamics,* vol. 79, pp. 11-35, 1999.

[62] M. P. Straw, C. J. Baker and A. P. and Roberston, "Experimental Measurements and Computations of the Wind-induced Ventilation of a Cubic Structure," *Journal of Wind Engineering and Industrial Aerodynamics,* vol. 88, pp. 213-230, 2000.

[63] H. Tamai, Y. Okuda and J. Katsura, "On relation between Reynolds number and Karman vortex formation on a bluff body in natural wind," *Journal of Wind Engineering and Industrial Aerodynamics,* no. 89, 2001.

[64] M. Ol, G. Parker, G. Abate and J. Evers, "Flight Controls and Performance Challenges for MAVs in Complex Environments," *AIAA Guidance, Navigation, and Control Conference and Exhibit,,* August 2008.

[65] E. Beyer, "Design, Testing, and Performance of a Hybrid Micro Vehicle – the Hopping Rotochute," *Ph.D. Dissertation, School of Aerospace Engineering, Georgia Institute of Technology,* 2009.

[66] G. Frost and M. Costello, "Simulation of a Mortar Launched Parachute Deployed Battlefield Imaging System," *Journal of Dynamic Systems, Measurement, and Control,* vol. 126, September 2004.

[67] D. A. Jenkins, P. G. Ifju, M. Abdulrahim and S. Olipra, "Assessment of Controllability of Micro Air Vehicles," in *Proc. 16th Int. Conf. on Unmanned Air Vehicle Systems,* Bristol, United Kingdom, 2001.

[68] Anon., "System-Side Impedance-Track Fuel Gauge With Direct Battery Connection," [Online]. Available: http://www.ti.com/product/bq27510-g2. [Accessed 26 July 2012].

[69] A. Mehta and K. Pister, "WARPWING: A complete open source control platform for miniature robots," *2010 IEEE/RSJ International Conference on Intelligent Robots and Systems (IROS 2010),* 2010.

[70] J. G. Leishman, Principles of Helicopter Aerodynamics, Cambridge: Cambridge University Press, 2006.

[71] J. Katz and A. Plotkin, Low-Speed Aerodynamics: From Wing Theory to Panel Methods, New York: McGraw-Hill, Inc., 1991.

[72] R. Prouty, Helicopter Performance, Stability, and Control, Malabar: Krieger Publishing Company, 2005.

[73] S. Hoerner, Fluid-dynamic drag: Practical Information on Aerodynamic Drag and Hydrodynamic Resistance, Bakersfield, CA: Hoerner Fluid Dynamics, 1985.

[74] M. Costello and E. Beyer, "Performance of a projectile/rotor kinetic energy reduction system," in *AHS International Specialists' Meeting - Unmanned Rotorcraft: Design, Control and Testing*, Chandler, AZ, 2007.

[75] V. Klein and E. A. Morelli, Aircraft System Identification: Theory and Practice, American Institute of Aeronautics and Astronautics, 2006.

[76] A. J. Wheeler and A. R. Ganji, Introduction to Engineering Experimentation, 2nd ed., Upper Saddle River, NJ: Person Prentice Hall, 2004.

[77] W. N. Venables and B. D. Ripley, Modern Applied Statistics with S, Springer Science + Business Media, Inc., 2002.

[78] J. Han, "From PID to Active Disturbance Rejection Control," *IEEE Transactions on Industrial Electrionics*, vol. 56, no. 3, 2009.

[79] Y. Hou, Z. Gao, F. Jiang and B. Bolter, "Active Distrubance Rejection Control for Web Tension Regulation," *Proceedings of the 40th IEEE Conference on Decision and Control*, 2001.

[80] Y. Su, B. Y. Duan, C. H. Zheng, Y. F. Zhang, G. D. Chen and J. W. Mi, "Disturbance-rejection high-precision motion control of a Stewart Platform," *IEE Trans. Control Sys. Technol.*, vol. 12, no. 3, pp. 364-374, 2004.

[81] Y. Huang, X. Kekang, H. Jingqing and J. Lam, "Flight Control Design Using Extended State Observer and Non-smooth Feedback," *Proceedings of the 40th IEEE Conference on Decision and Control*, 2001.

[82] I. Yayruck, J. V. R. Prasad and S. Unnikrishnan, "Envelope Protection for Autonomous Unmanned Aerial Vehicles," *Journal of Guidance, Control, and Dynamics*, vol. 32, no. 1, 2009.

[83] A. Kuehte and C. Chow, Foundations of Aerodynamics: Bases of Aerodynamic Design,

New York: John Wiley & Sons, Inc., 1998.

[84] S. Oikawa and Y. Meng, "Turbulence Characteristics and Organized Motion in a Suburban Roughness Sublayer," *Boundary-Layer Meteorology,* vol. 74, pp. 298-312, 1995.

[85] F. Riccardelli and S. Polimeno, "Some characteristics of the wind flow in the Lower Urban Boundary Layer," *Journal of Wind Engineering and Industrial Aerodynamics,* no. 94, pp. 815-8832, 2006.

[86] J. A. Peterka, R. N. Meroney and K. M. Kothari, "Wind Flow Patterns About Buildings," *Journal Wind Engineering and Industrial Aerodynamics,* no. 21, pp. 21-38, 1985.

[87] C. P. W. Geurts, H. S. Rutten and J. A. Wisse, "Spectral Characteristics of Wind Induced Pressures on a Full Scale Building in Suburban Terrain," *Journal of Wind Engineering and Industrial Aerodynamics,* no. 69-71, 1997.

[88] S. Campbell, J. Kaneshige, N. Nguyen and K. Krishnakumar, "An Adaptive Control Simulation Study using Pilot Handling Qualities Evaluations," in *AIAA Guidance, Navigation, and Control Conference,* Toronto, Ontario, Canada, 2010.

[89] S. Campbell, J. Kaneshige, N. Nguyen and K. Krishnakumar, "Implementation and Evaluation of Multiple Adaptive Control Technologies for a Generic Transport Aircraft Simulation," in *AIAA Infotech@Aerospace*, Atlanta GA, 2010.

[90] E. Johnson and S. Kanna, "Adaptive Flight Control for an Autonmous Unmanned Helicopter," in *AIAA Guidance, Navigation, and Control Conference and Exhibit*, Monterey, California, 2002.

[91] B. Crowther, A. Lanzon, M. Maya-Gonzalez and D. Langkamp, "Kinematic Analysis and Control Design for a Nonplanar Multirotor Vehicle," *Journal of Guidance, Control, and Dynamics,* vol. 34, no. 4, July-August 2011.

[92] M. Abraham and M. Costello, "In-Flight Estimation of Helicopter Gross Weight and Mass Center Location," *Journal of Aircraft,* vol. 46, no. 3, 2009.

[93] D. Simon, Optimal State Estimation: Kalman, H Inifinity, and Nonlinear Approaches, Hoboken, N.J.: Wiley-Interscience, 2006.

[94] M. Morales and D. Hass, "Feasiblity of Aircraft Gross Weight Estimation Using Artificial Neural Networks," *American Helicopter Society 57th Annual Forum,* pp. 1872-1880, 2001.

[95] M. Idan, G. Iosilevskii and S. Nazarov, "In-Flight Weight and Balance Identification Using

Neural Networks," *Journal of Aircraft,* vol. 41, no. 1, pp. 137-143, 2004.

[96] N. Apetre, S. Sarkar, N. Iyyer and N. and Phan, "Innovative Methods to Estimate Rotorcraft Gross Weight and Center of Gravity," in *American Helicopter Society 67th Annual Fourm,* Virginia Beach, VA, 2011.

[97] Anon., "Operator's Manual: Army Model UH-1H/V Helicopters," Headquarters, Department of the Army , TM 55-1520-210-10, February 1988.

[98] Anon., "Operator's Manual for Helicopter, Attack, AH-64A Apache," Headquarters, Department of the Army, TM 1-1520-238-10, August 1994.

[99] J. J. Howlett, "UH-60A Black Hawk Engineering Simulation Program: Volume I - Mathematical Model," NASA Contractor Report 166309, December 1981.